University of Liverpool, School of Engineering

ELECTROCHEMICAL PROPERTIES OF POROUS METALS MANUFACTURED BY LOST CARBONATE SINTERING PROCESS

Thesis submitted in accordance with the requirement of the University of Liverpool for the Doctor degree of Philosophy

By

Pengcheng Zhu

February 2019

ACKNOWLEDGEMENTS

I would like to thank my supervisor, Prof. Yuyuan Zhao, for his patient guidance, constant support and encouragement throughout the past three years. I appreciate all his contributions of time, ideas and funding to make my Ph.D. experience productive and stimulating. The joy and enthusiasm he has for his research was contagious and motivational for me. I am also thankful for the excellent example he has provided as a conscientious and dedicative professor.

I must express my gratitude to Dr. Liping Zhang for her continued support and encouragement in both my study and life. Her kindness and words of wisdom have inspired me a lot, especially during my tough period.

Sincere thanks to Dr. Richard Potter, my second supervisor, for providing me recommendation letter in my Ph.D. application and also giving me a lot of invaluable comments and suggestions during this journey.

Special thanks to Dr. Trevor Davies for his knowledge support in electrochemistry.

Special thanks to Mr. Dave Atkinson for his continued professional technical support.

I am also grateful to all friends in our research group, in particular, Kaikan, Jan, Edgar, Zhining, Yue, Xianke, Chen and Bhavik, who made this experience special.

Last but not least, I would like to thank my loving wife, Mengru Yang, my father, Zhinong Zhu, my mother, Ping Hu, and my family who have showered me with their unconditional love, sacrifice, support and motivation throughout this long journey to success.

LIST OF PUBLICATIONS

ZHU, P. & ZHAO, Y. 2017. Effects of electrochemical reaction and surface morphology on electroactive surface area of porous copper manufactured by Lost Carbonate Sintering. RSC Advances, 7, 26392-26400

ZHU, P. & ZHAO, Y. 2017. Mass transfer performance of porous nickel manufactured by Lost Carbonate Sintering process. Advanced Engineering Materials, 19, 1700392.

ABSTRACT

Porous metals have attracted considerable attention in academia and industry due to their unique combinations of material and structural characteristics, including high surface area, good catalytic ability, high permeability, light weight, and good mechanical properties. They have been considered as excellent materials for applications in electrochemical detection and energy generation.

This project measured the surface area and mass transfer coefficient of the porous metals manufactured by the Lost Carbonate Sintering (LCS) process and further studied the effects of structural parameters (porosity and pore size), manufacturing process (sintering temperature and metal particle size), chemical etching treatments and diffusion layer thickness. Additionally, a novel limiting current sensor with LCS porous Ni working electrode was developed for determination of ferricyanide concentration.

The surface area of porous metals is normally measured by either the BET gas absorption method or the mercury intrusion method. However, both methods have their own limitations. BET is not applicable for pores too big, while the mercury intrusion method is not suitable for pores too small. Besides, the BET method measures the surface area at an extremely small length scale and the mercury intrusion method assumes all pores are cylindrical. Neither is appropriate for the measurement of electrochemical surface area. In this thesis, the geometric, electroactive and real surface areas of the LCS porous Cu and Ni were measured using quantitative stereology, cyclic voltammetry (CV) peak current and double layer capacitance methods, respectively. The cyclic voltammetry peak current method exactly determines the effective surface area in electrochemical reactions and the

double layer capacitance method accurately measures the surface area where electrical double layer is formed.

For the first time, two reactions with different diffusion layer thicknesses were employed to study the effect of diffusion layer thickness on the electroactive surface area of the LCS porous Cu. The electroactive surface area was increased by up to 2 times when the diffusion layer thickness was decreased from 50 µm to 1 µm. The effects of Cu particle size, sintering temperature and chemical treatment on the surface morphology and therefore the electroactive and real surface areas were also investigated. Cu particle size had a modest effect, with the medium particle sizes, 20 – 45 µm and 45 – 75 µm, showing the highest surface areas. Increasing sintering temperature from 850˚C to 950˚C or etching the samples by 5 M nitric acid for 5 minutes reduced the electroactive and real surface areas by 31% – 61% and 9% – 25%, respectively.

For the surface area of the LCS porous Ni, the volumetric specific geometric, electroactive and real surface areas of the porous Ni samples, with pore sizes in the range of 250 – 1500 µm and porosities in the range of 0.55 – 0.85, are in the ranges of 20 – 100, 30 – 100 and 200 – 1000 cm^{-1}, respectively. Their gravimetric specific geometric, electroactive and real surface areas are in the ranges of 5 – 65, 9 – 70 and 100 – 300 cm^2/g, respectively. The electroactive surface area increases with increasing scan rate. The matrix material does not affect the geometric surface area and the real surface area is slightly affected by the metal particles used, while electroactive surface area is mainly affected by the diffusion layer thickness.

The mass transfer coefficient of porous Ni was measured by the limiting current technique. For porous Ni samples with a porosity of 0.55 – 0.75 and a pore size of 250 – 1500 µm, the

mass transfer coefficient, measured at an electrolyte flow velocity range of 1 – 12 cm/s, is in the range of 0.0007 – 0.014 cm/s, which is up to 7 times higher than that of a solid nickel plate electrode. The mass transfer coefficient increases with pore size but decreases with porosity. The porous nickel has Sherwood numbers considerably higher than the other nickel electrodes reported in the literature, due to its high real surface area and its tortuous porous structure, which promotes turbulent flow.

A novel limiting current sensor containing a pumping system and a three-electrode electrochemical cell was developed for the determination of ferricyanide concentration. A porous Ni sample with a porosity of 0.7 and a pore size range of 425 – 710 µm was used as the working electrode. The limiting current sensor showed a limit of detection (LOD) range of 5.35×10^{-6} – 8.7×10^{-6} M and a sensitivity range of 7.47 – 20.24 mM/mA. The sensitivity increases with increasing fluid flow rate. A conventional three-electrode electrochemical sensor, with the same LCS porous Ni working electrode, was also used for measuring the concentration of ferricyanide. The three-electrode electrochemical sensor showed a LOD range of 0.21×10^{-4} – 0.58×10^{-4} M and a sensitivity of 0.33 – 1.50 mM/mA. Both LOD and sensitivity increase with increasing scan rate. The limiting current sensor showed a much lower LOD and much higher sensitivity than the three-electrode electrochemical sensor due to the turbulent fluid flow through the porous matrix in the limiting current sensor.

Contents

List of figures

Chapter 2

Chapter 3

Chapter 4

Chapter 5

Chapter 6

Chapter 7

CHAPTER 1 INTRODUCTION

1.1 Background of the research

Porous metals are metals containing pores which are deliberately embedded in metal matrix (Lefebvre et al., 2008). Porous metals can be divided into two types: closed-cell and open-cell, depending on the connectivity of pores. If pores are separated by solid walls, the porous metal is called closed-cell. If pores are connected with each other, the porous metal is described as open-cell (Lefebvre et al., 2008). Porous metals with isolated and connected pores have been regarded as excellent multifunctional materials due to their unique mechanical, thermal, electrical, acoustic, physical and chemical properties (Lefebvre et al., 2008, Ashby et al., 2000, Banhart, 2001). In this thesis, only open-cell porous metals are considered.

Lost Carbonate Sintering (LCS) is a powder metallurgy (PM) based space holder technique for manufacturing open-cell porous metals (Zhao et al., 2005, Zhang and Zhao, 2008). In this process, metal and potassium carbonate powders are first mixed together with an intended ratio. The mixture is then compacted into a preform, followed by sintering in a vacuum furnace. The potassium carbonate particles can be removed by either dissolution in hot water or decomposition at high temperature. Other space holders like sodium chloride (Zhao and Sun, 2001) and urea (Laptev et al., 2004) have also been reported. Porous metals manufactured by the LCS process have highly controllable porosity, pore size and even pore shape. The porosity and pore size of the LCS porous metals are normally in the ranges of 0.5 – 0.85 and 75 – 1500 μm, respectively (Zhao et al., 2005).

High specific surface area is one of the most important characteristics of open-cell porous metals, especially for electrochemical applications. Surface area can be divided into three types: geometric, electroactive and real surface areas (Diao et al., 2015). The geometric surface area is the surface area of the primary pores, while the real surface area includes all the surface areas of pores and interstices where the electrical double layer can be formed (Li et al., 2014). The electroactive surface area is the effective surface area contributing to chemical reactions (Delahay, 1956, Bard et al., 1980), which is often different from the geometric and real surface areas. The electroactive surface area can be measured by an electrochemical method. It is sensitive to the applied scan rate (Tan et al., 2012) and is expected to be highly chemical reaction dependent. Previous work by Diao et al. (2015) has shown that the volumetric electroactive surface area of porous copper in 0.1 M KOH at a scan rate of 0.026 V/s increases slightly with increasing porosity but decreases with increasing pore size. The value of the electroactive surface area is one order of magnitude greater than the geometric surface area but is one order of magnitude less than the real surface area. However, there are still many questions remaining. For example, how do the scan rate and chemical reaction affect the electroactive surface area? Does the surface morphology affect the geometric, electroactive and real surface areas? Therefore, further work is needed to answer these questions.

Mass transfer property is another important characteristic of open-cell porous metals for electrochemical applications. It determines the rate of the movement of a chemical species from bulk solution to the surface of porous matrix and therefore limits the current density generated (Brown et al., 1992). The mass transfer performance is affected by several intrinsic factors, e.g. pore size and porosity. By decreasing pore size, the mass transfer

performance of SORAREC porous nickel has been increased (Zhou et al., 2015). The porous copper fibre sintered felt (PCFSF) sample with a porosity of 0.8 shows the best mass transfer performance compared with two other samples with porosities of 0.7 and 0.9. The mass transfer performance can also be affected by some extrinsic factors. For example, turbulence promoters (TPs) are employed to increase the mass transfer rate by up to 4 times because their tortuous structures can cause turbulent flow (Recio et al., 2013, Brown et al., 1992, Griffiths et al., 2005b). Increasing fluid velocity is another way to improve the mass transfer performance, but it is not always feasible due to high flow resistance and pumping power constraints (Brown et al., 1993). Although the mass transfer performance of many kinds of porous materials has been studied, little work has been conducted on the mass transfer properties of porous metals manufactured by the PM space holder based methods. Therefore, a systematic study on the mass transfer properties of porous metals manufactured by the LCS process is of significant importance.

Open-cell porous metals have been employed as electrodes and electrode support materials in energy generation and electrochemical detection because of their excellent electrochemical properties. Their applications include lithium-ion battery (Huang et al., 2008, Wang et al., 2009), alkaline zinc battery (Shivkumar et al., 1998), nickel-hydrogen battery (Naito et al., 1993), solid oxide fuel cell (Tucker et al., 2007, Molin et al., 2008), electrochemical capacitor (Ganesh et al., 2005), hydrogen peroxide detection (Akhtar et al., 2015), methanol detection (Yu et al., 2015) and glucose detection (Wang et al., 2015, Kung et al., 2014, Xia et al., 2017). However, the manufacturing processes used for these porous metals are complex and time-consuming, which makes them costly. Therefore, it is important to find alternative porous metals which are more cost effective.

1.2 Aims and objectives

The main aims of this project are to study the electrochemical properties of porous metals manufactured by the LCS process, including geometric, electroactive and real surface areas and mass transfer coefficient, and to explore the feasibility of using the LCS porous metals in electrochemical sensors.

The objectives of the project are:

- To measure the surface areas of the LCS porous metals and correlate surface area with the structural parameters (porosity and pore size).
- To optimise manufacturing conditions (sintering temperature and metal particle size) and subsequent chemical treatments to achieve high surface areas.
- To quantify the effect of diffusion layer thickness on the electroactive surface area.
- To measure the mass transfer coefficient of the LCS porous Ni and correlate mass transfer coefficient with the structural parameters (porosity and pore size).
- To develop an electrochemical sensor using the LCS porous Ni as the working electrode for the determination of ferricyanide concentration.

1.3 Structure of thesis

Chapter 2 of the thesis reviews the literature that is relevant to the present work, including manufacturing processes for porous metals, properties of porous metals, and current electrochemical applications of open-cell porous metals.

Chapter 3 presents the details of experimental apparatus and processes used in this work, including the manufacturing process for the LCS porous nickel and copper specimens, the procedures for the geometric, electroactive and real surface area measurements, the procedure for the mass transfer coefficient measurement, novel limiting current sensor and ferricyanide detection procedure.

Chapter 4 presents the results of the measurements of the geometric, electroactive and real surface areas of the LCS porous copper, and discusses the effects of pore size, porosity, particle size, sintering temperature and chemical etching. The effect of chemical reactions on the electroactive surface area is also analysed.

Chapter 5 presents the results of the measurements of the geometric, electroactive and real surface areas of the LCS porous nickel, and discusses the effects of pore size, porosity and particle size. The effect of scan rate on the electroactive surface area is also analysed.

Chapter 6 presents the results of the measurement of the mass transfer coefficient of the LCS porous nickel, and discusses the effects of pore size and porosity. The mass transfer performance of the LCS porous nickel is also compared with nickel plate and other nickel electrodes reported in the literature.

Chapter 7 presents the performance of the LCS porous nickel in detecting ferricyanide using two electrochemical sensors, and analyses the effects of scan rate and internal flow velocity on the detection performance. Particular attention is paid to the enhanced performance of the novel limiting current sensor, compared with conventional three-electrode electrochemical sensor.

Chapter 8 summarises the conclusions drawn from this thesis and recommends a few areas for future research.

CHAPTER 2 LITERATURE REVIEW

2.1 Manufacturing of porous metals

A range of techniques have been developed for manufacturing porous metals since early 1990's due to increasing commercialization. First systematic summary of the manufacturing methods for porous metals was made by Davies and Zhen (1983), followed by several important reviews published at the beginning of the 21st century (Banhart, 2001, Ashby et al., 2000, Liu and Liang, 2001). In these reviews, the manufacturing processes of porous metals developed have been classified into four 'families' according to the state the metal is processed in, namely: metal powder based, liquid metal based, metal vapour based and metal ions based. After 2000, a number of novel manufacturing processes, like Lost Carbonate Sintering (LCS) and Selective Laser Melting (SLM), have been developed. The appearance of these newly developed manufacturing processes has increased the vigor and vitality of research in porous metals. This chapter will review some important manufacturing processes for porous metals developed during the past decades. For simplicity, in this review, the manufacturing processes of porous metals are divided into two groups: conventional and novel. The former represents those manufacturing processes developed before 2000, while the later includes those manufacturing processes developed after 2000.

2.1.1 Conventional manufacturing techniques

There are many manufacturing techniques for porous metals developed before 2000. Most processes can be classified into four 'families' as mentioned above, represented by loose powder sintering, melt gas injection, chemical vapour deposition and electrodeposition. This section will detail these four manufacturing methods, including process, applicability, advantage and disadvantage.

2.1.1.1 Loose Powder Sintering

Loose powder sintering is a widely used manufacturing process for open-cell porous metals, especially for bronze bearings and nickel membranes (Banhart, 2001, Kennedy, 2012). The manufacturing process is simple, where a metal powder is poured into a die followed by sintering. Fig. 2.1 shows a porous bronze sample manufactured by the loose powder sintering process. It is obvious that the interconnected pores within the porous bronze sample are the interstices between adjacent bronze particles. The porosity of the porous metal produced by loose powder sintering is normally in the range of 40% – 60% (Banhart, 2001), dependent on the metal particle size, shape, sintering conditions and even vibration. The properties of the porous metals are dependent on the porous structures, which are in turn determined by the manufacturing parameters. For porous nickel samples manufactured by loose powder sintering process, increasing sintering temperature from 850 to 1050 ˚C and sintering duration from 2 to 15 minutes improved the strength up to 40% (Tracey, 1979). For porous titanium samples manufactured by the loose powder sintering process, the effects of sintering temperature on pore size and porosity have also been studied (Torres et al., 2014). It was found that a higher sintering temperature resulted in a larger pore size but a lower porosity. In terms of economy, loose powder sintering is one of the simplest and low-cost manufacturing processes without the need to use any pressure and other additives. It is also applicable for many kinds of materials, like copper, titanium and stainless steel. However, it produces samples with low porosities which sometimes limit its wide commercialization. To achieve high porosities, some space holders have been used to mix with metal particles and then removed by decomposition or dissolution. This kind of processes is called space holder methods and will be introduced in section 2.1.2.

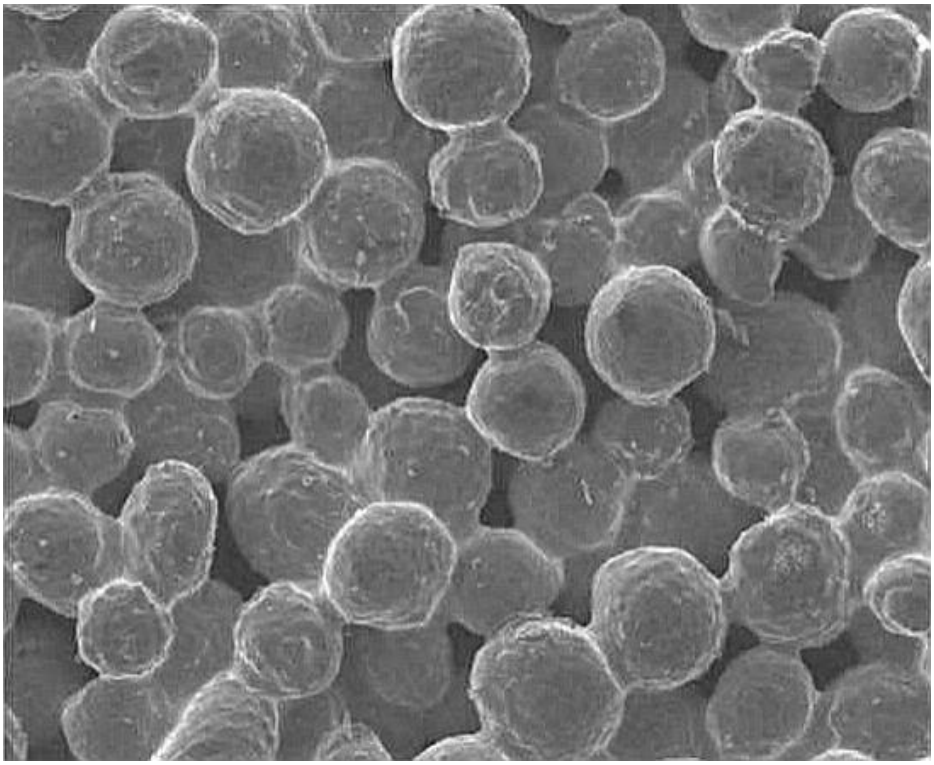

Fig. 2. 1 Porous bronze manufactured by loose powder sintering process with a spherical particle size of 45 – 100 μm (Eisenmann, 1998)

2.1.1.2 Melt gas injection

Melt gas injection is a commonly used manufacturing process for closed-cell porous aluminium or aluminium based alloys. A series of patents (Mangalick, 1977, Jin et al., 1990, Ruch and Kirkevag, 1990, Jin et al., 1992) were granted on this manufacturing technique. Fig. 2.2 shows a schematic diagram of this manufacturing process that mainly includes three steps. The first step of this process is preparation of metal or alloy melts. Aluminium oxide, silicon carbide or magnesium oxide particles are usually added in this step to enhance the viscosity of the melt and to stabilize the foam formed in the next step, as the bubbles within the melt can float to the melt surface too quickly to form an unstable porous structure before solidification (Ashby et al., 2000). The next step is gas injection. Air, nitrogen, argon, oxygen or carbon dioxide are normally injected by a nozzle or a propeller to create fine and

uniform bubbles (Ashby et al., 2000). The obtained liquid or semi-solid foam is then transported by a conveyor belt and followed by solidification.

The porosity, pore size and density of the porous aluminium manufactured by gas injection process are in the ranges of 80 – 98% , 3 – 25 mm and 0.069 – 0.54 g/cm^3, respectively (Banhart and Symposium, 1998, Banhart, 2001). Compared with other manufacturing processes, the melt gas injection process is relatively simple and cost effective. The limitations of the melt gas injection process are also very obvious. For example, it is not appropriate for manufacturing other porous metals except for aluminium because of high melting points. In theory, the porous structures, e.g. porosity and pore size, can be controlled by changing the viscosities of melts, gas injection speeds, cooling rates of the liquid and other parameters, and the effects of these parameters have been investigated by many research groups (Leitlmeier et al., 2002, Babcsán et al., 2003, Gergely and Clyne, 2004). In practice, it is still very difficult to control the porous structures accurately. More experimental and simulation research work in this area is still needed.

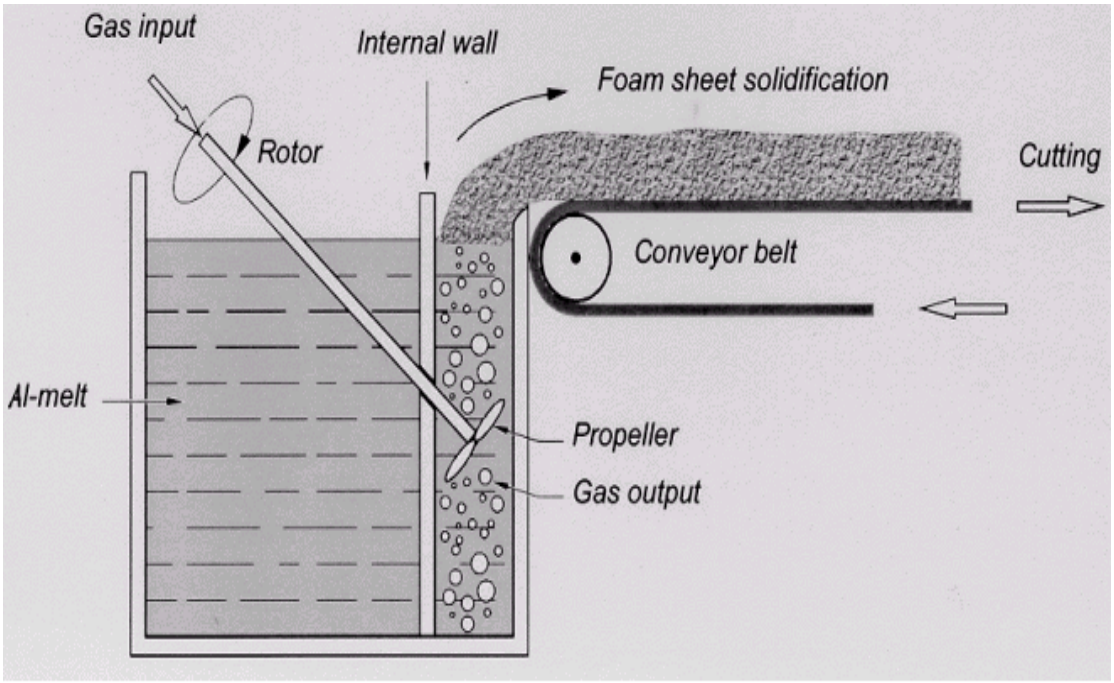

Fig. 2. 2 Schematic of melt gas injection process (Banhart et al., 1999)

2.1.1.3 Chemical vapour deposition

Chemical vapour deposition (CVD) is one of the most successfully commercialized manufacturing techniques for open-cell porous metals. A typical example is INCO nickel foam. The manufacturing process of INCO nickel foam has been reported by many researchers (Ashby et al., 2000, Banhart, 2001, Paserin et al., 2003, Paserin et al., 2004). The CVD process mainly contains three steps: vapour deposition on a sacrificial preform, burnout of the preform and then densification of the deposit, as shown in Fig. 2.3. The vapour is nickel carbonyl which has been used to refine nickel and produce nickel powder (Mond et al., 1890). It can be synthesised by reaction $Ni + CO \rightarrow Ni(CO)_4$ with a low boiling point of 43˚C and a decomposition temperature of 150 – 200 ˚C reported by Paserin et al. (2003) or above 120 ˚C reported by Banhart (2001). The decomposition reaction of nickel carbonyl is $Ni(CO)_4 \rightarrow Ni + CO$. In the first step, an open-cell polymer is used as a sacrificial preform and the open-cell polymer is coated by decomposition of nickel carbonyl

at a high temperature. The preform is then burnt out by heating in air. After the burn out, a porous metal structure with hollow ligaments is obtained. A subsequent sintering step is used to solidify the ligaments.

The INCO porous nickel manufactured by the CVD process has a wide range of porosity of 70 – 98% and a wide range of pore size of 450 – 3200 μm (Ashby et al., 2000). The pore architecture can be changed by using sacrificial preforms with different structures. The CVD technique can produce INCO porous nickel with the lowest density of 0.2 g/cm^3 because of the high porosity deriving from its unique hollow porous structure. More importantly, the CVD process allows fabricating porous nickel on a large scale. Despite these advantages, the CVD process is relatively complex and costly compared with the loose powder sintering and melt gas injection processes. The CVD process is also restricted to pure metals due to the nature of chemical deposition. Another problem is that nickel carbonyl is highly toxic and requires careful environmental control which adds extra cost to the manufacturing process (Paserin et al., 2003).

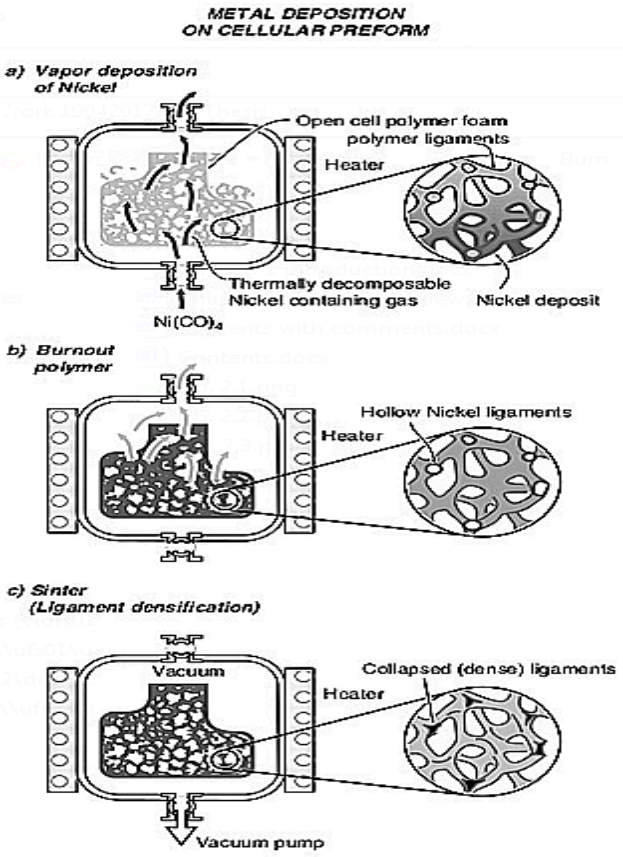

Fig. 2. 3 Schematic of chemical vapour deposition process (Ashby et al., 2000)

2.1.1.4 Electrodeposition

The electrodeposition process for manufacturing porous metals is similar to the CVD process. It also consists of three stages: treatment of a sacrificial preform for electrical conductivity, electrodeposition and reductive sintering. Polymers including polyurethane, polyester, olefin polymer, ethenyl polymer, phenylethene polymer and eurelon have been used as sacrificial preforms (Liu and Liang, 2001). Pre-treatment by acid or alkaline solutions is conducted to remove oil stain and roughen the surface followed by water washing. As most kinds of polymers are not electrically conductive, chemical oxidative polymerization or electrolysis polymerization treatment is necessary to make the sacrificial polymers electrically conductive (Myers, 1986, Gospodinova et al., 1993). The as-obtained sacrificial

polymers with conductive layers on surface can be electrodeposited by intended metals. During the electrodeposition process, the anode is the intended metal and the cathode is the conductive porous polymer. The solid metal oxidises at the surface of the anode and becomes metallic ions in the solution, followed by moving towards cathode and reducing to solid metal on the surface of the cathode. The as-obtained composite body is then sintered to remove the sacrificial preform and to densify the deposited metal particles. The current density during deposition is crucial as it can affect the surface morphology and mechanical properties of the porous metals produced (Marozzi and Chialvo, 2000). An impulse current has often been used to weaken the phenomena of concentration polarization during the electrodeposition process (Hanusa, 1970, Nielsch et al., 2000).

Unlike the CVD process, the electrodeposition process is applicable for both metals and alloys, including Ni, Cu, Cr, Zn, Cu, Sn, Co-Ni, Cu-Zn and many others. A porosity of 99% porous metals can be achieved by the electrodeposition process (Paserin et al., 2003), which is higher than that of samples manufactured by many other processes. However, the electrodeposition manufacturing process is relatively complex, costly and time-consuming. The global uniformity of the porous metal produced and potential pollution from waste solution are still the long-term limitations for this technique.

2.1.2 Novel manufacturing techniques

In the past two decades, a range of novel manufacturing techniques for porous metals have been developed. The most representative two processes are Lost Carbonate Sintering (LCS) and Selective Laser Melting (SLM).

2.1.2.1 Lost Carbonate Sintering

Lost Carbonate Sintering (LCS) is a typical space holder manufacturing process which was developed by Zhao et al. (2005). A schematic of the LCS process can be seen in Fig. 2.4. The LCS process uses potassium carbonate powder as the filler material. The metal powder and potassium carbonate powder are first mixed at a certain volume ratio according to the intended porosity. A small amount of ethanol is added and serves as the binder. The mixture is then compacted by a hydraulic press at 200 MPa. The obtained preform is then sintered in one of the two different routes, either at 850˚C for 4 hours or at 950˚C for 2 hours, termed as carbonate dissolution route and carbonate decomposition route, respectively. In the carbonate dissolution route, the potassium carbonate powder within the sintered preform is removed by hot water. In the decomposition route, the potassium carbonate powder is removed by thermal decomposition during sintering. The sample is then cooled down to room temperature.

In other space holder methods, sodium chloride (Zhao and Sun, 2001), ammonium bicarbonate and carbamide powders (Laptev et al., 2004) have also been used as space holders. Potassium carbonate is superior to these filler materials. For example, sodium chloride is difficult to be removed completely and any residual sodium chloride may result in contamination and corrosion of base metals. Ammonium bicarbonate and carbamide decompose at 200˚C (Haynes, 2014), which may lead to collapse of samples before strong bonding is formed between adjacent metal particles. Another issue of ammonium bicarbonate and carbamide is that they can release environmentally damaging gases during decomposition. In comparison, potassium carbonate is easy to be removed at high temperature or in hot water and does not contaminate many metals.

The LCS process can produce porous metals with controllable porous structures, including pore size, porosity and pore shape. The pore size and porosity of LCS porous samples can be in wide ranges of 53 – 1500 μm and 0.5 – 0.85, respectively (Zhao et al., 2005). However, the LCS process is not applicable for some metals due to reactions between potassium carbonate and base metals.

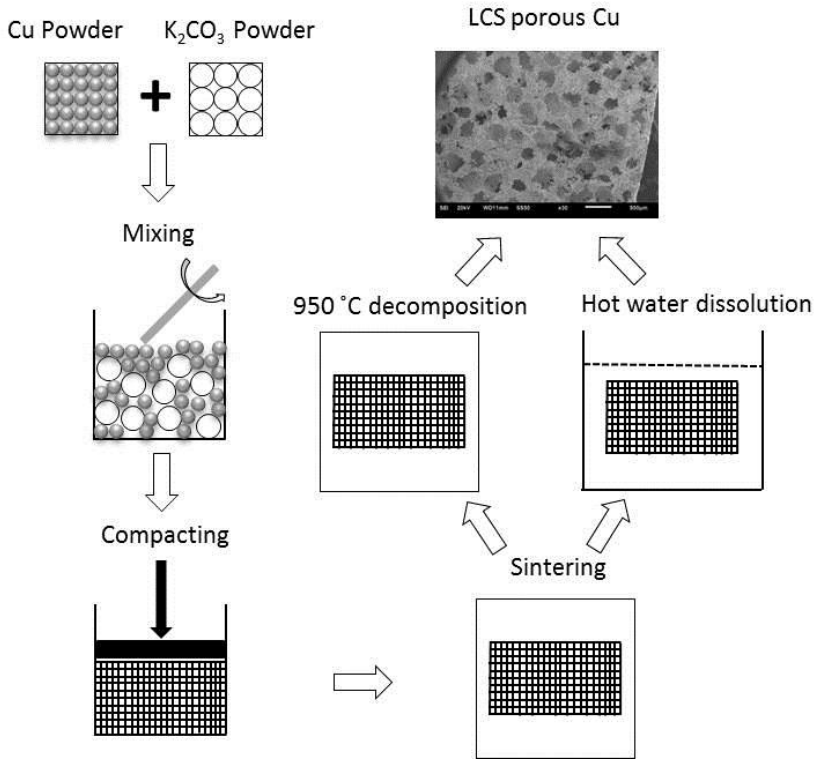

Fig. 2. 4 Schematic of the Lost Carbonate Sintering process

2.1.2.2 Selective Laser Melting

Selective laser melting (SLM) is a representative process of the additive manufacturing (AM) technique, which has been regarded as one of the most promising manufacturing techniques at present. Fig. 2.5 shows a schematic of the machine and working principle of the SLM system developed by Osaka University (Santos et al., 2006). A laser with a maximum peak powder of 3 kW and an average power of 50 W is guided by optical fibers to melt the metal powder in a chamber. The topside of the chamber is covered by a piece of

glass. Argon is flushed continuously in order to minimize oxygen and nitrogen pick-up. The laser head is connected with a XY table which is controlled by a computer. A piston is also connected by the computer to adjust the height (Z axis) of the chamber. The values of X, Y and Z axes can be set by CAD software. The melting process of the metal powder is carried out in a closed chamber. Metal powder is continuously supplied by a powder container.

This process is applicable for many kinds of metals and alloys, including aluminium (Louvis et al., 2011), steel (Li et al., 2010, Linxi et al., 2014), titanium (Li et al., 2010) and titanium alloys (Warnke et al., 2008, Thijs et al., 2010). The SLM technique can produce porous materials with desired structures, e.g. porosity and pore size, which is of particular interest to biomedical researchers in the artificial bone replacement field (Mullen et al., 2009, Hollander et al., 2003). The SLM technique can also produce porous metals with intended shapes, so subsequent cutting process can be omitted. Although the SLM technique is superior in many aspects, it is more complex and costly compared with other manufacturing processes. The precision of the porous structures produced by the SLM technique still needs to be improved.

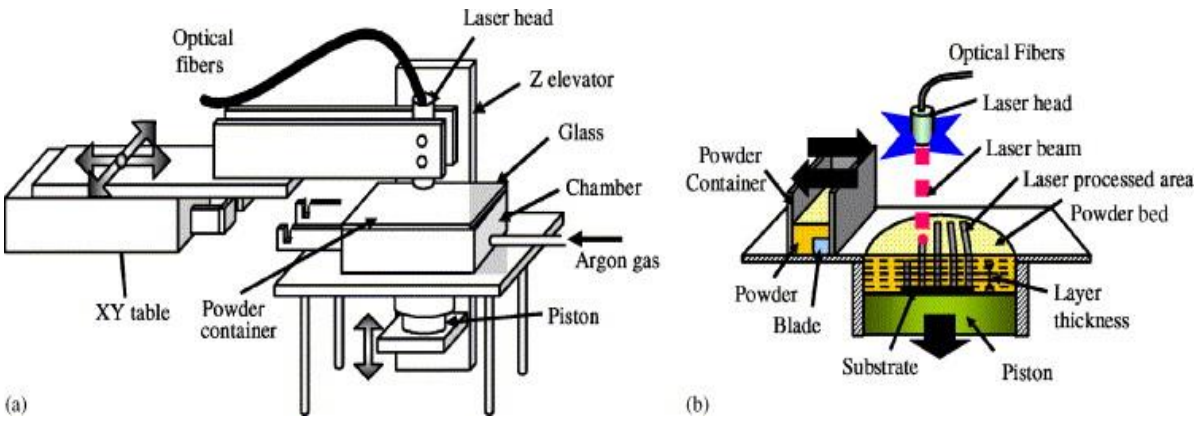

Fig. 2. 5 Selective laser melting: (a) illustration of the machine; and (b) working principle of the system (Santos et al., 2006)

2.1.3 Comparison of manufacturing processes

Table 2.1 summarizes some main advantages and disadvantages of the manufacturing processes discussed above. For the loose sintering and melt gas injection processes, despite their low cost, neither is applicable for fabricating open-cell porous metals with desired porosity ranges. In contrast, the chemical vapour deposition, electrodeposition and selective layer melting methods can produce open-cell porous metals with tailored structures. However, high cost is still a main challenge for these methods at present. Additionally, the toxic raw materials and wastes are potential problems that limit the commercialization of chemical vapour deposition and electrodeposition in the future. The LCS process is able to control the porous structure by changing the number, size and shape of the potassium carbonate particles. Additionally, the LCS process consists only of mixing, compacting and sintering, which is a relatively cheap and simple process. The only limitation is that potassium carbonate may react with some metals during sintering. For Cu and Ni studied in this thesis, there is no reaction between potassium carbonate and these two metals. Therefore, the LCS process is a good choice here to produce porous metals with good quality and low cost.

Table 2.1 Comparison of manufacturing processes

Process	Advantages	Disadvantages
Loose sintering	• Low cost and simple operation (no additive and pretreatment required)	• Low porosity (less than 60%)
Melt gas injection	• Relatively low cost • Large porosity range (80% - 98%)	• Not applicable for open-cell porous metals • Difficult for manufacturing high melting point metals
Chemical vapour deposition	• Large porosity range (70% - 98%) • Good control of porous structures	• Relatively costly, complicated operation • Non-environmental friendly
Electrodeposition	• Large porosity range • Very high porosity can be achieved • Good control of porous structures	• Relatively costly, complicated operation • Non-environmental friendly
Lost Carbonate Sintering (LCS)	• Relatively low cost and simple • Good control of porous structures • Large porosity ranges (50 – 85 %)	• Not applicable for some metals due to potential reactions between potassium carbonate and metals
Selective laser melting	• Precise control of porous structures	• Very costly (specific facilities and metal powders needed)

2.2 Properties of porous metals

Porous metals have attracted considerable attention because their specific structures can contribute to a wide range of novel properties, including mechanical properties, electrical conductivity, thermal conductivity, fluid flow properties, sound absorption, energy absorption and so on. All of these properties have been previously summarized by several important reviews (Ashby and Medalist, 1983, Ramamurty and Paul, 2004, Zardiackas et al., 2001, Imwinkelried, 2007). The importance of these properties is somewhat different depends on the specific applications. For example, the thermal conductivity is very important for porous metals employed in thermal management but not very important for porous metals serving as filtration materials. As this project mainly studies the electrochemical properties, this section will only describe a few related properties of porous metals, e.g. permeability, surface area and mass transfer property.

2.2.1 Permeability

For open-cell porous metals, a fluid, such as water, can be made to flow through the samples. The ability of the porous sample to allow the fluid to pass through is known as permeability. It is an important property of porous metals, especially for the applications in heat management (Antohe et al., 1996, Lu et al., 1998, Dai et al., 2012) and energy generation (Kumar and Reddy, 2003). Good permeability is a precondition for high heat and mass transfer performance of porous metals in fluid flow conditions. For applications like active cooling systems and fuel cells, the cooling liquid (water) or liquid fuel is forced to pass through the porous metals, resulting in good heat or mass transfer performance. A high permeability means less resistance for fluid to pass through, which can reduce the energy

consumption in pumping the fluid, although too high a permeability may result in a low efficiency in heat or mass transfer between the fluid and the matrix of the porous metals.

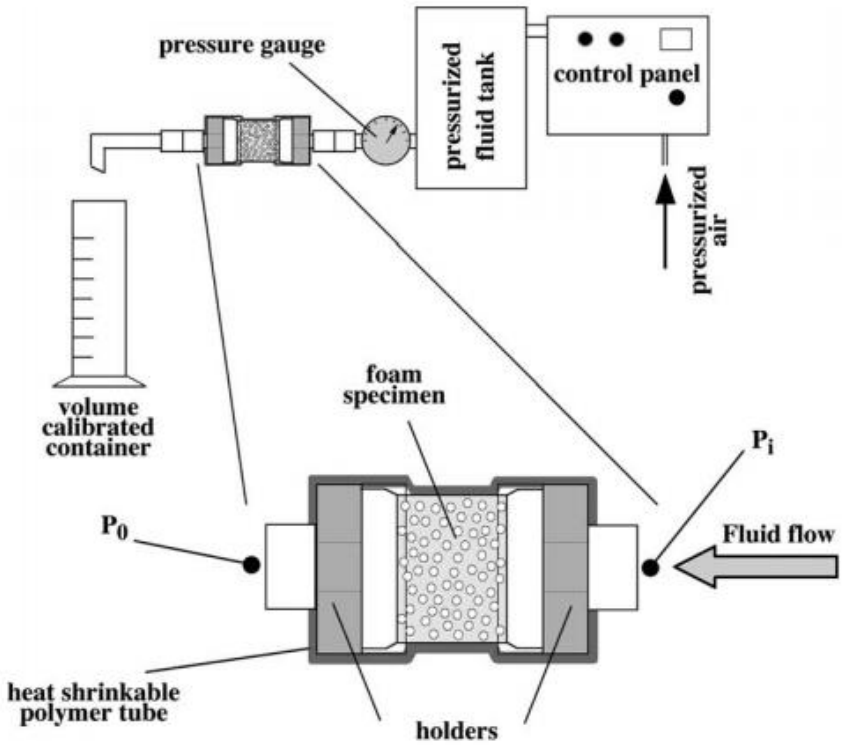

Fig. 2. 6 Schematic of permeability measurement apparatus (Despois and Mortensen, 2005)

The permeability of porous samples can be determined from the relation between the fluid pressure and the flow velocity (Despois and Mortensen, 2005). A schematic of a permeability measurement apparatus is shown in Fig. 2.6. In creeping flow regime, the permeability of a porous metal can be calculated from the Darcy's law which is shown below:

$$\frac{\Delta P}{\Delta x} = \frac{\mu}{K} v_0 \qquad 2.1$$

where ΔP is the pressure drop between the inlet and outlet fluid, the Δx is the distance along the direction of fluid flow, μ is the dynamic viscosity of the fluid, K is the permeability of the porous sample and v_0 is the Darcian velocity of the fluid flow. If the Reynolds number increases to a critical value, the fluid flow will change from laminar to turbulence flow, and

the permeability can be calculated by the Forchheimer equation (Despois and Mortensen, 2005):

$$\frac{\Delta P}{\Delta x} = \frac{\mu}{K} v_0 + \rho C {v_0}^2 \qquad 2.2$$

where ρ is the density of the fluid and C is the form drag coefficient.

Porosity and pore size are the two most important structural parameters of porous metals. They have great effects on the permeability and form drag coefficient of porous metals. Paek et al. (2000) measured the permeability of porous aluminium and found that the permeability increased with increasing porosity and pore size, while the effects of porosity and pore size on the form drag coefficient were not obvious. . Khayargoli et al. (2004) has also studied the effect of pore structure on the permeability of porous metals. They compared the permeability of IMI and RECEMAT metal foams, manufactured by powder metallurgy and electrodeposition methods, respectively. It was found that the RECEMAT samples are more permeable than the IMI samples. The minimum K of the RECEMAT samples is about 0.38 x 10^{-9} m^2, which is about 5 times of the maximum K of the IMI samples, whereas the maximum C (1.02 x 10^{-3} $m^{-1}s^2$) of the RECEMAT samples is about one fourth of the minimum C of the IMI samples (4.01 x 10^{-3} $m^{-1}s^2$).

Porous metals manufactured by the LCS process have good permeability. Xiao and Zhao (2013) reported that the permeability coefficient of the LCS porous Cu, with a porosity range of 60% - 80%, is up to 4 x 10^{10} m^2, which is comparable to the RECEMAT metal foams. Avalos Gauna and Zhao (2016) further presented a geometric model to simulate the permeability of porous metals and showed that the permeability increases with porosity and pore size,

agreeing with Paek et al. (2000). They have also shown that the form drag coefficient increases with pore size but decreases with porosity.

2.2.3 Specific surface area

High volumetric and gravimetric specific surface areas are advantageous for porous metals especially when they are employed as electrodes in batteries, fuel cells and capacitors (Huang et al., 2008, Wang et al., 2009, Shivkumar et al., 1998, Naito et al., 1993, Tucker et al., 2007, Molin et al., 2008, Ganesh et al., 2005). A higher specific surface area offers more reaction sites for reactants or a large storage capacity for electrons per unit volume or weight of electrodes, generating a higher energy density. Therefore, the measurement of surface area is critical for the characterization of porous metals.

BET and mercury intrusion are the two most common methods used for measuring the surface area of porous metals. However, they are inappropriate for measuring the electrochemical surface area. The BET method determines the surface area at an extremely small length scale (about 0.3 nm), depending on the kind of gas molecules used. Therefore, the BET surface area is much larger than the effective surface area in electrochemistry. The mercury intrusion method measures the surface area of porous metals by assuming that all pores are cylindrical. This assumption results in a big error for the surface area measurement. Additionally, the BET and mercury intrusion methods are not applicable for pores too big or too small, respectively.

Diao et al. (2015) studied the surface areas of porous copper manufactured by the LCS process and classified the surface area into three different types, namely geometric, electroactive and real surface area. The geometric surface area, which only includes the surface area of primary pores (formed by decomposition or dissolution of K_2CO_3 particles)

within porous samples, was measured by the quantitative stereology method. The electroactive surface area was measured by the cyclic voltammetry peak current method, based on the principle that the anodic or cathodic peak current for a diffusion controlled reaction is proportional to the electroactive surface area of the electrode (Delahay, 1954), as shown in equation 2.3

$$I_P = 268600 \times n^{\frac{3}{2}} \times A_e c D^{\frac{1}{2}} v^{\frac{1}{2}} \qquad 2.3$$

where I_P is the peak current, n is the electrons transferred in the equation, A_e is the electroactive surface area, c is the concentration of reactive species, D is the diffusion coefficient and v is the scan rate. A typical current-potential plot used for the measurement of the electroactive surface area of porous copper can be seen in Fig. 2.7. The electroactive surface area includes the surface areas of primary pores and interstices between adjacent metal particles, and is dependent on the nature of the reaction (Diao et al., 2015). The real surface area was measured by the double layer capacitance method, which is expected to include all the surface areas of primary pores, interstices and even the rough surface of metal particles (Diao et al., 2015), because the double layer capacitance method measures the surface area where ions can be stored. This method can determine the surface area at the nanoscale (Wang and Pilon, 2011). A typical current-potential plot used for the real surface area measurement of porous copper can be seen in Fig. 2.8. The value of the specific real surface area can be one order of magnitude larger than the specific electroactive surface area and two orders of magnitude larger than the specific geometric surface area (Diao et al., 2015). The details shown in Figs 2.7 and 2.8 will be explained in Sections 3.3.2 and 3.4.1.

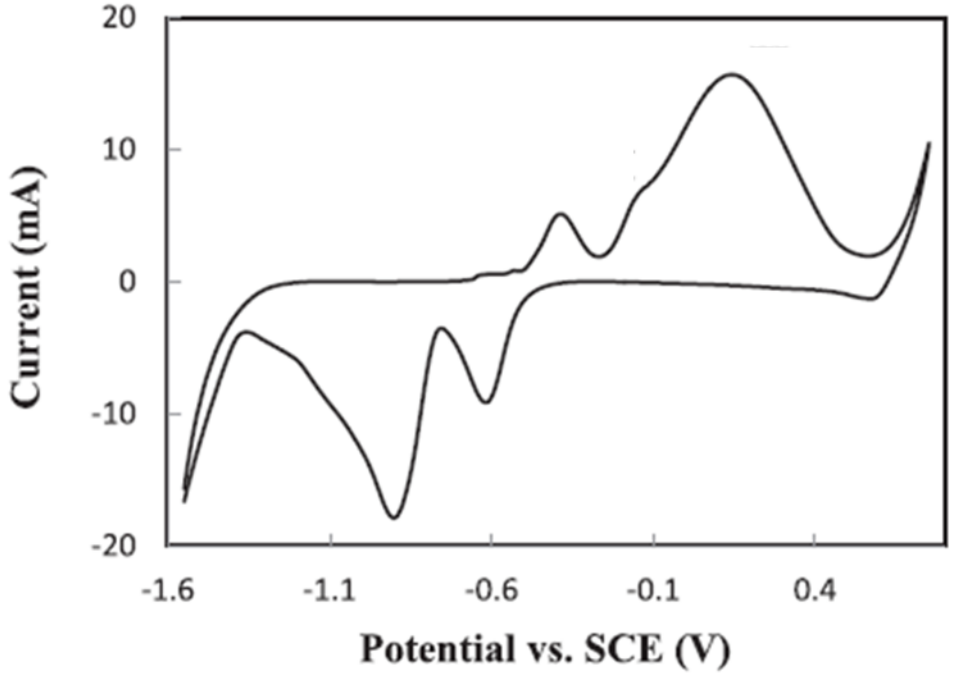

Fig. 2. 7 Current-potential plot of the porous Cu in 0.1M KOH for electroactive surface area measurement (Diao et al., 2015)

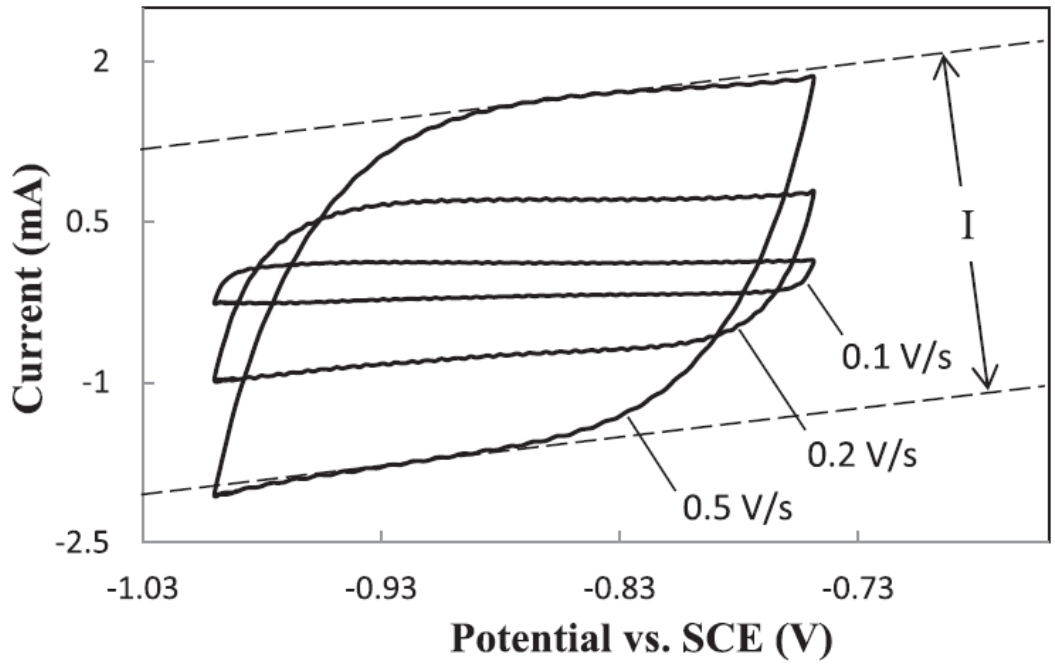

Fig. 2. 8 Current-potential plot of the porous Cu used for the real surface area measurement in 0.1M KOH (Diao et al., 2015)

The volumetric and gravimetric specific geometric surface areas of porous metals are affected by porosity and pore size. Diao et al. (2015) studied the specific geometric surface areas of the LCS porous copper and found that the specific geometric surface areas increased with increasing porosity but decreased with increasing pore size. This is because samples with high porosities have more primary pores, and therefore a higher geometric surface area. A larger pore size means the primary pores become larger, decreasing the geometric surface area. They also compared the experimental specific geometric surface areas with the theoretical predictions from a stochastic model developed by Zhao, (2003). The experimental and theoretical results agreed very well.

Like the specific geometric surface area, the specific electroactive surface area of porous metal increases with porosity but decreases with pore size (Diao et al., 2015). In addition, the specific electroactive surface area is also affected by the Nernst diffusion layer. Two different diffusion regimes have been studied in the literature (Barnes et al., 2014, Davies and Compton, 2005, Davies et al., 2005, Smith et al., 2015). If the Nernst diffusion layer is thinner than the size of the interstices, semi-infinite diffusion occurs near the surface of the interstices. If the diffusion layer is comparable to or greater than the interstices, then thin layer diffusion occurs near the surface of the interstices. The electroactive surface area can be measured by the cyclic voltammetry peak current method in the former case, but not in the latter case. In Diao et al. (2015), the diffusion layer thickness was about 30 μm, which meant the interstices with a size smaller than 30 μm could not be detected.

Diao et al. (2015) showed that the volumetric specific real surface area of the LCS porous copper decreases with porosity and pore size, while the gravimetric specific real surface area increases with porosity but decreases with pore size. They also compared the real

surface area with the total surface area of perfectly spherical copper particles with smooth surface and found that the former is more than 5 times larger than the latter. They showed that the rough surface of copper particles accounted for the majority of the real surface area.

The surface areas of porous metals can also be affected by other factors, such as manufacturing process, heat treatment and chemical etching. For porous nickel samples with a similar pore size and porosity, the MITSUBISHI porous sample manufactured by the slurry foaming method had a specific BET surface area of 19710 cm^2/g (Đukić et al., 2013), which was more than 65 times higher than that of the INCO porous sample manufactured by the chemical vapour deposition method (292 cm^2/g) (Bidault et al., 2009). Grdeń et al. (2012) compared the surface areas of INCO porous nickel samples before and after nitric acid etching and found that the electroactive surface area increased by about 150%. Tan et al. (2012) reported that the surface area of a nanoporous gold sample was decreased by up to 3.5 times after annealing at 400 ˚C.

2.2.4 Mass transfer performance

Mass transfer in porous electrodes, i.e., the movement of a chemical species from bulk solution to the surface of porous matrix (Incropera et al., 2007), is critical for electrochemical reactions because it is normally the rate-determining step (Bard et al., 1980). According to Fick's law, the rate of mass transfer is proportional to the difference between the concentrations in the bulk solution and at the electrode surface, with the proportionality coefficient being referred to as mass transfer coefficient. The mass transfer coefficient is an important parameter which is used to evaluate the mass transfer performance of porous metals.

The linear voltammetry technique has been used to study the mass transfer performance of porous Ni using the reduction of $Fe(CN)_6^{3-}$ (Recio et al., 2013). A typical current-potential plot can be seen in Fig. 2.9. There are three regions in the curve, i.e., hydrogen evolution, mass transfer control and mixed control regions (Recio et al., 2013), which signify different transfer mechanisms. The limiting current, I_L, can be determined from the mass transfer region and the mass transfer coefficient, k, was calculated by

$$k = \frac{I_L}{nFAc} \qquad 2.4$$

where n is the number of electrons transferred in the reaction, F is the Faraday constant, A is the surface area of the working electrode and c is the bulk concentration of the electroactive species.

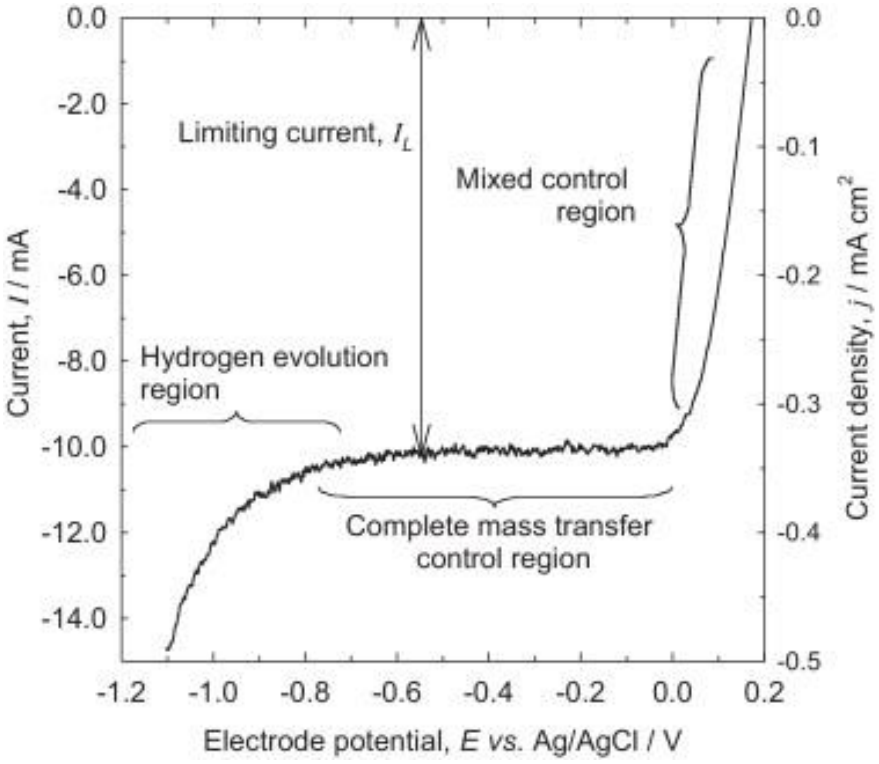

Fig. 2. 9 Current-potential plot for the reduction of Fe(CN)63- at a porous nickel electrode (Recio et al., 2013)

The mass transfer performance is normally studied in terms of the product of mass transfer coefficient and surface area (kA), which can be affected by porosity and pore size for porous electrodes. It was found that the mass transfer performance of the SORAREC porous nickel, manufactured by a metal decomposition method, decreased with increasing pore size as shown in Table 2.2 (Langlois and Coeuret, 1989, Cognet et al., 1995). The quantitative relations in Table 2.2 are related to porous structures and fluid flow. The pre-exponent is dependent on the surface area and the exponent is an indicator for flow regime (Recio et al., 2013). It is clear that the exponent does not change a lot for porous nickel with different pore sizes, while the pre-exponent decreases significantly when pore size increases, indicating that porous nickel samples with larger pore sizes have better mass transfer performance because of high surface areas. Zhou et al. (2015) investigated the mass transfer performance of porous copper fiber sintered felt (PCFSF) with three different porosities of 0.7, 0.8 and 0.9, and found that a porosity of 0.8 gave the best mass transfer performance. They attributed the best mass transfer performance to an appropriate residence time of electrolyte (Zhou et al., 2015). A sample with a small porosity has a long residence time, which results in an exhaust of reactive species in electrolyte and therefore a poor mass transfer performance. A sample with a high porosity has a short residence time, which leads to an insufficient contact between reactive species and electrode and therefore a poor mass transfer performance.

Table. 2. **2** Mass transfer performance of porous nickel (Langlois and Coeuret, 1989)

Metal Foam	Pore size (m)	Mass transfer performance
G100	2×10^{-4}	$kA = (0.80 \pm 0.08)u^{0.30}$
G60	3×10^{-4}	$kA = (0.28 \pm 0.03)u^{0.30}$
G45	4.4×10^{-4}	$kA = (0.075 \pm 0.01)u^{0.22}$

Mass transfer performance can be improved by many factors, such as increasing electrolyte flow velocity, increasing surface area and using turbulence promoters. The mass transfer coefficient is a function of electrolyte Darcian velocity (v_0), in the form of: $k = a{v_0}^b$ (Recio et al., 2013), where *a* and *b* are two constants. Therefore, the mass transfer coefficient can be increased by increasing electrolyte Darcian velocity. However, it is not always feasible to increase electrolyte velocity due to high flow resistance and pumping power constraints (Brown et al., 1993).

Recio et al. (2013) studied the mass transfer performance of a nanostructured nickel electrode. They found that the mass transfer performance of this nickel electrode was about 11 times better than that of nickel plate due to high effective surface area. The mass transfer performance can also be increased by using turbulence promoters. For the nanostructured nickel electrode, the mass transfer performance was improved by 23 times by using a turbulence promoter (Recio et al., 2013), because the turbulence promoter (TP) induced turbulence flow on the surface of electrodes, increasing mass transfer performance.

In order to compare different materials, the mass transfer performance are usually characterized by three dimensionless numbers, namely Sherwood number (Sh), Reynolds number (Re) and Schmidt number (*Sc*), as shown in equations 2.5 – 2.7 (Recio et al., 2013).

$$Sh = \frac{kd_e}{D} \quad 2.5$$

$$Re = \frac{vd_e}{u} \quad 2.6$$

$$Sc = \frac{v}{D} \quad 2.7$$

where d_e is the equivalent diameter of pores, D is the diffusion coefficient of the reactive species and u is the kinematic viscosity of the electrolyte. Sh and Re numbers are indicators of mass transfer property and flow velocity, respectively. The d_e has been determined by either the pore size or the size of the whole flow channel (cross section of the sample) in the literature. In our opinion, it is better to use the pore diameter as d_e. This is because pore diameter affects fluid flow and different pore diameters can result in different flow regimes even at the same flow rate. Ultimately, it is the flow regimes within pores that determines the flow and heat transfer behaviours.

Recio et al. (2013) compared the mass transfer performance of different electrodes in the literature, as shown in Fig. 2.10. It is clear that a nanostructured nickel electrode with a TP shows the highest Sherwood number, indicating that it has the best mass transfer performance. It is because of its high surface area and turbulence flow caused by the TP. A nickel electrode in the FM01-LC electrolyser (Brown et al., 1993) and a nickel electrode studied by Carlsson et al. (1983) had similar Sherwood numbers when measured without a TP. The nickel electrode studied by Carlsson et al. (1983) using a polypropylene TP (triangular threads) had a much higher Sherwood number than the nickel electrode in the presence of a different TP. The effect of the TP on the mass transfer performance of nickel solid electrodes is not obvious at high Reynolds numbers. The Sherwood numbers of a nickel electrode in fully developed laminar and turbulence flows are also shown in Fig. 2.10. The

transition from laminar flow to turbulent flow occurred at the Reynolds number of 1000. At low Reynolds numbers, the flow regime on the surface of the nickel electrode remains laminar. The flow regime turns into turbulent flow at higher Reynolds numbers. In both laminar and turbulent flow regimes, the Sherwood number increases with increasing Reynold number. The Sherwood number increases faster in the turbulent flow regime than in the laminar flow regime.

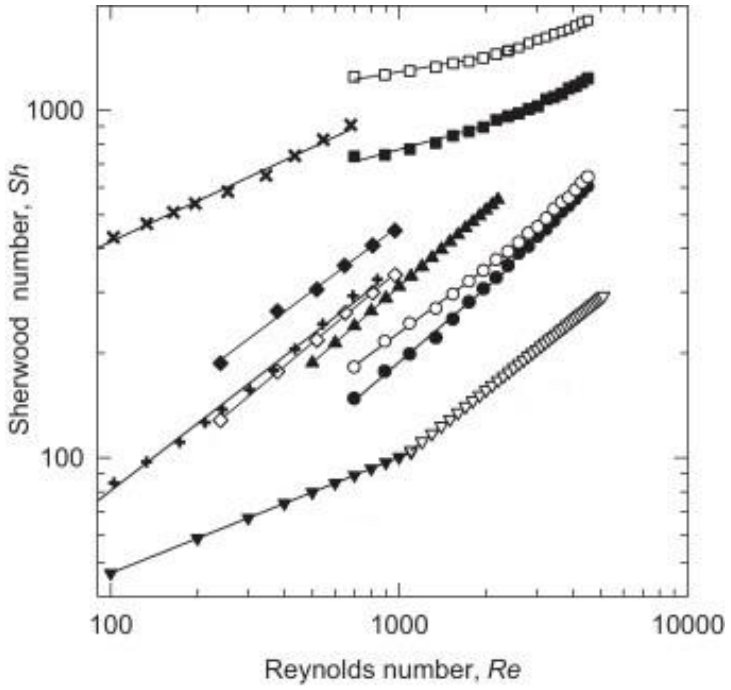

Fig. 2. 10 Log Sh vs. log Re for various rectangular flow channel cells in the presence and absence of a turbulence promoter (TP): (●) nickel solid electrode, this work: no TP, (○) with a TP. Nanostructured nickel deposit, this work: (■) no TP and (□) with a TP. Nickel electrode in the FM01-LC electrolyser (Brown et al., 1993): (⧫) no TP and (◊) with a TP. Nickel electrode in the FM01-LC (Griffiths et al., 2005a): (▲) in the absence of a TP. (▼) fully developed laminar flow (Pickett, 1979) and (▽) fully developed turbulent flow (Pickett, 1979). (+) Nickel electrode (Carlsson et al., 1983) in the absence of a TP and (×) with a polypropylene grid with triangular threads TP (Recio et al., 2013)

2.3 Electrochemical applications

Porous metals have attracted considerable attention in many electrochemical applications in the past decades. In the field of energy generation and storage, porous metals have been used as electrodes or current collectors in direct methanol fuel cells (DMFCs) (Chen and Zhao, 2007a) and lithium batteries (Chung and Manthiram, 2013). In the field of electrochemical detection, porous metals have been widely studied as sensor electrodes to detect various ions or molecules, such as hydrogen peroxide (Zhang et al., 2009) and glucose (Niu et al., 2014). Besides, porous metals have also been used as electrodes in proton exchange membrane (PEM) water electrolysers (Rahim et al., 2015). The porous metals provide enhanced performance in these applications, e.g. higher power density, larger capacitance, lower limit of detection and higher sensitivity. All of these enhanced performances can be attributed to some of the unique properties of porous metals reviewed in section 2.2, i.e. good permeability, high surface area and excellent mass transfer property.

2.3.1 Direct methanol fuel cells (DMFCs)

A direct methanol fuel cell is an electrochemical device using methanol as fuel to convert chemical energy into electrical energy. It has been regarded as one of the most promising portable fuel cells due to its compact volume. A typical DMFC consists of two end-plates, a gasket, a cathode, an anode and a membrane electrode assembly, as shown in Fig. 2.11. At the anode, methanol is oxidized to generate electrons. Oxygen, normally as air, is reduced to water or steam at the cathode (Hamnett, 1997). The chemical reactions at the anode and cathode can be seen in equations 2.8 and 2.9, respectively. In theory, a DMFC should have a

superior energy density and a short charging time (Park et al., 2008, Dillon et al., 2004, Dyer, 2002), which makes it best fit to replace the current commercial batteries.

$$CH_3OH + H_2O \rightarrow CO_2 + 6H^+ + 6e^- \quad (2.8)$$

$$\frac{3}{2}O_2 + 6e^- + 6H^+ \rightarrow 3H_2O \quad (2.9)$$

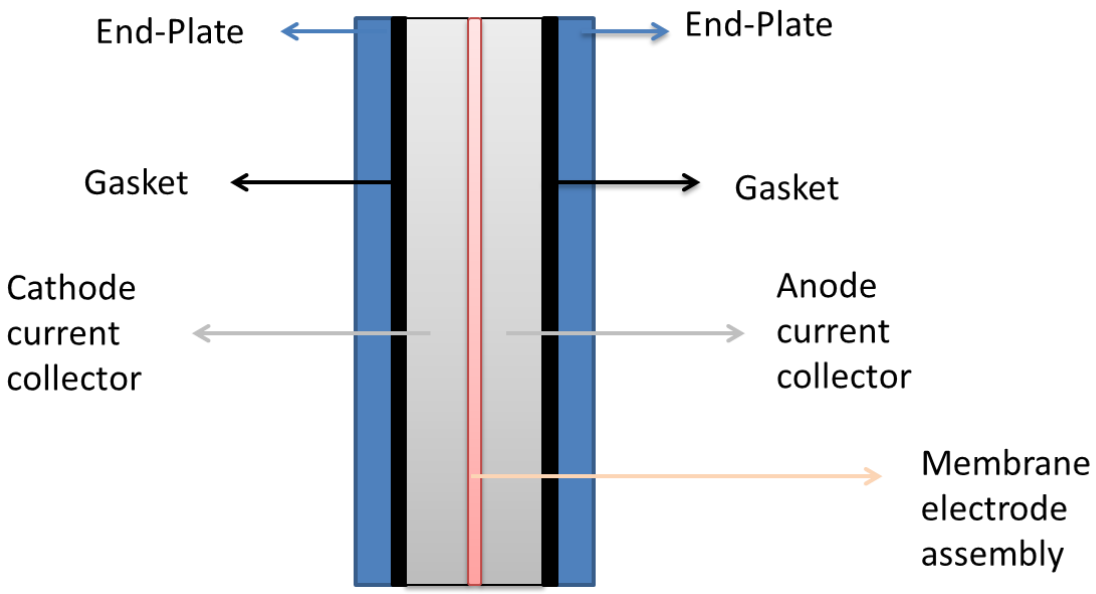

Fig. 2. 11 Basic components of a DMFC (Hamnett, 1997)

Despite the potential of DMFCs, there are several barriers for their commercialization as the source of portable devices. One of the most important barriers is the methanol crossover, as has been reviewed by Heinzel and Barragan (1999). It happens when methanol molecules diffuse through the membrane from anode to cathode and are directly oxidized by oxygen, especially when methanol with high concentration is used. Water flooding also limits the commercialization of DMFCs (Lu et al., 2005). As the chemical reaction (equation 2.9) generates water, the water accumulates at the cathode and prevents oxygen contact with the cathode, reducing the reaction rate and therefore energy density. Another barrier is the loss of heat (Kamarudin et al., 2009). During the operation of a DMFC, it can generate heat

and increase the temperature of the whole cell. The increased temperature is often advantageous for DMFCs as it can increase the chemical reaction kinetics. However, conventional anodes or cathodes are made by perforated metal plates which have high thermal conductivities, resulting in a large amount of heat loss.

To overcome all of these barriers mentioned above and improve the performance of DMFCs, porous metals have been used as cathode current collectors in DMFCs (Chen and Zhao, 2007a, Chen and Zhao, 2007b). The DMFCs with porous cathode current collectors yielded much higher and more stable performance than those with conventional perforated metal plates. The improved performance for the DMFCs mainly comes from three aspects.

Firstly, porous cathode current collectors can increase the transport rate of oxygen at the cathode due to enhanced mass transfer performance. Fig. 2.12 shows the Nyquist plots of DMFC impedance spectra with a perforated-plate current collector and a porous current collector, with the applied frequency changing from high frequency to low frequency, from left to right. The two start points of the two plots at the high frequency (left) indicate the internal cell resistances of the two different current collectors. It is obvious that the porous current collector shows a higher internal cell resistance than that of the perforated-plate current collector, because the porous current collector has a high porosity (over 95%) and a lower relative density. The two end points of the two plots at the low frequency (right) indicate the overall mass transfer resistances of the two current collectors. The distances between the start point and the end point are the mass transfer resistances of the two current collectors. It is clear that the porous current collector has a lower mass transfer resistance, which contributes to a higher mass transfer rate. The authors considered the high specific surface area being the main reason for the enhanced transport rate. According

to the latest research (Diao et al., 2017), however, the tortuous porous structure may also have contributed to a better transport rate. Chen and Zhao (2007b) also studied the effect of pore size on the performance of DMFCs and founded that a smaller pore size yielded a higher performance as a result of the lower cell resistance.

Secondly, porous current collectors have much higher surface area and good permeability. High surface area alone is not always beneficial for DMFCs. On one hand, the high surface area of porous metals provides more reaction sites for the reactions shown in equations 2.8 and 2.9 at anode and cathode, respectively, generating a higher power density. On the other hand, more water generated from the reactions may result in serious water flooding and therefore decrease the power density. The good permeability of porous metals allows fast removal of the water generated at cathode, preventing water flooding. Therefore, using porous metals as current collectors in DMFCs can increase power density and prevent water flooding.

Thirdly, porous current collectors have lower thermal conductivities than perforated current collectors and therefore maintain a high operating temperature of the cell. The thermal conductivity of porous metals normally decreases with porosity due to the loss of metal matrix (Boomsma and Poulikakos, 2001). Therefore, porous metals with high porosities have low thermal conductivities. Fig. 2.13 shows that fuel cells with porous current collectors have higher operating temperatures than the fuel cells with perforated plate current collectors regardless of the concentration of methanol (Chen and Zhao, 2007b).

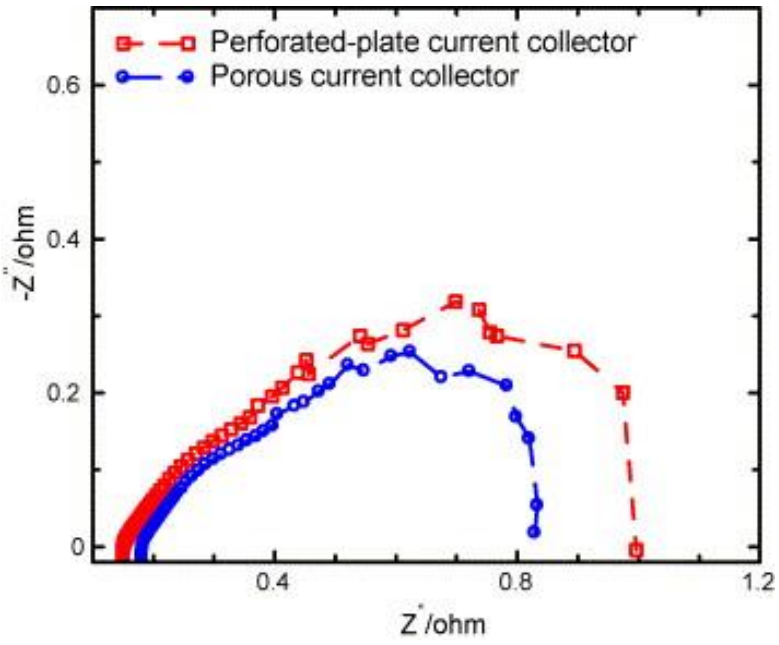

Fig. 2. 12 Nyquist plots of DMFC impedance spectra with a perforated-plate current collector and a porous current collector (Chen and Zhao, 2007b)

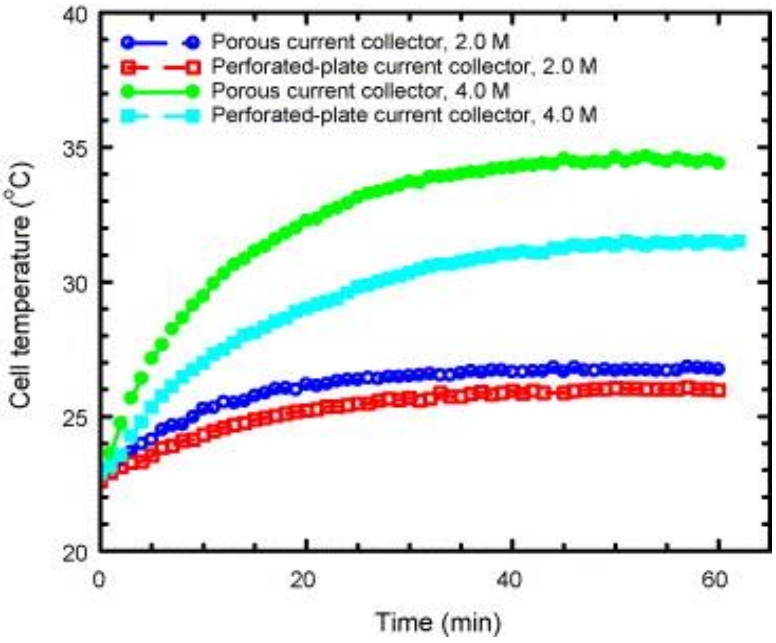

Fig. 2. 13 Operating temperature of cells with porous and perforated plate current collectors (Chen and Zhao, 2007b)

Porous metals can also improve the performance of DMFCs in other aspects. Yan et al. (2014) used a micro-porous metal as an anode current collector for a DMFC and found that high concentrations of methanol were allowed to be used without significant crossover. Unlike conventional current collectors, the micro-porous current collector allows an accumulation of CO_2 gas in the porous structure, forming a barrier to resist the methanol crossover. As discussed above, methanol crossover is one of the most important problems for DMFCs, especially at high methanol concentrations. As methanol crossover can be effectively prevented, the methanol concentration can be increased, and the reaction rate and energy density can be increased. It should be noted that the energy density may decrease with increasing methanol concentration because of limited water molecules. As shown in equation 2.8, methanol molecules react with water molecules at the anode. Less water becomes available when the methanol concentration increases, limiting the chemical reaction.

2.3.2 Lithium-Ion batteries (LIBs)

Lithium-ion batteries are one of the most important energy sources for portable devices worldwide during the past decades (Yoshio et al., 2009). The earliest study of lithium batteries started in the early 1970s. There are many kinds of lithium-ion batteries with different reaction systems, which can be classified into two categories: primary and secondary batteries.

One of the typical primary lithium batteries is primary lithium-manganese dioxide (Li-MnO_2) primary cell which uses lithium metal as the anode and manganese dioxide as the cathode. In working conditions, lithium is oxidized at the anode, generating electrons. It has an open-

circuit voltage about 3V which is about twice as that of many other kinds of batteries (Yoshio et al., 2009), making it a promising primary battery.

With the development of technologies, portable devices like phones, cameras and laptops are ubiquitous, and the demand of rechargeable secondary batteries become more and more significant. The most commonly used rechargeable secondary lithium-ion battery uses graphite as the anode and $LiCoO_2$ as the cathode (Goodenough and Park, 2013, Etacheri et al., 2011). Fig. 2.14 shows a schematic of the graphite-$LiCoO_2$ battery, including an anode, a cathode, a separator and an electrolyte. During the charging process, the lithium ions move from $LiCoO_2$ to graphite, namely delithiation of $LiCoO_2$. During the discharging process, the lithium ions move back from graphite to $LiCoO_2$, namely lithiation of $LiCoO_2$. The reactions at the anode and cathode can be seen in equations 2.10 and 2.11, respectively.

$$C_6 + Li^+ + e^- \Leftrightarrow LiC_6 \qquad 2.10$$

$$LiCoO_2 \Leftrightarrow \frac{1}{2}Li^+ + \frac{1}{2}e^- + Li_{0.5}CoO_2 \qquad 2.11$$

There are several challenges for LIBs to be commercialized as large-scale energy generation and storage devices (Goodenough and Kim, 2009). One of the most important challenges is capacity. For high voltage and high capacity applications, lithium-ion battery stacks are normally used. The lower capacities per LIB, the more LIBs are needed. Increasing the capacity of per LIB can effectively decrease the volume and weight of the whole battery stack. Another challenge is cycle stability. LIBs have low cycle stability, mainly as a result of the loss of active species or the formation of lithium dendrites.

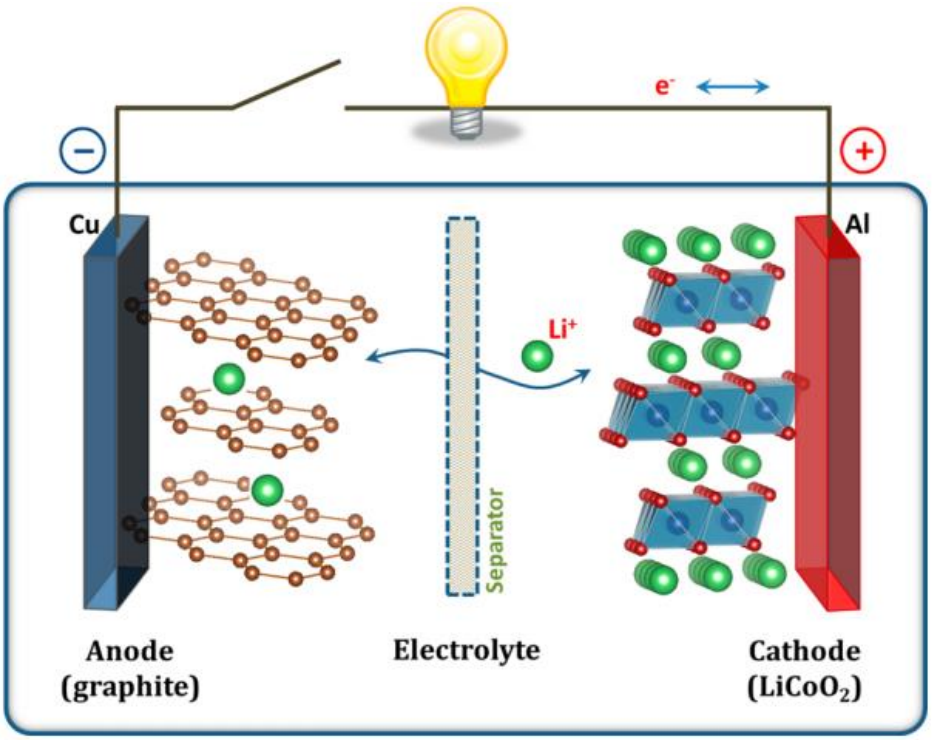

Fig. 2. 14 Schematic of the graphite-$LiCoO_2$ battery (Goodenough and Park, 2013)

Porous metals have been widely used to improve the capacity and cycle stability of LIBs. One of the most important reasons is the high surface area of porous metals. The high surface area offers more reaction sites, increasing capacity. Chung and Manthiram (2013) used a porous nickel as a current collector in a lithium-sulfur battery and found that the capacity of the battery was improved. They fabricated a sulfur-nickel foam cathode (SNF) using the paste-absorption method with a porous nickel sample serving as the cathodic current collector. As shown in Fig. 2.15, for 60 wt.% of sulfur in the paste, during the first 10 cycles, the discharging capacity of the battery with the SNF cathode was up to 1.5 times of that of the battery with a conventional cathode. Another possible reason for improved capacity is that the porous structure provided an intimate contact between active species and the current collector, resulting in low internal impedance and therefore higher capacity. Porous titanium (Bi et al., 2013), copper (Li et al., 2009), and other alloys like nickel-tin (Jung

et al., 2011), nickel-chromium (Yao et al., 2007), copper-tin (Shin and Liu, 2005) have also been used as current collectors in various LIBs to improve their capacity.

The stability of LIBs can also be improved by porous metals. As shown in Fig. 2.15, after 50 cycles, the discharging capacity of the battery with the SNF cathode retained 92% of its original capacity, while the retention rate of the battery with a conventional cathode was 85%. This is because the porous structure accommodates the active species and traps polysulfides in the cathode region, which provides good cycle stability. It is worth mentioning that the cycle stability of a LIB can be highly improved by using a porous lithium anode which effectively prohibits the formation of lithium dendrite (Wang et al., 2008). Yao et al. (2010) also studied the effect of annealing temperature of porous current collectors on the cycle stability of a LIB. They found that the annealed porous current collector provided the best cycle stability, followed by non-annealed porous current collector and then conventional current collector.

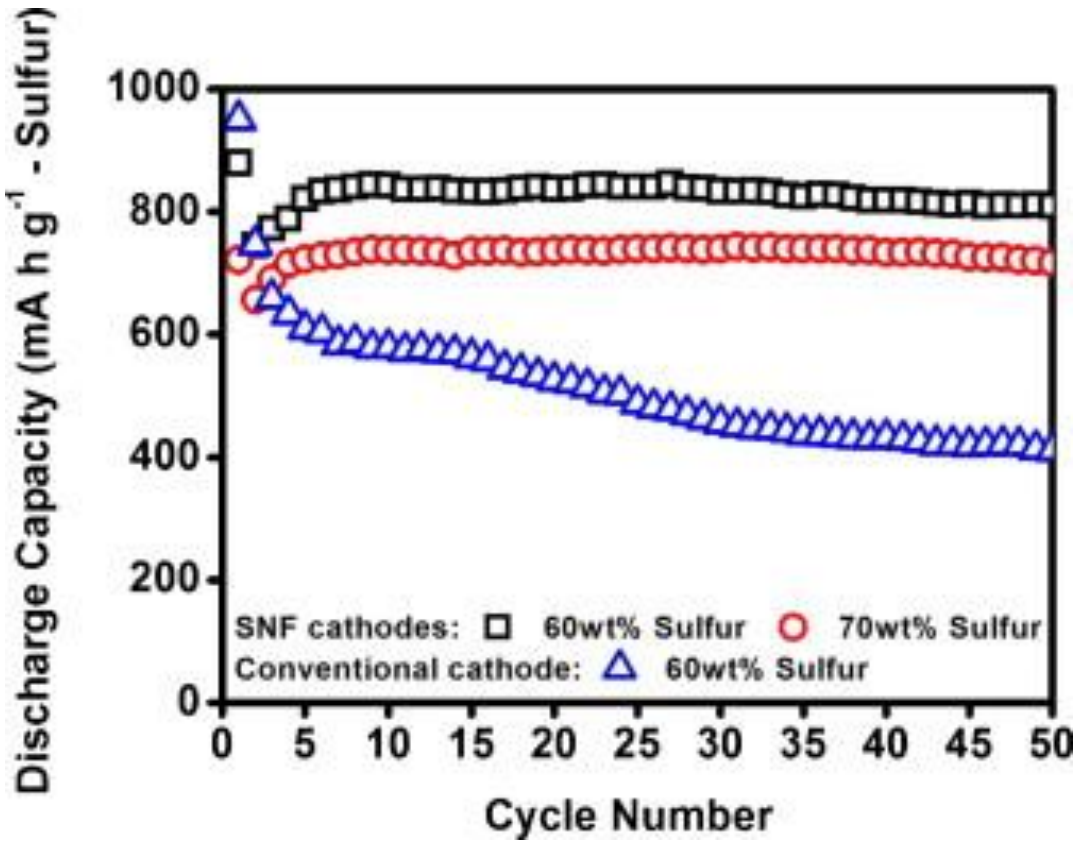

Fig. 2. 15 Cycling profiles of a lithium-sulfur battery with the SNF cathodes and a conventional cathode (Chung and Manthiram, 2013)

2.3.3 Proton exchange membrane (PEM) water electrolysers

Hydrogen has been regarded as one of the most environment-friendly energy source in the world (Dunn, 2002). However, the fact is that hydrogen does not exist in its molecular structure in nature. In the past, hydrogen is mainly produced by steam reforming natural gas or other fossil fuels, such as propane, gasoline, diesel, methanol, or ethanol (Ni et al., 2007). The limitation is that the produced hydrogen has low purities. To this end, PEM water electrolysers were developed to produce highly-purified hydrogen by the electrochemical conversion of water (also known as water electrolysis) (Barbir, 2005). Fig. 2.16 shows a schematic of a typical PEM water electrolyser, including a proton exchange membrane

(PEM), a cathode, an anode, a current collector and a bipolar plate. The overall reaction is shown in equation 2.12.

$$H_2O \rightarrow \frac{1}{2}O_2 + H_2 \qquad 2.12$$

Porous metals have been used as current collectors in PEM water electrolysers because of their good permeability, mass transfer property, high surface area and excellent corrosion resistance (Ito et al., 2012, Grigoriev et al., 2009). During the water electrolysis process, liquid water is pumped to pass through the anodic chamber and gaseous oxygen is generated from the surface of anode. Like the porous current collectors in the DMFCs mentioned in section 2.3.1, permeable porous structure offers a pathway for liquid water and gaseous oxygen, making them move more effectively and increasing the overall mass transfer performance. High surface area still plays an important role here, for providing large reaction site and increasing hydrogen productivity. Additionally, porous metals, e.g. porous titanium, with high corrosion resistance is crucial, because the potential of the anode during electrolysis is so cathodic that commonly used materials (like carbon) tend to corrode.

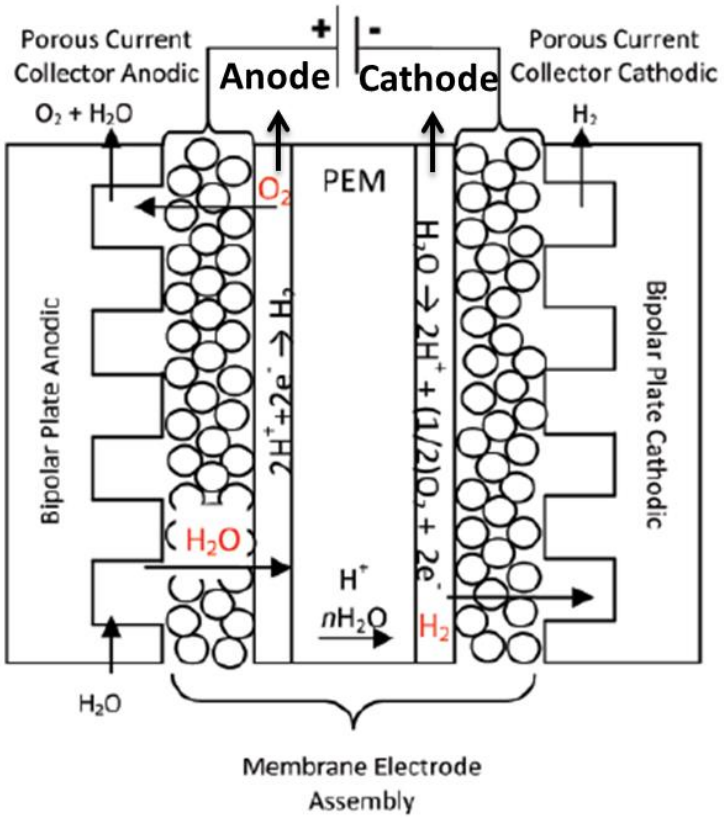

Fig. 2. 16 Schematic of the PEM water electrolyser (Rahim et al., 2015)

Grigoriev et al. (2009) studied the effects of the pore structure of porous current collectors on the performance of PEM water electrolysers and found that metal particle size and pore size have significant impacts on the mass transport performance in PEM water electrolysis. The optimum metal particle size and pore size of porous current collectors were determined as 50 – 75 and 12 – 13 microns, respectively. Although Grigoriev et al. (2009) optimized the pore structure of current collector from the mass transport point of view, the studies of the effects of pore size and porosity were not comprehensive. Ito et al. (2012) systematically studied the correlations between PEM performance and pore size and porosity. They found that the electrolysis performance increased with decreasing pore size until 10 µm, regardless of the type of porous current collector used. There was little effect of porosity when the porosity exceeded about 0.50. They also drew three conclusions: 1) the pore

diameter affects the flow regime, 2) mass transfer of liquid water to the electrode surface can be restricted by bubbles in the channel, and 3) larger bubbles generated from larger pores tend to become long slugs and thus hinder the water supply to the membrane.

There is no doubt that porous metals are promising materials in water electrolysis. However, the research for using porous metals as current collectors to improve water electrolysis is still very limited in the literature. Further work in this area is particularly necessary.

2.3.4 Electrochemical glucose sensor

Accurate detection of glucose is of particular importance for clinical diagnostics in diabetes control. In the past, sensors with immobilized enzymes were used to monitor glucose concentration (Wang, 2008, Wooten et al., 2013). Although enzymes have good selective catalytic abilities, which offer enzyme-based sensors good selectivity and sensitivity, there are some intrinsic limitations. For example, the purification and immobilization of enzyme are time-consuming and costly (Jin et al., 2013, Tang et al., 2014). More importantly, the enzyme-based sensors have short lifetime and poor stability in harsh environments due to the nature of enzyme (Park et al., 2006, Toghill and Compton, 2010).

Porous metals, including porous copper, nickel and gold, have been regarded as the best materials to develop enzyme-free biosensors for glucose detection, not only because these metals have good catalytic abilities for glucose oxidation reactions, but also because they have unique porous structures. The porous structure provides the sensors with a high specific surface area and makes it easier for glucose molecules to access the surface of the catalytic metals. This section introduces some typical enzyme-free glucose sensors made by various porous metals.

Porous copper manufactured by electrodeposition on a screen-printed carbon electrode substrate was used to detect glucose concentration (Niu et al., 2014). The porous copper sample was used as a working electrode in a three electrode electrochemical cell. It showed high sensitivities of 2.57 and 1.81 $mA/cm^{-2}mM^{-1}$ for glucose in a linear concentration ranges of 2 – 80 µM and 0.1 – 5 mM, respectively. The limit of detection was as low as 0.98 µM for a signal-to noise ratio of three. Fifteen identical measurements using the same porous copper sample provided reproducible responses with a relative standard deviation (RSD) of 5.1%. Measurements of the same glucose sample by fifteen new porous copper samples provided a RSD of 7.0%. The long-term stability of this kind of porous copper is attractive, with only a 5% loss in sensitivity after one month working. The selectivity of the porous copper was also tested by adding other similar biomolecules, including xylose, galactose, fructose, mannose, arabinose, ribose, rhamnose, ascorbic acid, dopamine, uric acid and acetamidophenol. All of these biomolecules had little effect on the amperometric results, indicating a good selectivity of porous copper in glucose detection. The reliability of this kind of porous copper was also verified by a commercial glucometer in detecting the glucose concentration in rat and rabbit blood serum. The non-enzymatic porous copper sensor showed good agreement with the results from the commercial glucometer, indicating that the porous copper had favourable accuracy and precision in glucose detection. To further improve the performance of porous copper as non-enzymatic glucose sensors, a porous copper sample was used as a precursor for in-situ growth of copper oxide nanowire on its surface (Li et al., 2015). The as-obtained porous copper/copper oxide nanowires sample showed an improved performance in glucose detection. It had a limit of detection of 0.3 µM which is lower than that of porous copper studied by Niu et al. (2014). This was probably because of the enhanced surface area from the growth of copper oxide nanowires. The

sensitivity of the porous copper/copper oxide nanowire sample was about 2.22 mA/cm^{-2}mM^{-1} in the linear concentration range from 10 µM to 18.8 mM, which is similar to that studied by Niu et al. (2014). The selectivity and long-term stability of this sample were also good. More importantly, it can be used in detecting glucose in human serum. The result agreed very well with a commercial glucose sensor, suggesting that this kind of porous sensor has the possibility of non-invasive glucose detection.

Porous nickel samples have been used as non-enzymatic glucose sensors by Lu et al. (2013). The commercially available porous nickel samples were manufactured by electrodeposition. They exhibited a good linear range and a limit of detection of 0.05 – 7.35 mM and 2.2 µM, respectively. More importantly, it was found that the oxidation of glucose to glucolactone was catalysed by the $Ni(OH)_2$/NiOOH redox couple on the surface of porous nickel. The formation of $Ni(OH)_2$/NiOOH can be seen in equations 2.13 – 2.15 (Nie et al., 2011).

$$Ni + 2OH^- \rightarrow Ni(OH)_2 + 2e^- \quad (2.13)$$

$$Ni(OH)_2 + OH^- \rightarrow NiOOH + H_2O + e^- \quad (2.14)$$

$$NiOOH + glucose \rightarrow Ni(OH)_2 + glucolactone \quad (2.15)$$

Kung et al. (2014) applied an electrochemical cyclic voltammetry treatment on a pure porous nickel sample for 100 cycles in 1.0 M NaOH solution to obtain a single layer of nickel hydroxide nanoparticles covered on the full surface of the porous nickel sample. The as-obtained sample was used as a glucose sensor with a linear range from 0.6 to 6 mM and a limit of detection of 0.16 µM. Niu et al. (2013) used a nanostructured porous nickel sample, which was grown in situ on a screen-printed carbon electrode substrate with a hydrogen-

evolution-assisted electrodeposition strategy. The nanostructured porous nickel sample had a wider linear range from 0.5 μM to 4 mM and a lower limit of detection of 0.07 μM. The better performance can probably be attributed to the increased surface area.

Porous gold can also be used as non-enzymatic glucose sensors due to its excellent catalytic abilities. Li et al. (2007) produced a porous gold film with interconnected macroporous walls and nanoparticles using the hydrogen bubble dynamic template synthesis followed by a galvanic replacement reaction. The as-obtained porous gold sample provided good performance in detecting glucose, with a sensitivity of 11.8 μA cm^{-2} mM^{-1} in a linear range from 2 to 10 mM and a limit of detection of 5 μM. Han et al. (2014) produced a hierarchically porous gold-cluster film sample by calcination of Au@BSA microspheres developed in their previous work (Wang et al., 2012). This kind of porous gold showed a sensitivity of 10.76 μA cm^{-2} mM^{-1} in a linear range from 0.01 to 10 mM and a limit of detection of 1 μM (Han et al., 2014).

2.3.5 Properties and functions of porous metals in electrochemical applications

Table 2.3 summarizes the electrochemical applications discussed above as well as the properties and functions of porous metals in these applications. It is obvious that the permeability, surface area and mass transfer are the most important properties in these electrochemical applications. In other words, if a porous metal is superior in these three properties, it has a great potential in many electrochemical applications. This thesis studied some of these properties of the porous metals manufactured by the LCS process and further explored the feasibility of this type of porous metal in electrochemical detection.

Table 2.3 Properties and functions of porous metals in electrochemical applications

Electrochemical Applications	Properties, functions of porous metals
DMFCs	• High surface area, providing large reaction site and generating high power density • Good mass transfer property, increasing the transport rate of oxygen at the cathode and therefore increasing power density • Good permeability, allowing fast removal of water generated and preventing water flooding. • Low thermal conductivity, decreasing heat loss during operation
LIBs	• High surface area, providing large reaction site and increasing battery capacity • Good mass transfer property, increasing the transport rate of reactive species and increasing power density • High volume of voids, accommodating active materials and preventing the formation of some undesirable materials, resulting in good stability.
PEM water electrolysers	• High surface area, providing large reaction site and increasing hydrogen productivity • Good mass transfer property, increasing the transport rate of liquid water and increasing hydrogen productivity • Good permeability, allowing quick liquid water supply and fast removal of gaseous oxygen • Good corrosive resistance, avoiding corrosion during operation
Glucose sensors	• High surface area, providing large reaction site and improving detection performance • Good mass transfer property, increasing the transport rate of glucose molecules and improving detection performance • Good catalytic ability, contributing to fast oxidation of glucose

2.4 Summary

This chapter reviewed some of the commonly used manufacturing processes, important properties and current electrochemical applications of porous metals. Manufacturing techniques, including loose powder sintering, melt gas injection, chemical vapour deposition, electrodeposition, Lost Carbonate Sintering and selective laser melting, have been comprehensively reviewed. Lost Carbonate Sintering is one of the best processes in terms of cost and quality of samples. Three properties, i.e. permeability, surface area and mass transfer, of porous metals were also reviewed. In general, if a porous metal is superior in these three properties, it has a great potential in many electrochemical applications. Using porous metals in direct methanol fuel cells, lithium-ion batteries, proton exchange membranes and electrochemical glucose sensors, provides enhanced performances. All of these enhanced performances can be attributed to the three properties studied in section 2.2.

Table 2.4 summarises the main knowledge gap for the LCS porous metals. Although LCS is an established process and has been successfully used to manufacture porous Cu, Ni, Al and Fe, there are still several limitations. The LCS process is not applicable for some metals, like Ti, due to reaction between K_2CO_3 and the metals. Additionally, the applicability of the LCS process for manufacturing extremely high melting point (>2000 ˚C) metals has not been explored.

Permeability, surface area and mass transfer are three crucial properties for porous metals. The permeability of the LCS porous metals has been well studied, including the effects of porosity, pore size, as well as homogenous and hierarchical structures. The electrochemical surface area of porous Cu has been studied using cyclic voltammetry techniques, including

the effects of porosity and pore size. However, there are still some remaining questions. How do sintering temperature, metal particle size, chemical etching and diffusion layer thickness affect the surface area? Can the surface area of other porous metals be measured by the cyclic voltammetry technique? The mass transfer property of the LCS porous metals has not been systematically studied. Therefore, further work is needed to study the electrochemical surface area and mass transfer performance of the LCS porous metals, and the effects of porosity and pore size.

Porous metals have great potentials for many electrochemical applications. Currently, the main applications of the LCS porous metals are confined to heat management. Other applications, especially for electrochemical sensors and energy generation, need to be explored.

Table 2.4 Knowledge gap for the LCS porous metal

		knowledge gap
Manufacturing process		• Not applicable for some specific metals. e.g. Ti, due to reaction between K_2CO_3 and metals. • Applicability for extremely high melting point metals.
Properties	**Permeability**	• The permeability of the LCS porous metals have been well studied.
	Surface area	• The effects of sintering temperature, metal particle size and chemical etching treatment are still unknown. • The effect of diffusion layer thickness on the electrochemical surface area has not been studied. • The electrochemical surface area of other porous metals, apart from Cu, have not been measured
	Mass transfer	• The mass transfer property of the LCS porous metals has not been well studied. • The effects of porosity and pore size on mass transfer property are still unknown.
Applications		• Applications in electrochemical detection need to be explored. • Applications in energy generation need to be explored.

CHAPTER 3 EXPERIMENTAL METHODS

This project mainly focuses on the electrochemical properties and electrochemical detection performance of the LCS porous metals. This chapter describes the experimental processes and methods used in this project, including the LCS manufacturing process, physical and chemical treatments, structural and surface characterizations, electrochemical property characterizations and electrochemical detection of some specific ions.

3.1 Preparations of porous metals

All porous metal samples with porosities in the range of 0.5 – 0.8 and pore sizes in the range of 250 – 1500 μm were manufactured by the LCS process. As mentioned in Section 2.1.2.1, the LCS process consists of mixing metal and carbonate powders, compaction of the mixture, sintering and removal of carbonate (Zhao et al., 2005). The carbonate particles were removed either by dissolution in hot water or decomposition during sintering, depending on different manufacturing routes. Different metal particle sizes were used to investigate the effects of metal particle size on the specific surface areas. To further study the effects of surface morphology on the specific surface areas of the LCS porous metals, porous samples were also treated by chemical acid etching. Porous structural parameters (porosity and pore size) of all porous samples were determined before measurements.

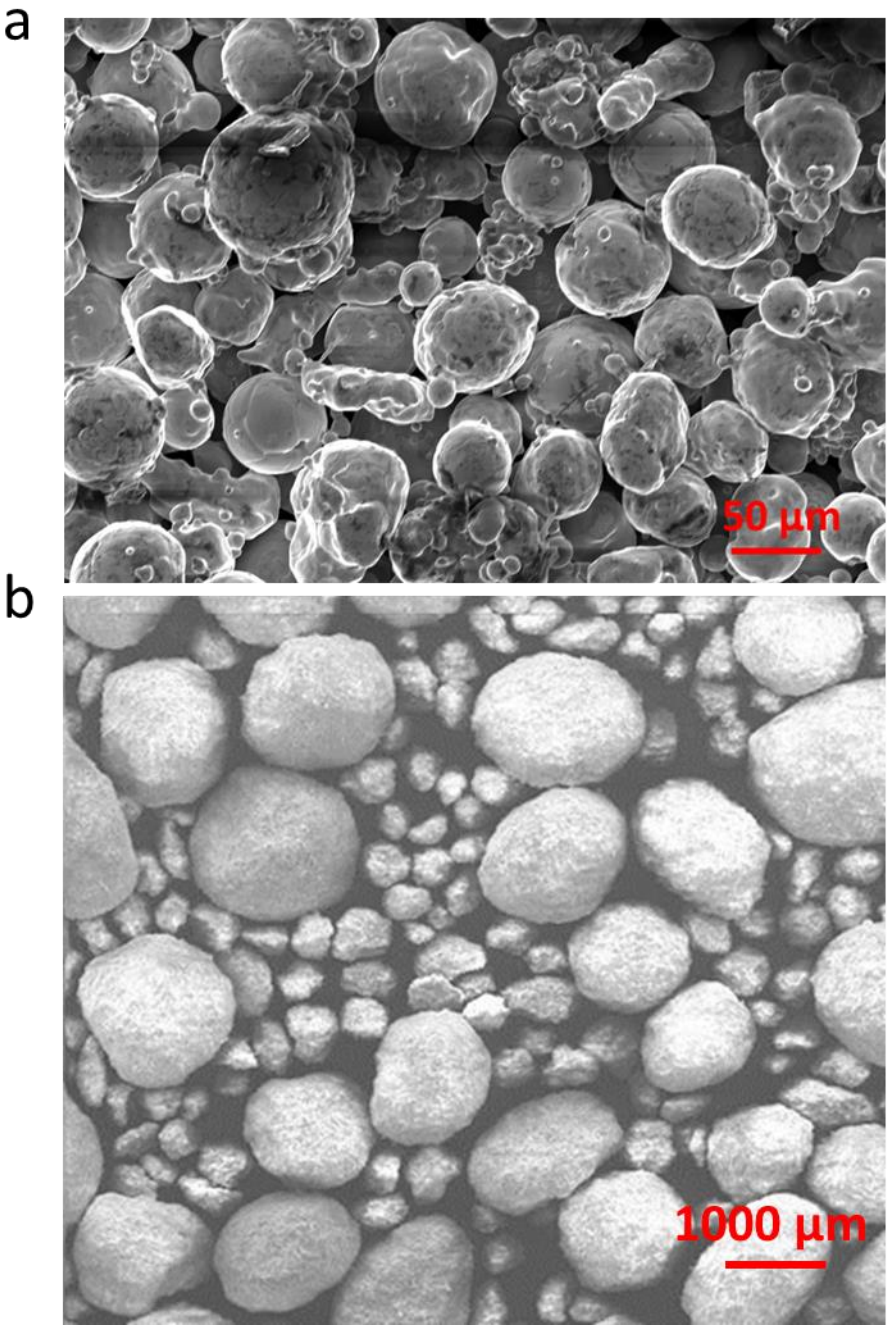

Fig. 3. 1 Images of metal and K_2CO_3 powders. (a) Spherical Ni powder with a mean particle size of 45 µm. (b) Rounded K_2CO_3 powder with a particle size range of 250 – 1500 µm

3.1.1 Raw materials

Food grade K_2CO_3 powder (Fig 3.1 a) with a rounded shape and a purity of 99% was supplied by E&E Ltd, Australia. The K_2CO_3 powder was sieved and divided into four different particle

size ranges: 250 – 425 μm, 425 – 710 μm, 710 – 1000 μm and 1000 – 1500 μm to manufacture porous metals with different pore sizes, as pore sizes are the same as the particle sizes of K_2CO_3.

Cu powder with a spherical shape and a purity of 99.5% was supplied by Ecka Grannules Metal Powder Ltd, UK. The Cu powder was sieved and divided into four different particle size ranges: <20 μm, 20 – 45 μm, 45 – 75 μm and 75 – 90 μm in order to study the effects of Cu particle size on the specific surface areas.

Ni powder (Fig 3.1 b) with a spherical shape and a purity of 99% was supplied by Changsha Tianjiu LTD, China. Similarly, the Ni powder has three different particle sizes with average particle sizes of 25 μm, 38 μm and 75 μm in order to study the effects of Ni particle size on the specific surface areas.

3.1.2 Mixing and compaction

K_2CO_3 powder was mixed with the Cu or Ni metal powder at pre-specified volume ratios to achieve target porosities. A certain rectangular or a cylindrical mould was used to make porous samples with a uniform thickness of 5 mm. With the target volume of the porous metal sample fixed, i.e. the total volume of the metal and K_2CO_3 powders, the masses of the powders required were determined by

$$M_{Metal} = (1 - \varepsilon_n) V \rho_{Metal} \quad 3.1$$

$$M_{K_2CO_3} = \varepsilon_n V \rho_{K_2CO_3} \quad 3.2$$

where M_{Metal} and $M_{K_2CO_3}$ are the masses of the metal and K_2CO_3 powders, respectively, ε_n is the target porosity (also known as nominal porosity), V is the target volume of the porous metal sample, ρ_{Metal} (8.96 g/cm^3 for copper and 8.91 g/cm^3 for nickel) and $\rho_{K_2CO_3}$ (2.34

g/cm^3) are the densities of the metal and K_2CO_3 powders, respectively. Ethanol, approximately 3 – 5% in volume, was added as a binder between the metal and carbonate powders before mixing.

The mixture was poured into either a rectangular or a cylindrical mould before compaction depending to different sintering routes. The rectangular mould had a length of 30 mm, a width of 20 mm and a height of 5 mm, while the cylinder mould had a diameter of 50 mm and a height of 60 mm. The mixture in the mould was compacted by a hydraulic press (Moore Hydraulic Press, UK) at a pressure of 200 MPa for 10 seconds to make preforms for subsequent sintering.

3.1.3 Sintering

Two sintering routes, namely decomposition and dissolution, were used in this work to investigate the effect of sintering temperature on the surface morphology and therefore the specific surface areas of the LCS porous metals.

One set of porous metal samples were manufactured by the decomposition route. The rectangular mould was used for preparing the preforms. The compacted preforms were removed from the mould and then placed into a high vacuum furnace for sintering. The sintering curve in the decomposition route is shown in Fig. 3.2 a. The temperature was increased from room temperature (≈25˚C) to 200˚C at a heating rate of 5˚C/minute and stayed at 200˚C for 30 minutes in order to evaporate the ethanol in the preforms. The temperature was then increased to 800˚C at a heating rate of 10˚C/minute and stayed at 800˚C for another 30 minutes for preliminary sintering in order to prevent the samples from collapse. The temperature was finally increased to 950˚C at a heating rate of 5˚C/minute and stayed at 950˚C for 120 minutes to achieve strong bonding between the metal particles.

As the decomposition temperature of K_2CO_3 is 891˚C, all K_2CO_3 particles within the preforms decomposed completely during the sintering process, generating open-cell porous metals with desired porosities and pore sizes. The as-obtained porous metal samples were cooled down in an argon environment to prevent oxidization.

Another set of porous metal samples were manufactured by the dissolution route. The sintering process was carried out in atmosphere in a muffle furnace. The cylindrical mould was used for preparing the preforms. The compacted preform was kept in the cylinder mould with two ends sealed with compacted steel layers. There was a compacted K_2CO_3 layer between the preform and each of the steel layers to prevent direct contact between the preform and steel. The sintering curve in the dissolution route can be seen in Fig. 3.2 b. The temperature was increased from room temperature ($\approx$25˚C) to 200˚C at a heating rate of 5˚C/minute and stayed at 200˚C for 30 minutes in order to evaporate the ethanol in the preforms. The temperature was then increased to 850 ˚C at a heating rate of 5˚C/minute and stayed at 850 ˚C for 240 minutes to strengthen the bonding between the metal particles, followed by cooling in air to room temperature. As sintering temperature was lower than the decomposition temperature of K_2CO_3, all K_2CO_3 particles were still in the samples after sintering. The sintered samples were then immersed in 100 ˚C hot water to remove all K_2CO_3 particles, generating open-cell porous metals with desired porosities and pore sizes.

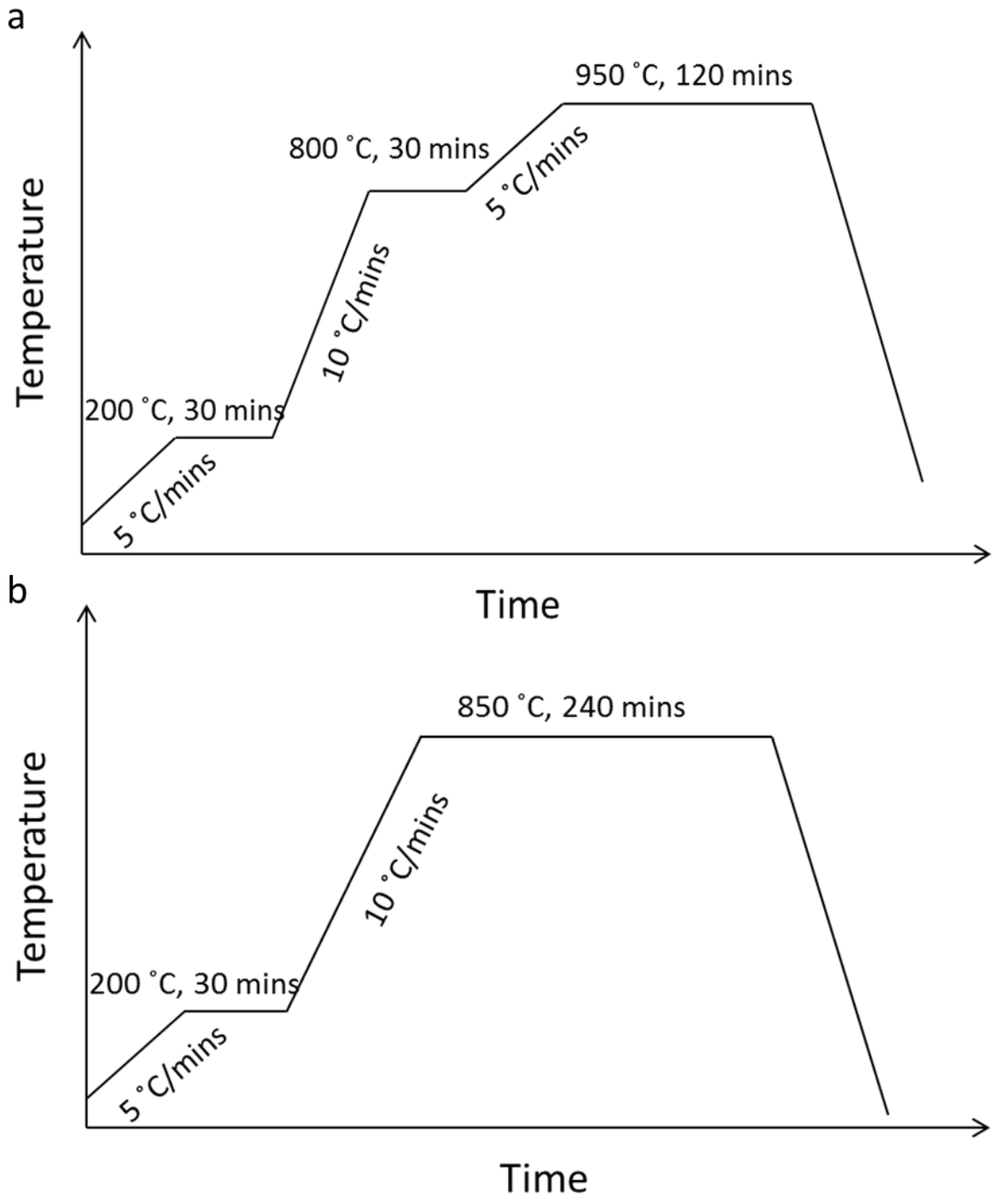

Fig. 3. 2 Sintering curves for the decomposition route (a) and the dissolution route (b)

The as-obtained porous metal samples were cut by an electrical discharging machine (Prima E250, ONA Ltd., Bristol, UK) into rectangular or cylindrical specimens. The specimens had a rectangular shape with dimensions of $5 \times 5 \times 4.8$ mm for surface area measurement. The

specimens had a cylindrical shape with a diameter of 6mm and a height of 5 mm for mass transfer measurement and electrochemical detection.

3.1.4 Chemical etching

All the as-produced porous metal samples were ultrasonically cleaned in dilute hydrochloric acid to remove the metal oxides from the surface and then washed with distilled water. To study the effects of chemical etching on surface morphology and in turn the surface areas of the LCS porous metals, some of the samples were chemically etched by immersing the samples in 5 M nitric acid under ultrasonication at room temperature for 5 minutes. The weight loss of the etched samples was less than 5%. Samples with porosities higher than 70% were not etched, because the etching process could easily result in a weight loss higher than 10% and therefore significantly change the porous structures.

3.1.5 Real porosity determination

The real porosity of the samples, ε_r, was determined from the relative density, which was calculated by dividing the apparent density of the porous metal sample by the density of the metal (see equation 3.3).

$$\varepsilon_r = 1 - Relative\ dentivy = 1 - \frac{M/V}{\rho_{Metal}} \qquad 3.3$$

where *M* and *V* are the mass and volume of the porous sample, respectively. M/V is the apparent density of the porous sample. The mass of the sample was measured by an analytical balance and the volume was calculated by multiplying its length, width and height (for rectangular samples) or cross-sectional surface area and height (for cylindrical samples).

3.2 Geometric surface area measurement

Quantitative stereology (QS) was used to measure the geometric surface areas of the porous copper and nickel with porosities in the range of 0.5 – 0.8 and pore sizes in the range of 250 – 1500 µm. Before measurements, the outer surface of porous samples (before electrical discharging machine cutting) was well ground by sandpapers with grits of 80 and 320 to achieve a good surface finish. A micrograph of the porous metal sample was then taken by a digital microscope camera (Veho VMS-004) and a counting grid was then superimposed onto the micrograph, as shown in Fig. 3.3. In the micrograph, the light region indicates pores and the dark region represents the metal matrix, the counting grid was in black with each square having a 1 mm side length. The intersects between the pore perimeters and grid lines were counted by Image J (Diao et al., 2015). The volumetric specific geometric surface area, A_{VG} ,and the gravimetric specific geometric surface area, A_{MG}, can be calculated by the Equations 3.4 and 3.5 below (Underwood et al., 1970):

$$A_{VG} = \frac{2N}{L} \tag{3.4}$$

$$A_{MG} = \frac{2N}{L(1-\varepsilon)\rho_{metal}} \tag{3.5}$$

where N is the number of intercepts between the pore perimeters and grid line, L is the total length of the grid lines, ε is the porosity of porous metal and ρ_{metal} is the density of pure solid metal (Cu or Ni). It should also be noted that porous samples with pore sizes smaller than 250 µm were not measured by this method because it was difficult to distinguish pores and interstices between adjacent metal particles in the metal matrix.

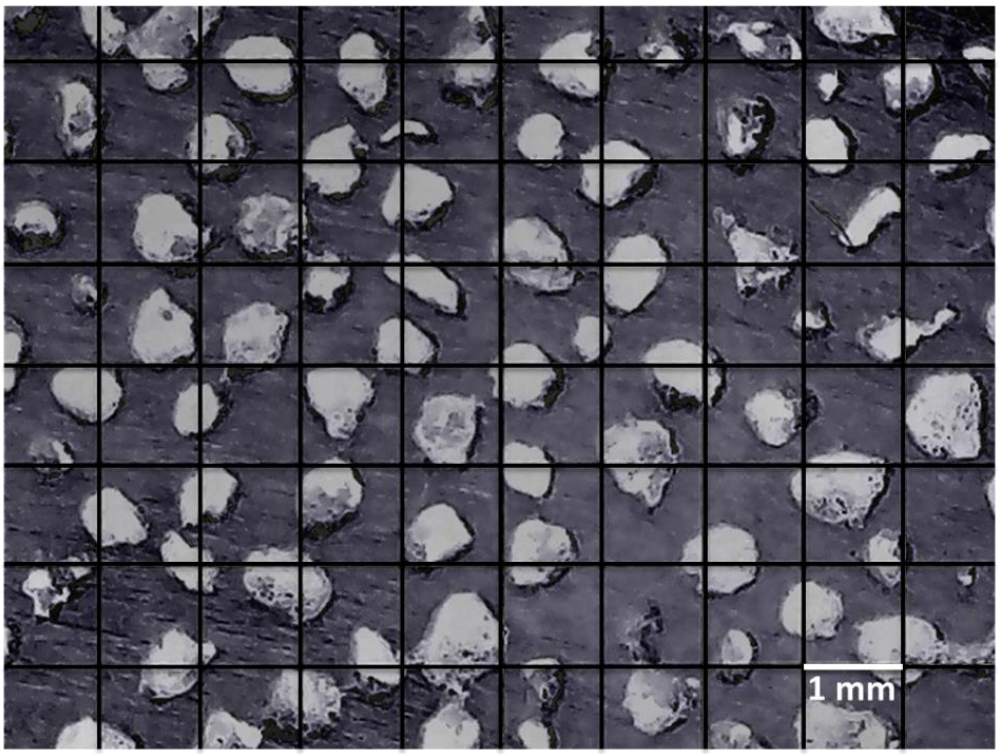

Fig. 3. 3 Micrograph of the outer surface of a porous copper sample (dark regions: Cu matrix, light regions: pores)

3.3 Electroactive surface area measurement

The electroactive surface areas of the LCS porous copper and nickel samples were measured by the cyclic voltammetry (CV) peak current method (Diao et al., 2015). According to the literature (Delahay et al., 1954, Bard et al., 1980), the CV peak current is linearly proportional to the electroactive surface area of an electrode. The quantitative relations between peak current and electroactive surface area of porous coper and porous nickel samples were determined by the Berzins–Delahay and the Randles–Sevcik equations, respectively, because of different natures of the reactions used (Shen and Akolkar, 2017). Porous samples with porosities in the range of 0.5 – 0.8 and pore sizes in the range of 250 – 1500 µm were measured.

3.3.1 Experimental apparatus

A three-electrode electrochemical cell connected with a potentiostat (Autolab PGSTAT101) was used for all electroactive surface area measurements. Fig. 3.4 shows a schematic diagram of the three-electrode electrochemical cell. It consisted of a working electrode, reference electrode and counter electrode. The porous sample served as the working electrode. The reference electrode was a saturated calomel electrode (SCE). A platinum coil was used as the counter electrode for the CV measurements of porous samples, while a platinum plate was used as the counter electrode for the CV measurements of metal plates. For electroactive surface area measurements of porous Cu and Ni, the electrolytes were 0.1 M KOH and 1 mM potassium ferrocyanide in 0.1 M KOH, respectively.

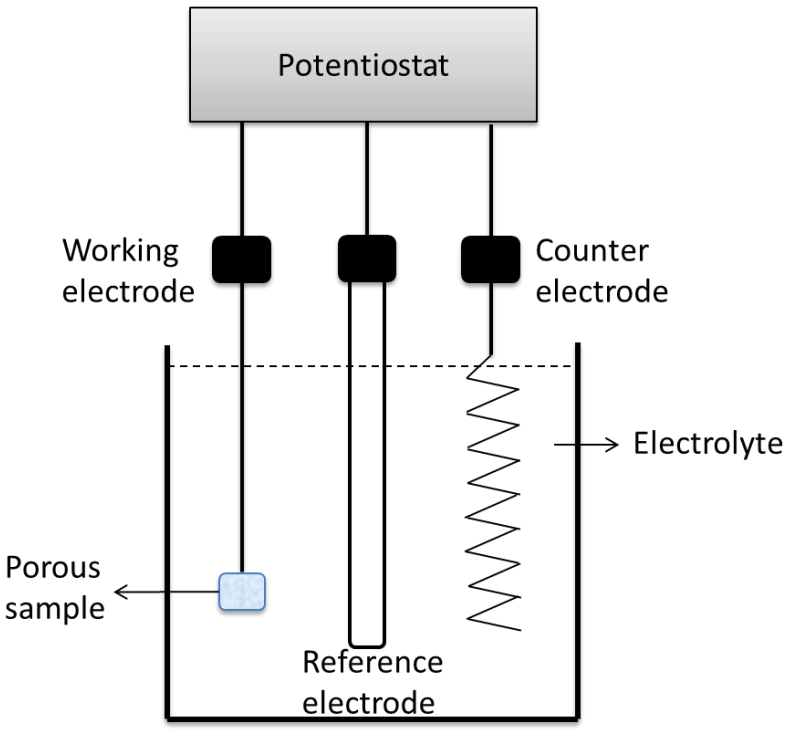

Fig. 3. 4 Schematic of the three-electrode electrochemical cell used for the CV measurements

3.3.2 Procedure for porous Cu

Fig. 3.5 shows a typical current-potential plot of porous copper in 0.1 M KOH. The applied potential was in the range from -1.6 to 0.7 V and the scan rate was 0.01 V/s. There are two current peaks in the forward sweeping part of the curve. The peaks, *1* and *2*, indicate two different chemical reactions, Equations 3.6 and 3.7, respectively (Hampson et al., 1972, Ambrose et al., 1973):

$$2Cu + 2OH^- \rightarrow Cu_2O + H_2O + 2e \quad (3.6)$$

$$Cu + 2OH^- \rightarrow Cu(OH)_2 + 2e \quad (3.7)$$

Peaks *1* and *2* were controlled by the diffusion of Cu^+ in the solid electrode and the diffusion of OH^- in the electrolyte, respectively (Hampson et al., 1972, Ambrose et al., 1973). Both peaks were used to measure the electroactive surface areas with an aim to study the effects of the chosen reaction and the diffusion layer thickness. As the products Cu_2O and $Cu(OH)_2$ are in solid state, the reactions 3.6 and 3.7 follow the Berzins–Delahay reversible soluble–insoluble redox transitions model (Shen and Akolkar, 2017). The quantitative relations between the peak current and electroactive surface area can be expressed in Equation 3.8 (Delahay, 1954):

$$I_p = 3.67 \times 10^5 n^{\frac{3}{2}} A_E c D^{\frac{1}{2}} v^{\frac{1}{2}} \quad (3.8)$$

where I_p is the peak current, n is the number of electrons in the reaction, A_E is the electroactive surface area of the working electrode, c is the bulk concentration of reactive species, D is the diffusion coefficient of the reactive species and v is the scan rate.

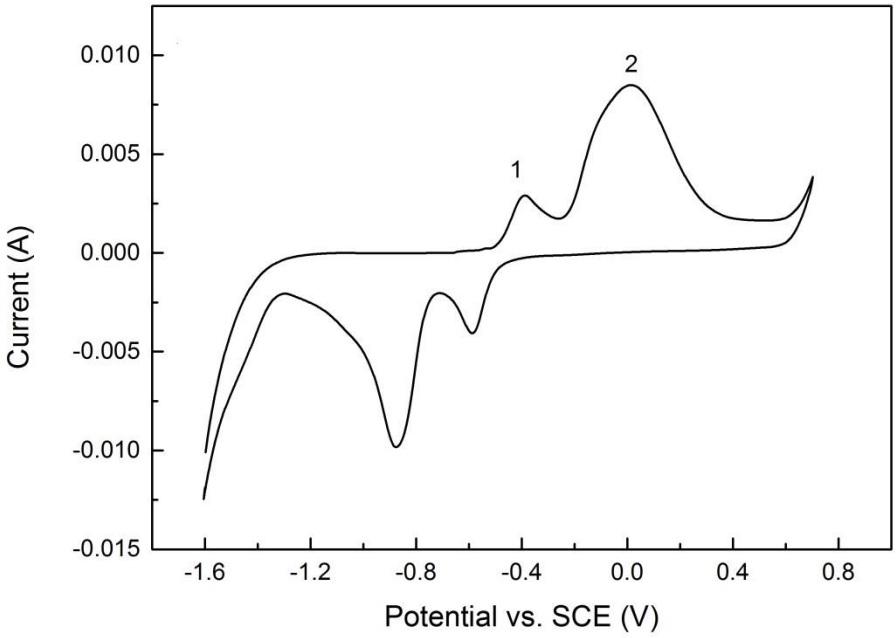

Fig. 3. 5 Typical current-potential plot of porous copper in 0.1 M KOH in the potential range of -1.6 to 0.7 V at a scan rate of 0.01 V/s

Equation 3.8 cannot be used directly to calculate the surface area of the Cu electrode due to passivation (Diao et al., 2015). Therefore, seven copper plates with known geometric surface areas as shown in Fig. 3.6 were used to calibrate the relation between the peak current and electroactive surface area for porous copper. The copper plates were ground by sandpapers (grits 80, 320, 600 and 1200), polished by cloths (6 and 1µm) and further polished by a silk-type cloth pad with a 0.04 µm colloidal silica suspension to achieve a mirror finish. The current-potential plots of the copper plates (see Fig 4.4 Chapter 4) are similar to those of the porous copper in Fig. 3.5. The quantitative relation between peak current and electroactive surface area was determined by measuring the peak currents of the mirror-polished copper plates, because the electroactive surface areas of the mirror-polished copper plates was their geometric surface areas.

This quantitative relation is also applicable for porous copper. Therefore, the electroactive surface area of porous copper can be determined from the peak current. The volumetric, A_{VE}, or gravimetric, A_{ME}, specific electroactive surface area of porous copper was calculated by dividing the electroactive surface area over volume or mass of the porous copper samples.

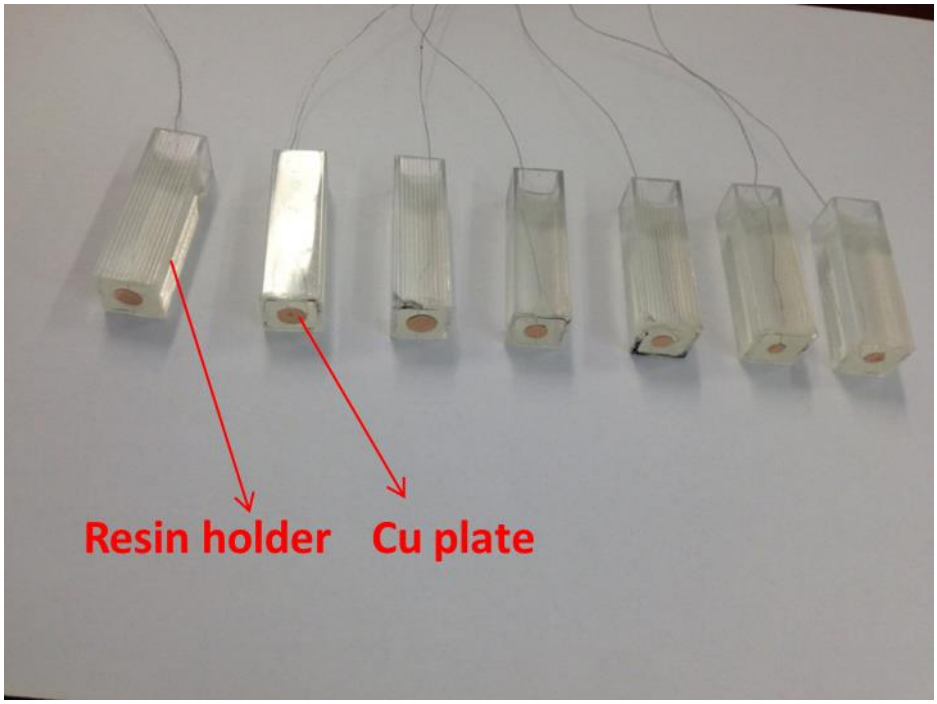

Fig. 3.6 Mirror polished copper plates surrounded by resin holder

3.3.3 Procedure for porous Ni

Fig. 3.7 shows a typical current-potential plot of porous nickel in the electrolyte of 1 mM potassium ferrocyanide in 0.1 M KOH. The applied potential was in the range from -0.3 to 0.4 V. The applied scan rate was in the range from 0.005 to 0.05 V/s in order to study the effect of scan rate on the electroactive surface area of porous nickel. The current peak at a potential about 0.22 V in Fig. 3.7 corresponds to the oxidation of ferrocyanide to ferricyanide:

$$[Fe(CN)_6]^{4-} \xrightarrow{Oxidation} [Fe(CN)_6]^{3-} + e \qquad 3.9$$

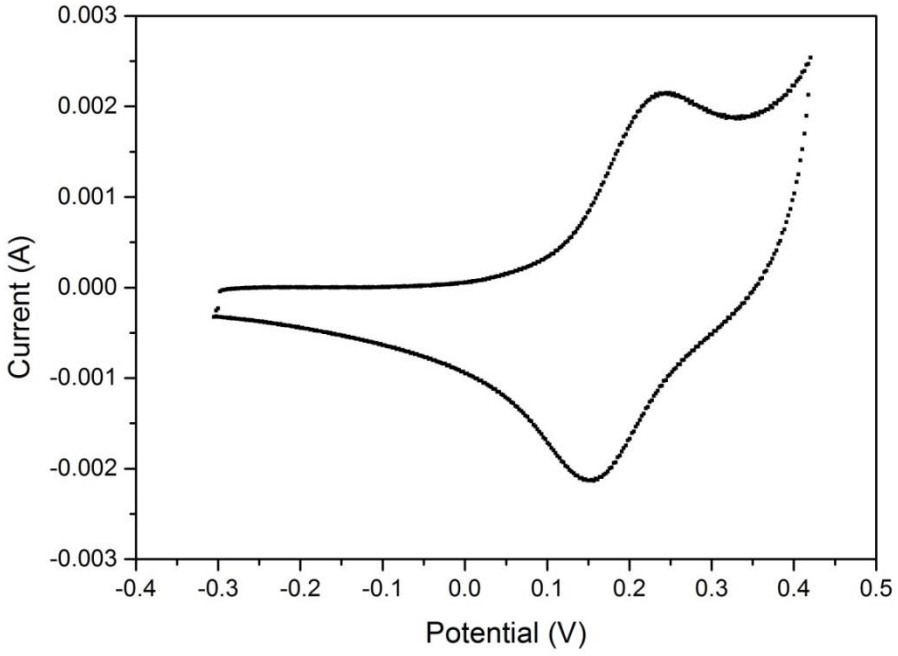

Fig. 3. 7 Typical current-potential plot of porous nickel in the electrolyte of 1 mM potassium ferrocyanide in 0.1 M KOH in the potential range of -0.3 – 0.4 V

As both ferrocyanide and ferricyanide are soluble, the reaction 3.9 follows the classical Randles–Sevcik reversible soluble–soluble redox transitions model (Bard et al., 1980). The quantitative relation between the peak current and the electroactive surface area is determined by the Randles–Sevcik equation (Bard et al., 1980):

$$I_p = 268600 n^{\frac{3}{2}} A_E D^{\frac{1}{2}} C v^{\frac{1}{2}} \qquad 3.10$$

In order to calibrate the quantitative relation in Eq. 3.10, six mirror-polished nickel plates (the same polishing process as for copper plates) with known geometric surface areas were used. The volumetric, A_{VE}, or gravimetric, A_{ME}, specific electroactive surface area of porous

nickel was further calculated by dividing the electroactive surface area over volume or mass of the porous nickel samples.

3.3.4 IR-compensation

The large surface areas of the porous samples resulted in currents of magnitude in the order of ~10 mA , which could cause significant distortions in voltammetry due to uncompensated solution resistance (Smith et al., 2015). The measured solution resistance in the cell was about 8 – 10 Ohm. The "*IR*-compensation" feature in the potentiostat was used to automatically compensate the potential signal for solution resistance (where *I* is the current and *R* is the solution resistance between the reference and working electrodes). For mirror-polished metal plates, the solution resistance was not compensated due to low currents generated.

3.4 Real surface area measurement

The real surface area of the porous metal samples was measured by the cyclic voltammetry double layer capacitance method (Diao et al., 2015). Porous copper and nickel samples with porosities in the range of 0.5 – 0.85 and pore sizes in the range of 250 – 1500 μm were measured. The experimental apparatus was the same as that used in the electroactive surface area measurement (Fig. 3.4). The electrolytes used for porous copper and nickel samples were 0.1 M KOH and 8 M KOH, respectively. The applied potential ranges for porous copper and nickel were -1 to -0.75 V and -0.3 to -0.2 V, respectively. The applied scan rates were 0.05, 0.1, 0.2, 0.3 and 0.5 V/s.

3.4.1 Procedure for porous Cu

The current-potential plot of a porous copper sample in the potential range -1 to -0.75 V is shown in Fig. 3.8. As there is no Faradaic current in this potential range, the capacitance, C (F), of the porous copper can be determined by (Lewandowski et al., 2012):

$$C = \frac{\Delta I}{2v} \tag{3.11}$$

where ΔI is the difference between charge and discharge current, as shown in Fig. 3.8, v is the applied scan rate. As the specific capacitance of the copper/0.1M KOH interface is 2×10^{-5} F/cm^2 (Łukomska and Sobkowski, 2004), the real surface area, A_R(cm^2), of porous copper could be determined:

$$A_R = \frac{C}{2 \times 10^5} \tag{3.12}$$

The volumetric, A_{VR}, or gravimetric, A_{MR}, specific real surface area of porous copper was calculated by dividing the real surface area over volume or mass of the porous copper samples.

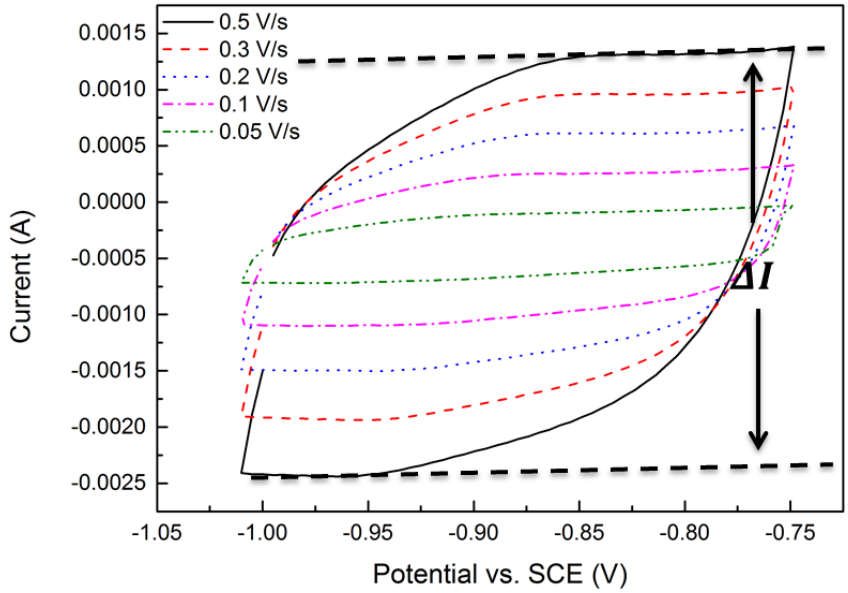

Fig. 3. 8 Current-potential plot of the LCS Cu for real surface area measurement

3.4.2 Procedure for porous Ni

The current-potential plot of a porous nickel sample in the potential range of Faradaic current is shown in Fig. 3.9. The capacitance was determined from Eq. 3.11, following the same process as for porous copper. As the specific capacitance of the nickel/8 M KOH interface is 2.8×10^{-5} F/cm^2 (Gagnon, 1976), the real surface area of porous nickel can be calculated by:

$$A_R = \frac{C}{2.8 \times 10^{-5}} \tag{3.13}$$

The volumetric, A_{VR}, or gravimetric, A_{MR}, specific real surface area of porous nickel was calculated by dividing the real surface area over volume or mass of the porous nickel samples.

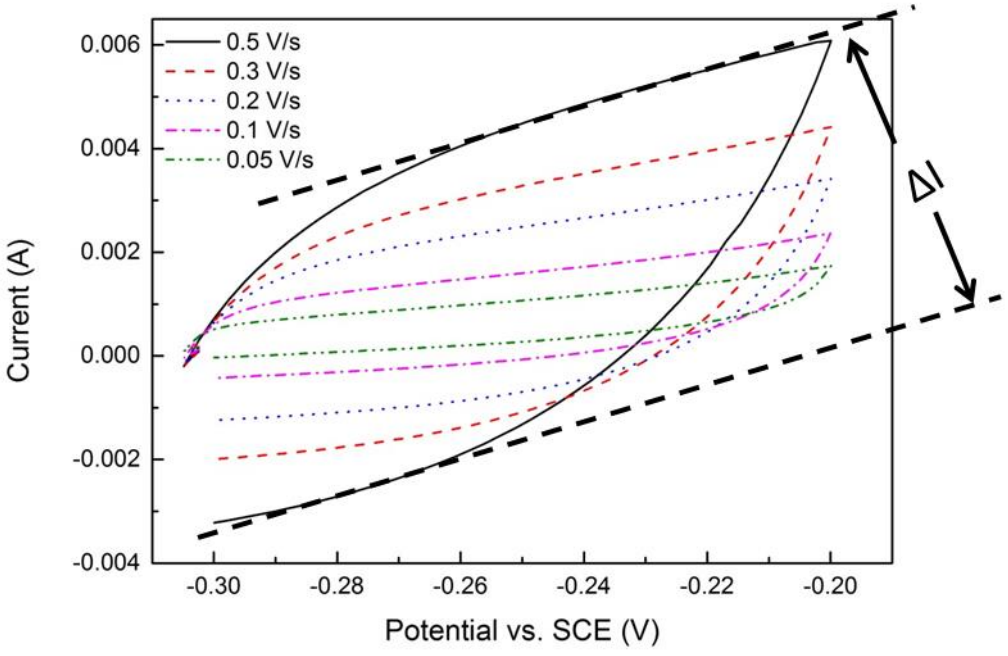

Fig. 3. 9 Current-potential plot of the LCS Ni for real surface area measurement

3.5 Mass transfer coefficient measurement

The mass transfer coefficient of porous nickel was measured by the limiting current technique (Recio et al., 2013). Porous nickel samples with porosities in the range of 0.5 – 0.85 and pore sizes in the range of 250 – 1500 µm were measured. A mirror-polished nickel plate was also measured in order to compare the mass transfer performance between the LCS porous nickel samples and nickel plate.

3.5.1 Experimental apparatus

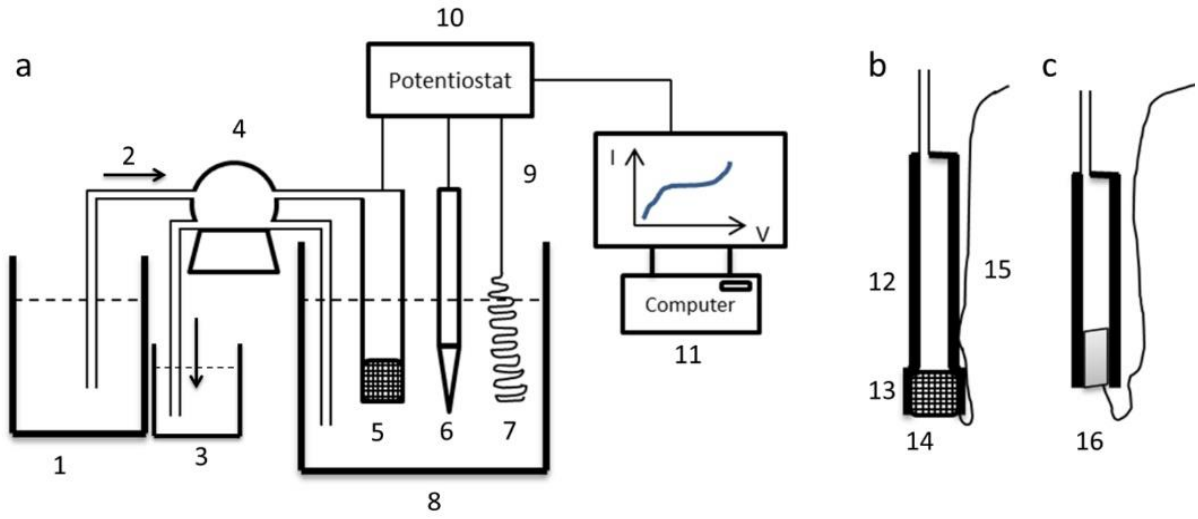

Fig. 3. 10 Schematics of (a) mass transfer experimental apparatus, (b) porous nickel working electrode and (c) nickel plate working electrode: (1) electrolyte reservoir, (2) pumping pipe, (3) waste solution reservoir, (4) peristaltic pump, (5) working electrode, (6) reference electrode (SCE), (7) counter electrode (platinum coil), (8) glass beaker, (9) wire, (10) potentiostat, (11) computer, (12) acrylic tube, (13) water proof shrinkage tube, (14) LCS porous nickel sample, (15) nickel wire, (16) solid nickel plate.

Fig. 3.10 is a schematic diagram of the mass transfer experimental apparatus. It consists of a plastic electrolyte reservoir, a peristaltic pump (Masterlex L/S Computer-Compatible Digital Pump), a three electrode cell, a potentiostat (Autolab PGSTAT101) and a computer. The

sample to be tested served as the working electrode. A water proof shrinkage tube was used to connect the porous nickel sample to an acrylic tube with an outer diameter of 6 mm (Fig. 3.10 b). The nickel plate was inserted into the acrylic tube, parallel to the tube and the flow of the electrolyte (Fig. 3.10 c). The electrolyte was forced to pass through the porous electrode, or flow past the solid plate electrode, and exhausted by the peristaltic pump.

1 M Na_2CO_3 solution was used as the background electrolyte. In characterising the nickel plate electrode, the electrolyte contained 10^{-3} M $K_3Fe(CN)_6$ and 10^{-2} M $K_4Fe(CN)_6$. In characterising the LCS porous nickel electrodes, the concentrations of the reactive species were reduced by 10 times and the electrolyte contained 10^{-4} M $K_3Fe(CN)_6$ and 10^{-3} M $K_4Fe(CN)_6$. This is because porous metals have high surface areas (Diao et al., 2015), which can generate high currents, causing distortions in the measurements due to uncompensated solution resistance. Reducing the concentrations of the reactive species eliminated the effect of uncompensated solution resistance (Smith et al., 2015).

The limiting current was measured by linear sweep voltammetry in the potential from 0.2 V to -1.2 V at a scan rate of 5 mV/s. The pumping rate was in the range 16.8 to 240 mL/min.

3.5.2 Determination of mass transfer coefficient

The electrochemical reaction used in this work was the reduction of the ferricyanide ion:

$$[Fe(CN)_6]^{3-} + e^- \rightarrow [Fe(CN)_6]^{4-} \qquad 3.14$$

A typical current-potential plot of the porous nickel electrode can be seen in Fig. 3.11. There are three regions in the curve, i.e., hydrogen evolution, mass transfer control and mixed control regions, which signify different transfer mechanisms. The limiting current, I_L, was

determined from the mass transfer region and the mass transfer coefficient, k, was calculated by (Recio et al., 2013):

$$k = \frac{I_L}{nFA_R c} \qquad 3.15$$

where n is the number of electrons exchanged in the reaction (n=1), F is the Faraday constant, A_R is the real surface area of the working electrode and c is the bulk concentration of the electroactive species.

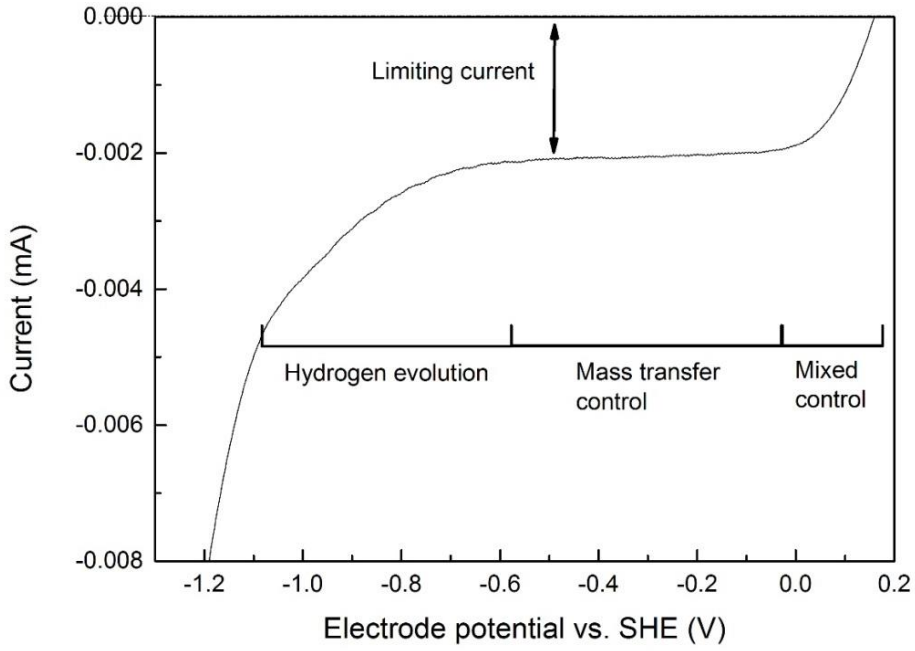

Fig. 3. 11 Typical current vs potential plot for the reduction of Fe(CN)63- in 10-4 M K3Fe(CN)6 + 10-3 M K4Fe(CN)6 + 1 M Na2CO3 at a porous nickel electrode with a scan rate of 0.005 V/s

3.6 Electrochemical detection of ferricyanide

A porous nickel sample with a pore size of 250 – 425 µm and porosity of 0.7 was used to electrochemically detect ferricyanide with different concentrations, using 1 M Na_2CO_3 as the

background electrolyte. The detection was conducted by both a conventional three-electrode electrochemical sensor and a novel limiting current sensor.

3.6.1 Three-electrode electrochemical sensor

The schematic graph of the three-electrode electrochemical sensor was the same as that in Fig. 3.4. A series of solutions with a volume of 250 ml and different ferricyanide concentrations in the range of 0.001 mM to 10 mM were made before testing. According to the Randles–Sevcik equation (Eq. 3.10), the peak current is linearly proportional to the concentration of ferricyanide. The detection limit was considered as the concentration when the signal to noise ratio dropped below 3. The detection sensitivity was determined by dividing peak current over the concentration with a unit of ampere per mole. As the sensitivity is related to scan rate, the applied scan rates were chosen from 0.005 to 0.1 V/s in order to investigate the effect of scan rate on the detection sensitivity.

3.6.2 Limiting current sensor

The schematic graph of the limiting current sensor was shown in Fig. 3.12. A series of solutions with a volume of 2 L and different ferricyanide concentration in the range of 0.001 mM to 10 mM were required. The applied scan rate constantly stayed at 0.005 V/s. According to Eq. 3.15, the limiting current is linear proportional to the concentration of ferricyanide. Like the cyclic voltammetry detection, the detection limit was considered as the concentration when the signal to noise ratio was dropped to below 3. The detection sensitivity was determined by dividing peak current over the concentration with a unit of ampere per mole. As the sensitivity is related to solution pumping rate, the pumping rates were chosen from 16.8 to 84 mL/min in order to investigate the effect of pumping rate on the detection sensitivity.

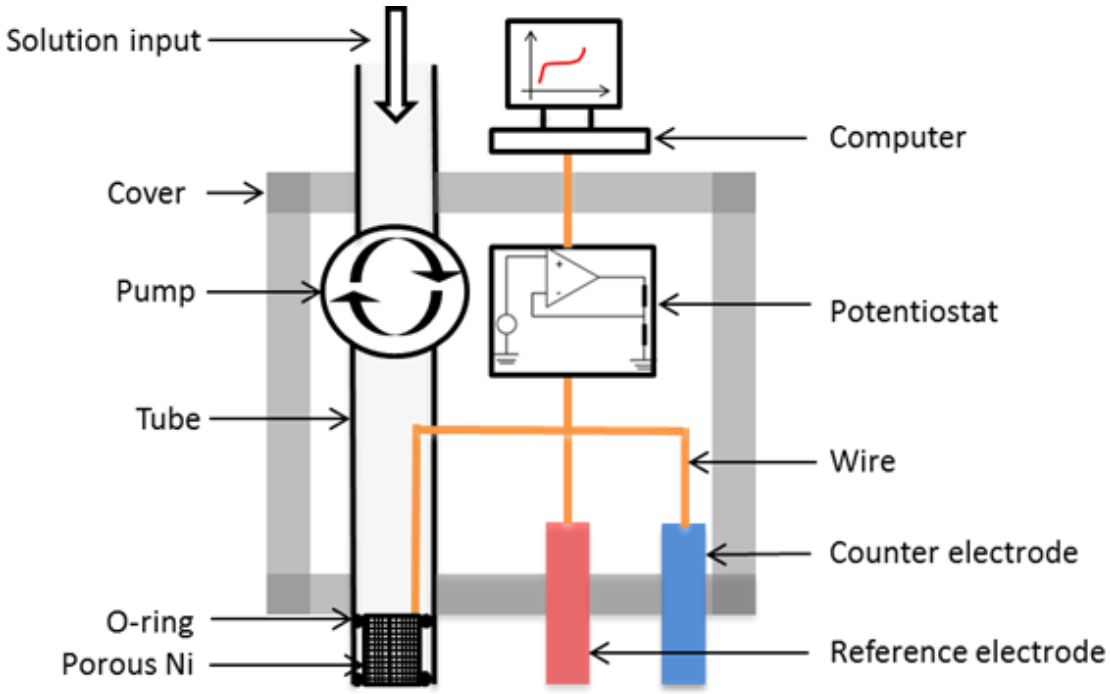

Fig. 3. 12 Schematic illustration of the limiting current sensor prototype.

CHAPTER 4 SURFACE AREA OF POROUS Cu

4.1 Surface morphology of the LCS porous Cu

Fig. 4.1 shows the SEM images of the LCS porous Cu samples manufactured with different Cu particle sizes (<20, 20 – 45, 45 – 75 and 75 – 90 μm), sintering temperatures (850 and 950˚C) and chemical treatment conditions (with and without nitric acid etching). The samples sintered at 850˚C (A – D) have rough surfaces, with the initial spherical Cu particles easily discernible. It can also be observed that the smaller the Cu particles, the thicker the sintering necks relative to the particle size. The samples sintered at 850˚C and etched (second column, E – H) show smoother surfaces, revealing strong sintering necks and making original particles less visible, especially in the small Cu particle sample (Fig. 4.1 E). The samples sintered at 950˚C (I – L) are apparently denser and have thicker sintering necks than the samples sintered at 850˚C (A – D) for any given Cu particle size. The sample made by the smallest particles (Fig. 4.1 I) is fully sintered with the original particles barely discernible. The original particles can still be seen in the samples made by larger particles (Fig. 4.1 J – L), but they are less noticeable than in the samples sintered at 850˚C (A – D). The samples sintered at 950˚C and subsequently etched (M – P) show more flat surfaces, with the original particles hardly noticeable for all samples. Surface morphology characterization is essential for studying the surface area of porous metals because the morphology can affect the surface area directly. These SEM images will be used to discuss how particle size, sintering temperature and chemical etching affect the surface morphology and therefore the surface areas of porous Cu.

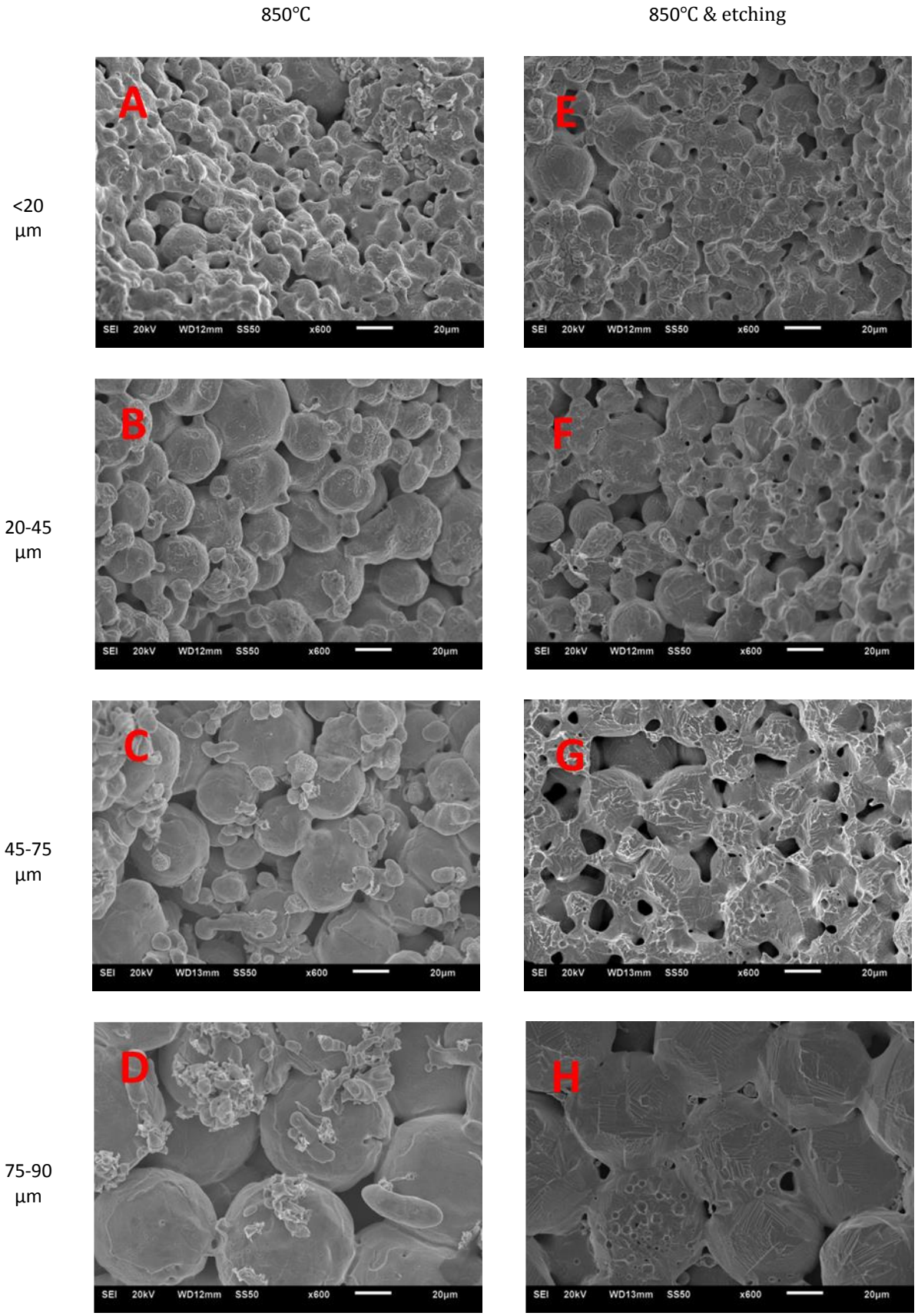

Fig. 4.1 SEM images of the LCS porous Cu samples with different Cu particle sizes and processing conditions (to be continued)

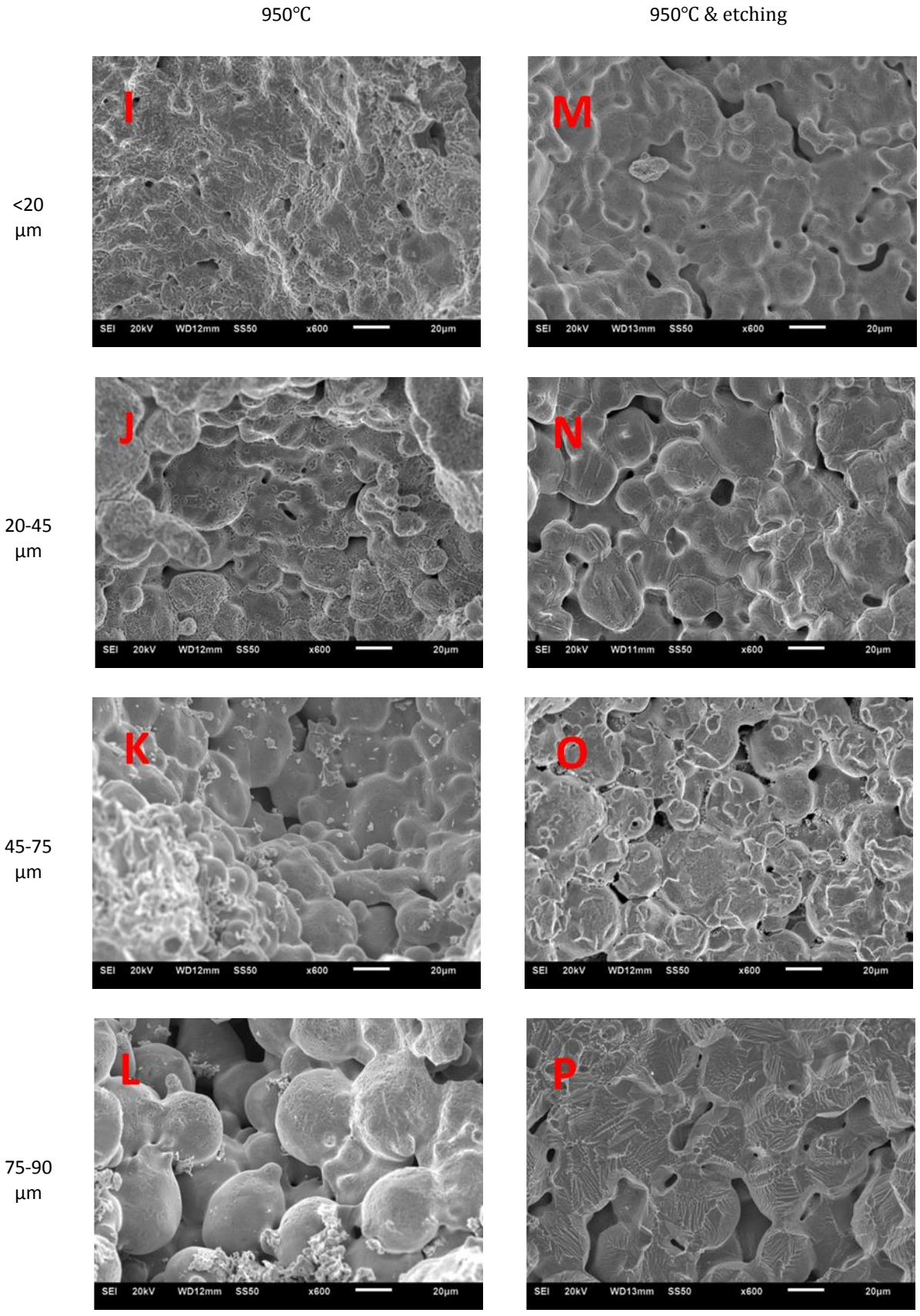

Fig. 4.1 (continued) SEM images of the LCS porous Cu samples with different Cu particle sizes and processing conditions

4.2 Geometric surface area

The geometric surface area of porous Cu only includes the surface area of the primary pores formed from the decomposition or dissolution of the K_2CO_3 particles. The geometric surface areas of the porous Cu samples manufactured using the Cu powder with a particle size of 20 – 45 μm were measured by the quantitative stereology method. The porous Cu samples had different porosities in the range of 0.50 – 0.80 and different pore sizes in the range of 250 – 1500 μm.

4.2.1 Effects of porosity and pore size

Figs. 4.2 and 4.3 show the variations of the volumetric (A_{VG}) and gravimetric (A_{MG}) specific geometric surface areas of the porous Cu samples with porosity at different pore sizes. The volumetric and gravimetric specific geometric surface areas are in the ranges of 20 – 100 cm^{-1} and 5 – 50 cm^2/g, respectively. The values are similar to those of the specific geometric surface areas of the porous Cu samples with an average particle size of 75 μm (Diao et al., 2015), indicating that the Cu particle size does not affect the geometric surface area. A systematic study on the effect of particle size on the specific geometric surface areas of porous Ni will be shown in Chapter 5.

Porosity and pore size are the two most important parameters affecting the geometric surface area of porous Cu. Both volumetric and gravimetric specific geometric surface areas increase with increasing porosity but decrease with increasing pore size. For a porous sample with a fixed pore size, a higher porosity means more pores within the porous sample, thus greater geometric surface area. For a sample with a fixed porosity, a larger pore size means a smaller number of pores within a certain volume, thus less geometric surface area.

The effect of pore size on the specific geometric surface areas is more significant than the effect of porosity.

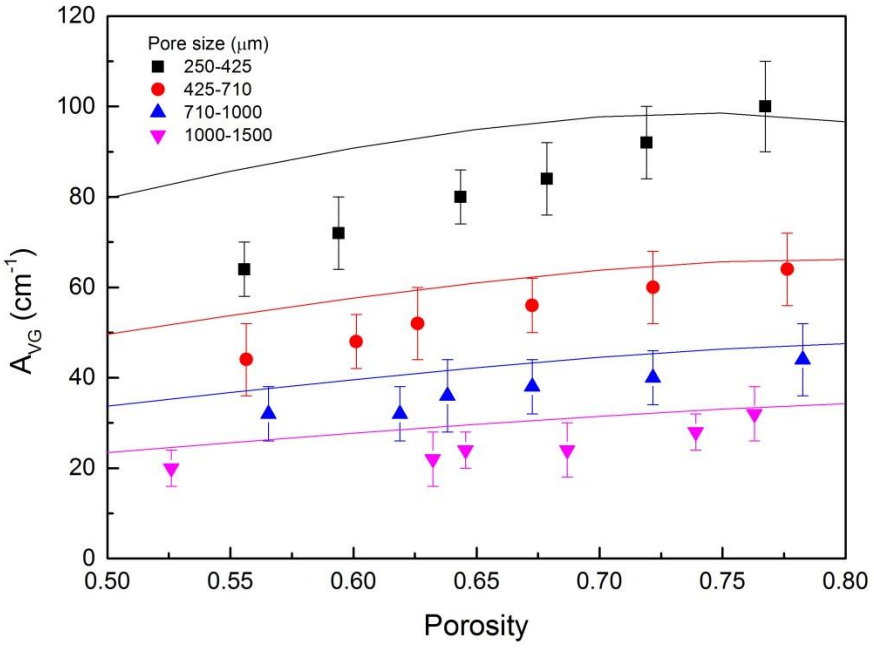

Fig. 4.2 Variations of volumetric specific geometric surface area of porous Cu samples with porosity at different pore sizes (the lines designate the results from theoretical predictions)

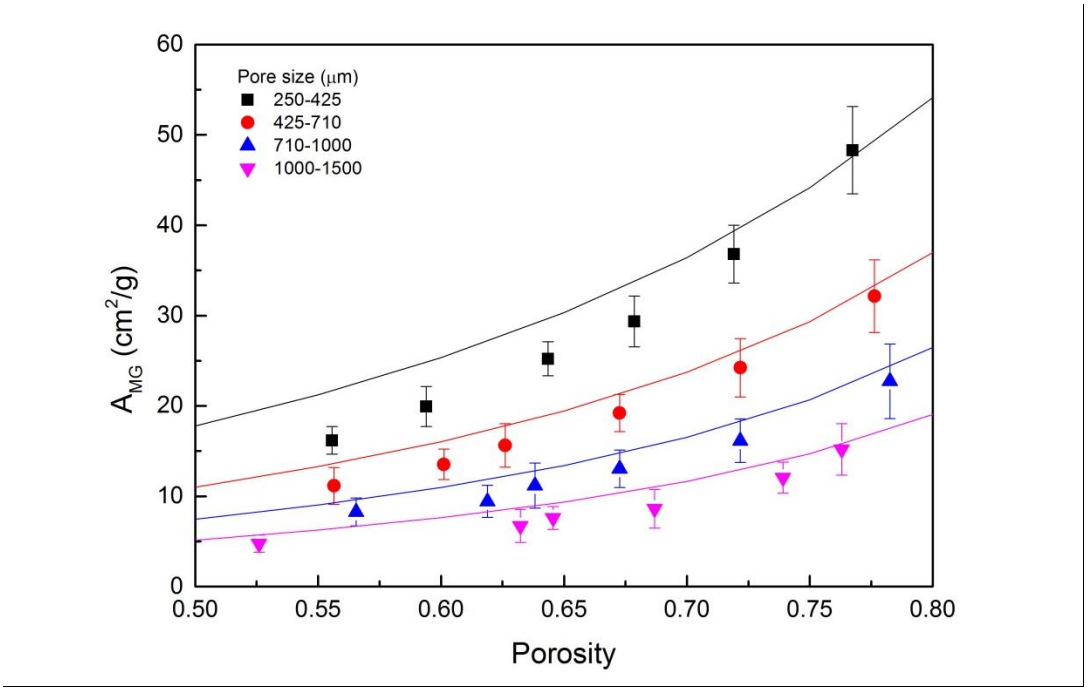

Fig. 4.3 Variations of gravimetric specific geometric surface area of porous Cu samples with porosity at different pore sizes (the lines designate the results from theoretical prediction)

4.2.2 Comparison with theoretical prediction

The specific geometric surface areas of porous Cu can also be predicted theoretically (Diao et al., 2015). The theoretical prediction is based on a stochastic model developed by Zhao (2003). According to the model, the geometric surface area of a porous sample is equal to the total surface area of the K_2CO_3 particles minus the surface area of the contact necks between the K_2CO_3 particles. The volumetric and gravimetric specific geometric surface areas of porous Cu can be expressed by Eqs. 4.1 and 4.2, respectively.

$$A_{VG} = \frac{3}{\frac{r}{1-\varepsilon} + \frac{R}{\varepsilon}} \quad 4.1$$

$$A_{MG} = \frac{3}{\rho_{Cu}(r + \frac{R(1-\varepsilon)}{\varepsilon})} \quad 4.2$$

where r is the surface weighted mean radius of the Cu particles (19 μm), R is the surface weighted mean radius of the K_2CO_3 particles (171, 312, 468 and 645 μm for K_2CO_3 size ranges 250 – 425, 425 – 710, 710 – 1000 and 1000 – 1500 μm, respectively (Diao et al., 2015)), $\rho_{Cu}$is the copper density (8.96 g/cm^3) and ε is the porosity. The volumetric and gravimetric specific geometric surface areas from theoretical calculations obtained from Eqs.4.1 and 4.2 are also shown in Figs. 4.2 and Fig. 4.3 (coloured lines). It is shown that the experimental results agree reasonably well with the theoretical predictions, especially for the effects of porosity and pore size on the geometric surface area. However, the accuracy of the theoretical prediction still needs to be improved. Further improvement should take the metal particle size distribution, potassium carbonate size distribution and the random arrangement of potassium carbonate particles, into consideration.

4.3 Electroactive surface area

The electroactive surface area can include the contributions from the primary pores and the interstices between the Cu particles. In this project, the cyclic voltammetry peak current method was used to measure the electroactive surface area of porous Cu. Two chemical reactions were employed in order to study the effect of chemical reactions. Samples with different porosities in the range of 0.5 – 0.8, a fixed pore size in the range of 1000 – 1500 µm and different particle sizes of <20, 20 – 45, 45 – 75 and 75 – 90 µm, manufactured by different sintering temperatures, before and after chemical etching were measured.

4.3.1 Cu plate calibration

Fig. 4.4 shows a typical current-potential plot of a mirror-polished copper plate with a geometric surface area of 0.0543 cm^2 in 0.1 M KOH at a scan rate of 0.01 V/s. The polishing process was shown in Section 3.3.2 and the surface roughness can be as low as 0.03 µm (Onwubu et al., 2018). Both peak 1 and peak 2 were used to measure the electroactive surface area with an aim to study the effects of the chosen reaction and the diffusion layer thickness. The corresponding reactions can be seen from Eqs. 3.6 and 3.7 in Chapter 3. Because of the mirror surface finish, the geometric surface area can be regarded as equal to the electroactive surface area.

Fig. 4.5 shows the linear relations between the peak current (µA) and the electroactive surface area (cm^2) of a series of mirror-polished Cu plates at peak 1 and peak 2, which can be expressed by Eqs. 4.3 and 4.4, respectively.

$$Electroactive\ surface\ area = 0.017 * peak\ current \quad (4.3)$$

$$Electroactive\ surface\ area = 0.00353 * peak\ current \quad (4.4)$$

It is worth mentioning that the proportionality coefficient in equation 4.4 has a different value from that reported by Diao et al. (2015), because of different scan rates and different units of current used. Considering that the peak current is proportional to the square root of scan rate, the difference between the coefficient in Eq. 4.4 and that in (Diao et al., 2015) is less than 15%, mainly due to experimental variability. The effect of scan rate on the electroactive surface area of porous Ni will be studied in Chapter 5.

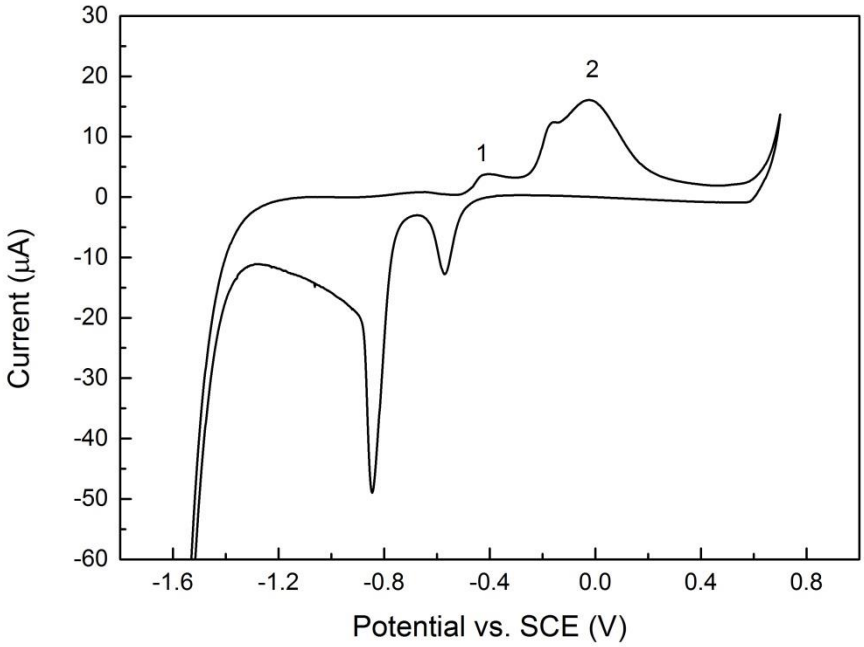

Fig. 4.4 The current-potential plot of a mirror-polished copper plate with a geometric surface area of 0.0543 cm^2 in 0.1 M KOH in the potential range of -1.6 to 0.7 V at a scan rate of 0.01 V/s

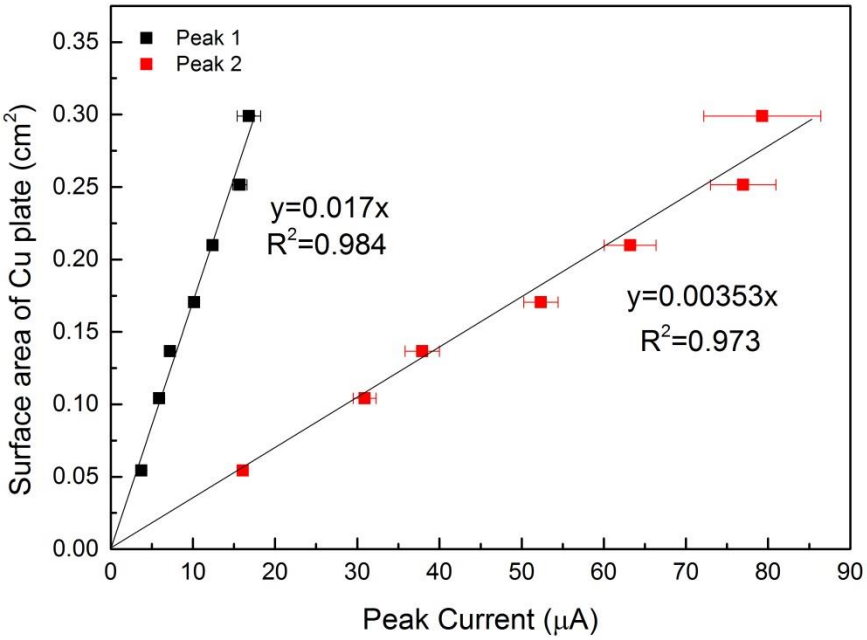

Fig. 4.5 Linear relations between peak current and electroactive surface area of mirror-polished Cu plates

4.3.2 Effect of Cu particle size

The volumetric specific electroactive surface areas, measured by peak 1 (A_{VE_p1}) and peak 2 (A_{VE_p2}) of the LCS porous Cu samples with different Cu particle sizes and porosities, manufactured under different process conditions, are shown in Figs. 4.6 and 4.7, respectively. The porosities used here are nominal porosities. It is obvious that the specific electroactive surface areas are affected by both Cu particle size and porosity for all manufacturing and treatment conditions. For each process condition, the surface areas vary with porosity without any particular pattern, in agreement with (Diao et al., 2015). In order to remove the effect of porosity and focus on the effect of particle size, the average volumetric specific electroactive surface area for each particle size is also shown in the graphs. Figs. 4.6 and 4.7 show that Cu particle size has a moderate effect on the

electroactive surface areas. As a general trend, both the electroactive surface areas measured by peak 1 and peak 2 first increase and then decrease with particle size. The maximum surface area values are achieved in the samples either with a particle size of 20 – 45 µm or with a particle size of 45 – 75 µm.

The effect of Cu particle size on surface area is twofold. On the one hand, smaller particles offer a higher total surface area (Diao et al., 2015). On the other hand, it is easier to sinter smaller particles to achieve a denser structure, resulting in a huge loss in surface area. In contrast, larger Cu particles have lower total surface area but experience less loss in surface area during sintering. Overall, the effect of particle size on the surface area depends on which of the two mechanisms is more significant. As a consequence, samples with a medium particle size range often have the highest surface areas.

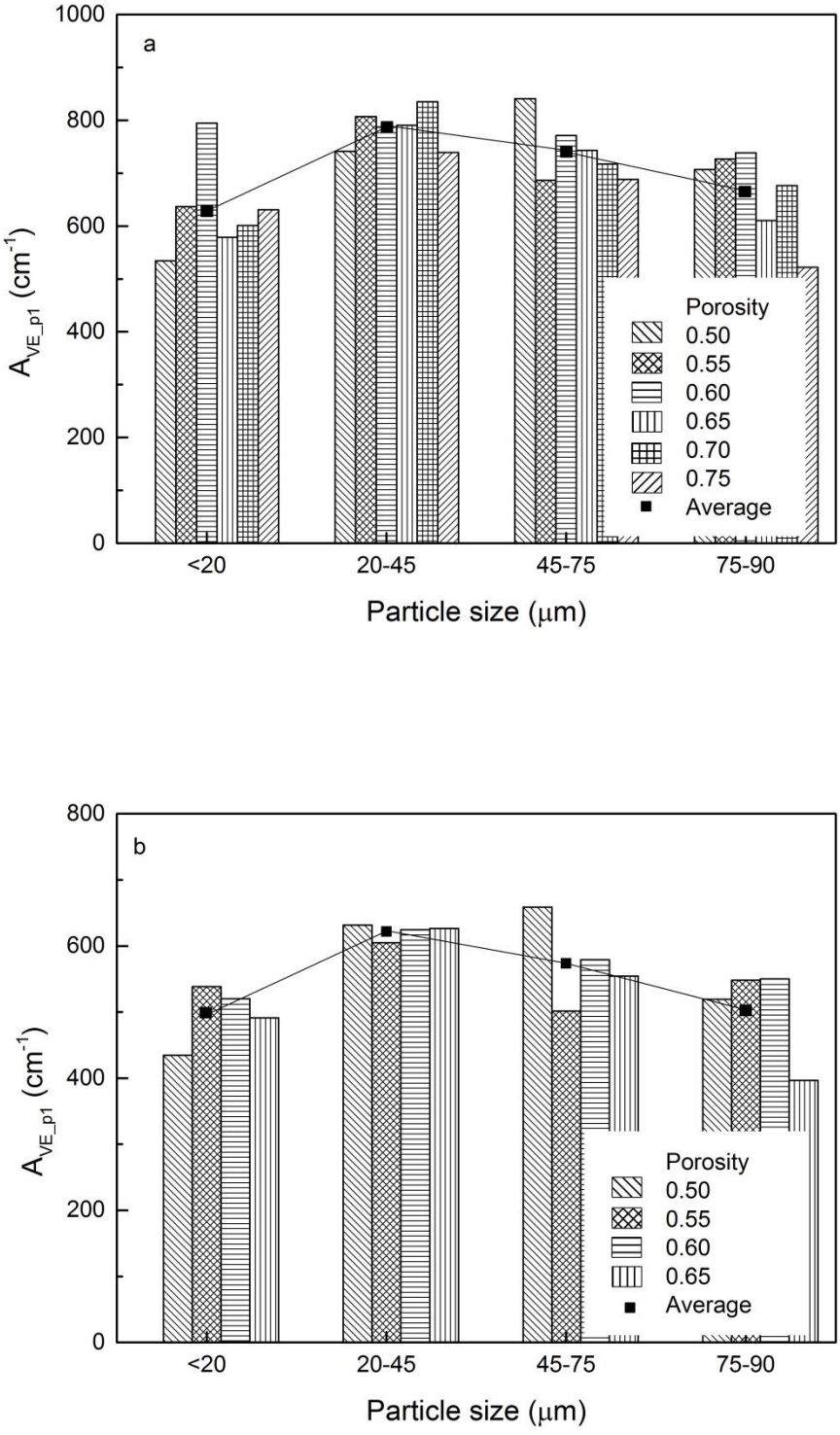

Fig. 4. 6 Volumetric specific electroactive surface areas, measured by peak 1, of the LCS porous Cu samples with different Cu particle sizes and different porosities, manufactured by (a) 850˚C sintering, (b) 850˚C sintering and etching, (c) 950˚C sintering and (d) 950˚C sintering and etching (to be continued)

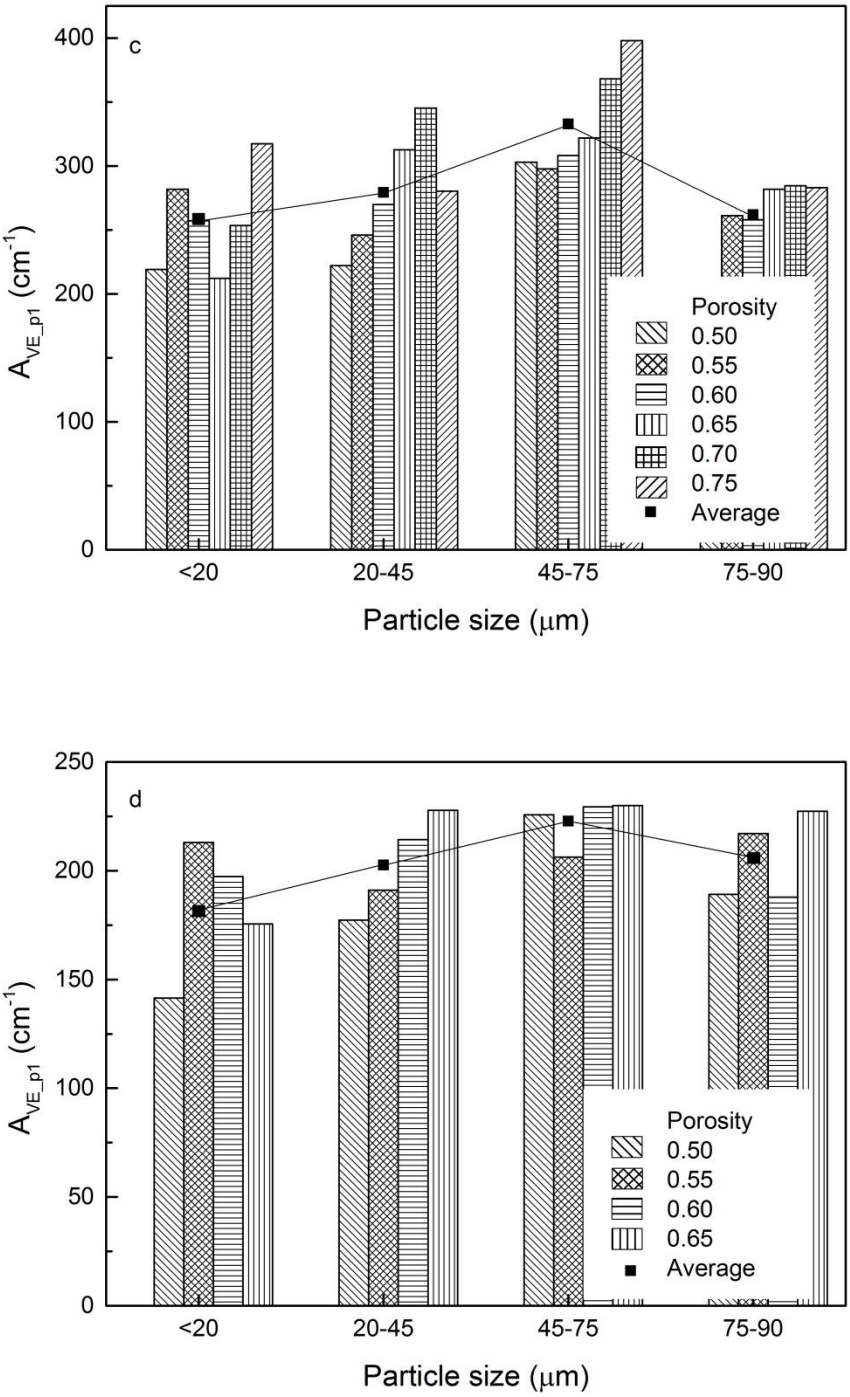

Fig. 4.6 (continued) Volumetric specific electroactive surface areas, measured by peak 1, of the LCS porous Cu samples with different Cu particle sizes and different porosities, manufactured by (a) 850˚C sintering, (b) 850˚C sintering and etching, (c) 950˚C sintering and (d) 950˚C sintering and etching

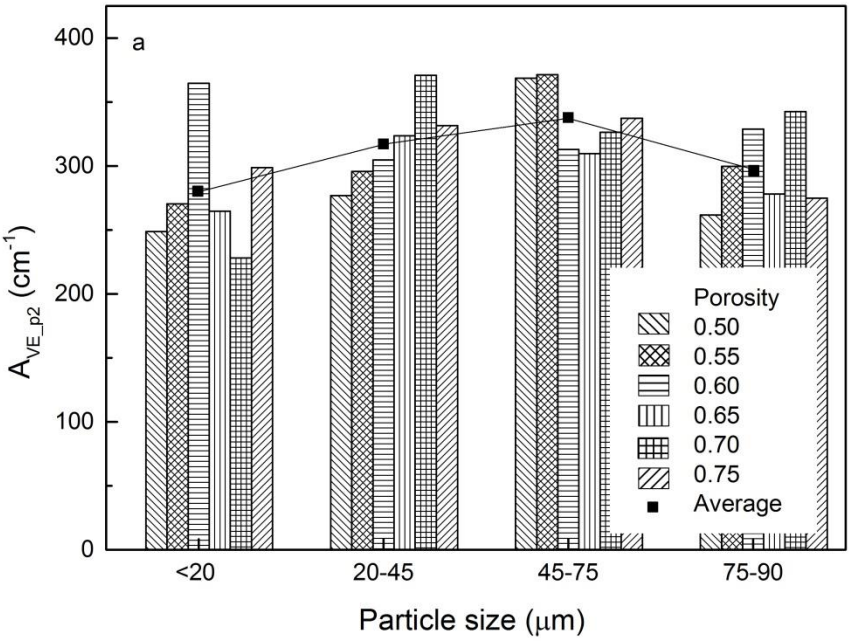

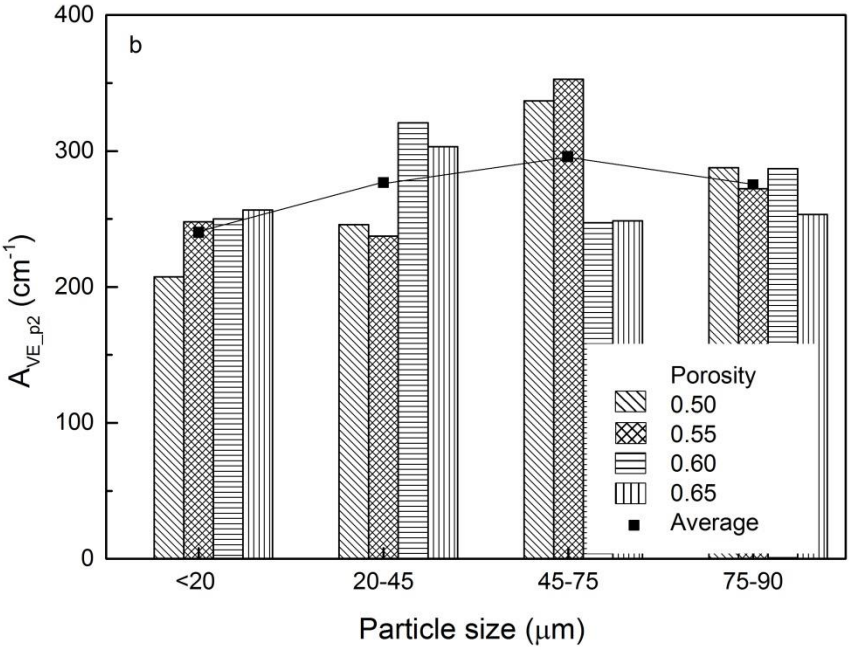

Fig. 4.7 Volumetric specific electroactive surface areas, measured by peak 2, of the LCS porous Cu samples with different Cu particle sizes and different porosities, manufactured by (a) 850˚C sintering, (b) 850˚C sintering and etching, (c) 950˚C sintering and (d) 950˚C sintering and etching (to be continued)

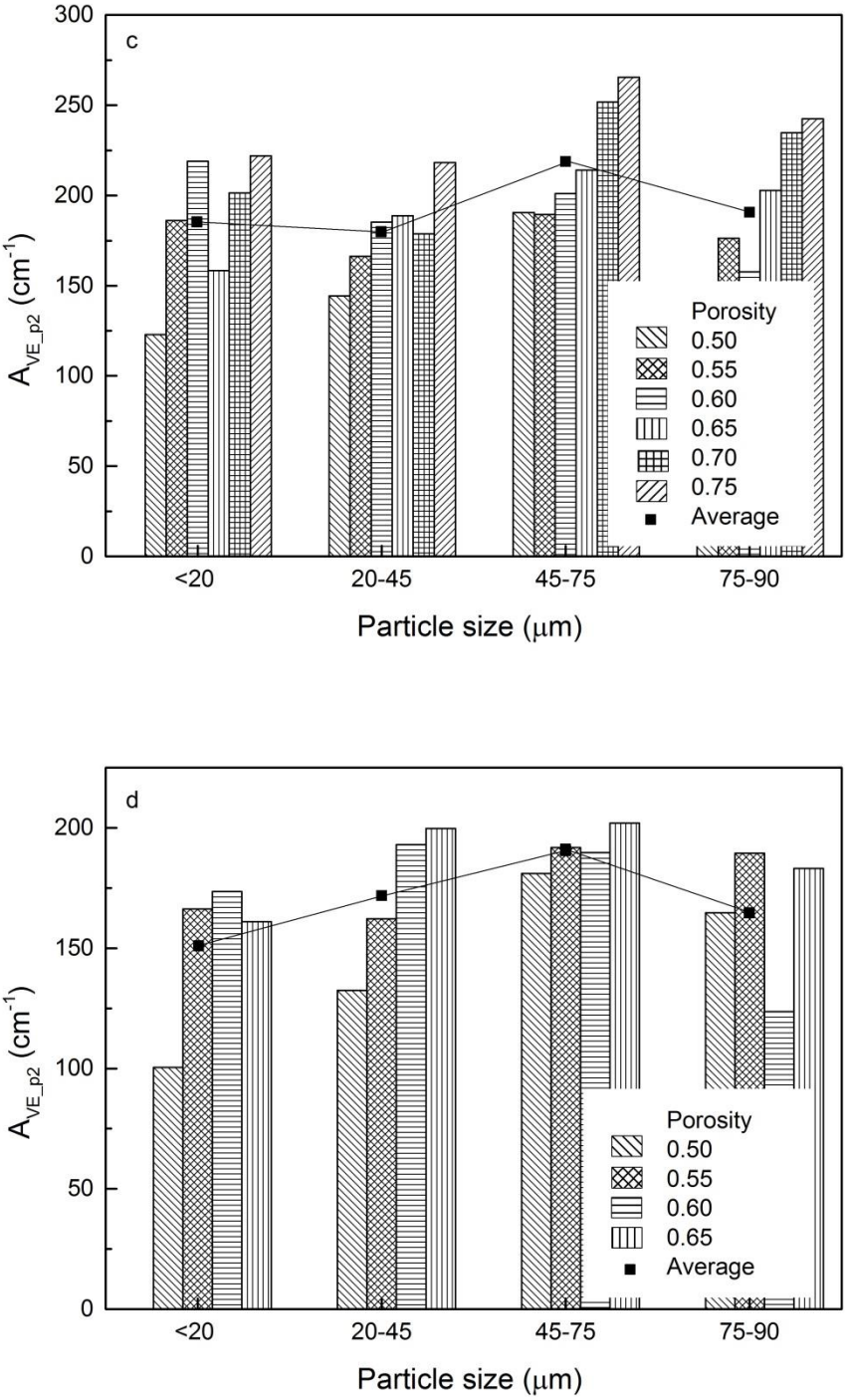

Fig. 4.7 (continued) Volumetric specific electroactive surface areas, measured by peak 2, of the LCS porous Cu samples with different Cu particle sizes and different porosities, manufactured by (a) 850˚C sintering, (b) 850˚C sintering and etching, (c) 950˚C sintering and (d) 950˚C sintering and etching

4.3.3 Effects of sintering temperature and chemical etching

Fig. 4.8 shows the effects of sintering temperature and etching treatment on the specific electroactive surface areas of porous Cu measured by peak 1 and peak 2. Sintering temperature has a great effect on the electroactive surface areas. The volumetric specific electroactive surface areas measured by peaks 1 and 2 of samples sintered at 850 ˚C before etching are in the ranges of 500 – 850 and 250 – 350 cm^{-1}, respectively, while those of the samples sintered at 950˚C before etching are in the ranges of 200 – 350 and 100 – 250 cm^{-1}, respectively. Therefore, increasing the sintering temperature from 850 ˚C to 950 ˚C can result in reductions of approximately 60%, on average, in the electroactive surface area measured by peak 1 (Fig. 4.8 a) and 40% in the electroactive surface area measured by peak 2 (Fig. 4.8 b). The effects of sintering temperature on the volumetric specific electroactive surface areas of the porous Cu samples after etching are similar, with reductions of about 65% and 45% for the electroactive surface areas measured by peaks 1 and 2, respectively. The reductions are due to smoother surfaces and thickened sintering necks, as a result of the increased densification at a higher sintering temperature, as evidenced in Fig. 4.1.

Etching treatment also has a significant effect on the specific electroactive surface areas. There is a strong correlation between the surface areas before and after etching. The chemical etching resulted in reductions of 25% in the electroactive surface area measured by peak 1 (Fig. 4.8 a) and 9% in the electroactive surface area measured by peak 2 (Fig. 4.8 b). It is because chemical etching significantly reduced the surface roughness of the LCS Cu samples, as evidenced in Fig. 4.1. It is interesting to see that there is no mutual interference between the effects of sintering temperature and chemical etching, indicating that both sintering temperature and chemical etching modify surface morphology uniformly.

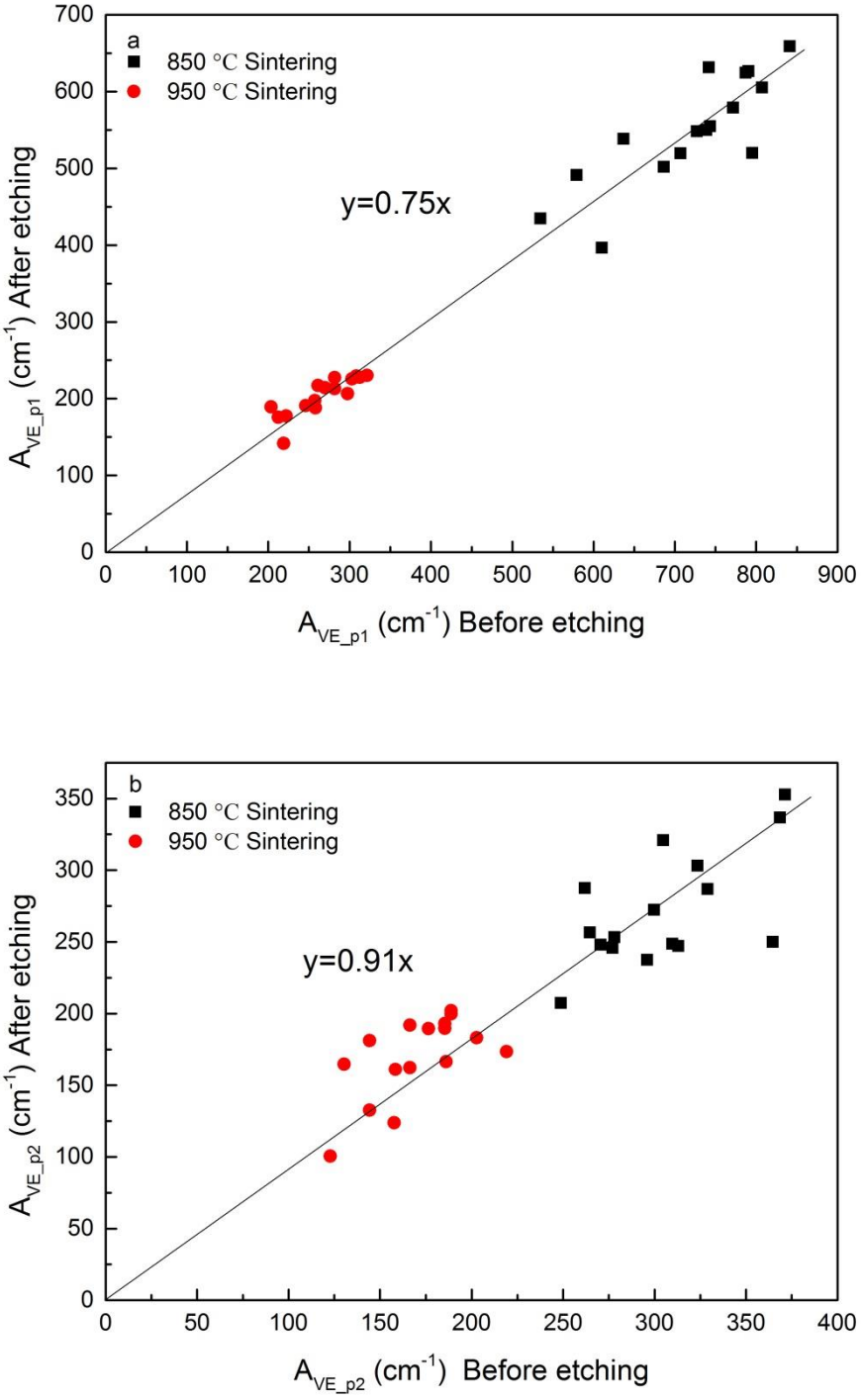

Fig. 4.8 Correlations between electroactive surface areas of samples with and without the etching treatment for the LCS porous Cu samples sintered at two different temperatures: (a) measured by peak 1 and (b) measured by peak 2

4.4. Real surface area

The real surface area includes the surface areas of the primary pores, interstices between the Cu particles and even the surface features on the Cu particles at an extremely small length scale. In this project, the cyclic voltammetry double layer capacitance method was used to measure the real surface area of porous Cu samples. Samples with different porosities in the range of 0.5 – 0.8, pore size in the range of 1000 – 1500 μm and different particle sizes of <20, 20 – 45, 45 – 75 and 75 – 90 μm, manufactured at different sintering temperatures, before and after chemical etching were measured.

4.4.1 Effect of Cu particle size

Fig. 4.9 shows the volumetric specific real surface area, A_{VR} (cm^{-1}), of the LCS porous Cu samples with different Cu particle sizes and porosities, manufactured under different process conditions. The overall volumetric specific real surface areas of the LCS porous Cu are in the ranges of 1400 – 2000 cm^{-1}, 1000 – 1800 cm^{-1}, 600 – 1600 cm^{-1} and 600 – 1400 cm^{-1} for samples sintered at 850˚C without etching, 850˚C with etching, 950˚C without etching and 950˚C with etching, respectively. Like the volumetric specific electroactive surface areas in Figs. 4.6 and 4.7, porous Cu samples with medium particle sizes show the maximum volumetric specific real surface areas because of the effects discussed in section 4.2.2. The optimum particle size range for the samples sintered at 850˚C is 20 – 45 μm no matter with or without chemical etching, while the optimum particle size range for the samples sintered at 950˚C is 45 – 75 μm. We can probably draw a conclusion that the optimum particle size increases with sintering temperature because the loss in surface area of Cu particles during sintering process becomes more serious at higher sintering temperatures.

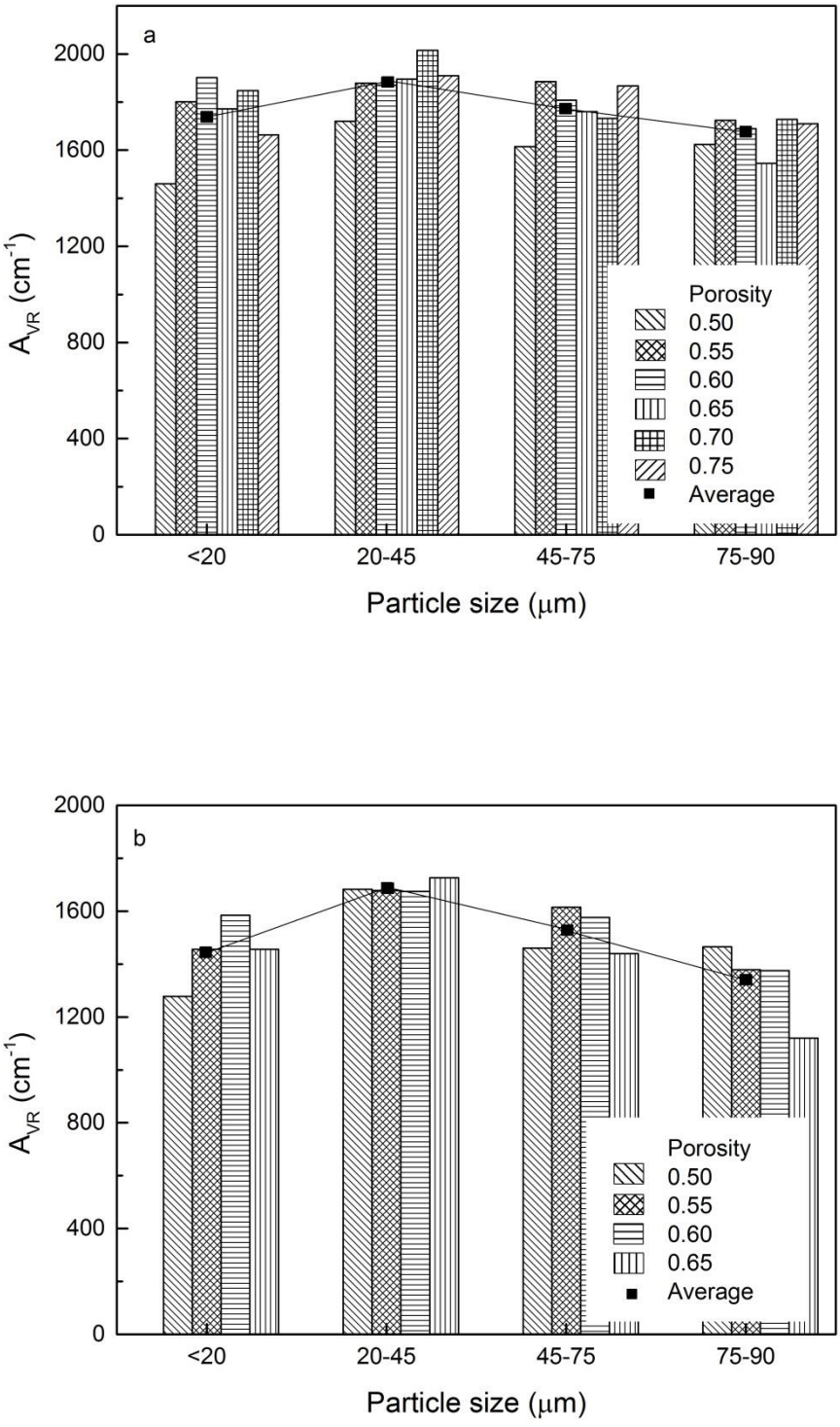

Fig. 4.9 Volumetric specific real surface areas of the LCS porous Cu samples with different Cu particle sizes and different porosities, manufactured by (a) 850˚C sintering, (b) 850˚C sintering and etching, (c) 950˚C sintering and (d) 950˚C sintering and etching (to be continued)

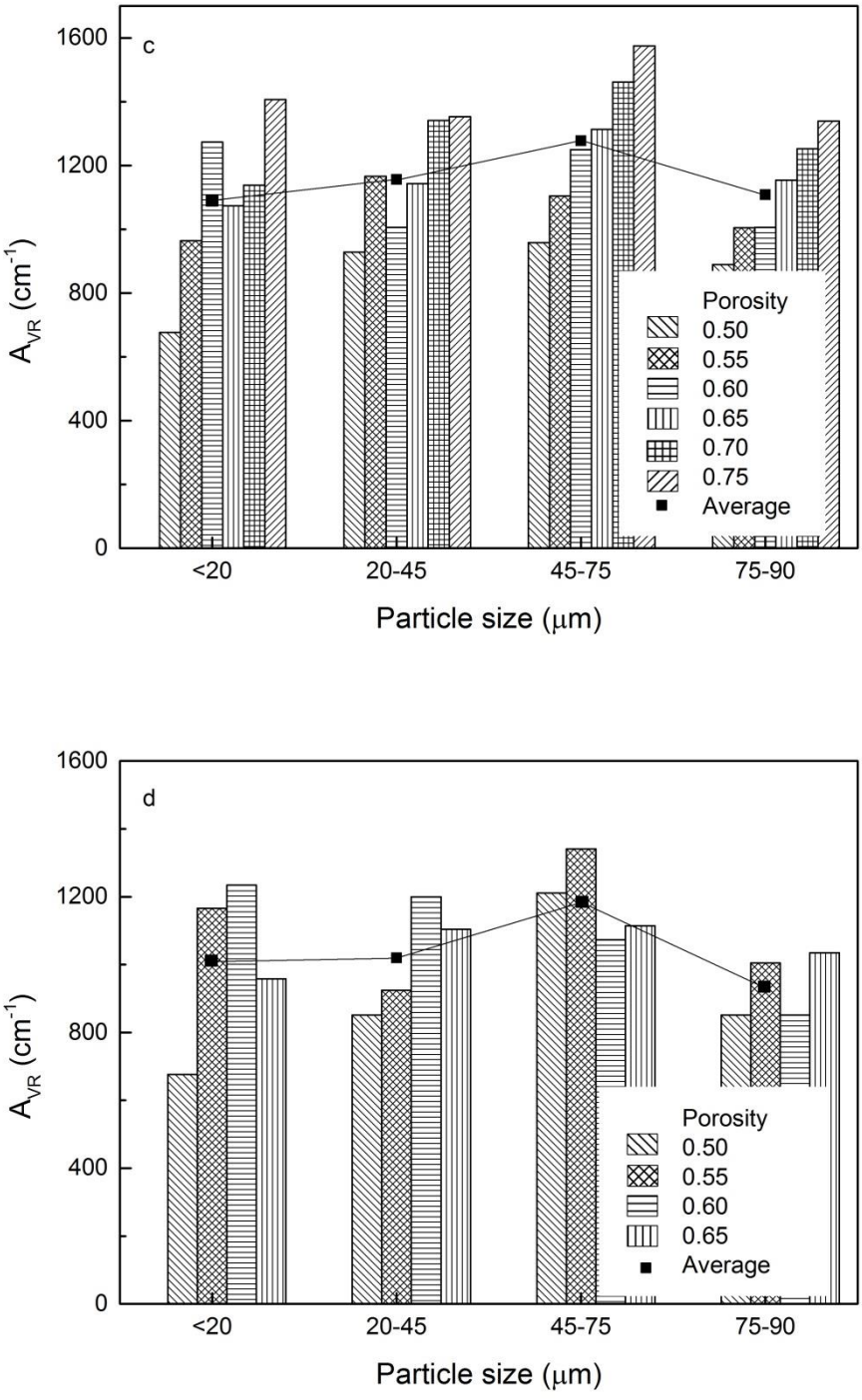

Fig. 4.9 (continued) Volumetric specific real surface areas of the LCS porous Cu samples with different Cu particle sizes and different porosities, manufactured by (a) 850˚C sintering, (b) 850˚C sintering and etching, (c) 950˚C sintering and (d) 950˚C sintering and etching.

4.4.2 Effects of sintering temperature and chemical etching

Fig 4.10 shows the effects of sintering temperature and etching treatment on the real surface area of porous Cu. Like the volumetric specific electroactive surface areas in Fig 4.8, the volumetric specific real surface area of porous Cu decreases from approximately 1300 – 1900 cm^{-1} to 600 – 1400 cm^{-1} by increasing the sintering temperature from 850˚C to 950˚C, with a reduction of about 40%. Similarly, chemical etching can decrease the volumetric specific real surface area from 700 – 1900 cm^{-1} to 500 – 1700 cm^{-1}, with a reduction of 11%. This is because a higher sintering temperature or chemical etching can flatten the surface of porous Cu. Similarly, the sintering temperature and chemical etching modify the surface morphology uniformly.

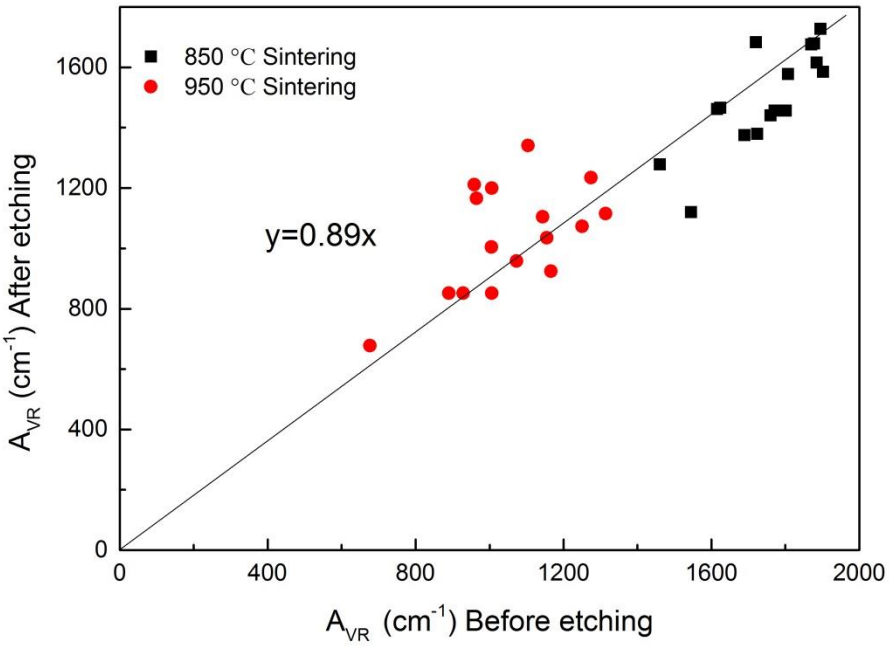

Fig. 4.10 Correlation between real surface areas of samples with and without etching treatment for the LCS porous Cu samples sintered at two different temperatures

4.4.3 Relation between electroactive and real surface areas

Fig. 4.11 shows the relations between the volumetric electroactive surface area and real surface area for the LCS porous Cu samples manufactured with different Cu particle sizes and sintered at 850˚C and 950˚C, before and after chemical etching. A moderate level correlation exists between the electroactive and real surface areas. The electroactive surface area measured by peak 2 is approximately 16 – 18% of the real surface area, regardless of the manufacturing temperature and treatment conditions. The ratio between the electroactive surface area measured by peak 1 and the real surface area depends on the manufacturing conditions. The ratio was approximately 40% for samples sintered at 850℃, and reduced to 37% after etching. The ratio was 24% for samples sintered at 950℃ and further reduced to 19% after etching.

It was evident that the electroactive surface area depends on the electrochemical reaction being considered and the diffusion species involved in the reaction. For peak 1, the diffusion species is Cu^+ in the solid phase. For peak 2, the diffusion species is OH^- in the electrolyte (Hampson et al., 1972). The differences between A_{VE_p1} and A_{VE_p2} and A_{VR} can be explained by considering the thickness of the diffusion layer involved in the reaction. The Nernst diffusion layer thickness, δ, can be calculated by (Amatore, 1995):

$$\delta = \sqrt{\frac{DRT}{nFv}} \qquad 4.5$$

where D is the diffusion coefficient (2×10^{-5} cm/s for OH^- in the electrolyte and 1×10^{-8} cm/s for Cu^+ in solid Cu (Hampson et al., 1972), R is the gas constant (8.134 J/ Kmol), T is the temperature (298 K), n is the number of electrons transferred in the reaction (2 for both reactions 1 and 2), F is the Faraday's constant (96485 C/mol) and v is the applied scan rate

(0.01 V/s). The diffusion layer thicknesses for OH^- and Cu^+, calculated by Eq. (7), are about 50 μm and 1 μm, respectively.

The real surface area is the maximum electroactive surface area that can contribute to any electrochemical reactions. Because no diffusion of reactive species is involved in the measurements of real surface area, the Nernst diffusion layer thickness can be regarded as zero. The surface features at all length scales contribute to the surface area. For the reaction controlled by the diffusion of Cu^+, however, any features less than 1 μm in the LCS porous Cu, e.g., the very fine interstices/protrusions in the metal matrix formed by the sintered Cu particles, will be depleted with Cu^+ ions rapidly due to limited supply, characteristic of thin layer diffusion, as shown schematically in Fig. 4.12. The species are depleted because of a longer distance of diffusion from the electrolyte reservoir to the electrode surface at which the reaction takes place. Those interstices or protrusions with a size smaller than 1 μm can be ignored by the reaction (Barnes et al., 2014, Davies and Compton, 2005, Davies et al., 2005), as they do not contribute fully to the current density and thus cannot be detected. The electroactive surface area is effectively the contour or boundary of the diffusion layer within the solid Cu. Similarly, for the reaction controlled by the diffusion of OH^-, any features less than 50 μm in the LCS porous Cu will not contribute fully to the current density and thus cannot be detected as part of the electroactive surface area. In this case, the electroactive surface area is effectively the contour or boundary of the diffusion layer within the electrolyte (Fig. 4.12).

In short, the double layer capacitance method and the cyclic voltammetry method based on diffusion controlled reactions can measure the electroactive surface areas at different length scales. The double layer capacitance method can detect all features of the surface.

The CV method based on the diffusion of Cu^+ ions can only detect surface features bigger than 1 µm, while the CV method based on the diffusion of OH^- ions can only detect surface features bigger than 50 µm. As a consequence, the real surface area is greater than the electroactive surface area for Cu^+ diffusion, which in turn is greater than the electroactive surface area for OH^- diffusion.

Fig. 4.11 also shows that while the ratio between A_{VE_p2} and A_{VR} did not change with process conditions, the ratio between A_{VE_p1} and A_{VR} changes with sintering temperature and chemical etching. The different behaviour in A_{VE_p1} is likely because the reaction at peak 1 is not solely controlled by Cu^+ diffusion. In the region of the solid electrode near the interface with the electrolyte, there is sufficient supply of OH^- ions and the reaction is controlled by the Cu^+ diffusion in the solid phase. In the region farther away from the interface with the electrolyte, i.e., in the interior of the cell wall, the supply of OH^- ions is also limited by the diffusion of the OH^- ions in the electrolyte. The reaction becomes both Cu^+ and OH^- diffusion controlled.

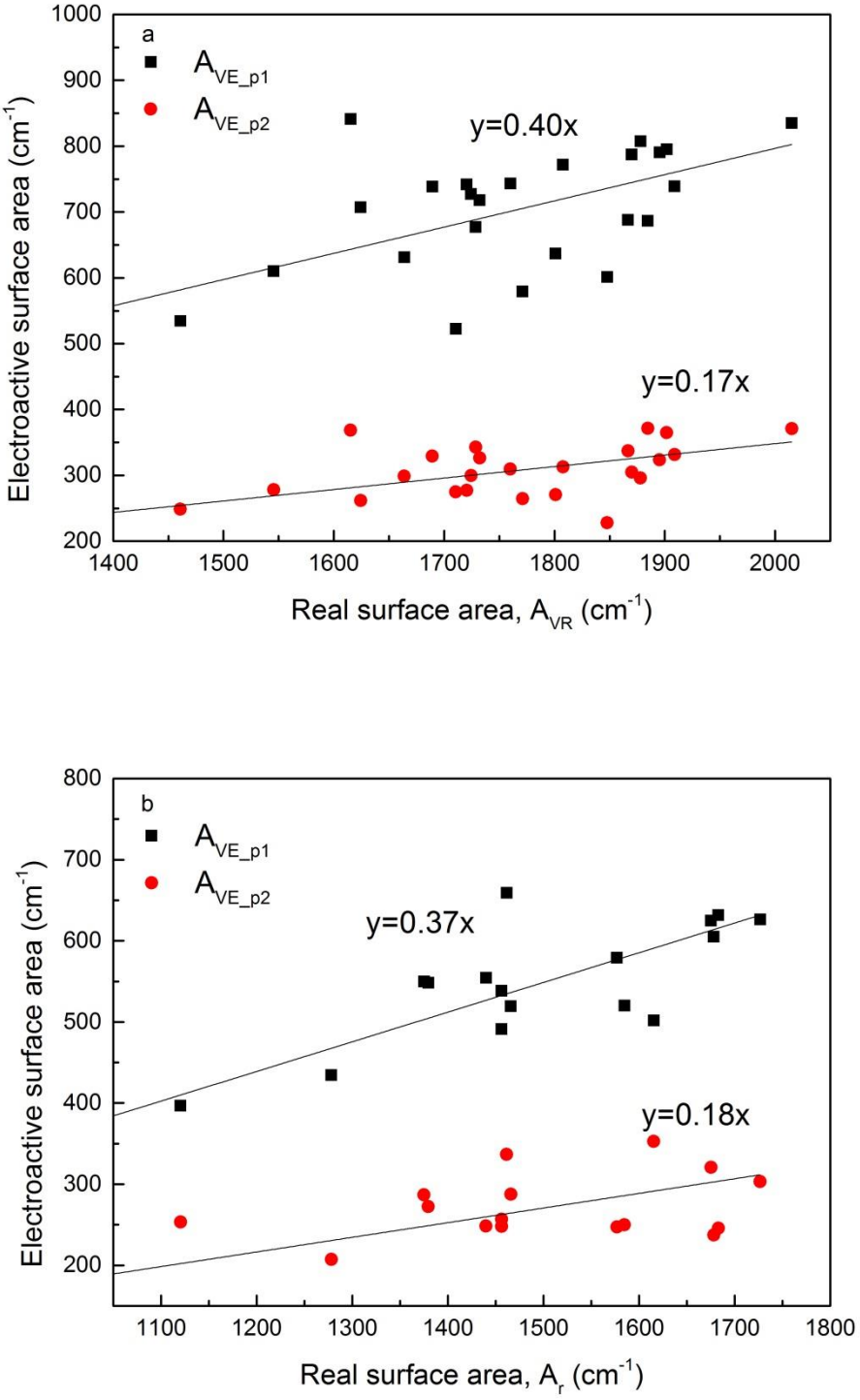

Fig. 4.11 Correlations between electroactive surface area and real surface area for the LCS porous Cu samples sintered at (a) 850℃, (b) 850℃ and etching, (c) 950℃, and (d) 950℃ and etching (to be continued)

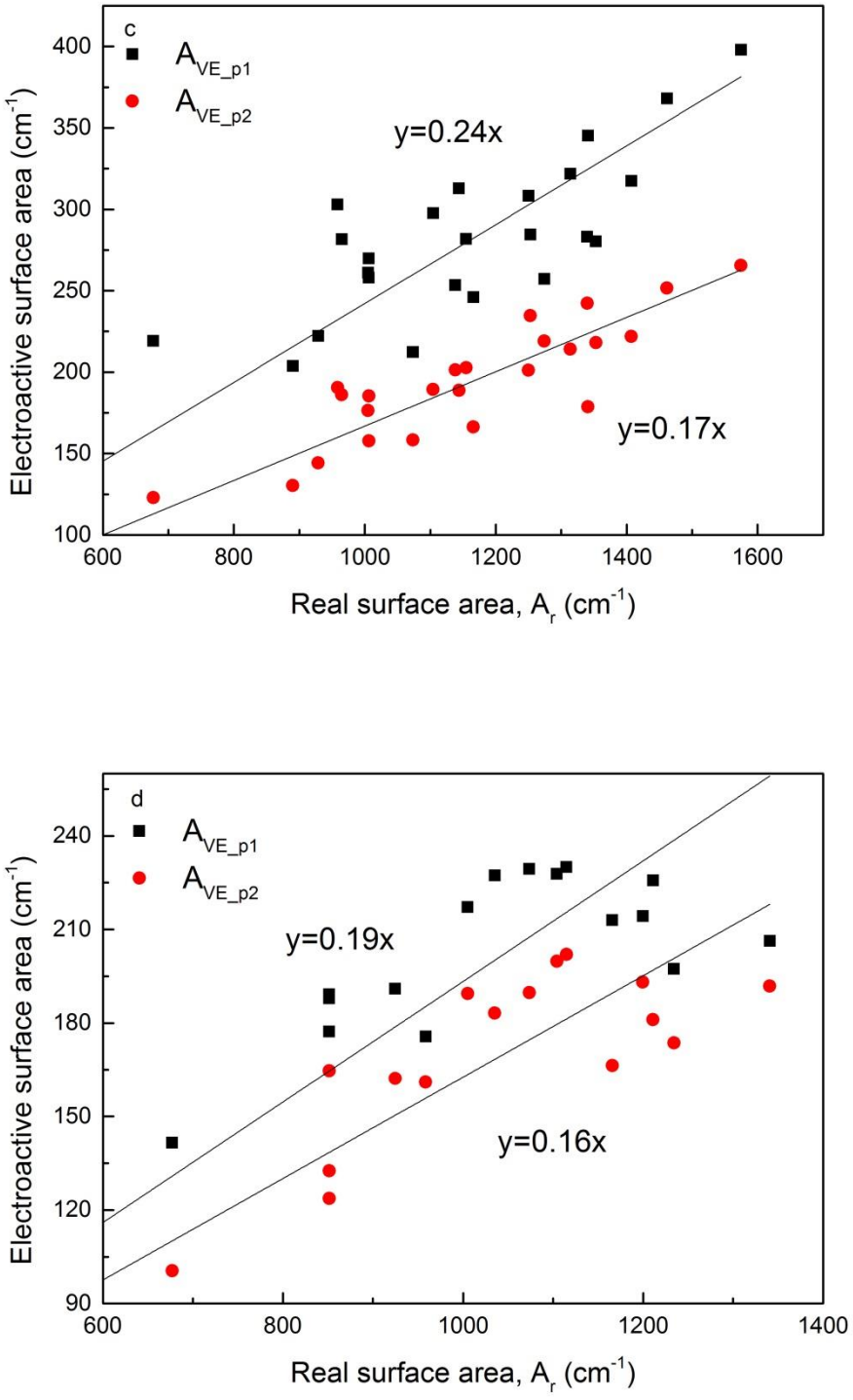

Fig. 4.11 (continued) Correlations between electroactive surface area and real surface area for the LCS porous Cu samples sintered at (a) 850℃, (b) 850℃ and etching, (c) 950℃, and (d) 950℃ and etching.

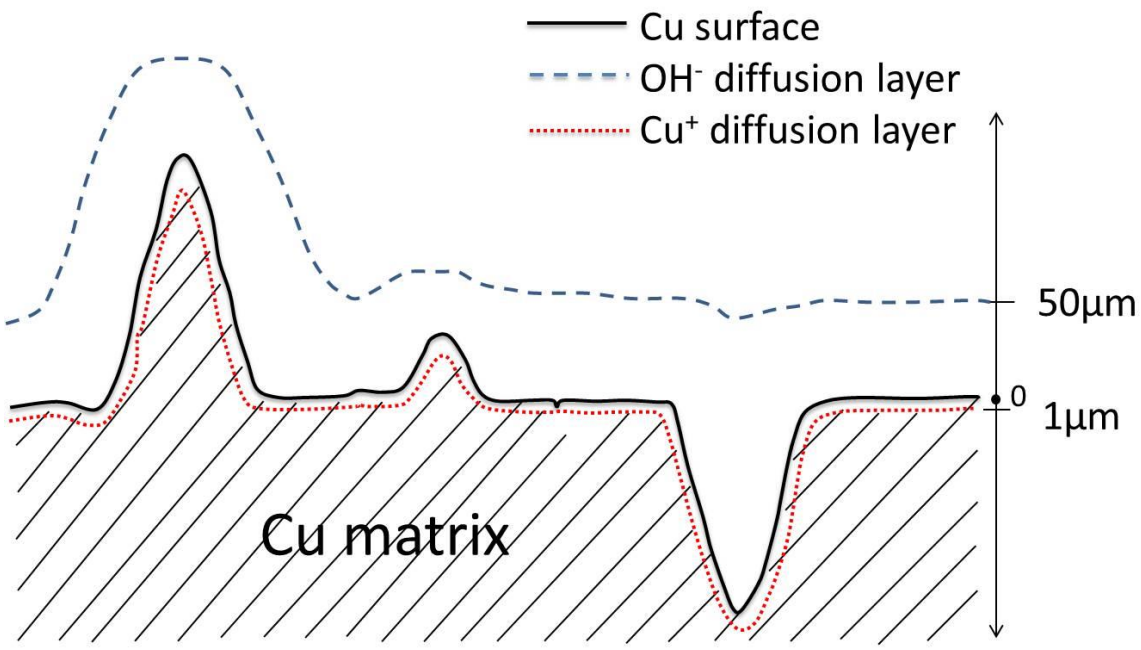

Fig. 4.12 Schematic of diffusion layers of OH^- and Cu^+ at the interface between Cu matrix and electrolyte

4.5. Summary

The specific geometric, electroactive and real surface areas of porous Cu samples manufactured by the LCS process, with pore sizes in the range of 250 – 1500 µm and porosities in the range of 0.5 – 0.8, were measured by quantitative stereology, cyclic voltammetry peak current and double layer capacitance methods, respectively.

The volumetric and gravimetric geometric surface areas of the LCS porous Cu are in the ranges of 20 – 100 cm^{-1} and 5 – 50 cm^2/g, respectively. They increase with increasing porosity and decreasing pore size. The experimental results agree reasonably well with the theoretical results from a stochastic model. However, the model still needs to be improved by considering the metal particle size distribution, potassium carbonate size distribution and the random arrangement of potassium carbonate particles.

The electroactive surface area of the LCS porous Cu depends on the reaction being considered and the diffusion layer thickness associated with the reaction. A thicker diffusion layer results in a lower electroactive surface area. The electroactive surface area of the LCS porous Cu can be increased up to twice by decreasing the diffusion layer thickness from 50 µm to 1 µm.

Both electroactive and real surface areas of the LCS porous Cu can be affected by metal particle size and sintering temperature. The particle size of the Cu powder used to manufacture the LCS porous Cu had a modest effect on the electroactive and real surface areas, with the medium particle sizes, 20-45 µm or 45-75 µm, showing the highest surface areas. Increasing sintering temperature from 850°C to 950°C reduced the electroactive and real surface areas by 31-61%. Chemical etching reduced the electroactive and real surface areas by 9-25%.

CHAPTER 5 SURFACE AREA OF POROUS Ni

5.1 Geometric surface area of porous Ni

The effects of porosity, pore size and particle size on the geometric surface area of porous Ni were investigated. The porous Ni samples have porosities and pore sizes in the ranges of 0.5 – 0.85 and 250 – 1500 μm, respectively. All of the porous Ni samples were manufactured by the decomposition route (950˚C sintering for 2 hours) with particle sizes of 25, 38 and 75 μm. Two typical SEM images of a LCS porous Ni sample are shown in Fig. 5.1. The geometric surface area of the porous Ni samples was compared with that of the porous Cu samples reported by Diao et al. (2015) in order to study the effect of material type on the geometric surface area of porous metals.

5.1.1 Effects of porosity and pore size

Fig. 5.1 shows the volumetric and gravimetric specific geometric surface areas of the porous Ni samples with different pore sizes and different porosities. The volumetric and gravimetric specific surface areas are in the ranges of 20 – 100 cm^{-1} and 5 – 65 cm^2/g, respectively. Both volumetric and gravimetric specific geometric surface areas increase with porosity but decrease with pore size, agreeing with the results for the porous Cu samples reported by Diao et al. (2015). This is because the geometric surface area is the surface area of the primary pores. For a fixed pore size, a higher porosity means more pores within the porous Ni samples. For a fixed porosity, a smaller pore size means a larger number of pores within a certain volume of the porous Ni samples, both increasing the geometric surface area.

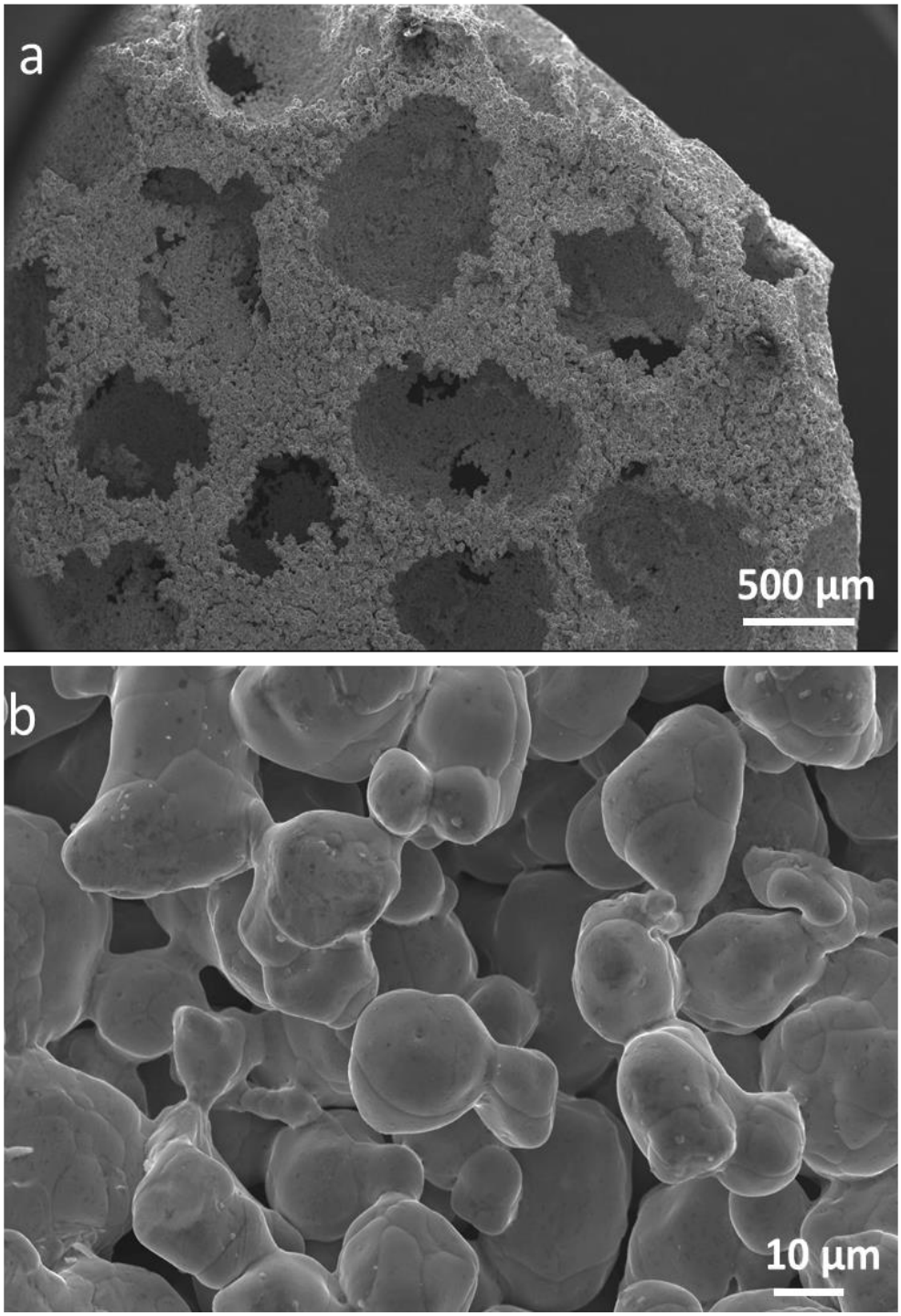

Fig. 5.1 SEM images of a porous Ni sample manufactured by Lost Carbonate Sintering process at magnifications of (a) 30 and (b) 1000

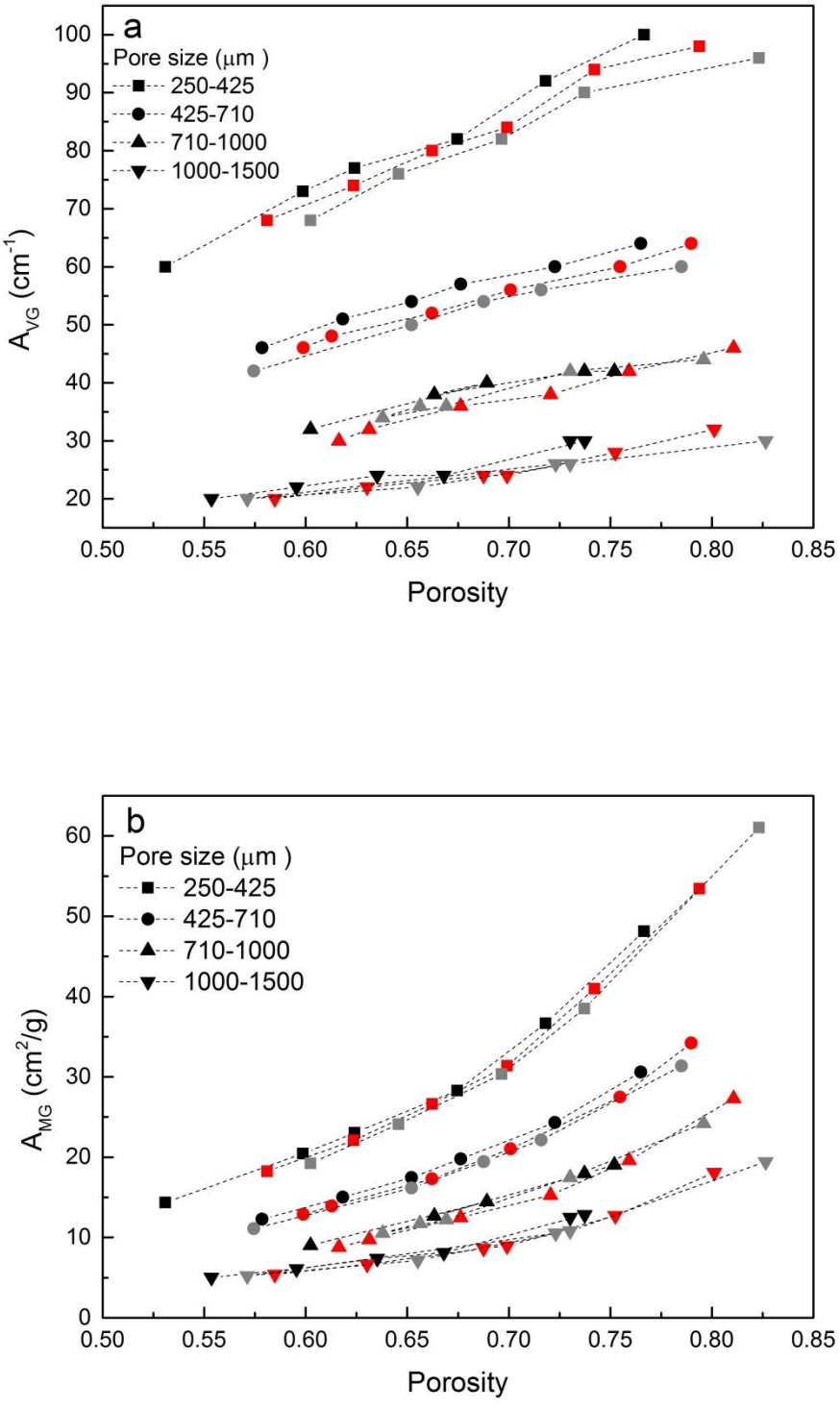

Fig. 5. 2 Volumetric (a) and gravimetric (b) geometric specific surface areas of porous nickel made by 25 μm (Black), 38 μm (Red) and 75 μm (Grey) nickel particles

5.1.2 Effect of particle size

Fig. 5.2 also shows that the porous Ni samples made using different particle sizes of 25, 38 and 75 µm, have similar specific geometric surface areas, indicating that the particle size has little effect on the geometric surface area. The effects of metal particle size on the volumetric and gravimetric specific geometric surface areas can be estimated by Eqs. 5.1 and 5.2, (Diao et al., 2015) respectively,

$$A_{VG} = \frac{3}{\frac{r}{1-\varepsilon} + \frac{R}{\varepsilon}} \quad 5.1$$

$$A_{MG} = \frac{3}{\rho_{Ni}(r + \frac{R(1-\varepsilon)}{\varepsilon})} \quad 5.2$$

where r is the mean radius of the Ni particles (37.5 µm), R is the mean radius of the K_2CO_3 particles (171, 312, 468 and 645 µm for K_2CO_3 size ranges 250 – 425, 425 – 710, 710 – 1000 and 1000 – 1500 µm, respectively (Diao et al., 2015), ρ_{Ni} is the Nickel density (8.91 g/cm3) and ε is the porosity. The mean radius of the Ni particles (r) is only 2% to 25% of the mean radius of the K_2CO_3 particles (R). According to Eqs. 5.1 and 5.2, the volumetric and gravimetric specific geometric surface areas increase with decreasing particle size, and they increase by less than 30% when the particle size is decreased from 75 µm to 25 µm. Therefore, the metal particle size theoretically has a moderate theoretical effect on the geometric surface area. The theoretical results are in agreement with the experimental results.

5.1.3 Effect of matrix material

The geometric surface area of the porous Ni samples is compared with that of the porous Cu samples produced by the LCS process studied by Diao et al. (2015). The porous Cu samples with porosity in the range of 0.55 – 0.75 and pore size in the range of 250 – 1500 µm were

made using a Cu powder with a mean particle size of 72 μm. Their specific geometric surface areas are in the ranges of 15 – 90 cm^{-1} and 5 – 40 cm^2/g, respectively, which are similar to the specific geometric surface areas of the porous Ni samples made using a slightly larger particle size of 75 μm. As discussed in Section 5.1.2, the metal particle size has little effect on the geometric surface area. Therefore, the matrix material is also shown to have little effect on the geometric surface area.

5.2 Electroactive surface area of porous Ni

In this thesis, the porous Ni samples with porosity and pore size in the ranges of 0.5 – 0.85 and 250 – 1500 μm, respectively, were measured to investigate the effects of porosity and pore size. As the electroactive surface area also depends on the diffusion layer thickness and surface morphology (Diao et al., 2015), it is expected to be sensitive to scan rate and particle size. This is because the diffusion layer thickness varies with scan rate and the surface morphology can be changed using different particle sizes. In this project, three scan rates of 0.005, 0.01 and 0.05 V/s, and three different particle sizes of 25, 38 and 75 μm were used in order to study the effects of scan rate and particle size on the electroactive surface area.

5.2.1 Ni plate calibration

Fig. 5.3 (a) shows a typical current-potential plot of a mirror-polished Ni plate with a geometric surface area of 0.0177 cm^2 measured in a solution of 1 mM ferrocyanide and 0.1 M KOH at a scan rate of 0.05 V/s. For a mirror-polished Ni plate, the electroactive surface area is the same as the geometric surface area. The anodic peak current at a potential of about 0.22 V can be used to measure the electroactive surface area of Ni plates or porous Ni samples. The reaction corresponding to the anodic peak is the oxidation of ferrocyanide, as shown in Eq. 3.9.

Fig. 5.3 (b) shows the relations between the peak current and the electroactive surface area of the mirror-polished Ni plates at different scan rates. The lines are the theoretical results as calculated from the Rendles-Sevcik equation (Eq. 3.10) with a known diffusion coefficient of 6×10^{-6} cm/s (Smith et al., 2015). The experimental results are obtained from the averages of the data from six mirror-polished Ni plates. The error in measuring the peak current of mirror-polished Ni plates is not shown in Fig. 5.3, because it is too small (less than 5%) to be clearly distinguished. It is obvious that the experimental results agree well with the theoretical results.

It is reasonable to assume that the Rendles-Sevcik equation also applies to porous samples. The electroactive surface area, A_E (cm^2), of porous Ni can be calculated from the anodic peak current, I_p (μA), measured at scan rates of 0.005, 0.01 and 0.05 V/s by Eqs. 5.3, 5.4 and 5.5, respectively.

$$I_p = 46.5A_E \quad 5.3$$

$$I_p = 65.8A_E \quad 5.4$$

$$I_p = 147.1A_E \quad 5.5$$

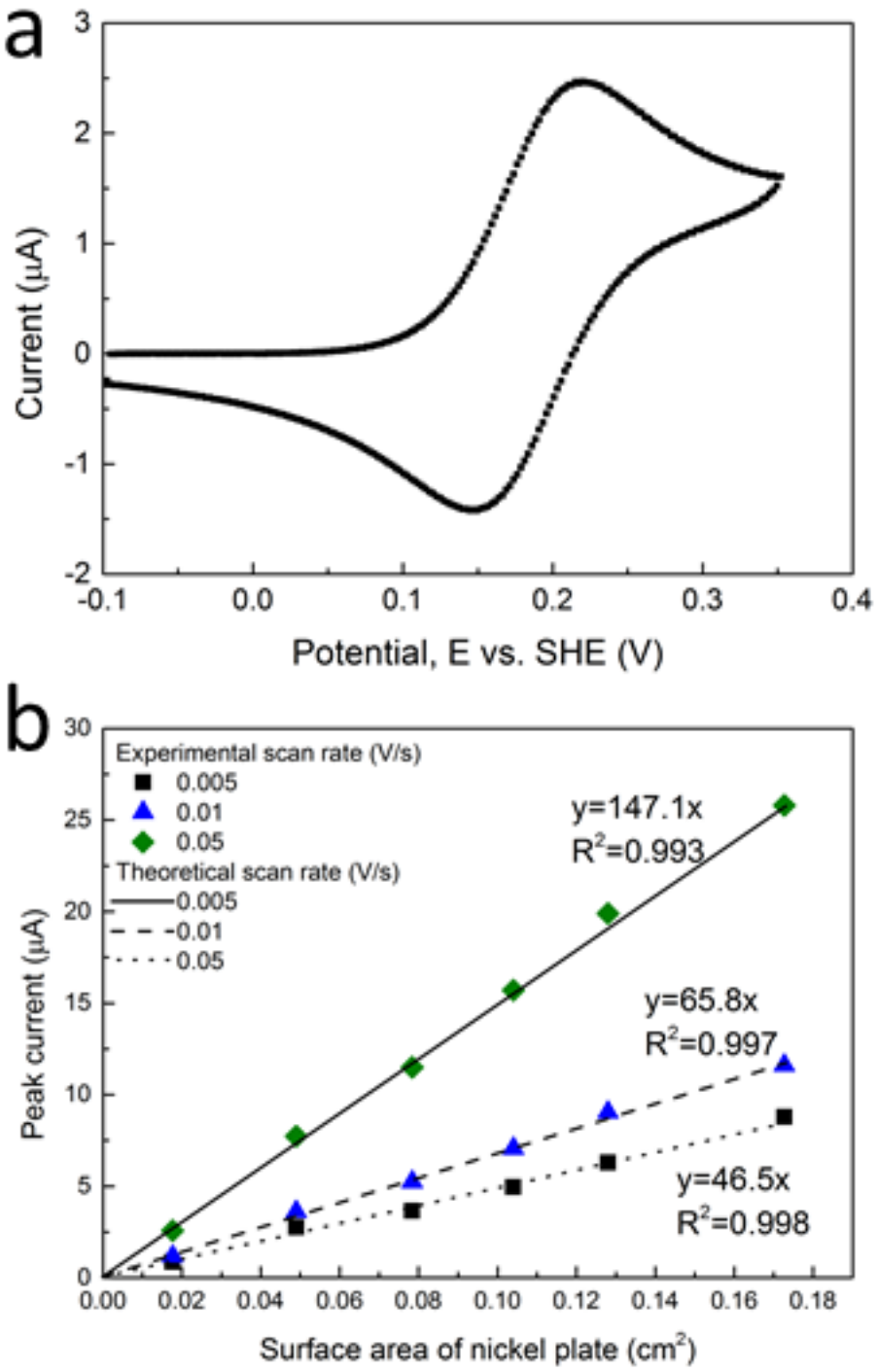

Fig. 5.3 (a) Current-potential plot of a mirror-polished nickel plate with a geometric/electroactive surface area of 0.0177 cm^2 measured in a solution of 1 mM ferrocyanide and 0.1 M KOH at a scan rate of 0.05 V/s. (b) Relations between peak current and surface area

5.2.2 Effects of porosity and pore size

Figs. 5.4 and 5.5 show the variations of the volumetric and gravimetric specific electroactive surface areas with porosity measured at different scan rates for the porous Ni samples. In order to study the effects of porosity and pore size, all of the samples shown in Figs. 5.4 and 5.5 have an identical particle size of 38 μm. The volumetric specific electroactive surface areas of porous Ni with pore sizes of 250 – 425, 425 – 710, 710 – 1000 and 1000 – 1500 μm are in the ranges of 40 – 120, 40 – 100, 30 – 100 and 30 – 90 cm^{-1}, respectively. The gravimetric specific electroactive surface areas of porous Ni with pore sizes of 250 – 425, 425 – 710, 710 – 1000 and 1000 – 1500 μm are in the ranges of 10 – 70, 10 – 65, 10 – 60 and 5 – 60 cm/g, respectively. In each graph in Figs. 5.4 and 5.5, the volumetric or the gravimetric specific electroactive surface area increases with increasing porosity. Comparing graphs a – d in Figs. 5.4 and 5.5 shows that both volumetric and gravimetric specific electroactive surface areas decrease with pore size.

Overall, the volumetric and gravimetric electroactive surface areas are in the ranges of 30 - 100 cm^{-1} and 5 – 70 cm^2/g, respectively, and the volumetric and gravimetric geometric surface areas are in the ranges of 15 – 90 cm^{-1} and 5 – 40 cm^2/g, respectively. The electroactive surface area is only slightly larger than the geometric surface area, indicating that the contribution from the primary pores is dominant and the contribution from the interstices between the Ni particles to the electroactive surface area is very small. Besides, both electroactive and geometric surface areas increase with increasing porosity and decreasing pore size. This is because the electroactive surface area of the porous Ni samples mainly comes from the surface area of the primary pores.

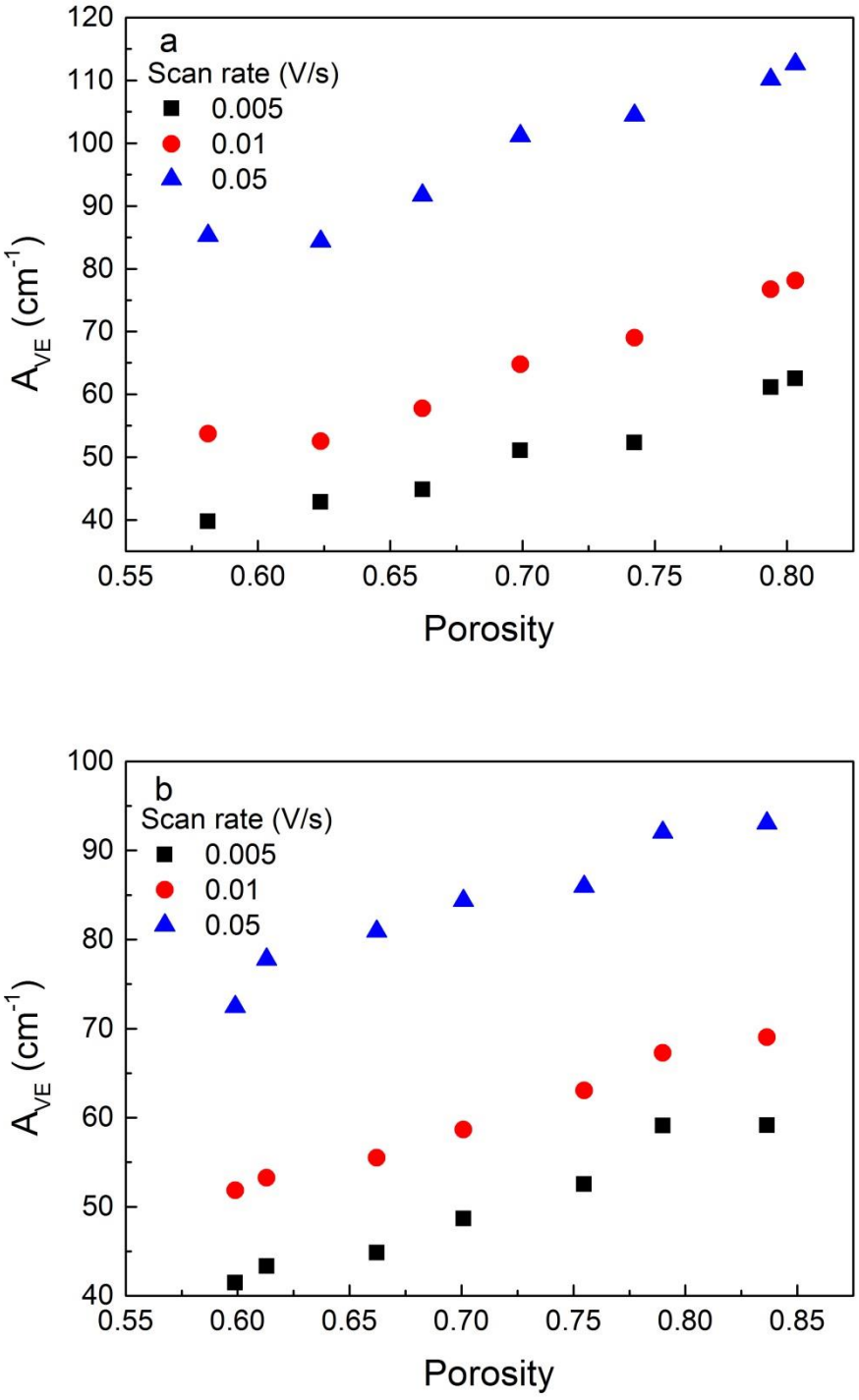

Fig. 5.4 Variations of the volumetric specific electroactive surface area with porosity measured at different scan rates for porous Ni with pore sizes of (a) 250 – 425 µm, (b) 425 – 710 µm, (c) 710 – 1000 µm and (d) 1000 – 1500 µm (to be continued)

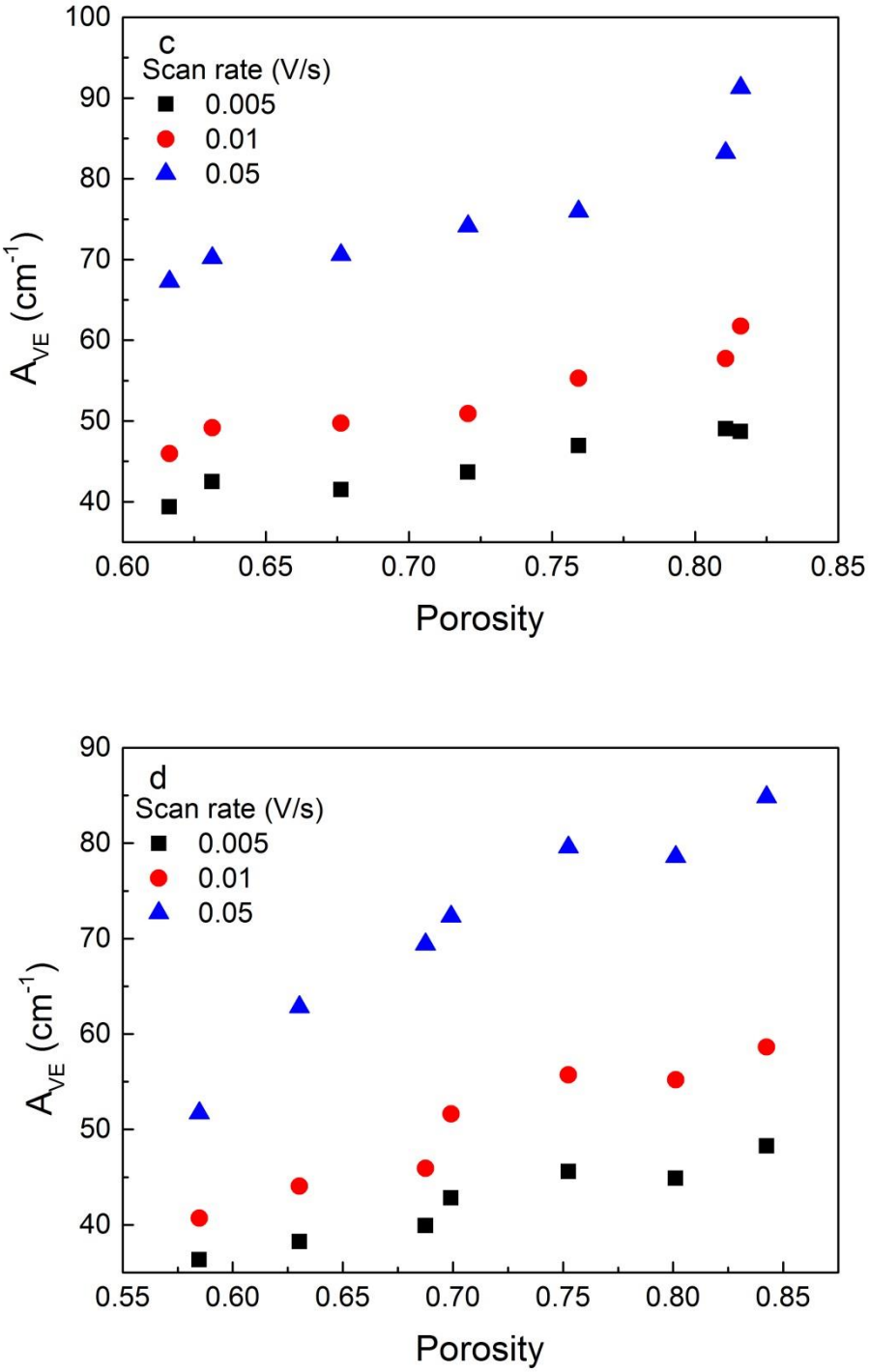

Fig. 5.4 (continued) Variations of the volumetric specific electroactive surface area with porosity measured at different scan rates for porous Ni with pore sizes of (a) 250 – 425 µm, (b) 425 – 710 µm, (c) 710 – 1000 µm and (d) 1000 – 1500 µm

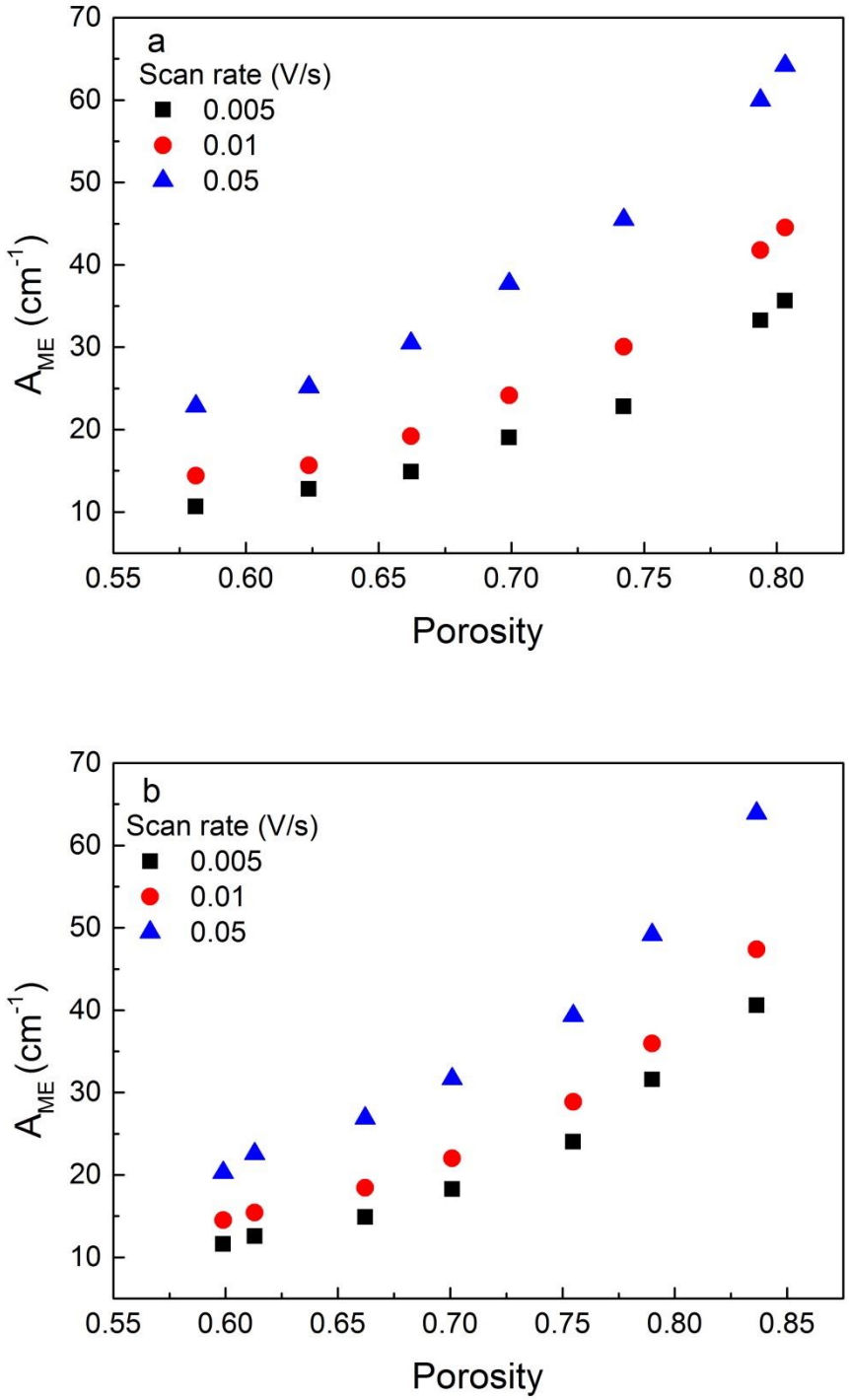

Fig. 5.5 Variations of the gravimetric specific electroactive surface area with porosity measured at different scan rates for porous Ni with pore sizes of (a) 250 – 425 µm, (b) 425 – 710 µm, (c) 710 – 1000 µm and (d) 1000 – 1500 µm (to be continued)

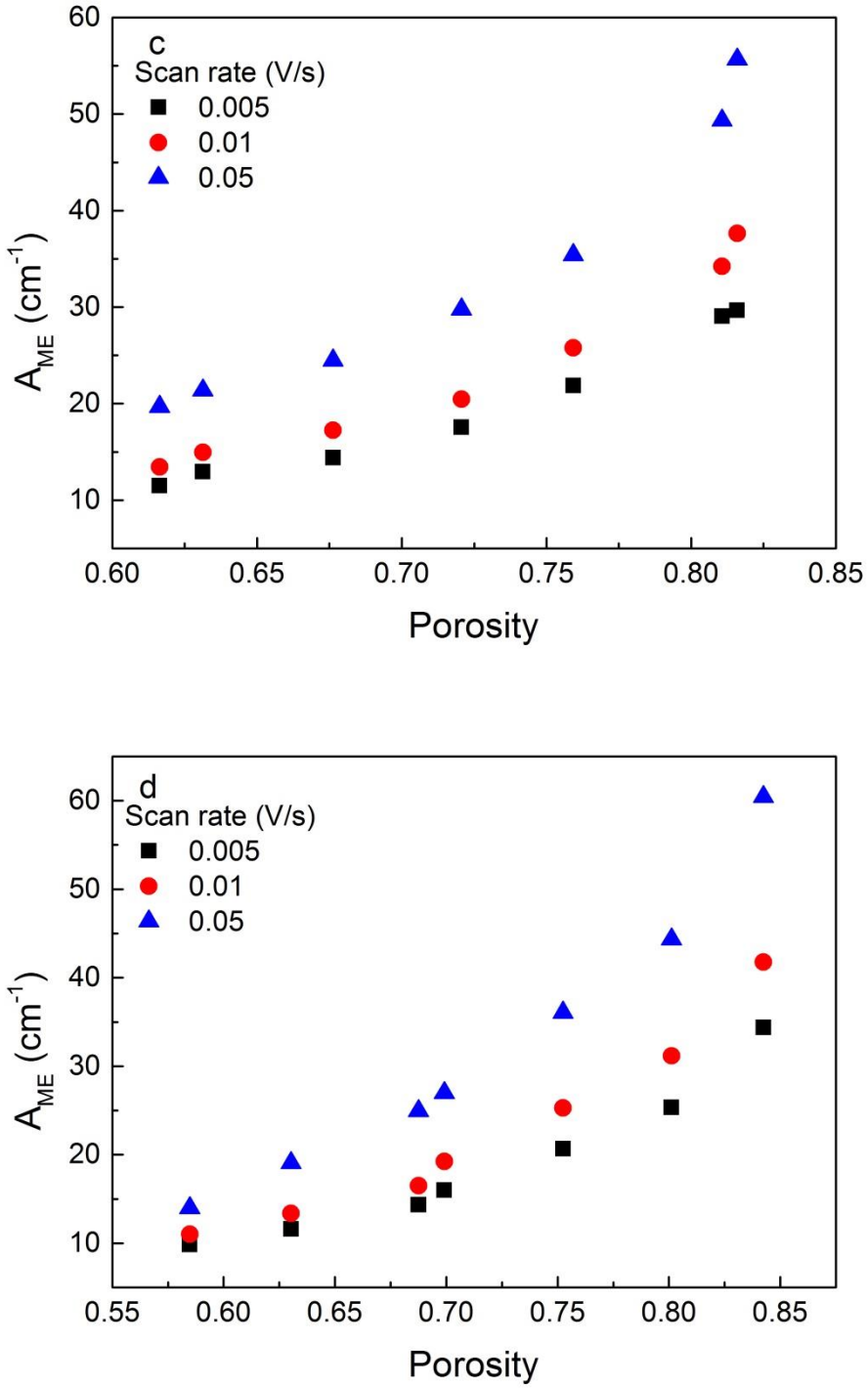

Fig. 5.5 (continued) Variations of the gravimetric specific electroactive surface area with porosity measured at different scan rates for porous Ni with pore sizes of (a) 250 – 425 µm, (b) 425 – 710 µm, (c) 710 – 1000 µm and (d) 1000 – 1500 µm

5.2.3 Effect of scan rate

Figs. 5.4 and 5.5 also show the volumetric and gravimetric electroactive surface areas of porous Ni samples measured at different scan rates. The volumetric specific electroactive surface areas measured at the scan rates of 0.005, 0.01 and 0.05 V/s are in the ranges of 30 – 60, 40 – 80 and 50 – 120 cm^{-1}, respectively, and the gravimetric specific electroactive surface areas measured at the scan rates of 0.005, 0.01 and 0.05 V/s are in the ranges 5 – 40, 10 – 50 and 15 – 70 cm^2/g, respectively. Both volumetric and gravimetric specific electroactive surface areas increase with increasing scan rate.

The effect of scan rate on the electroactive surface area can be explained by the effect of the Nernst diffusion layer thickness. The Nernst diffusion layer thickness (δ_{Nernst}) is expressed by (Prasad and Sangaranarayanan, 2004, Compton and Banks, 2007, Amatore et al., 2001, Molina et al., 2010):

$$\delta_{Nernst} = \frac{nFA_E Dc}{I_p} \tag{5.6}$$

where I_p is the peak current, n is the number of electrons in the reaction ($n = 1$), F is the Faraday constant ($F = 96485\ C/mol$), A_E is the electroactive surface area of the working electrode, D is the diffusion coefficient of the reactive species ($D = 6 \times 10^{-6}\ cm^2/s$) and v is the scan rate, c is the bulk concentration of the reactive species ($c = 10^{-6}\ mol/cm^3$). Substituting I_p by using Rendles-Sevcik equation (Eq. 3.10) gives,

$$\delta_{Nernst} = 0.36\sqrt{\frac{D}{v}} \tag{5.7}$$

The Nernst diffusion layer thicknesses are 125, 88 and 39 µm at scan rates of 0.005, 0.01 and 0.05 V/s, respectively. The diffusion layer thickness decreases with increasing scan rate.

As discussed in Chapter 4, a thinner diffusion layer results in more surface features being detected and therefore a larger electroactive surface area. The electroactive surface area of the porous Ni samples nearly doubles by increasing the scan rate from 0.005 to 0.05 V/s, or decreasing the diffusion layer thickness from 125 to 39 μm. It should be noted that Eq. 5.6 is different from Eq. 4.5, because the reaction on the surface of the porous Ni samples is reversible (Bard et al., 1980), while the reaction on the surface of the porous Cu samples is irreversible (Ambrose et al., 1973).

5.2.4 Effect of the ratio between δ_{Nernst} and pore size

Fig. 5.6 shows the ratios between the electroactive and geometric surface areas for the porous Ni samples. The electroactive surface area of the porous Cu samples manufactured by the LCS process was found to be much greater than the geometric surface area because of the additional contributions from the interstices between the Cu particles (Diao et al., 2015). However, this is not always the case for the porous Ni samples. The ratio between the electroactive and geometric surface areas is in the range of 0.5 – 3, i.e., the electroactive surface area of the porous Ni samples is similar to and sometimes even smaller than their geometric surface area. The ratio does not change much with porosity but decreases significantly with decreasing scan rate and decreasing pore size. The variation of the ratio between the electroactive and geometric surface areas with scan rate can be explained in terms of the magnitude of the diffusion layer thickness relative to the pore size. For the scan rates used in this study, the diffusion layer thicknesses (39 – 125 μm) are 3% – 40% of the pore size (250 – 1500 μm). For a large pore size, the diffusion layer thickness at a high scan rate is much smaller than the pore radius. The curvature of the pore surface has little effect on the measurement and the electroactive surface area is always greater than the geometric surface area. For a small pore size, however, the diffusion layer thickness

becomes comparable to the pore radius, especially at low scan rates. The curvature of the pore surface has to be taken into account. As the electroactive surface area measures the surface of a diffusion layer thickness inside the pore away from the pore surface, it can be significantly smaller than the geometric surface area.

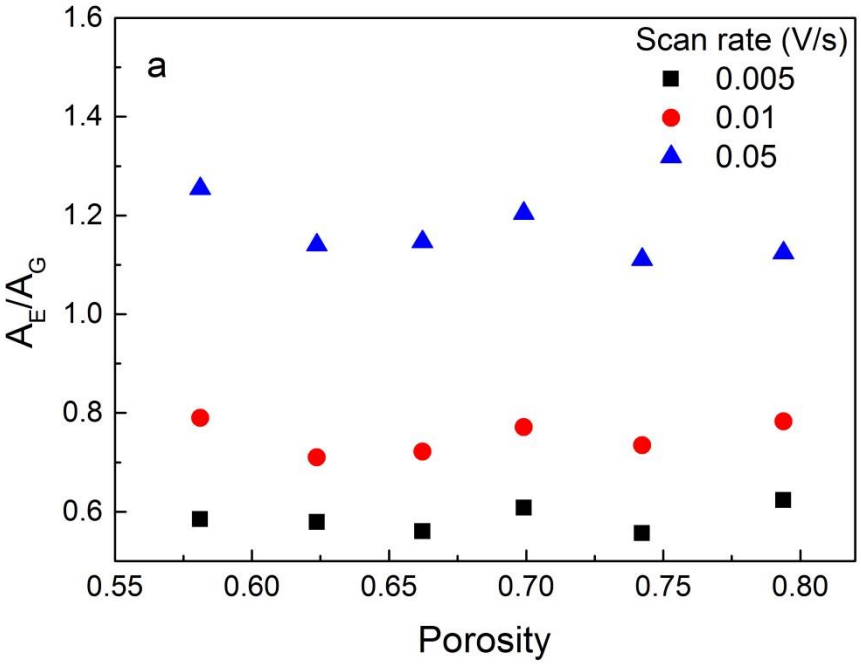

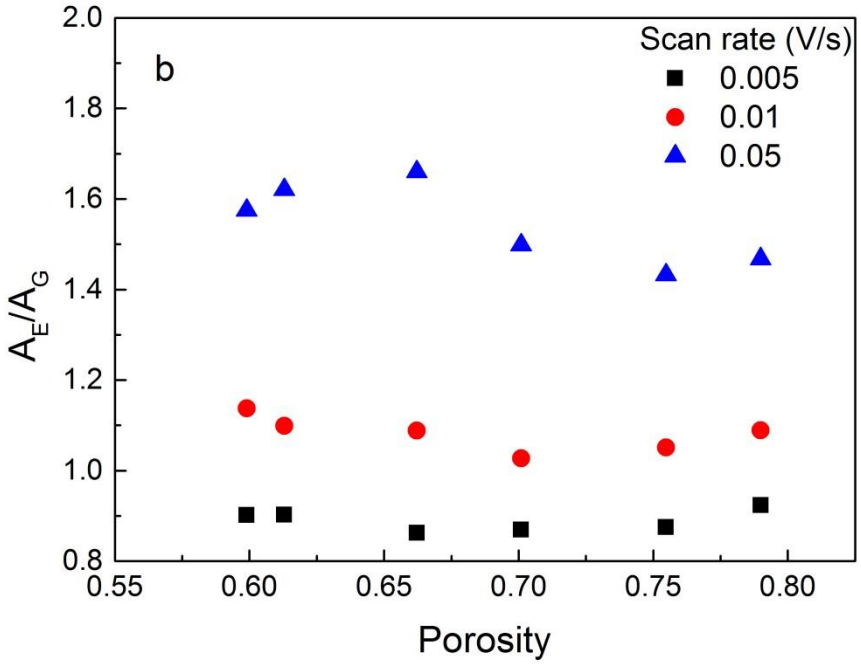

Fig. 5.6 Variations of the ratio between the electroactive surface area (A_E) measured at different scan rates and the geometric surface area (A_G) for porous Ni samples with porosity at different pore sizes: (a) 250 – 425 µm, (b) 425 – 710 µm, (c) 710 – 1000 µm and (d) 1000 – 1500 µm (to be continued)

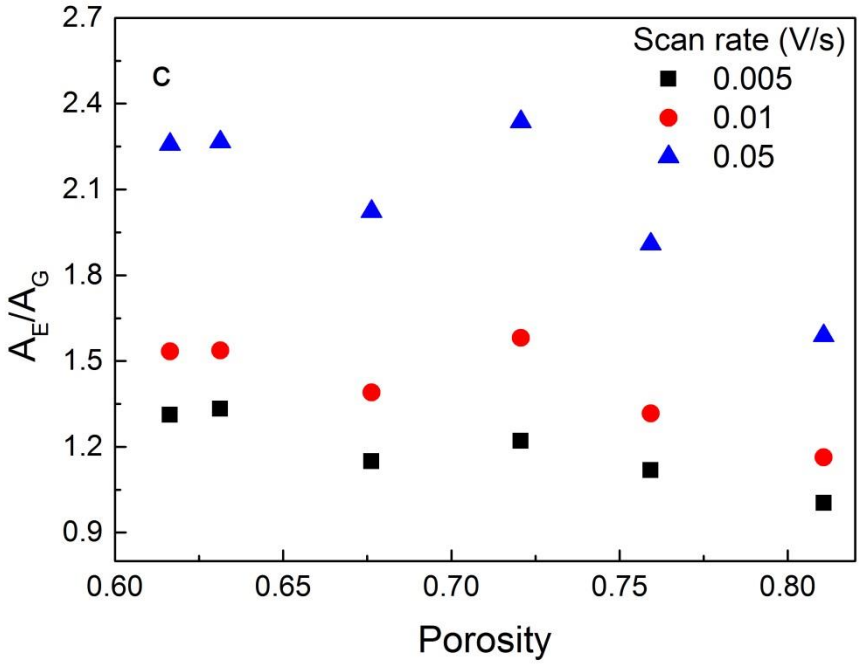

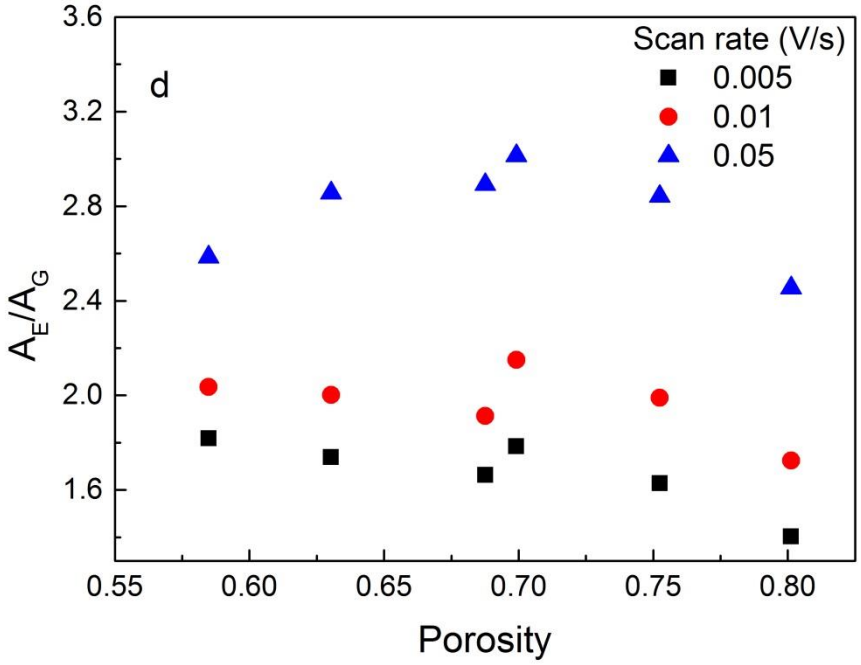

Fig. 5.6 (continued) Variations of the ratio between the electroactive surface area (A_E) measured at different scan rates and the geometric surface area (A_G) for porous Ni samples with porosity at different pore sizes: (a) 250 – 425 µm, (b) 425 – 710 µm, (c) 710 – 1000 µm and (d) 1000 – 1500 µm

5.2.5 Effect of Ni particle size

Fig. 5.7 shows the variations of the volumetric specific electroactive surface area of porous Ni with porosity for different Ni particle sizes at different pore sizes. In order to study the effect of particle size, all the samples were measured at an identical scan rate of 0.05 V/s. For a pore size of 250 – 425 μm, the volumetric specific electroactive surface areas of porous Ni manufactured with different particle sizes of 25, 38 and 75 μm are in the ranges of 55 – 140, 50 – 120 and 60 – 120 cm^{-1}, respectively (Fig. 5.7a). The samples manufactured by the 25 μm particles show the largest volumetric specific electroactive surface area, compared with the samples manufactured by the 38 μm and 75 μm particles. This is probably because of the different surface roughness of the samples made by different particle sizes, sintered at a temperature of 950 ˚C. In general, smaller particles lead to rougher surface morphology, increasing the electroactive surface area. For larger pore sizes (especially Fig. 5.7 c and Fig. 5.7 d), the effect of particle size on the electroactive surface area becomes less significant. There are two possible reasons. On the one hand, for a fixed porosity, samples with large pore sizes have less pores and therefore less internal surface area. The electroactive surface area mainly comes from the outer surface area of the porous samples. As the outer surface is finished by the EDM machining, the roughness of the outer surfaces should be the same for all samples. Therefore, the effect of particle size on the electroactive surface area becomes not pronounced. On the other hand, for pore sizes of 710 – 1000 and 1000 – 1500 μm, the pore size is about 12 – 25% of the diameter of the sample (6 mm) and the random arrangement of pores can result in significant experimental variability.

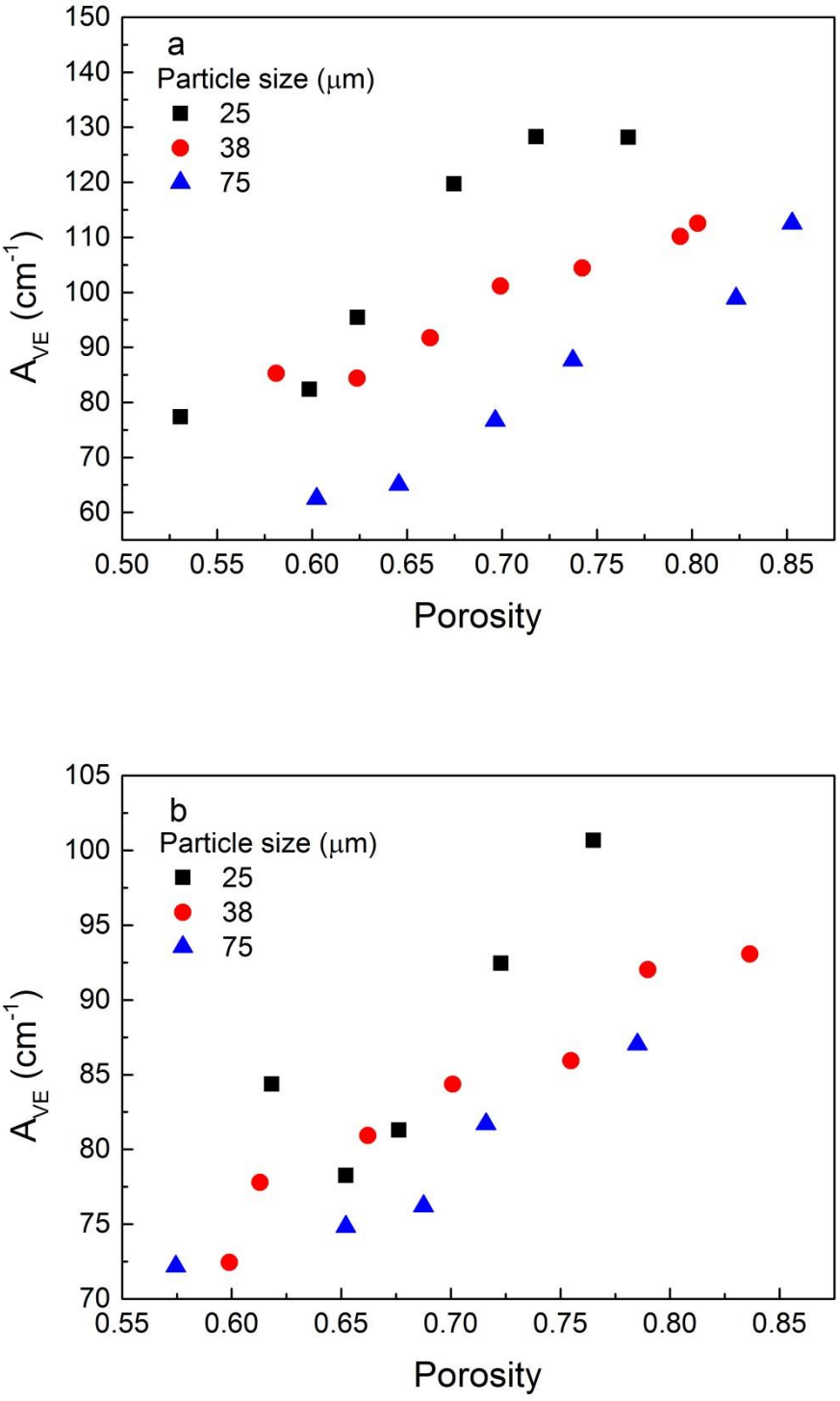

Fig. 5.7 Variations of volumetric specific electroactive surface area of porous Ni with porosity for different Ni particle sizes at different pore sizes: (a) 250 – 425 μm, (b) 425 – 710 μm, (c) 710 – 1000 μm and (d) 1000 – 1500 μm (to be continued)

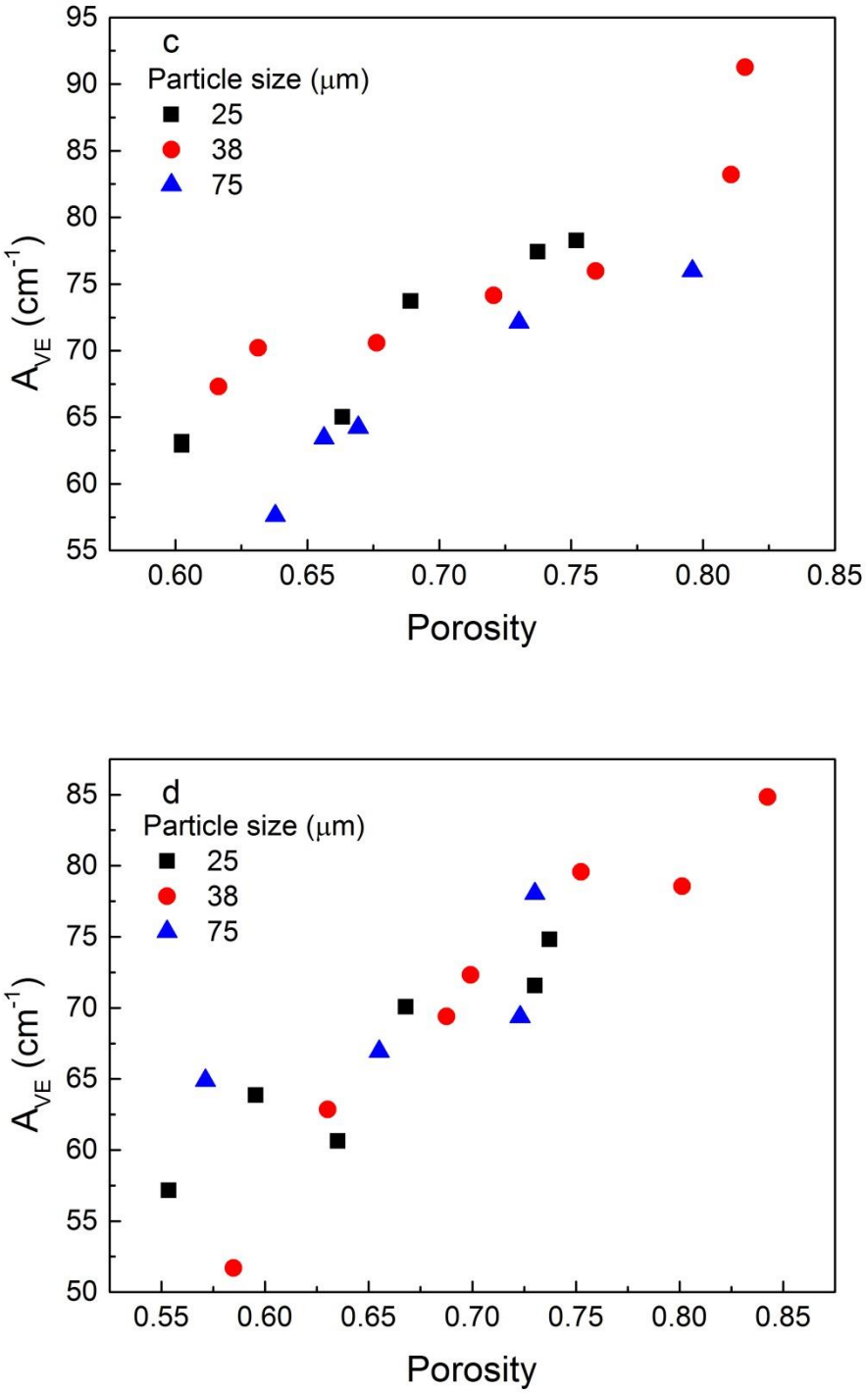

Fig. 5.7 (continued) Variations of volumetric specific electroactive surface area of porous Ni with porosity for different Ni particle sizes at different pore sizes: (a) 250 – 425 µm, (b) 425 – 710 µm, (c) 710 – 1000 µm and (d) 1000 – 1500 µm

5.3 Real surface area of porous Ni

In this thesis, the cyclic voltammetry double layer capacitance method was used to measure the real surface area of the porous Ni samples. The porosity and pore size are in the ranges of 0.5 – 0.85 and 250 – 1500 μm, respectively. Different Ni particle sizes of 25, 38 and 75 μm were used in order to study the effect of particle size on the real surface area. The real surface area of the porous Ni samples was compared with that of the porous Cu samples reported by Diao et al. (2015) to investigate the effect of matrix material.

5.3.1 Effects of porosity and pore size

Figs. 5.8 and 5.9 show the variations of volumetric and gravimetric specific real surface areas with porosity for samples with different pore sizes. For any fixed Ni particle size, the volumetric specific real surface area decreases with increasing porosity and pore size, agreeing very well with that reported by Diao et al. (2015). This is because, for a fixed pore size, a higher porosity means less nickel matrix and therefore less real surface area. If the porosity approaches unity, there will be no nickel matrix left and therefore no surface area. For a fixed porosity, a larger pore size means fewer pores within a fixed volume and thicker pore walls, which are difficult for the electrolyte to fully penetrate to form an electrical double layer, and therefore decreased real surface area. The gravimetric specific real surface area also decreases with increasing pore size due to the same reason. The effect of porosity on the gravimetric specific real surface area is not pronounced.

5.3.2 Effect of particle size

Figs. 5.8 and 5.9 also show that the volumetric and gravimetric specific real surface areas of the porous Ni samples manufactured using Ni powders with particle sizes of 25, 38 and 75 μm are in the ranges of 500 – 1600 cm^{-1} and 200 – 400 cm^2/g, 200 – 1400 cm^{-1} and 150 –

400 cm^2/g, 200 – 1000 cm^{-1} and 100 – 300 cm^2/g, respectively. Comparing Figs. 5.7 and 5.8 (a), (b) and (c) shows that both the volumetric and gravimetric specific real surface areas decrease with particle size. This is because a smaller particle has more specific surface area than a larger particle. Diao et al. (2015) have founded that the specific real surface area of porous Cu is roughly proportional to the specific surface area of the Cu particles. Therefore, smaller particles can contribute to larger specific real surface areas.

5.3.3 Effect of matrix material

The volumetric specific real surface areas of the porous Ni samples manufactured using a powder with a particle size of 75 μm are in the range of 200 – 1000 cm^{-1}. The volumetric specific real surface areas of the porous Cu samples manufactured using a powder with a particle size of 72 μm studied in Chapter 4 are in the range of 600 – 1600 cm^{-1}. The real surface areas of the porous Ni and Cu samples are in the same order of magnitude but the latter is slightly higher, indicating that the material has a moderate effect on the real surface area. This is likely due to the different surface roughness of the metal particles.

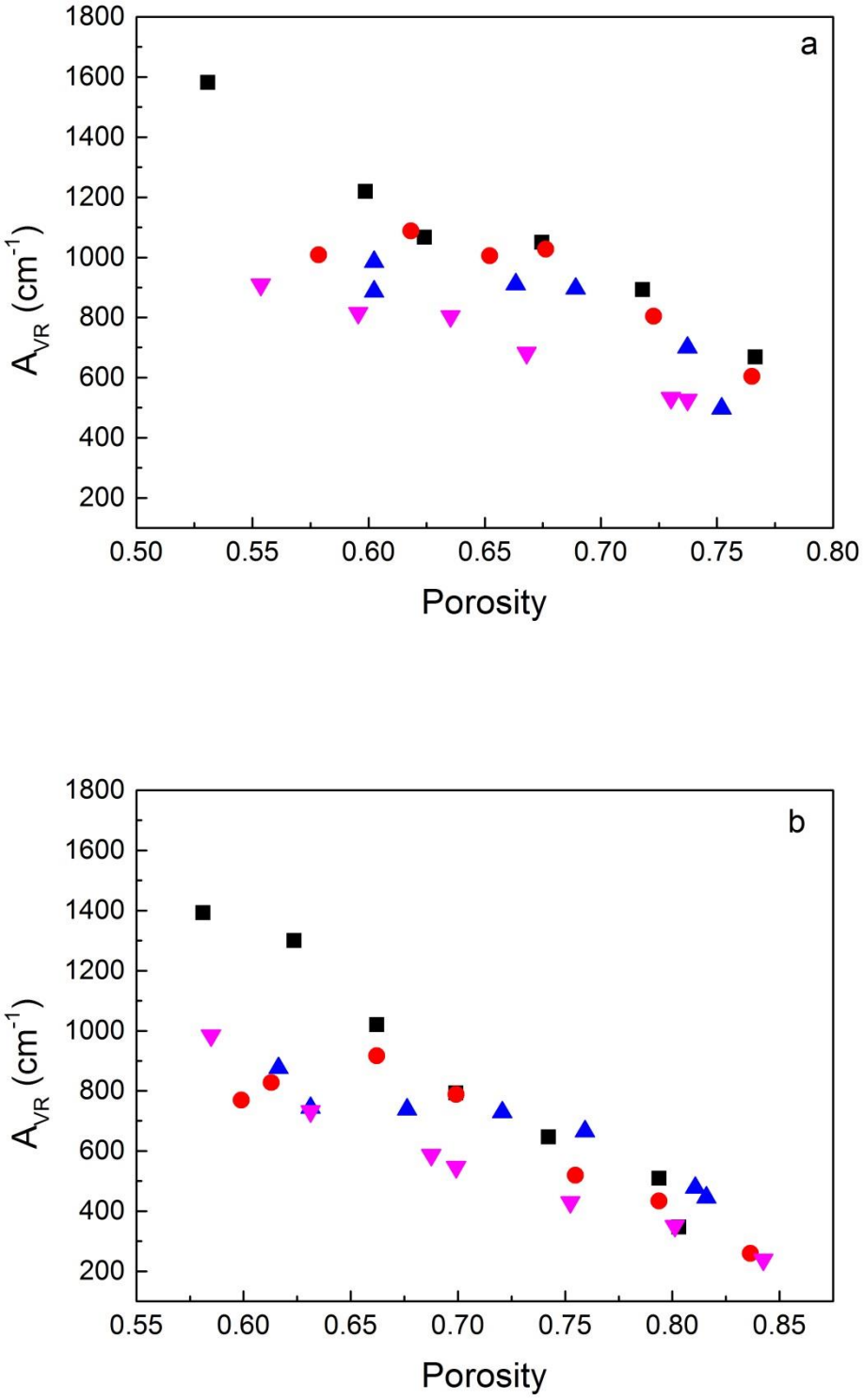

Fig. 5.8 Variations of volumetric specific real surface area with porosity for samples with different pore sizes and different particle sizes: (a) 25 µm, (b) 38 µm and (c) 75 µm (to be continued)

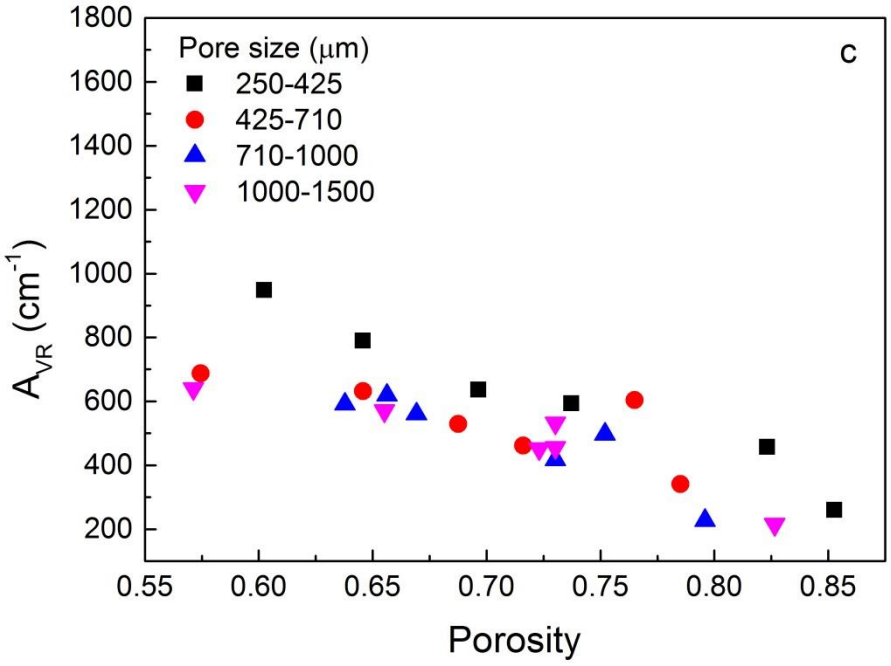

Fig. 5.8 (continued) Variations of volumetric specific real surface area with porosity for samples with different pore sizes and different particle sizes: (a) 25 μm, (b) 38 μm and (c) 75 μm

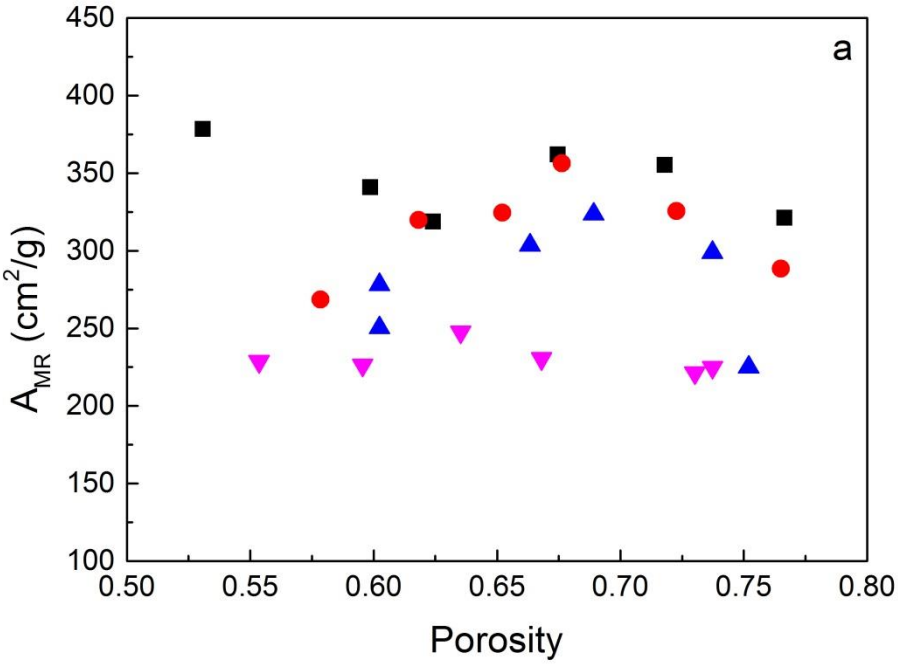

Fig. 5.9 Variations of gravimetric specific real surface area with porosity for samples with different pore sizes and different particle sizes: (a) 25 μm, (b) 38 μm and (c) 75 μm (to be continued)

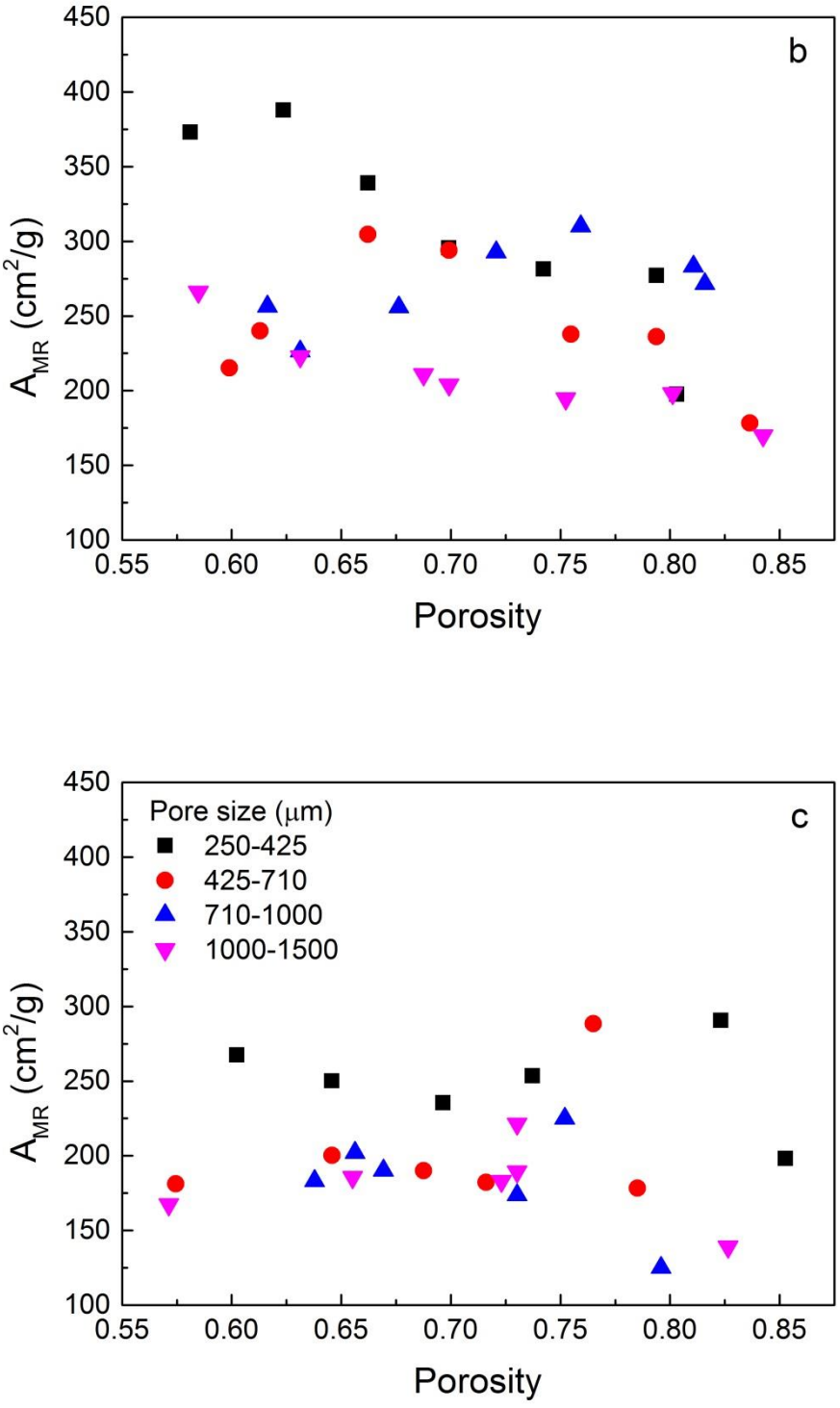

Fig. 5.9 (continued) Variations of gravimetric specific real surface area with porosity for samples with different pore sizes and different particle sizes: (a) 25 μm, (b) 38 μm and (c) 75 μm

5.4 Summary

The specific geometric, electroactive and real surface areas of porous Ni samples manufactured by the LCS process, with pore sizes in the range of 250 – 1500 μm and porosities in the range of 0.55 – 0.85, were measured by quantitative stereology, cyclic voltammetry peak current and double layer capacitance methods, respectively.

The volumetric and gravimetric specific geometric surface areas of the porous Ni samples are in the ranges of 20 – 100 cm^{-1} and 5 – 65 cm^2/g, respectively. The geometric surface area increases with increasing porosity and decreasing pore size. Matrix material and metal particle size have no effect on the geometric surface area.

The volumetric and gravimetric specific electroactive surface areas of the porous Ni samples measured at the scan rate range of 0.005 – 0.05 V/s are in the ranges of 30 – 100 cm^{-1} and 9 – 70 cm^2/g, respectively. The electroactive surface area of the LCS porous Ni mainly comes from the primary pores. The electroactive surface area can be significantly affected by the ratio between δ_{Nernst} and pore size. The effect of Ni particle size on the electroactive surface area is not obvious, except for porous Ni with a pore size of 250 – 425 μm.

The volumetric and gravimetric specific real surface areas of the porous Ni samples are in the ranges of 200-1000 cm^{-1} and 100-300 cm^2/g, respectively. The real surface area is slightly affected by the metal particles used.

CHAPTER 6 MASS TRANSFER COEFFICIENT OF POROUS Ni

Mass transfer coefficient is an indicator of mass transfer performance of a porous electrode. It is related to the rate of the movement of a chemical species from bulk solution to the surface of the porous electrode (Incropera et al., 2007). In this thesis, the mass transfer coefficients of porous Ni with porosities in the range of 0.5 – 0.8 and pore sizes in the range of 250 – 1500 μm were measured by a linear voltammetry technique. All samples were manufactured using a Ni powder with an average particle size of 75 μm and had an identical cylindrical shape with a diameter of 6 mm and a height of 5 mm. The flow rate of electrolyte was changed in the range from 0.28 to 1.87 mL/s in order to investigate the effect of flow rate. The mass transfer coefficient of porous Ni was also compared with those of a mirror-polished solid Ni plate and other Ni electrodes.

6.1 Effects of pore size and porosity

Fig. 6.1 shows the variations of the mass transfer coefficient with porosity at different electrolyte flow rates in the range of 0.28 – 1.87 mL/s for the LCS porous Ni samples with various pore size ranges. For the conditions investigated in this work, the mass transfer coefficient of the LCS porous Ni is in the range of 0.00069 to 0.0135 cm/s. For any given electrolyte flow rate, the mass transfer coefficient decreases with porosity, and more pronounced at high electrolyte flow rates than at low flow rates. Comparing Fig. 6.1 (a) – (d) shows that the mass transfer coefficient increases with pore size for the samples with a fixed porosity and measured at a fixed electrolyte flow rate. The reason behind the effects of porosity and pore size will be discussed in Section 6.3.

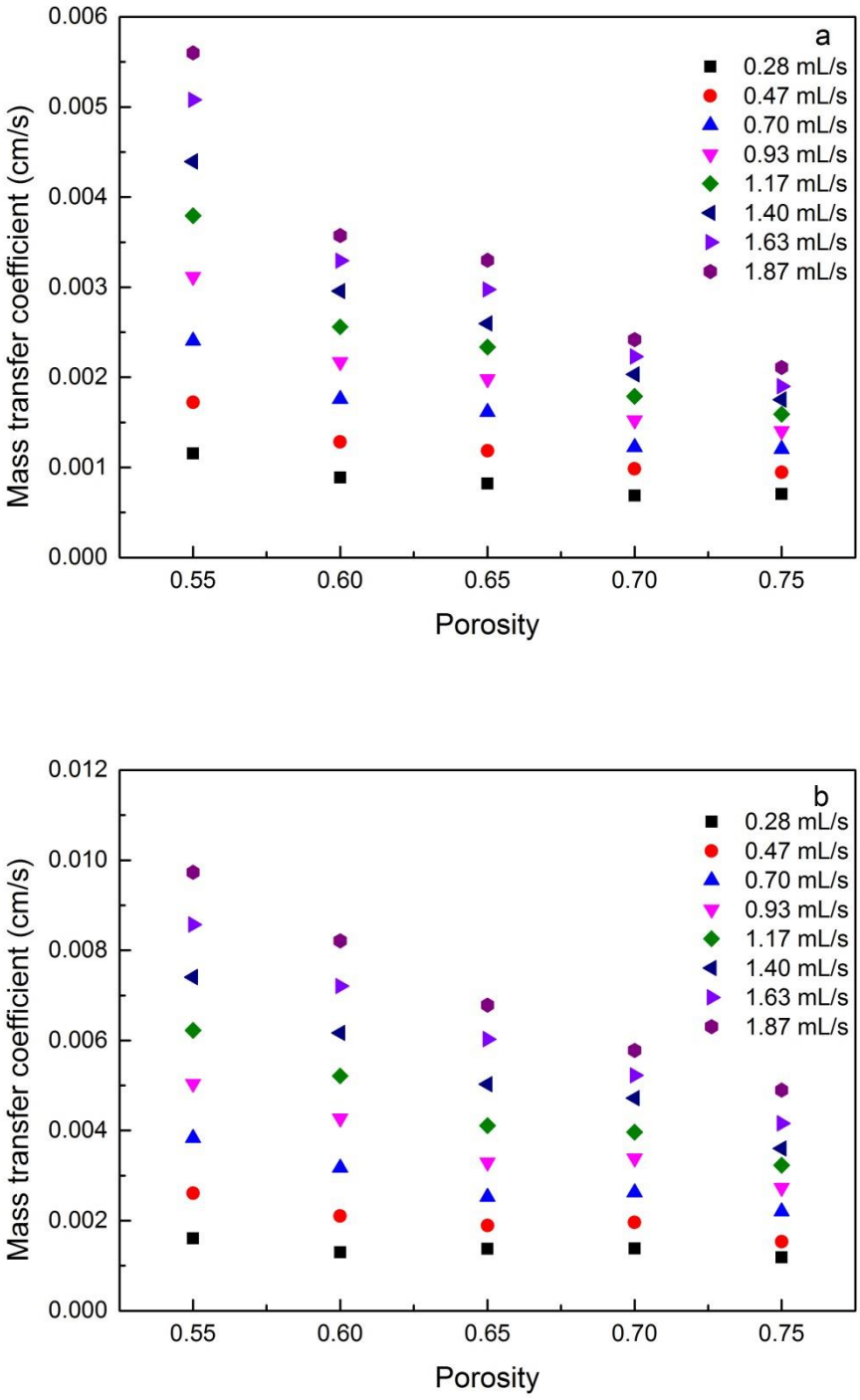

Fig. 6.1 Mass transfer coefficient as a function of porosity at different electrolyte flow rates for the LCS porous Ni samples with various pore sizes: (a) 250–425, (b) 425–710, (c) 710–1000 mm and (d) 1000–1500 μm (to be continued).

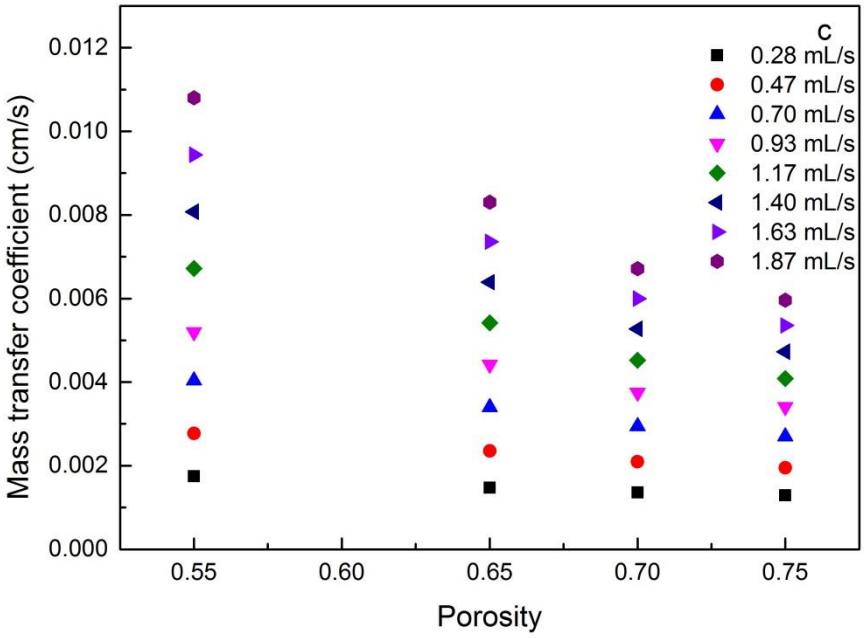

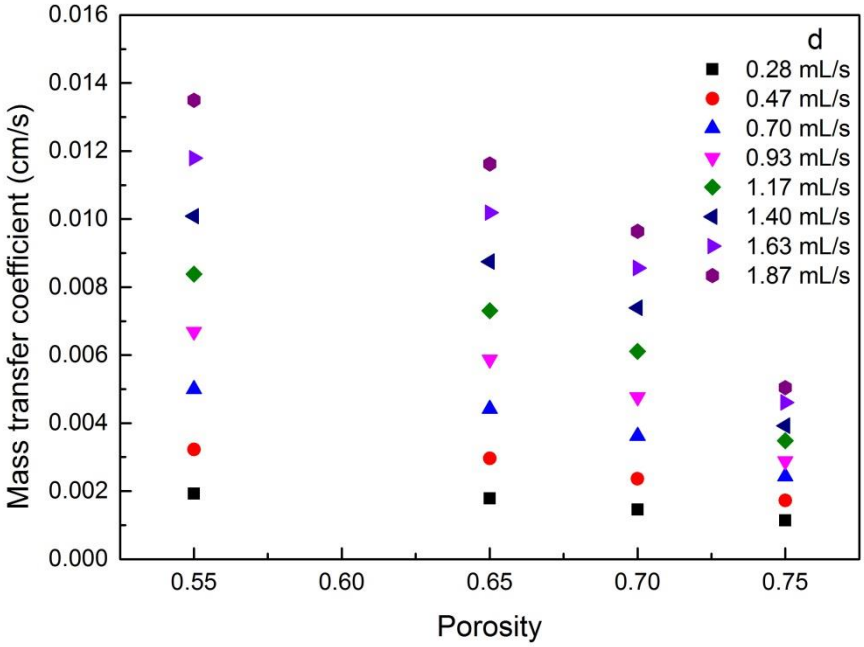

Fig. 6.1 (continued) Mass transfer coefficient as a function of porosity at different electrolyte flow rates for the LCS porous Ni samples with various pore sizes: (a) 250–425, (b) 425–710, (c) 710–1000 mm and (d) 1000–1500 µm

6.2 Effect of flow velocity

It is shown in Fig. 6.1 that the mass transfer coefficient of the LCS porous Ni samples increases with the electrolyte flow rate. While it is convenient to describe the mass transfer performance of a porous sample at an overall electrolyte flow rate, the effect of flow rate is better understood by the resultant flow velocity in the pore channels. The internal flow velocity, u, can be determined by:

$$u = \frac{Q}{A_C \varepsilon} \tag{6.1}$$

where Q is the flow rate of the electrolyte, A_C (0.283 cm^2) is the cross sectional area of the flow channel, i.e., the acrylic tube, and ε is the porosity of the porous Ni sample.

Fig. 6.2 shows the variations of the mass transfer coefficient of the porous Ni samples with internal flow velocity, plotted in the logarithmic scale. The data for the solid Ni plate are also presented for comparison. The mass transfer coefficient increases exponentially with electrolyte flow velocity, which agrees well with the literature (Recio et al., 2013, Cognet et al., 1995). The relation between mass transfer coefficient, k, and internal flow velocity, u, can be described by (Langlois and Coeuret, 1989, Cognet et al., 1995):

$$k = au^b \tag{6.2}$$

where a is a constant associated with the structural properties of the working electrode and b is a constant dependent on the hydrodynamic regime. The value of the exponent b can serve as an indicator of the nature of the flow (Incropera et al., 2007). The values of b for laminar or turbulent flows are about 0.33 and 0.8, respectively. The value of b is expected to increase during the transition from laminar to turbulent flow.

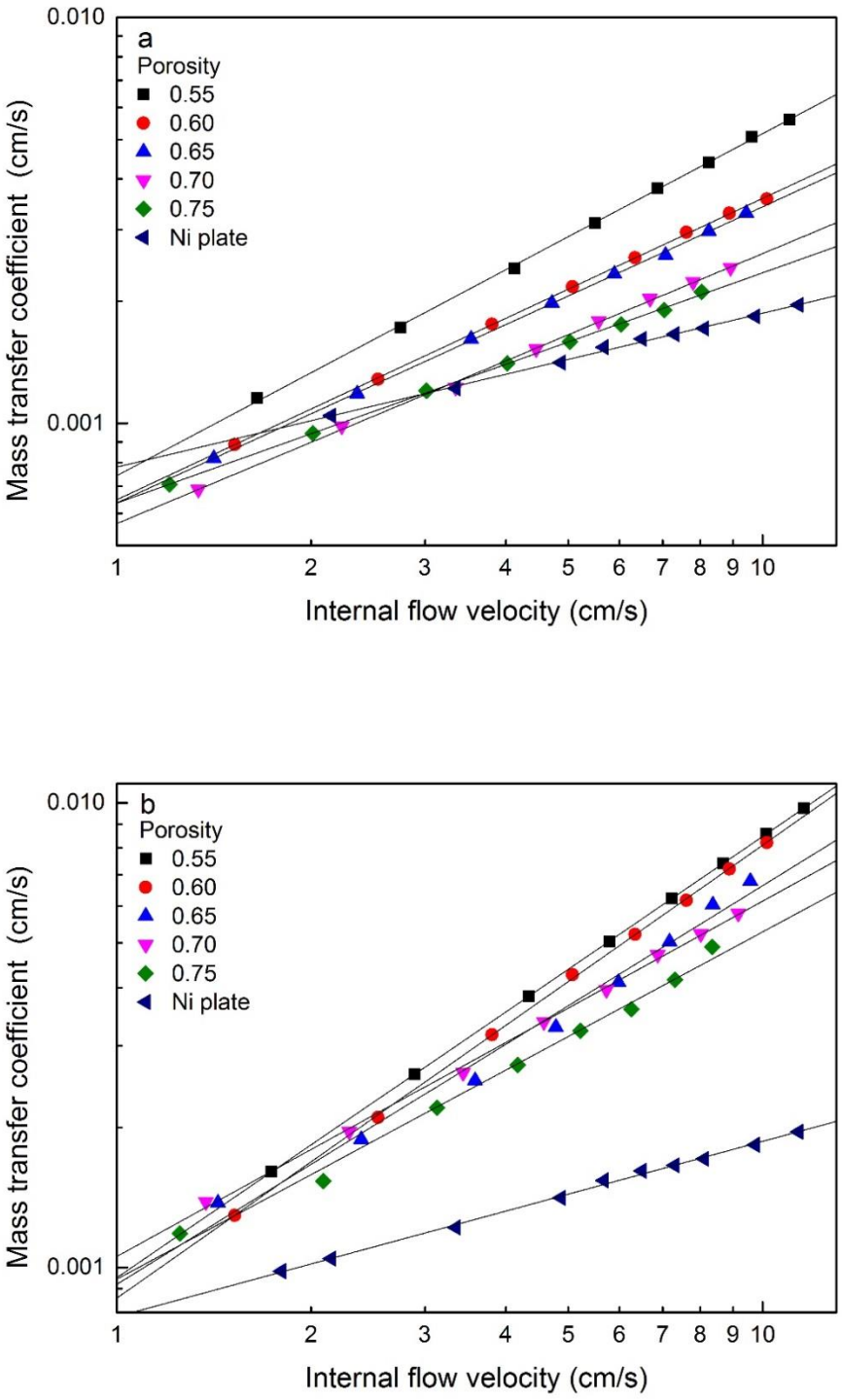

Fig. 6. 2 Mass transfer coefficient as a function of electrolyte flow velocity for the LCS porous Ni samples with different porosities and various pore sizes of: (a) 250 – 425, (b) 425 – 710, (c) 710 – 1000 and (d) 1000 – 1500 µm (to be continued)

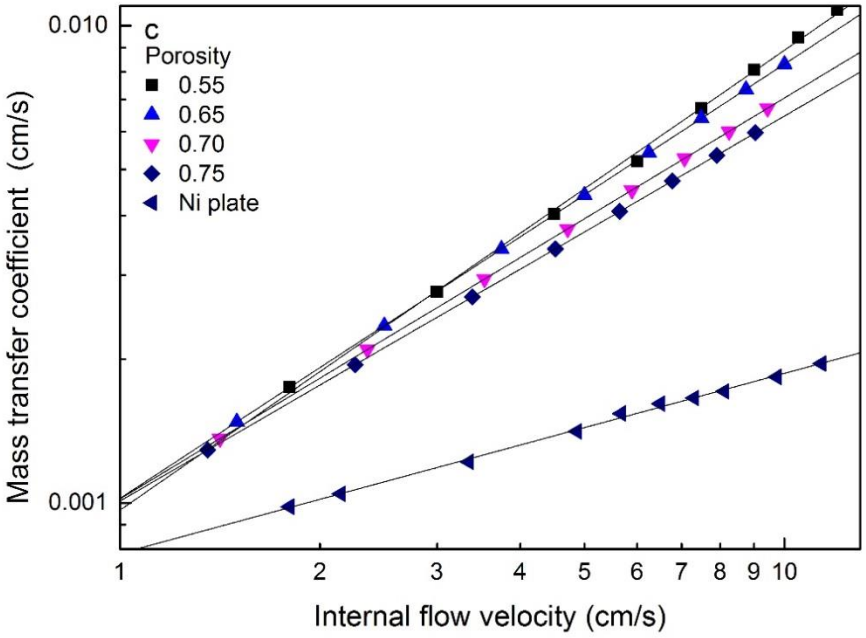

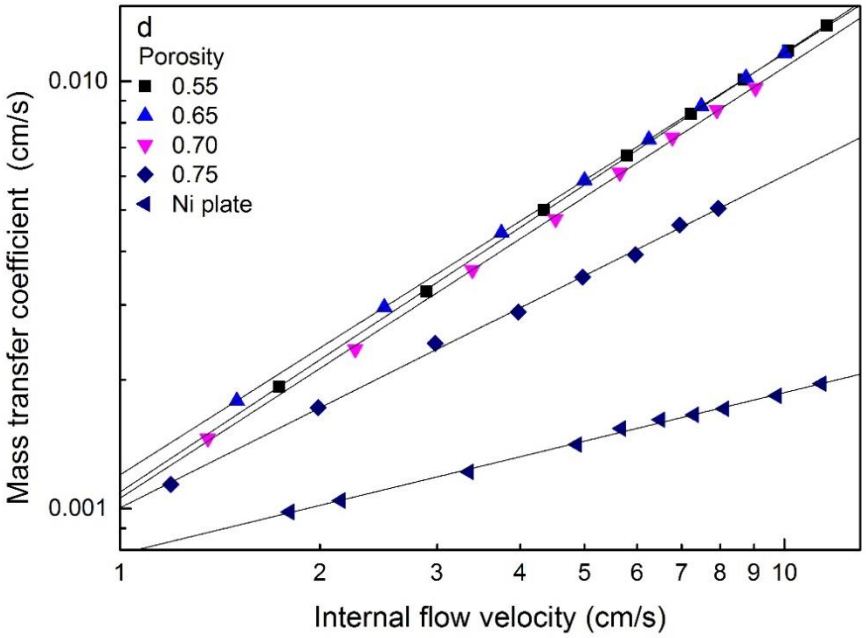

Fig. 6.2 (continued) Mass transfer coefficient as a function of electrolyte flow velocity for the LCS porous Ni samples with different porosities and various pore sizes of: (a) 250 – 425, (b) 425 – 710, (c) 710 – 1000 and (d) 1000 – 1500 µm

6.3 Interpretation of the effects of porosity and pore size

Fig. 6.3 shows the variations of the pre-exponential constant, a, and the exponent, b, in Eq. 6.2 as a function of the geometric surface area of the LCS porous Ni samples. The values of a and b were obtained from Fig. 6.2 and the values of the geometric surface area are shown in Chapter 5. It is clearly shown that the pre-exponential constant a and the exponent b are strongly correlated with the geometric surface area. The higher the volumetric geometric surface area, the lower the pre-exponential constant a and the exponent b.

The effect of geometric surface area on the constant a may arise from its effect on the spatial distribution of the electrolyte in the porous channels. For a fixed porosity, different geometric surface areas lead to different thicknesses of electrolyte in the porous channel. A higher volumetric geometric surface area means a thinner electrolyte near the surface of the metal matrix, i.e., the electrolyte being spread more thinly against the surface. If the depth of the electrolyte becomes comparable to or even thinner than the Nernst diffusion layer (Diao et al., 2015), it can cause exhaustion of the reactive species. This may effectively lead to a reduced bulk concentration of the reactive species, which in turn can result in a reduced pre-exponential constant.

Geometric surface area is probably not a direct causative parameter for the exponent b. The exponent is an indicator of flow turbulence (Recio et al., 2013) which is more likely affected by the tortuosity of the porous structure. Tortuosity of a porous medium characterizes the convoluted pathways, or channels, formed by pores through the porous medium. It is defined as the ratio of the average length of pathways between two points to the straight-line distance between the points in the porous medium. Lower porosities and large pores in LCS porous metals generally result in high tortuosity values (Diao et al., 2017). At the same

time, Lower porosities and large pores lead to lower volumetric geometric surface areas. A low volumetric geometric surface area is therefore associated with a high tortuosity and high turbulence, resulting in a high exponent value.

Fig. 6.3 also shows that the effects of porosity and pore size on the constants are different, although both affect the volumetric geometric surface area. The pre-exponential constant a increases significantly with pore size but does not change much with porosity for any given pore size. The effect of pore size can be explained by the relative magnitudes of the electrolyte reservoir and the diffusion layer. On the one hand, smaller pores contain smaller pockets of electrolyte and thus thinner electrolyte. On the other hand, smaller pores have greater surface curvatures and consequently thicker diffusion layers. The higher ratios between diffusion layer and electrolyte depth can lead to more severe exhaustion of reactive species and thus a reduced pre-exponential constant. The exponent b generally decreases significantly with porosity, but does not change as much with pore size for any given porosity. Although the porous Ni samples with the smallest pore size (250 – 425 μm) show lower exponent values, the samples with the other pore sizes have similar exponent values. These results indicate that the spatial distribution of the electrolyte is mainly influenced by pore size while the flow turbulence is mainly dependent on porosity.

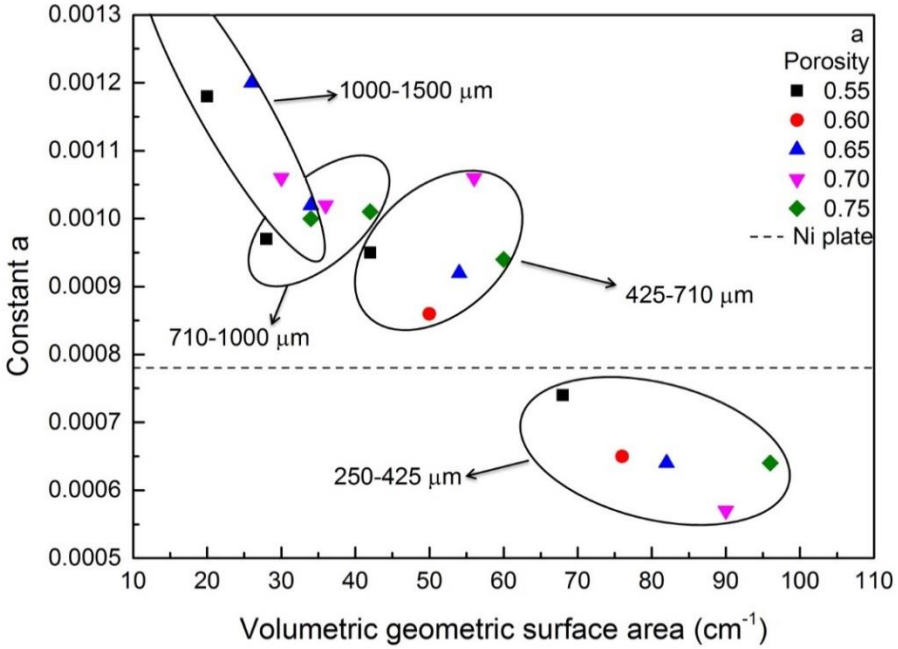

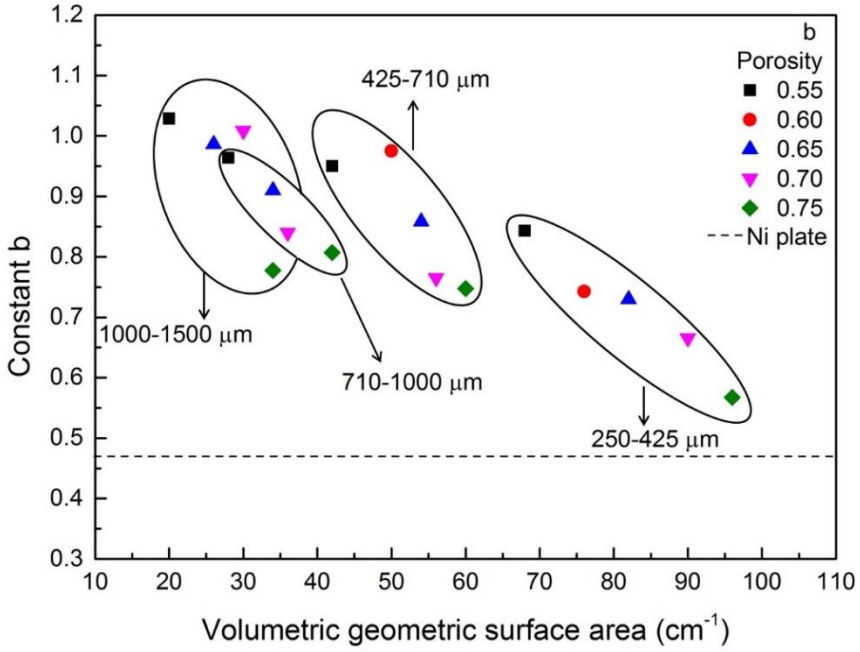

Fig. 6. 3 Variations of (a) pre-exponential constant a and (b) exponent b with volumetric geometric surface area

6.4 Comparison with solid Ni electrode

Fig. 6.2 shows that nearly all the LCS porous Ni samples have higher mass transfer coefficients (up to 7 times) than the solid Ni plate at the same electrolyte flow velocities. This is very likely because the LCS porous structure promotes a highly turbulent flow, which is well known to lead to a high mass transfer coefficient (Szánto et al., 1996). The exception is the samples with the smallest pores of 250 – 425 µm at low electrolyte velocities, which have mass transfer coefficients similar to those of the Ni plate at the same velocity (Fig. 6.2a). This is because the flow within the LCS porous Ni samples with small pores may remain laminar at low flow velocities, as in the case of the flow on the surface of a Ni plate.

The mass transfer performance of porous electrodes depends not only on the mass transfer coefficient but also on the internal surface area. The mass transfer performance is described by the product of the mass transfer coefficient and the real surface area (kA). The volumes of the porous Ni samples and Ni plate used in this study are almost identical, about 0.14 cm^3. The porous Ni samples have a geometric surface area in the range of 2.83—13.56 cm^2 and a real surface area in the range of 45 – 135 cm^2, which are about 1 – 5 times and 16 – 50 times of the geometric/real surface area of the solid Ni plate (2.8 cm^2). Given that the porous Ni samples have a mass transfer coefficient 1 – 7 times of that of the solid Ni plate at the same electrolyte flow velocities, the mass transfer performance (*kA*) of the LCS porous Ni can be up to 300 times better than the solid Ni plate.

The limiting current can also be used as a direct indicator of the mass transfer performance, provided the electrodes to be compared are measured under the same conditions with the same electrolyte concentrations. The maximum limiting current of the porous Ni samples was 0.0131 A, which is about 30 times of the limiting current of the Ni plate measured at the

same electrolyte velocity (0.0046 A). However, the concentration of Ferricyanide used in the measurements for the Ni plate was 10 times higher than that used in the measurements for the porous Ni samples. Therefore, the mass transfer performance of the porous Ni is therefore up to 300 times better than the solid Ni plate, the same conclusion as reached by comparing the mass transfer performance in terms of kA.

The value of pre-exponential constant a for the solid Ni working electrode is 0.00078, which is higher than the a values of the LCS porous Ni samples with the smallest pore size (250 – 425 μm) but lower than those of the porous samples with larger pore sizes (Fig. 6.3 a). The value of exponent b for the solid Ni working electrode is 0.37, which is similar to the value reported in the literature for a fully developed laminar flow ($\approx$ 0.33) (Szánto et al., 1996). This indicates that, in the range of flow velocity studied in this work (1 to 12 cm/s), the electrolyte flow on the surface of the Ni plate remains laminar. The values of b for the porous Ni electrodes, however, are much higher, ranging from 0.57 to 1.03 (Fig. 6.3 b). The flow within the LCS porous structure can change to turbulence flow, due to the highly tortuous nature of the pore channels.

Fig. 6.4 replots the constant b values against the porosity values of the LCS porous Ni samples. It is interesting to note that the trend lines for the samples with pore sizes of 250 – 425 μm, 425 – 710 μm and 710 – 1000 μm approach 0.37 at a porosity of 1, i.e., the b value of the Ni plate, which can be seen as a "porous sample" with a porosity of 1. The data points for the samples with a pore size of 1000 – 1500 μm do not show a clear trend, because the pore size is about one sixth of the diameter of the sample and the random arrangement of pores can result in significant experimental variability.

Fig. 6.4 shows that the constant b decreases with porosity but increases with pore size. As a general trend, the enhancement of the mass transfer coefficient therefore decreases with porosity but increases with pore size (Fig. 6.1 and Fig. 6.2). As discussed previously in Section 6.3, this is because tortuosity of the porous samples generally increases with decreasing porosity and increasing pore size and a high tortuosity in turn increases flow turbulence (Diao et al., 2017).

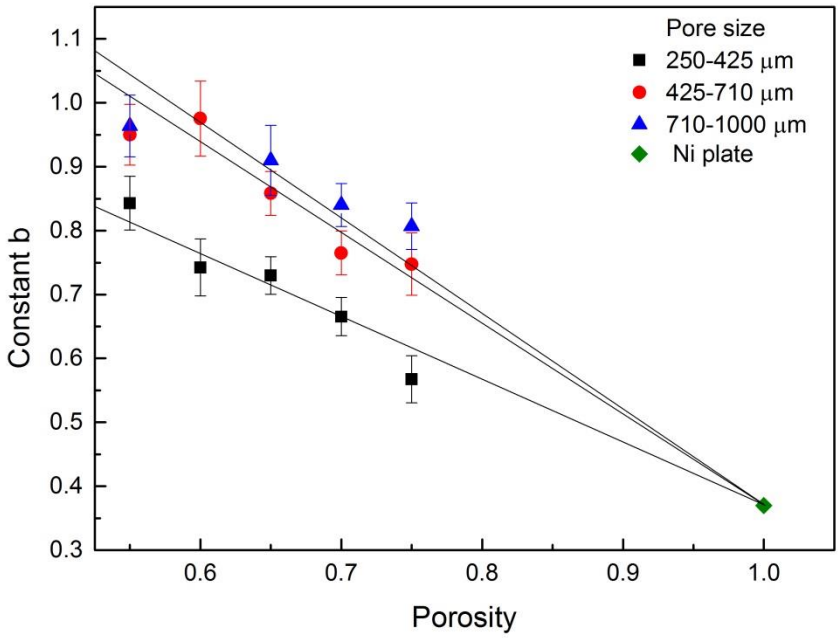

Fig. 6. 4 Variation of exponent b with porosity at different pore sizes

6.5 Comparison with other Ni electrodes

Mass transfer to a porous electrode can be characterized by three dimensionless parameters, namely the Sherwood (Sh), Reynolds (Re) and Schmidt (Sc) numbers:

$$Sh = \frac{kd_e}{D} \quad 6.3$$

$$Re = \frac{vd_e}{\upsilon} \quad 6.4$$

$$Sc = \frac{\upsilon}{D} \quad 6.5$$

where k is the mass transfer coefficient, d_e is the diameter of the flow channel, D is the diffusion coefficient of electroactive species, υ is the kinematic viscosity of the electrolyte, and v is the superficial or Darcian flow velocity of the electrolyte, which is simply the flow rate divided by the cross sectional area of the sample or the flow channel. In this work, the diameter of the flow channel d_e = 0.6 cm, the diffusion coefficient of ferricyanide ion D = 6×10^{-6} cm^{2}s^{-1} and the kinematic viscosity of the electrolyte υ=9.56×10^{-3} cm^{2}s^{-1} (Recio et al., 2013). It should be noted that in calculating the Sherwood number (Eq. 6.3) for the LCS porous Ni samples, the geometric surface area was used for calculating the mass transfer coefficient, k, instead of the real surface area as in Eq. 6.2. This is to facilitate comparison with other electrode materials, because geometric surface area was often used to characterize the mass transfer performance of different types of electrodes in the literature.

Fig. 6.5a shows the correlations between Sherwood and Reynolds numbers for the LCS porous Ni samples. The Sherwood number increases exponentially with the Reynolds number in the range of 60 – 415. The sample with a low porosity of 0.55 and a large pore size of 1000 – 1500 µm shows the highest Sherwood number (5770 – 40429), while the

sample with a high porosity of 0.75 and a small pore size of 250 – 425 μm shows the lowest Sherwood number (315 – 942). Fig. 6.5b compares the LCS porous Ni electrode with a number of other Ni electrodes and shows that the LCS porous Ni has superior performance in terms of the Sherwood number in a modest range of Reynolds number.

The relationship among the dimensionless parameters at a constant temperature can be expressed as (Taama et al., 1996, Brown et al., 1992, Brown et al., 1993, Griffiths et al., 2005a, Kinoshita and Leach, 1982) :

$$Sh = \alpha Re^{\beta} Sc^{0.33} \qquad 6.6$$

where α is a constant associated with the geometry and surface area of the electrode and β is a constant dependent on the hydrodynamic regime. Constant β is the same as the constant b in Eq. 6.2. Constant α is different from but related to the pre-exponential constant a in Eq. 6.2.

Table 6.1 shows the values of α and β for the LCS porous Ni samples, obtained by fitting the experimental data to equation 6.6. Constant α generally increases with pore size except for two samples. The two exceptions are likely due to the experimental errors or variability. The effect of porosity on constant α shows no clear trend. Constant β increases with increasing pore size but decreases with increasing porosity.

Table 6.2 shows the values of α and β for the LCS porous Ni samples in comparison with various Ni electrodes taken from the literature. The values of constant α of the LCS porous Ni samples are about 100 – 350 times higher than that of the Ni plate (Brown et al., 1993) and about 3 – 8 times higher than those of the Ni foams with a high porosity of 0.97 (Cognet et al., 1995). This is because the LCS porous Ni has a large effective (real) surface area, which

is about one to two orders of magnitude higher than its geometric surface area. For the nanostructured Ni electrode which was reported with a high effective surface area (Recio et al., 2013), the values of constant α are comparable to that of the LCS porous Ni samples

The values of constant β of the LCS porous Ni samples are similar to that of the Ni plate under turbulent flow but higher than that of the Ni plate under laminar flow (Szánto et al., 1996). They are considerably higher than those of the Ni foams (Cognet et al., 1995) and the nanostructured Ni (Recio et al., 2013).

Table. 6. 1 Constants α and β for the porous Ni samples

Porosity / Pore size (μm)	α					β				
	0.55	0.60	0.65	0.70	0.75	0.55	0.60	0.65	0.70	0.75
250 – 425	45.53	40.2	29.28	27.2	30.35	0.84	0.74	0.73	0.67	0.57
425 – 710	48.69	27.31	33.22	44.1	27.17	0.95	0.98	0.86	0.77	0.75
710 – 1000	51.24	-	56.18	61.94	42.94	0.96	-	0.91	0.84	0.81
1000 – 1500	82.63	-	73.85	44.38	47.17	1.03	-	0.99	1.01	0.78

Table. 6. 2 Constants α and β for various electrodes (TP stands for turbulence promoter)

Electrode		Re	α	β
LCS porous Ni	Porosity: 0.55 – 0.75 & Pore size:1000 – 1500 μm	60 – 415	27.17 – 82.63	0.57 – 1.03
Ni plate (Brown et al., 1993, Szánto et al., 1996)	No TP	200 – 1000	0.22	0.71
	With TP		0.74	0.62
	Laminar flow	<2300	2.54	0.33
	Turbulent flow	>2300	0.023	0.8
Ni foam (Cognet et al., 1995)	MN020	30 – 250	10.8	0.28
	MN060		7.1	0.36
	MN100		10.5	0.42
Nano Ni (Recio et al., 2013)	Without a TP	250 – 1000	28.4	0.23
	With a TP		86.2	0.14

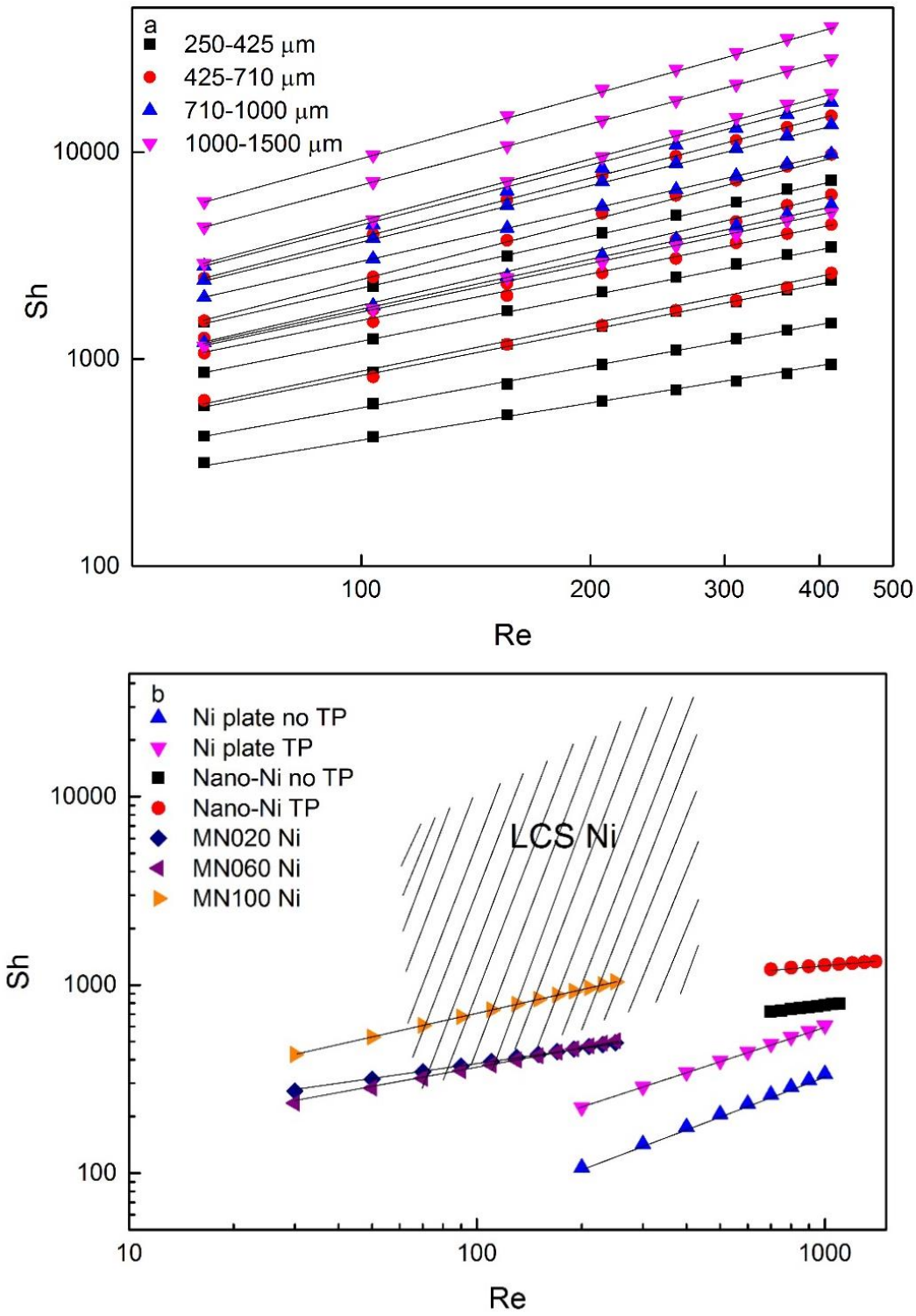

Fig. 6. 5 Correlations between Sherwood and Reynolds numbers for (a) LCS porous Ni samples and (b) various Ni electrodes. For each pore size range in (a), the lines correspond to porosities of 0.55, 0.60, 0.70 and 0.75 (from top to bottom). The legends in (b) designate solid Ni plate in the absence and presence of a TB (Brown et al., 1993), nanostructured Ni in the absence and presence of a TB (Recio et al., 2013), Ni foam MN020, MN060 and MN100 (Cognet et al., 1995).

6.6 Summary

The mass transfer coefficient of the LCS porous nickel samples with a porosity of 0.55-0.75 and a pore size of 250-1500 μm was measured at an electrolyte flow velocity range from 1 to 12 cm/s. The mass transfer coefficient of the LCS porous nickel is in the range 0.0007-0.014 cm/s. It increases with pore size and decreases with porosity. At low flow velocities, the mass transfer coefficient is similar to that of the nickel plate. At high flow velocities, it can be up to 7 times larger than that of the nickel plate due to turbulence. The overall mass transfer performance (kA) of the LCS porous nickel samples is up to 300 times better than the nickel plate. The LCS porous nickel has a higher Sherwood number than many other nickel electrodes in the modest range of Reynolds number, due to its high real surface area and its tortuous porous structure, which promotes turbulent flow.

CHAPTER 7 MEASUREMENT of FERRICYANIDE CONCENTRATION

Porous metals manufactured by the LCS process are expected to be good materials for electrochemical sensors due to their high specific surface areas and excellent mass transfer property. In general, the specific surface area increases with increasing porosity and decreasing pore size, while the mass transfer performance decreases with increasing porosity and decreasing pore size. In order to balance the surface area and mass transfer property, a porous Ni sample with a medium pore size of 425 – 710 μm and a medium porosity of 0.7 was used as the working electrode to measure the concentration of ferricyanide. The porous Ni sample has a volumetric geometric surface area of about 13 cm^{-1}. Two electrochemical sensors with the same LCS porous Ni working electrode, one is a conventional three-electrode electrochemical sensor and another one is a newly-developed limiting current sensor, were used to measure the concentration of ferricyanide. The detection performances of these two electrochemical sensors were compared.

7.1 Three-electrode sensor

Fig. 7.1 shows typical current-potential plots of the porous Ni sample in various concentrations of ferricyanide using the three-electrode sensor. When the concentration of ferricyanide is zero (black line), there is no anodic peak current. As the concentration increases to 0.1 mM, the anodic peak current occurs at a potential of about 0.22 V. The lines with different colours indicate different concentrations. It is obvious that the anodic peak current increases with increasing ferricyanide concentration. According to the Randles–

Sevcik equation (Eq 3.10), the peak current is proportional to the concentration of ferricyanide.

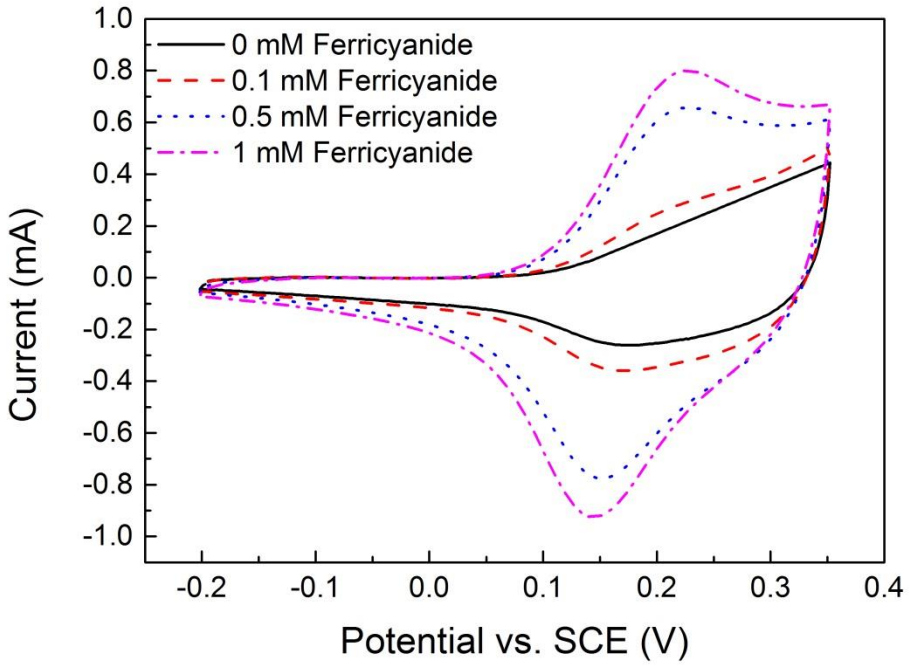

Fig. 7. 1 Typical current-potential plots of a porous Ni sample in various concentrations of ferricyanide using the three-electrode sensor

Fig. 7.2 shows the linear relations between the anodic peak current and the ferricyanide concentration at different scan rates. The solutions with ferricyanide concentrations of 0.1, 0.2, 0.3, 0.4, 0.5, 0.6, 0.7, 0.8, 0.9, 1, 2, 3, 4, 5, 6, 7, 8, 9, 10 mM were prepared for measurement. Higher concentrations, i.e., higher than 10 mM, were not measured because they can be easily measured even by Ni plates. The relations at low concentrations, i.e., lower than 1 mM, are shown as an extended graph at the top-right corner. It is obvious that the same linear relations exist at all concentrations, indicating that the LCS porous Ni sample is applicable to measure the ferricyanide concentration at a wide range of concentration from 0.1 to 10 mM using the three-electrode sensor.

For an electrochemical sensor, the sensitivity and limit of detection (LOD) are two most important parameters. The sensitively of the three-electrode sensor is expressed by the change in the anodic peak current over the change in the ferricyanide concentration and the LOD is determined as the concentration when the signal/noise=3, i.e.,

$$Sensitivity = \frac{change\ in\ the\ anodic\ peak\ current}{change\ in\ the\ concentration} \quad 7.1$$

$$LOD = \frac{3\,\sigma}{sensitivity} \quad 7.2$$

where σ is the standard deviation of the linear regression of the peak current vs concentration curve.

In Fig. 7.2a, the trend line between the anodic peak current (y-axis) and the concentration (x-axis) is expressed as $y = 0.331x + 0.11$. According to Eq. 7.1, the sensitivity should be equal to the value of the slope which is 0.331 mA/mM. The value of the intercept is 0.11, which is an indicator of the background current. The correlation coefficient, R^2, is 0.99957, indicating that the trend line fits the data very well. Comparing Fig. 7.2 (a) – (d) shows that the sensitivity increases with increasing scan rate. The sensitivities at scan rates of 0.005, 0.01, 0.05 and 0.1 V/s are 0.33, 0.50, 1.12 and 1.50 mA/mM, respectively. This can be explained by two reasons. First, according to the Randles–Sevcik equation (Eq 3.10), the anodic peak current generated from a solution at a fixed concentration increases with increasing scan rate. Second, the effective surface area of the porous Ni sample, also known as electroactive surface area, increases with increasing scan rate (as explained in Chapter 5), resulting in a higher anodic peak current. A higher anodic peak current results in a higher sensitivity. Although a higher scan rate provides a higher current and sensitivity, scan rates

higher than 0.1 V/s are normally not used for detection because the effect of the resistance of the solution will be more serious at higher scan rates.

The standard deviations of the linear regressions are 0.0227, 0.0532, 0.202 and 0.290 mA at scan rates of 0.005, 0.01, 0.05 and 0.1 V/s, respectively. Therefore, the LODs of the three-electrode sensor are about 0.21×10^{-4}, 0.32×10^{-4}, 0.54×10^{-4} and 0.58×10^{-4} M at scan rates of 0.005, 0.01, 0.05 and 0.1 V/s, respectively. It is clear that the LOD increases with increasing scan rate. This is because of the effect of increasing measurement noise. A larger noise can result in a higher LOD.

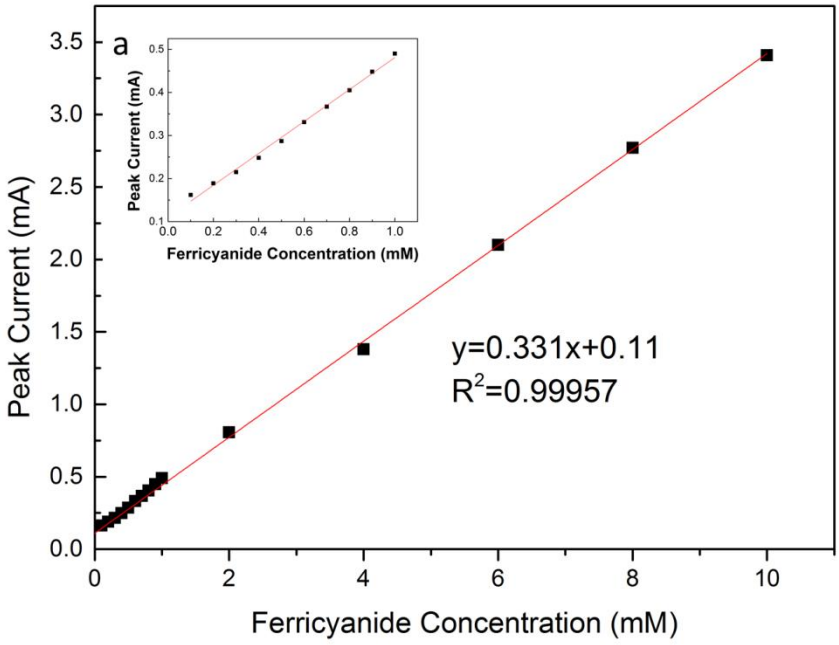

Fig. 7. 2 Relations between anodic peak current and ferricyanide concentration at different scan rates: (a) 0.005 V/s, (b) 0.01 V/s, (c) 0.05 V/s and (d) 0.1 V/s (to be continued)

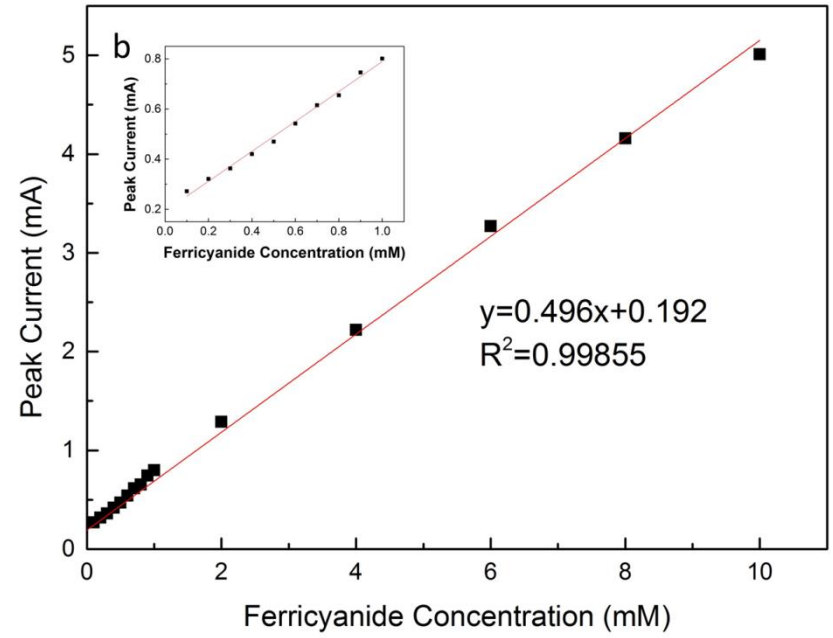

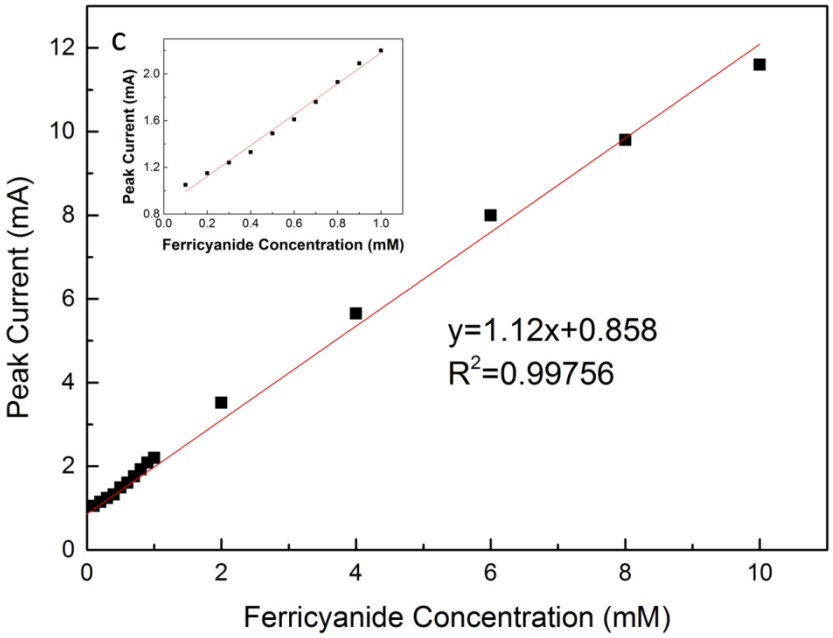

Fig. 7.2 (continued) Relations between anodic peak current and ferricyanide concentration at different scan rates: (a) 0.005 V/s, (b) 0.01 V/s, (c) 0.05 V/s and (d) 0.1 V/s (to be continued).

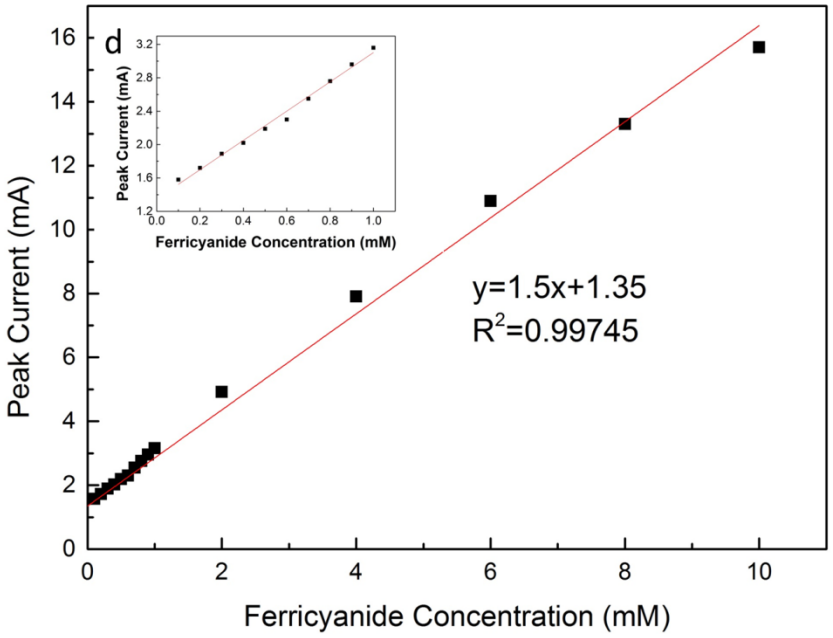

Fig. 7.2 (continued) Relations between anodic peak current and ferricyanide concentration at different scan rates: (a) 0.005 V/s, (b) 0.01 V/s, (c) 0.05 V/s and (d) 0.1 V/s.

7.2 Limiting current sensor

Fig. 7.3 shows typical current-potential plots of the porous Ni sample in various concentrations of ferricyanide using the limiting current sensor. When the concentration of ferricyanide is zero (black line), the limiting current is nearly zero. As the concentration of ferricyanide increases to 0.005 mM, the limiting current becomes distinguishable from the limiting current obtained without ferricyanide. The lines with different colours indicate different concentrations. It is obvious that the limiting current increases with increasing ferricyanide concentration. According to Eq. 3.15, the limiting current is proportional to the concentration of ferricyanide. The determinations of the sensitivity and LOD are similar as those used in the cyclic voltammetry measurement. The sensitivity of the limiting current

sensor is expressed by the change in the limiting current over the change in the ferricyanide concentration,

$$Sensitivity = \frac{change\ in\ the\ limiting\ current}{change\ in\ the\ concentration} \quad 7.3$$

and the LOD is determined by Eq. 7.2.

Fig. 7.4 shows the linear relations between the limiting current and the ferricyanide concentration at different electrolyte flow rates. The solutions with ferricyanide concentrations of 0.005, 0.006, 0.007, 0.008, 0.009, 0.01, 0.02, 0.03, 0.04 , 0.05, 0.06, 0.07, 0.08, 0.09, 0.1, 0.2, 0.3, 0.4, 0.5 mM were prepared for measurement. The relations at low concentrations, i.e., lower than 0.01 mM, are shown as an extended graph at the top-right corner. It is obvious that the same linear relations exist at all concentrations, indicating that the LCS porous Ni sample is applicable to measure the ferricyanide concentration at a wide range of concentration from 0.005 to 0.5 mM using the limiting current sensor.

In Fig. 7.4a, the trend line between the anodic peak current (y-axis) and the concentration (x-axis) is expressed as $y = 7.47x - 0.008$. According to Eq. 7.1, the sensitivity is equal to the value of the slope which is 7.47 mA/mM. The value of the intercept is 0.008, which is an indicator of the background current. The correlation coefficient, R^2, is 0.99957, indicating that the trend line fits the data very well. The sensitivities of the limiting current sensor at flow rates of 16.8, 42 and 84 mL/min are 7.47, 13.35 and 20.24 mA/mM, respectively. The sensitivity increases with increasing flow rate because of two reasons. First, the limiting current increases with increasing electrolyte flow rate, resulting in a higher sensitivity. Second, a higher electrolyte flow rate can result in a more turbulent flow (Diao et al., 2017), which further increases the limiting current and thus sensitivity. Although a higher flow rate

provides a higher limiting current and sensitivity, care should be taken in using high flow rates. Firstly, high flow rates can result in high pressure within the porous samples, which may damage the porous structures. Secondly, high flow rates require large pumping energy, increasing the cost of the measurement.

The standard deviations of the linear regressions are 0.0218, 0.0363 and 0.0361 mA at flow rates of 16.8, 42 and 84 mL/min, respectively. Therefore, the LODs using the linear voltammetry technique are 8.7×10^{-6}, 8.15×10^{-6} and 5.35×10^{-6} M, respectively. It is clear that the LOD decreases with increasing flow rate. As discussed before, a higher flow rate results in a higher sensitivity. According to Eq. 7.2, the LOD decreases with increasing sensitivity.

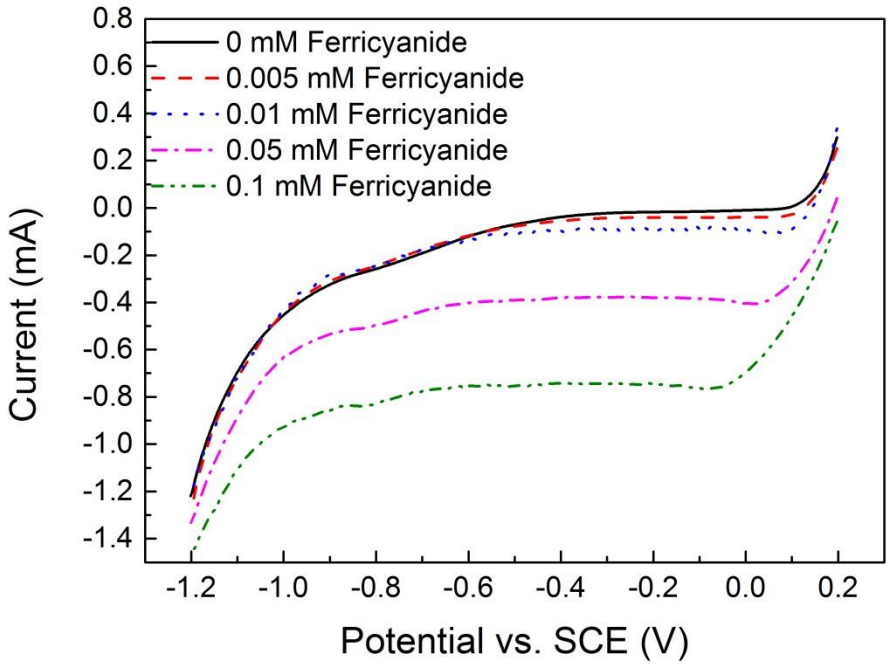

Fig. 7.3 Typical current-potential plots of the porous Ni sample in various concentrations of ferricyanide using the limiting current sensor

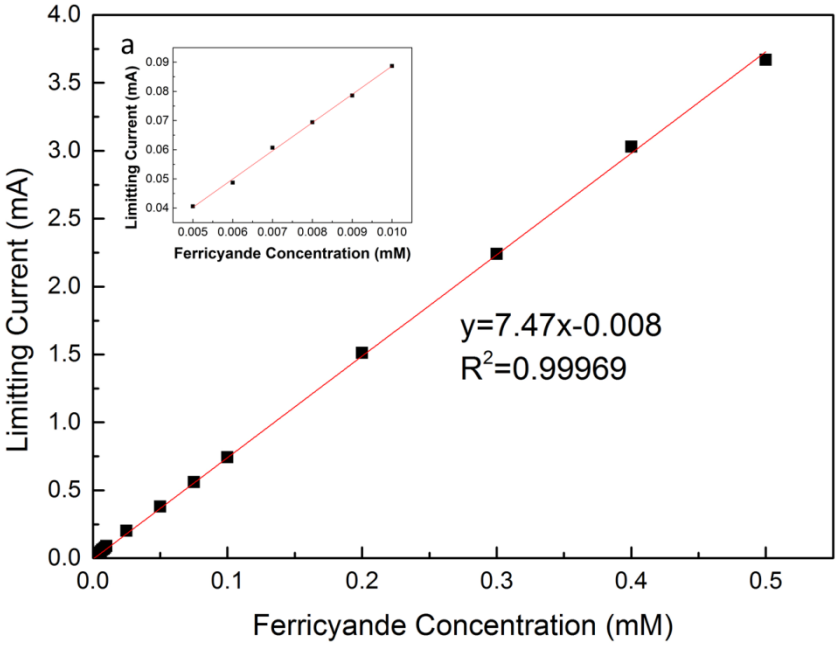

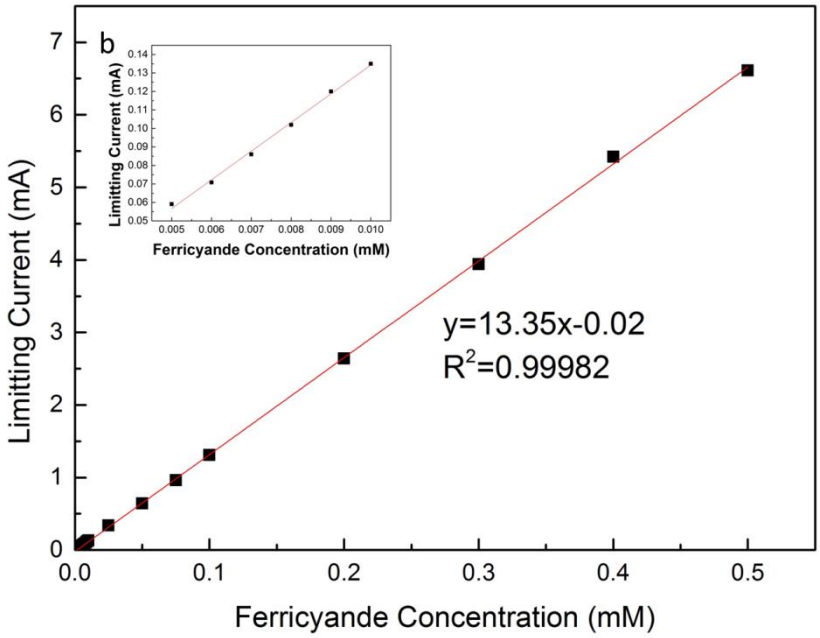

Fig. 7.4 Relations between limiting current and ferricyanide concentration at different electrolyte flow rates of: (a) 16.8 mL/min, (b) 42 mL/min and (c) 84 mL/min.(to be continued)

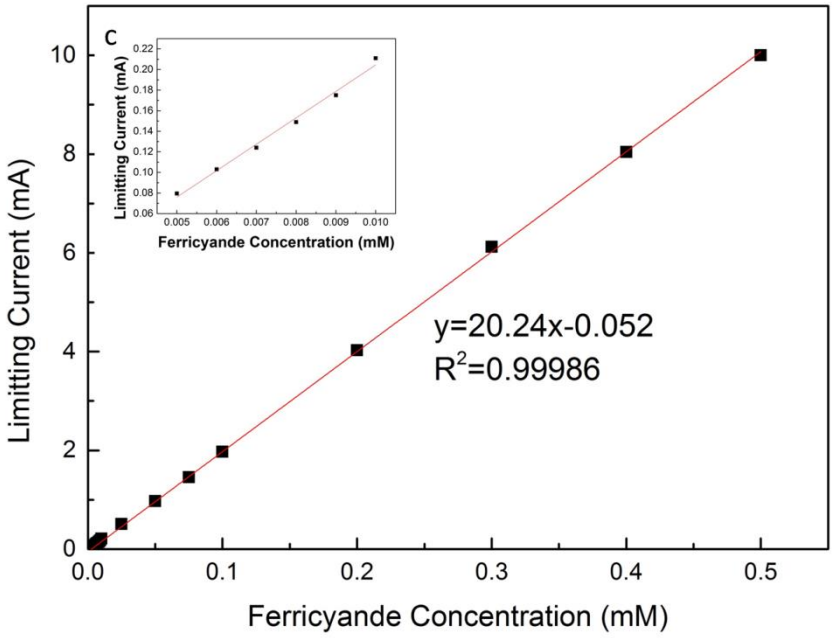

Fig. 7.4 (continued) Relations between limiting current and ferricyanide concentration at different electrolyte flow rates of: (a) 16.8 mL/min, (b) 42 mL/min and (c) 84 mL/min.

7.3 Comparison of three-electrode sensor and limiting current sensor

Table 7.1 shows the performances of the LCS porous Ni sample in the measurement of the concentration of ferricyanide using the two electrochemical sensors. The three-electrode sensor shows LODs of 0.21×10^{-4}, 0.32×10^{-4}, 0.54×10^{-4} and 0.58×10^{-4} M and sensitivities of 0.33, 0.50, 1.12 and 1.5 mA/mM at different scan rates of 0.005, 0.01, 0.05, and 0.1 V/s, respectively. The sensitivity and LOD increase with increasing scan rate and the reasons have been discussed in section 7.1. The limiting current sensor shows LODs of 8.7×10^{-6}, 8.15×10^{-6} and 5.35×10^{-6} M and sensitivities of 7.47, 13.35 and 20.24 mA/mM at flow rates of 16.8, 42 and 84 mL/min, respectively. The LOD of the limiting current sensor is as low as one tenth of the three-electrode sensor and the sensitivity of the limiting current sensor is up to 60 times higher than the three-electrode sensor.

The enhanced performance of the limiting current sensor can be attributed to the forced fluid flow within the porous samples. For the three-electrode electrochemical sensor, the anodic peak current is used to express the ferricyanide concentration. The anodic peak current depends on the mass transfer rate of ferricyanide. A higher mass transfer rate can contribute to a higher anodic peak current. As the three-electrode sensor measures the ferricyanide concentration in a static condition, the mass transfer process mainly includes diffusion of ferricyanide. For the limiting current sensor, the limiting current is used to express the ferricyanide concentration. The limiting current also depends on the mass transfer rate of ferricyanide. As the limiting current sensor measures the ferricyanide concentration in a dynamic condition, the mass transfer process includes not only diffusion but also convection, resulting in much higher limiting currents and thus higher sensitivities and lower LODs.

Table. 7. 1 Comparison of ferricyanide detection performance between the three-electrode sensor and limiting current sensor

Technique			LOD (M)	Sensitivity (mA/mM)
Three-electrode sensor	**Scan rate** (V/s)	0.005	0.21×10^{-4}	0.33
		0.01	0.32×10^{-4}	0.50
		0.05	0.54×10^{-4}	1.12
		0.1	0.58×10^{-4}	1.50
Limiting current senor	**Flow rate** (mL/min)	16.8	8.7×10^{-6}	7.47
		42	8.15×10^{-6}	13.35
		84	5.35×10^{-6}	20.24

7.4 Comparison with other sensor materials

Table 7.2 shows the ferricyanide detection performance of various materials, including the LCS porous Ni, glassy carbon electrode and carbon paste electrode. For the LCS porous Ni, two electrochemical sensors were used to detect the concentration of ferricyanide. While only three-electrode sensor was used for other materials. For the three-electrode sensor with the LCS porous Ni working electrode, the LOD and sensitivity are in the ranges of $0.21 \times 10^{-4} - 0.58 \times 10^{-4}$ M and $0.33 - 1.50$ mA/mM, respectively. For the limiting current sensor with the LCS porous Ni working electrode, the LOD and sensitivity are in the ranges of $5.35 \times 10^{-6} - 8.7 \times 10^{-6}$ M and $7.47 - 20.24$ mA/mM, respectively.

Perenlei et al. (2011) used a glassy carbon electrode with modified surface to measure the concentration of ferricyanide using the three-electrode sensor. The modified glassy carbon electrode has a LOD of $4.86 \times 10^{-5} - 1.1 \times 10^{-6}$ M and a sensitivity of 0.0776 mA/mM. The LOD has a large range, with its upper limit and lower limit in the same order of magnitude as those of the LCS porous Ni in three-electrode sensor and limiting current sensor, receptivity. The sensitivity of the modified glassy carbon electrode is one order of magnitude smaller than that of the LCS porous Ni using the three-electrode sensor and two orders of magnitude smaller than that of the LCS porous Ni using limiting current sensor.

Niranjana et al. (2009) and (Pandurangachar et al., 2010) used modified carbon paste electrodes to measure the concentration of ferricyanide using the three-electrode sneor. The LODs of the carbon paste electrodes are about 10^{-4} M, which is similar to that of the LCS porous Ni using the three-electrode sensor. The sensitivities of the carbon paste electrodes are one order of magnitude smaller than that of the LCS porous Ni using the three-electrode sensor.

The excellent detection performance of the LCS porous Ni can be attributed to its high specific surface area and tortuous porous structure. For the three-electrode sensor, the high specific surface area provides more reaction sites for the oxidation of ferricyanide, resulting in a high peak current and thus higher sensitivity. For the limiting current sensor, the tortuous structure leads to a high turbulence flow within porous sample, increasing the limiting current and improving the sensitivity. The limiting current sensor is expected to be suitable for many other sensor materials.

Table. 7. 2 Ferricyanide detection performance of various materials

Material	**LOD (M)**	**Sensitivity** (mA/mM)
LCS Ni[1] (This work)	5.35×10^{-6} – 8.7×10^{-6}	7.47 – 20.24
LCS Ni[2] (This work)	0.21×10^{-4} – 0.58×10^{-4}	0.33 – 1.50
Glassy Carbon Electrode[2] (Perenlei et al., 2011)	4.86×10^{-5} – 1.1×10^{-6}	0.0776
Carbon Paste Electrode[2] (CV)(Niranjana et al., 2009)	10^{-4}	0.0233
Carbon Paste Electrode[2] (Pandurangachar et al., 2010)	10^{-4}	0.012

[1]means the limiting current sensor and [2] means the three-electrode sensor

CHAPTER 8 CONCLUSIONS AND FUTURE WORK

8.1 Conclusions

8.1.1 Surface area of LCS porous Cu

The geometric surface area of porous Cu is the surface area of the primary pores only. The volumetric and gravimetric specific geometric surface areas of the porous Cu samples with porosities in the range of 0.5 – 0.8 and pore sizes in the range of 250 – 500 μm measured by the quantitative stereology method are in the ranges of 20 – 100 cm^{-1} and 5 – 50 cm^2/g, respectively. Both volumetric and gravimetric specific geometric surface areas increase with porosity but decrease with increasing pore size.

The electroactive surface area of porous Cu includes the contributions from the primary pores and some of the interstices between the Cu particles. The volumetric specific electroactive surface area of the porous Cu samples was measured by the cyclic voltammetry peak current method using two different reactions. The electroactive surface area depends on the reaction being considered and the diffusion layer thickness associated with the reaction. A thinner diffusion layer results in a higher electroactive surface area. By decreasing the diffusion layer from 50 μm to 1 μm, the electroactive surface area is nearly doubled. The particle size of the Cu powder used to manufacture the LCS porous Cu has a modest effect on the electroactive surface area, with the medium particle sizes, 20 – 45 μm or 45 – 75 μm, showing the highest electroactive surface areas. Increasing sintering temperature from 850˚C to 950˚C and using chemical etching can reduce the electroactive surface area of the LCS porous Cu samples up to 70% and 30%, respectively.

The real surface area includes the surface areas of the primary pores, interstices between the Cu particles and even the surface features on the Cu particles at a small length scale. The volumetric real surface area of the porous Cu samples was measured by the cyclic voltammetry double layer capacitance method. Like the volumetric electroactive surface area, the volumetric real surface area varies with Cu particle size. The porous Cu samples manufactured using the medium particle sizes 20 – 45 μm and 45 – 75 μm show the highest volumetric specific real surface areas. Increasing sintering temperature from 850˚C to 950˚C and using chemical etching can reduce the real surface area about 50% and 11%, respectively.

8.1.2 Surface area of LCS porous Ni

The volumetric and gravimetric specific geometric surface areas of the LCS porous Ni samples with porosities in the ranges of 0.5 – 0.85 and pore sizes in the range of 250 – 1500 μm are in the ranges of 20 – 100 cm^{-1} and 5 – 60 cm^2/g, respectively. Like the geometric surface areas of the LCS porous Cu, the volumetric and gravimetric specific geometric surface areas increase with porosity but decrease with pore size. The Ni particle size and the matrix material have little effect on the geometric surface areas.

The volumetric specific electroactive surface area of the LCS porous Ni samples measured at scan rates of 0.005, 0.01 and 0.05 V/s are in the ranges of 30 – 60 cm^{-1}, 40 – 80 cm^{-1} and 50 – 120 cm^{-1}, respectively. The electroactive surface area increases with increasing scan rate or decreasing diffusion layer thickness. The electroactive surface area was further found to be dependent on the ratio between the diffusion layer thickness and the pore size. When the diffusion layer thickness is much smaller than the pore size, the electroactive surface area is much larger than the geometric surface area. When the diffusion layer thickness is

comparable to the pore size, the electroactive surface area becomes similar to or even smaller than the geometric surface area because of large surface curvature. The samples manufactured using the Ni powder of 25 μm particles show the highest electroactive surface area.

The volumetric specific real surface area of the LCS porous Ni is in the range of 200 – 1600 cm^{-1}. It decreases with increasing porosity and pore size. The LCS porous Ni samples manufactured using 25 μm Ni particles show the highest real surface areas.

8.1.3 Mass transfer coefficient of LCS porous Ni

The mass transfer coefficient of the LCS porous Ni samples with porosities of 0.55 – 0.75 and pore sizes of 250 – 1500 μm was measured at electrolyte flow velocities of 1 – 12 cm/s. The mass transfer coefficient of the LCS porous Ni samples is in the range of 0.0007 – 0.0014 cm/s. It increases with pore size but decreases with porosity. At low flow velocities, the mass transfer coefficient is similar to that of the Ni plate. At high flow velocities, it can be up to 7 times larger than that of the Ni plate due to turbulence. As the real surface area of the LCS porous Ni is about 50 times larger than that of the Ni plate, the overall mass transfer performance, determined either by the product of mass transfer coefficient and real surface area(kA) or the limiting current of the LCS porous Ni samples, is up to 300 times better than the Ni plate. This work has also compared the mass transfer properties of various materials and found that the LCS porous Ni has higher Sherwood numbers than many other Ni electrodes in the modest range of Reynolds number, due to its high real surface area and its tortuous porous structure, which promotes turbulent flow.

8.1.4 Ferricyanide detection

A LCS porous Ni sample with a porosity of 0.7 and pore size of 425 – 710 μm has been used to measure the concentration of ferricyanide using two electrochemical sensors. The three-electrode electrochemical sensor shows a limit of detection of $0.21 \times 10^{-4} - 0.58 \times 10^{-4}$ M and a sensitivity of 0.33 – 1.50 mM/mA. The limit of detection increases with increasing scan rate because the measurement noise increases, and the sensitivity increases with increasing scan rate because the peak current increases with scan rate. The limiting current sensor shows a much lower limit of detection of $5.35 \times 10^{-6} - 8.7 \times 10^{-6}$ M and a much higher sensitivity of 7.47 – 20.24 mM/mA. The limit of detection decreases with increasing electrolyte flow rate, and the sensitivity in the linear voltammetry measurement increases with increasing electrolyte flow rate because a higher electrolyte flow rate contributes to a higher limiting current. The enhanced performance of the limiting current sensor compared with the three-electrode sensor is mainly due to the turbulent fluid flow through the porous matrix. It is worth mentioning that this is the first time to develop the limiting current sensor. This technique has shown much improved performance compared with the cyclic voltammetry peak current technique. Also, this work has proved that the LCS porous Ni has potentials in electrochemical detection.

8.2 Future work

8.21 Surface area measurements

The porous Cu and Ni manufactured by the LCS process have been proved to be good electrode materials in electrochemical detection due to their high specific surface areas and excellent mass transfer performance. Other porous metals, e.g., Fe, Al, Ti may also have potentials in some electrochemical applications. Therefore, surface area measurements are

required for these porous metals. Their surface areas can also be measured by the same methods.

The effects of sintering temperature, particle size, and chemical etching on the surface areas of porous metals have been studied. The other process parameters, e.g. compaction pressure and potassium carbonate shape, in the LCS manufacturing process may also have significant effects on the surface areas. Future work is required to study the effects of compaction pressure and potassium carbonate shape on the surface areas of the LCS porous metals.

Porous metals manufactured by different processes have different structures and therefore different surface areas. It is therefore important to study the effect of manufacturing process, e.g. loose sintering, selective laser melting or electrodeposition, on the surface areas of porous metals. Future work can be carried out to compare the surface areas of the porous metals manufactured by these processes.

8.2.2 Mass transfer characterization

The mass transfer coefficient of porous Ni manufactured by the LCS process has been studied by the limiting current technique. The effects of porosity and pore size have also been studied. However, other factors, e.g., particle size, sintering temperature and pore shape, can also affect the porous structures and further change the mass transfer property. Therefore, the effects of these factors need to be studied.

The mass transfer coefficient of porous Cu cannot be measured by the limiting current technique using the same electrolyte. To study the mass transfer performance of porous Cu,

a methanol reformation cell is needed to measure the conversional percentage of methanol needs to be measured.

Porous metals manufactured by different processes have different porous structures and are expected to have different mass transfer coefficients. Future work can be carried out to compare the mass transfer performance of porous metals manufactured by LCS, loose sintering, selective laser melting and electrodeposition processes.

8.2.3 Electrochemical sensor applications

Porous Ni manufactured by the LCS process has shown outstanding performance in measuring the concentrations of ferricyanide due to its high surface area and excellent mass transfer property. The LCS porous Ni is expected to have great potential in detecting other ions and molecules. Future work can explore the applicability of the LCS porous metals in various ions and molecules detection.

REFERENCES

ABO-HAMAD, A., ALSAADI, M. A., HAYYAN, M., JUNEIDI, I. & HASHIM, M. A. 2016. Ionic liquid-carbon nanomaterial hybrids for electrochemical sensor applications: a review. *Electrochimica Acta,* 193**,** 321-343.

AKHTAR, N., EL-SAFTY, S. A., KHAIRY, M. & EL-SAID, W. A. 2015. Fabrication of a highly selective nonenzymatic amperometric sensor for hydrogen peroxide based on nickel foam/cytochrome c modified electrode. *Sensors and Actuators B: Chemical,* 207**,** 158-166.

AMATORE, C. 1995. Electrochemistry at ultramicroelectrodes. *Physical Electrochemistry: Principles, Methods and Applications,* 4**,** 131-208.

AMATORE, C., SZUNERITS, S., THOUIN, L. & WARKOCZ, J.-S. 2001. The real meaning of Nernst's steady diffusion layer concept under non-forced hydrodynamic conditions. A simple model based on Levich's seminal view of convection. *Journal of electroanalytical chemistry,* 500**,** 62-70.

AMBROSE, J., BARRADAS, R. & SHOESMITH, D. 1973. Investigations of copper in aqueous alkaline solutions by cyclic voltammetry. *Journal of Electroanalytical Chemistry and Interfacial Electrochemistry,* 47**,** 47-64.

ANTOHE, B., LAGE, J., PRICE, D. & WEBER, R. M. 1996. Numerical characterization of micro heat exchangers using experimentally tested porous aluminum layers. *International Journal of Heat and Fluid Flow,* 17**,** 594-603.

ARVIA, A., MARCHIANO, S. & PODESTA, J. J. 1967. The diffusion of ferrocyanide and ferricyanide ions in aqueous solutions of potassium hydroxide. *Electrochimica Acta,* 12**,** 259-266.

ASHBY, M. F., EVANS, T., FLECK, N. A., HUTCHINSON, J., WADLEY, H. & GIBSON, L. 2000. *Metal foams: a design guide*, Elsevier.

ASHBY, M. F. & MEDALIST, R. M. 1983. The mechanical properties of cellular solids. *Metallurgical Transactions A,* 14**,** 1755-1769.

AVALOS GAUNA, E. & ZHAO, Y. 2016. Numerical simulation of heat transfer in porous metals for cooling applications. *Metallurgical and Materials Transactions B,* 48**,** 1925–1932.

BABCSÁN, N., LEITLMEIER, D. & DEGISCHER, H.-P. 2003. Foamability of particle reinforced aluminum melt. *Materialwissenschaft und Werkstofftechnik,* 34**,** 22-29.

BANHART, J. 2001. Manufacture, characterisation and application of cellular metals and metal foams. *Progress in materials science,* 46**,** 559-632.

BANHART, J., ASHBY, M. F. & FLECK, N. A. 1999. Metal foams and porous metal structures. *Proc. MetFoam,* 99.

BANHART, J. & SYMPOSIUM, M. F. 1998. *Metal foams: Fraunhofer USA Symposium" Metal Foam" Symposium, Stanton, Delaware, 7-8 October 1997*, MIT.

BARBIR, F. 2005. PEM electrolysis for production of hydrogen from renewable energy sources. *Solar energy,* 78**,** 661-669.

BARD, A. J., FAULKNER, L. R., LEDDY, J. & ZOSKI, C. G. 1980. *Electrochemical methods: fundamentals and applications,* New York, Wiley

BARNES, E. O., CHEN, X., LI, P. & COMPTON, R. G. 2014. Voltammetry at porous electrodes: A theoretical study. *Journal of Electroanalytical Chemistry,* 720**,** 92-100.

BAZAN, J. & ARVIA, A. 1965. The diffusion of ferro-and ferricyanide ions in aqueous solutions of sodium hydroxide. *Electrochimica Acta,* 10**,** 1025-1032.

BIDAULT, F., BRETT, D., MIDDLETON, P., ABSON, N. & BRANDON, N. 2009. A new application for nickel foam in alkaline fuel cells. *international journal of hydrogen energy,* 34**,** 6799-6808.

BOOMSMA, K. & POULIKAKOS, D. 2001. On the effective thermal conductivity of a three-dimensionally structured fluid-saturated metal foam. *International Journal of Heat and Mass Transfer,* 44**,** 827-836.

BROWN, C., PLETCHER, D., WALSH, F., HAMMOND, J. & ROBINSON, D. 1992. Local mass transport effects in the FM01 laboratory electrolyser. *Journal of Applied Electrochemistry,* 22**,** 613-619.

BROWN, C., PLETCHER, D., WALSH, F., HAMMOND, J. & ROBINSON, D. 1993. Studies of space-averaged mass transport in the FM01-LC laboratory electrolyser. *Journal of applied electrochemistry,* 23**,** 38-43.

BROWNLEE, B. J., MARR, K. M., CLAUSSEN, J. C. & IVERSON, B. D. 2017. Improving sensitivity of electrochemical sensors with convective transport in free-standing, carbon nanotube structures. *Sensors and Actuators B: Chemical,* 246**,** 20-28.

CARLSSON, L., SANDEGREN, B., SIMONSSON, D. & RIHOVSKY, M. 1983. Design And Performance Of A Modular, Multi‐Purpose Electrochemical Reactor. *Journal of the Electrochemical Society,* 130**,** 342-346.

CHEN, R. & ZHAO, T. 2007a. A novel electrode architecture for passive direct methanol fuel cells. *Electrochemistry Communications,* 9**,** 718-724.

CHEN, R. & ZHAO, T. 2007b. Porous current collectors for passive direct methanol fuel cells. *Electrochimica Acta,* 52**,** 4317-4324.

CHUNG, S.-H. & MANTHIRAM, A. 2013. Lithium–sulfur batteries with superior cycle stability by employing porous current collectors. *Electrochimica Acta,* 107**,** 569-576.

COGNET, P., BERLAN, J., LACOSTE, G., FABRE, P.-L. & JUD, J.-M. 1995. Application of metallic foams in an electrochemical pulsed flow reactor Part I: Mass transfer performance. *Journal of applied electrochemistry,* 25**,** 1105-1112.

COMPTON, R. G. & BANKS, C. E. 2007. *Understanding voltammetry*, World Scientific.

DAI, Z., NAWAZ, K., PARK, Y., CHEN, Q. & JACOBI, A. 2012. A comparison of metal-foam heat exchangers to compact multilouver designs for air-side heat transfer applications. *Heat Transfer Engineering,* 33**,** 21-30.

DAVIES, G. & ZHEN, S. 1983. Metallic foams: their production, properties and applications. *Journal of Materials Science,* 18**,** 1899-1911.

DAVIES, T. J. & COMPTON, R. G. 2005. The cyclic and linear sweep voltammetry of regular and random arrays of microdisc electrodes: Theory. *Journal of Electroanalytical Chemistry,* 585**,** 63-82.

DAVIES, T. J., WARD-JONES, S., BANKS, C. E., DEL CAMPO, J., MAS, R., MUNOZ, F. X. & COMPTON, R. G. 2005. The cyclic and linear sweep voltammetry of regular arrays of microdisc electrodes: fitting of experimental data. *Journal of Electroanalytical Chemistry,* 585**,** 51-62.

DELAHAY, P. 1954. *New Instrumental Methods in Electrochemistry: Theory, Instrumentation, and Applications to Analytical and Physical Chemistry. With a Chapter on High-frequency Methods*, Interscience Publishers.

DELAHAY, P. 1956. New instrumental methods in electrochemistry. JSTOR.

DELAHAY, P., REILLEY, C. N. & KOLTHOFF, I. M. 1954. *New instrumental methods in electrochemistry: theory, instrumentation, and applications to analytical and physical chemistry*, Interscience Publishers New York.

DESPOIS, J.-F. & MORTENSEN, A. 2005. Permeability of open-pore microcellular materials. *Acta Materialia,* 53**,** 1381-1388.
DIAO, K., ZHANG, L. & ZHAO, Y. 2017. Measurement of tortuosity of porous Cu using a diffusion diaphragm cell. *Measurement,* 110**,** 335–338.
DIAO, K. K., XIAO, Z. & ZHAO, Y. Y. 2015. Specific surface areas of porous Cu manufactured by Lost Carbonate Sintering: Measurements by quantitative stereology and cyclic voltammetry. *Materials Chemistry and Physics,* 162**,** 571-579.
DILLON, R., SRINIVASAN, S., ARICO, A. & ANTONUCCI, V. 2004. International activities in DMFC R&D: status of technologies and potential applications. *Journal of Power Sources,* 127**,** 112-126.
ĐUKIĆ, A., ALAR, V., FIRAK, M. & JAKOVLJEVIĆ, S. 2013. A significant improvement in material of foam. *Journal of Alloys and Compounds,* 573**,** 128-132.
DUNN, S. 2002. Hydrogen futures: toward a sustainable energy system. *International journal of hydrogen energy,* 27**,** 235-264.
DYER, C. K. 2002. Fuel cells for portable applications. *Fuel Cells Bulletin,* 2002**,** 8-9.
EISENMANN, M. 1998. Metal powder technologies and applications. *ASM Handbook,* 7**,** 1031.
ETACHERI, V., MAROM, R., ELAZARI, R., SALITRA, G. & AURBACH, D. 2011. Challenges in the development of advanced Li-ion batteries: a review. *Energy & Environmental Science,* 4**,** 3243-3262.
GAGNON, E. 1976. Determination of the double-layer capacity of porous nickel in KOH in the presence of faradaic current. *Journal of Applied Electrochemistry,* 6**,** 95-98.
GANESH, V., LAKSHMINARAYANAN, V. & PITCHUMANI, S. 2005. Assessment of liquid crystal template deposited porous nickel as a supercapacitor electrode material. *Electrochemical and Solid-State Letters,* 8**,** A308-A312.
GERGELY, V. & CLYNE, T. 2004. Drainage in standing liquid metal foams: modelling and experimental observations. *Acta Materialia,* 52**,** 3047-3058.
GOODENOUGH, J. B. & KIM, Y. 2009. Challenges for rechargeable Li batteries. *Chemistry of materials,* 22**,** 587-603.
GOODENOUGH, J. B. & PARK, K.-S. 2013. The Li-ion rechargeable battery: a perspective. *Journal of the American Chemical Society,* 135**,** 1167-1176.
GOSPODINOVA, N., MOKREVA, P. & TERLEMEZYAN, L. 1993. Chemical oxidative polymerization of aniline in aqueous medium without added acids. *Polymer,* 34**,** 2438-2439.
GRDEŃ, M., ALSABET, M. & JERKIEWICZ, G. 2012. Surface science and electrochemical analysis of nickel foams. *ACS applied materials & interfaces,* 4**,** 3012-3021.
GRIFFITHS, M., DE LEÓN, C. P. & WALSH, F. C. 2005a. Mass transport in the rectangular channel of a filter-press electrolyzer (the FM01-LC reactor). *AIChE Journal,* 51**,** 682-687.
GRIFFITHS, M., DE LEÓN, C. P. & WALSH, F. C. 2005b. Mass transport in the rectangular channel of a filter‐press electrolyzer (the FM01‐LC reactor). *AIChE Journal,* 51**,** 682-687.
GRIGORIEV, S., MILLET, P., VOLOBUEV, S. & FATEEV, V. 2009. Optimization of porous current collectors for PEM water electrolysers. *International Journal of Hydrogen Energy,* 34**,** 4968-4973.
HAMNETT, A. 1997. Mechanism and electrocatalysis in the direct methanol fuel cell. *Catalysis Today,* 38**,** 445-457.

HAMPSON, N., LEE, J. & MACDONALD, K. 1972. Oxidations at copper electrodes: Part 41. The oxidation of α-amino acids. *Journal of Electroanalytical Chemistry and Interfacial Electrochemistry,* 34**,** 91-99.

HAN, L., ZHANG, S., HAN, L., YANG, D.-P., HOU, C. & LIU, A. 2014. Porous gold cluster film prepared from Au@ BSA microspheres for electrochemical nonenzymatic glucose sensor. *Electrochimica acta,* 138**,** 109-114.

HANUSA, H. G. 1970. Reticular structures and methods of producing same. Google Patents.

HAYNES, W. M. 2014. *CRC handbook of chemistry and physics*, CRC press.

HEINZEL, A. & BARRAGAN, V. 1999. A review of the state-of-the-art of the methanol crossover in direct methanol fuel cells. *Journal of Power Sources,* 84**,** 70-74.

HOLLANDER, D., WIRTZ, T., WALTER, M. V., LINKER, R., SCHULTHEIS, A. & PAAR, O. 2003. Development of individual three-dimensional bone substitutes using “selective laser melting”. *European Journal of Trauma,* 29**,** 228-234.

HUANG, X., TU, J., XIA, X., WANG, X. & XIANG, J. 2008. Nickel foam-supported porous NiO/polyaniline film as anode for lithium ion batteries. *Electrochemistry Communications,* 10**,** 1288-1290.

IMWINKELRIED, T. 2007. Mechanical properties of open‐pore titanium foam. *Journal of biomedical materials research Part A,* 81**,** 964-970.

INCROPERA, F. P., LAVINE, A. S., BERGMAN, T. L. & DEWITT, D. P. 2007. *Fundamentals of heat and mass transfer*, Wiley.

ITO, H., MAEDA, T., NAKANO, A., HWANG, C. M., ISHIDA, M., KATO, A. & YOSHIDA, T. 2012. Experimental study on porous current collectors of PEM electrolyzers. *International journal of hydrogen energy,* 37**,** 7418-7428.

JIN, I., KENNY, L. D. & SANG, H. 1990. Method of producing lightweight foamed metal. Google Patents.

JIN, I., KENNY, L. D. & SANG, H. 1992. Stabilized metal foam body. Google Patents.

JIN, Z., HAN, S.-Y., ZHANG, L., ZHENG, S.-P., WANG, Y. & LIN, Y. 2013. Combined utilization of lipase-displaying Pichia pastoris whole-cell biocatalysts to improve biodiesel production in co-solvent media. *Bioresource technology,* 130**,** 102-109.

KAMARUDIN, S. K., ACHMAD, F. & DAUD, W. R. W. 2009. Overview on the application of direct methanol fuel cell (DMFC) for portable electronic devices. *International Journal of hydrogen energy,* 34**,** 6902-6916.

KENNEDY, A. 2012. *Porous metals and metal foams made from powders*, INTECH Open Access Publisher.

KHAYARGOLI, P., LOYA, V., LEFEBVRE, L. & MEDRAJ, M. The impact of microstructure on the permeability of metal foams. CSME forum, 2004. 220-228.

KINOSHITA, K. & LEACH, S. 1982. Mass‐Transfer Study of Carbon Felt, Flow‐Through Electrode. *Journal of The Electrochemical Society,* 129**,** 1993-1997.

KONOPKA, S. & MCDUFFIE, B. 1970. Diffusion coefficients of ferri-and ferrocyanide ions in aqueous media, using twin-electrode thin-layer electrochemistry. *Analytical Chemistry,* 42**,** 1741-1746.

KUMAR, A. & REDDY, R. G. 2003. Polymer electrolyte membrane fuel cell with metal foam in the gas flow-field of bipolar/end plates. *Journal of New Materials for Electrochemical Systems,* 6**,** 231-236.

KUNG, C.-W., CHENG, Y.-H. & HO, K.-C. 2014. Single layer of nickel hydroxide nanoparticles covered on a porous Ni foam and its application for highly sensitive non-enzymatic glucose sensor. *Sensors and Actuators B: Chemical,* 204**,** 159-166.

LANGLOIS, S. & COEURET, F. 1989. Flow-through and flow-by porous electrodes of nickel foam. II. Diffusion-convective mass transfer between the electrolyte and the foam. *Journal of applied electrochemistry,* 19**,** 51-60.
LAPTEV, A., BRAM, M., BUCHKREMER, H. & STÖVER, D. 2004. Study of production route for titanium parts combining very high porosity and complex shape. *Powder metallurgy,* 47**,** 85-92.
LEFEBVRE, L. P., BANHART, J. & DUNAND, D. C. 2008. Porous metals and metallic foams: current status and recent developments. *Advanced engineering materials,* 10**,** 775-787.
LEITLMEIER, D., DEGISCHER, H. P. & FLANKL, H. J. 2002. Development of a foaming process for particulate reinforced aluminum melts. *Advanced Engineering Materials,* 4**,** 735-740.
LEWANDOWSKI, A., JAKOBCZYK, P. & GALINSKI, M. 2012. Capacitance of electrochemical double layer capacitors. *Electrochimica Acta,* 86**,** 225-231.
LI, C. W., CISTON, J. & KANAN, M. W. 2014. Electroreduction of carbon monoxide to liquid fuel on oxide-derived nanocrystalline copper. *Nature,* 508**,** 504-507.
LI, R., SHI, Y., WANG, Z., WANG, L., LIU, J. & JIANG, W. 2010. Densification behavior of gas and water atomized 316L stainless steel powder during selective laser melting. *Applied surface science,* 256**,** 4350-4356.
LI, Y., SONG, Y.-Y., YANG, C. & XIA, X.-H. 2007. Hydrogen bubble dynamic template synthesis of porous gold for nonenzymatic electrochemical detection of glucose. *Electrochemistry Communications,* 9**,** 981-988.
LI, Z., CHEN, Y., XIN, Y. & ZHANG, Z. 2015. Sensitive electrochemical nonenzymatic glucose sensing based on anodized CuO nanowires on three-dimensional porous copper foam. *Scientific reports,* 5.
LINXI, Z., QUANZHAN, Y., GUIRONG, Z., FANGXIN, Z., GANG, S. & BO, Y. 2014. Additive manufacturing technologies of porous metal implants. *China Foundry,* 11**,** 322-331.
LIU, C., LEE, H., CHANG, Y.-H. & FENG, S.-P. 2016. The study of electrical conductivity and diffusion behavior of water-based and ferro/ferricyanide-electrolyte-based alumina nanofluids. *Journal of colloid and interface science,* 469**,** 17-24.
LIU, P. & LIANG, K. 2001. Review Functional materials of porous metals made by P/M, electroplating and some other techniques. *Journal of Materials Science,* 36**,** 5059-5072.
LOUVIS, E., FOX, P. & SUTCLIFFE, C. J. 2011. Selective laser melting of aluminium components. *Journal of Materials Processing Technology,* 211**,** 275-284.
LU, G., LIU, F. & WANG, C.-Y. 2005. Water transport through Nafion 112 membrane in DMFCs. *Electrochemical and Solid-State Letters,* 8**,** A1-A4.
LU, T., STONE, H. & ASHBY, M. 1998. Heat transfer in open-cell metal foams. *Acta Materialia,* 46**,** 3619-3635.
LU, W., QIN, X., ASIRI, A. M., AL-YOUBI, A. O. & SUN, X. 2013. Ni foam: a novel three-dimensional porous sensing platform for sensitive and selective nonenzymatic glucose detection. *Analyst,* 138**,** 417-420.
ŁUKOMSKA, A. & SOBKOWSKI, J. 2004. Potential of zero charge of monocrystalline copper electrodes in perchlorate solutions. *Journal of Electroanalytical Chemistry,* 567**,** 95-102.
MANGALICK, M. C. 1977. Gas injection method. Google Patents.

MAROZZI, C. & CHIALVO, A. 2000. Development of electrode morphologies of interest in electrocatalysis. Part 1: Electrodeposited porous nickel electrodes. *Electrochimica Acta,* 45**,** 2111-2120.

MOLIN, S., KUSZ, B., GAZDA, M. & JASINSKI, P. 2008. Evaluation of porous 430L stainless steel for SOFC operation at intermediate temperatures. *Journal of Power sources,* 181**,** 31-37.

MOLINA, A., GONZÁLEZ, J. N., MARTÍNEZ-ORTIZ, F. & COMPTON, R. G. 2010. Geometrical insights of transient diffusion layers. *The Journal of Physical Chemistry C,* 114**,** 4093-4099.

MOND, L., LANGER, C. & QUINCKE, F. 1890. L.—Action of carbon monoxide on nickel. *Journal of the Chemical Society, Transactions,* 57**,** 749-753.

MULLEN, L., STAMP, R. C., BROOKS, W. K., JONES, E. & SUTCLIFFE, C. J. 2009. Selective Laser Melting: A regular unit cell approach for the manufacture of porous, titanium, bone in‐growth constructs, suitable for orthopedic applications. *Journal of Biomedical Materials Research Part B: Applied Biomaterials,* 89**,** 325-334.

MYERS, R. E. 1986. Chemical oxidative polymerization as a synthetic route to electrically conducting polypyrroles. *Journal of electronic materials,* 15**,** 61-69.

NAITO, K., MATSUNAMI, T., OKUNO, K., MATSUOKA, M. & IWAKURA, C. 1993. Factors affecting the characteristics of the negative electrodes for nickel-hydrogen batteries. *Journal of applied electrochemistry,* 23**,** 1051-1055.

NI, M., LEUNG, D. Y. & LEUNG, M. K. 2007. A review on reforming bio-ethanol for hydrogen production. *International Journal of Hydrogen Energy,* 32**,** 3238-3247.

NIE, H., YAO, Z., ZHOU, X., YANG, Z. & HUANG, S. 2011. Nonenzymatic electrochemical detection of glucose using well-distributed nickel nanoparticles on straight multi-walled carbon nanotubes. *Biosensors and Bioelectronics,* 30**,** 28-34.

NIELSCH, K., MÜLLER, F., LI, A.-P. & GÖSELE, U. 2000. Uniform nickel deposition into ordered alumina pores by pulsed electrodeposition. *Advanced Materials,* 12**,** 582-586.

NIRANJANA, E., SWAMY, B. K., NAIK, R. R., SHERIGARA, B. & JAYADEVAPPA, H. 2009. Electrochemical investigations of potassium ferricyanide and dopamine by sodium dodecyl sulphate modified carbon paste electrode: A cyclic voltammetric study. *Journal of Electroanalytical Chemistry,* 631**,** 1-9.

NIU, X., LAN, M., ZHAO, H. & CHEN, C. 2013. Highly sensitive and selective nonenzymatic detection of glucose using three-dimensional porous nickel nanostructures. *Analytical chemistry,* 85**,** 3561-3569.

NIU, X., LI, Y., TANG, J., HU, Y., ZHAO, H. & LAN, M. 2014. Electrochemical sensing interfaces with tunable porosity for nonenzymatic glucose detection: A Cu foam case. *Biosensors and Bioelectronics,* 51**,** 22-28.

ONWUBU, S. C., MDLULI, P. S. & SINGH, S. 2018. The effect of colloidal silica and diamond suspensions on the surface roughness of automatically finished heat-polymerized acrylic resin. *The Journal of prosthetic dentistry,* 120**,** 485. e1-485. e5.

PAEK, J., KANG, B., KIM, S. & HYUN, J. 2000. Effective thermal conductivity and permeability of aluminum foam materials. *International Journal of Thermophysics,* 21**,** 453-464.

PANDURANGACHAR, M., SWAMY, B. K., CHANDRASHEKAR, B., GILBERT, O., REDDY, S. & SHERIGARA, B. 2010. Electrochemical investigations of potassium ferricyanide and dopamine by 1-butyl-4-methylpyridinium tetrafluoro borate modified carbon paste electrode: A cyclic voltammetric study. *Int J Electrochem Sci,* 5**,** 1187-1202.

PARK, J.-Y., LEE, J.-H., KANG, S., SAUK, J.-H. & SONG, I. 2008. Mass balance research for high electrochemical performance direct methanol fuel cells with reduced methanol crossover at various operating conditions. *Journal of Power Sources,* 178**,** 181-187.

PARK, S., BOO, H. & CHUNG, T. D. 2006. Electrochemical non-enzymatic glucose sensors. *Analytica Chimica Acta,* 556**,** 46-57.

PASERIN, V., MARCUSON, S., SHU, J. & WILKINSON, D. S. 2003. The chemical vapor deposition technique for Inco nickel foam production–manufacturing benefits and potential applications. *Cellular Metals and Metal Foaming Technology*.

PASERIN, V., MARCUSON, S., SHU, J. & WILKINSON, D. S. 2004. CVD technique for Inco nickel foam production. *Advanced engineering materials,* 6**,** 454-459.

PICKETT, D. J. 1979. *Electrochemical reactor design*, Elsevier Science Ltd.

PRASAD, M. A. & SANGARANARAYANAN, M. 2004. Analysis of the diffusion layer thickness, equivalent circuit and conductance behaviour for reversible electron transfer processes in linear sweep voltammetry. *Electrochimica acta,* 49**,** 445-453.

QUIROZ, M. A., MARTÍNEZ-HUITLE, U. A. & MARTÍNEZ-HUITLE, C. A. 2005. Mass transfer measurements in a parallel disk cell using the limiting current technique. *Journal of the Mexican Chemical Society,* 49**,** 279-283.

RAHIM, A. A., TIJANI, A. S. & SHUKRI, F. H. 2015. Simulation Analysis of the Effect of Temperature on Overpotentials in PEM Electrolyzer System. *Journal of Mechanical Engineering,* 12**,** 47-65.

RAMAMURTY, U. & PAUL, A. 2004. Variability in mechanical properties of a metal foam. *Acta Materialia,* 52**,** 869-876.

RECIO, F., HERRASTI, P., VAZQUEZ, L., DE LEÓN, C. P. & WALSH, F. 2013. Mass transfer to a nanostructured nickel electrodeposit of high surface area in a rectangular flow channel. *Electrochimica Acta,* 90**,** 507-513.

RUCH, W. & KIRKEVAG, B. 1990. A process of manufacturing particle reinforced metal foam and product thereof. *European Patent 0,* 483**,** 1994.

SANTOS, E. C., SHIOMI, M., OSAKADA, K. & LAOUI, T. 2006. Rapid manufacturing of metal components by laser forming. *International Journal of Machine Tools and Manufacture,* 46**,** 1459-1468.

SHEN, D. & AKOLKAR, R. 2017. Electrodeposition of Neodymium from NdCl3-Containing Eutectic LiCl–KCl Melts Investigated Using Voltammetry and Diffusion-Reaction Modeling. *Journal of The Electrochemical Society,* 164**,** H5292-H5298.

SHI, Y., SLATERBECK, A. F., SELISKAR, C. J. & HEINEMAN, W. R. 1997. Spectroelectrochemical sensing based on multimode selectivity simultaneously achievable in a single device. 1. Demonstration of concept with ferricyanide. *Analytical chemistry,* 69**,** 3679-3686.

SHIVKUMAR, R., KALAIGNAN, G. P. & VASUDEVAN, T. 1998. Studies with porous zinc electrodes with additives for secondary alkaline batteries. *Journal of power sources,* 75**,** 90-100.

SHRIVASTAVA, A. & GUPTA, V. 2011. Methods for the determination of limit of detection and limit of quantitation of the analytical methods. *Chronicles of Young Scientists,* 2**,** 21-21.

SMITH, R. E., DAVIES, T. J., BAYNES, N. D. B. & NICHOLS, R. J. 2015. The electrochemical characterisation of graphite felts. *Journal of Electroanalytical Chemistry,* 747**,** 29-38.

STEGEMILLER, M. L., HEINEMAN, W. R., SELISKAR, C. J., RIDGWAY, T. H., BRYAN, S. A., HUBLER, T. & SELL, R. L. 2003. Spectroelectrochemical sensing based on multimode selectivity simultaneously achievable in a single device. 11. Design and evaluation of

a small portable sensor for the determination of ferrocyanide in hanford waste samples. *Environmental science & technology,* 37**,** 123-130.

ŠVANCARA, I., VYTŘAS, K., KALCHER, K., WALCARIUS, A. & WANG, J. 2009. Carbon paste electrodes in facts, numbers, and notes: a review on the occasion of the 50 ‐ years jubilee of carbon paste in electrochemistry and electroanalysis. *Electroanalysis: An International Journal Devoted to Fundamental and Practical Aspects of Electroanalysis,* 21**,** 7-28.

SZÁNTO, D., CLEGHORN, S., PONCE ‐ DE ‐ LEÓN, C. & WALSH, F. 2008. The limiting current for reduction of ferricyanide ion at nickel: the importance of experimental conditions. *AIChE Journal,* 54**,** 802-810.

SZÁNTO, D., TRINIDAD, P., WHYTE, I. & WALSH, F. Electrosynthesis and mass transport measurements in laboratory filter-press reactors. Proceedings of 4th European Symposium on Electrochemical Engineering: Contemporary Trends in Electrochemical Engineering,''Prague, Czech Republic, 1996.

TAAMA, W., PLIMLEY, R. & SCOTT, K. 1996. Mass transfer rates in a DEM electrochemical cell. *Electrochimica acta,* 41**,** 543-548.

TAN, Y. H., DAVIS, J. A., FUJIKAWA, K., GANESH, N. V., DEMCHENKO, A. V. & STINE, K. J. 2012. Surface area and pore size characteristics of nanoporous gold subjected to thermal, mechanical, or surface modification studied using gas adsorption isotherms, cyclic voltammetry, thermogravimetric analysis, and scanning electron microscopy. *Journal of materials chemistry,* 22**,** 6733-6745.

TANG, J., WANG, Y., LI, J., DA, P., GENG, J. & ZHENG, G. 2014. Sensitive enzymatic glucose detection by TiO 2 nanowire photoelectrochemical biosensors. *Journal of Materials Chemistry A,* 2**,** 6153-6157.

THIJS, L., VERHAEGHE, F., CRAEGHS, T., VAN HUMBEECK, J. & KRUTH, J.-P. 2010. A study of the microstructural evolution during selective laser melting of Ti–6Al–4V. *Acta Materialia,* 58**,** 3303-3312.

TOGHILL, K. E. & COMPTON, R. G. 2010. Electrochemical non-enzymatic glucose sensors: a perspective and an evaluation. *Int. J. Electrochem. Sci,* 5**,** 1246-1301.

TOGHILL, K. E., XIAO, L., PHILLIPS, M. A. & COMPTON, R. G. 2010. The non-enzymatic determination of glucose using an electrolytically fabricated nickel microparticle modified boron-doped diamond electrode or nickel foil electrode. *Sensors and actuators B: Chemical,* 147**,** 642-652.

TORRES, Y., LASCANO, S., BRIS, J., PAVÓN, J. & RODRIGUEZ, J. A. 2014. Development of porous titanium for biomedical applications: A comparison between loose sintering and space-holder techniques. *Materials Science and Engineering: C,* 37**,** 148-155.

TRACEY, V. 1979. Effect of sintering conditions on structure and strength of porous nickel. *Powder Metallurgy,* 22**,** 45-48.

TUCKER, M. C., LAU, G. Y., JACOBSON, C. P., DEJONGHE, L. C. & VISCO, S. J. 2007. Performance of metal-supported SOFCs with infiltrated electrodes. *Journal of Power Sources,* 171**,** 477-482.

UNDERWOOD, E., STEREOLOGY, Q. & ADDISON-WESLEY, R. 1970. Massachusetts.

WANG, C., WANG, D. & DAI, C. 2008. High-rate capability and enhanced cyclability of rechargeable lithium batteries using foam lithium anode. *Journal of the Electrochemical Society,* 155**,** A390-A394.

WANG, H., PAN, Q., WANG, X., YIN, G. & ZHAO, J. 2009. Improving electrochemical performance of NiO films by electrodeposition on foam nickel substrates. *Journal of applied electrochemistry,* 39**,** 1597-1602.
WANG, H. & PILON, L. 2011. Accurate simulations of electric double layer capacitance of ultramicroelectrodes. *The Journal of Physical Chemistry C,* 115**,** 16711-16719.
WANG, J. 2008. Electrochemical glucose biosensors. *Chemical reviews,* 108**,** 814-825.
WANG, L., XIE, Y., WEI, C., LU, X., LI, X. & SONG, Y. 2015. Hierarchical NiO superstructures/foam Ni electrode derived from Ni metal-organic framework flakes on foam Ni for glucose sensing. *Electrochimica Acta,* 174**,** 846-852.
WANG, X., YANG, D.-P., HUANG, P., LI, M., LI, C., CHEN, D. & CUI, D. 2012. Hierarchically assembled Au microspheres and sea urchin-like architectures: formation mechanism and SERS study. *Nanoscale,* 4**,** 7766-7772.
WARNKE, P. H., DOUGLAS, T., WOLLNY, P., SHERRY, E., STEINER, M., GALONSKA, S., BECKER, S. T., SPRINGER, I. N., WILTFANG, J. & SIVANANTHAN, S. 2008. Rapid prototyping: porous titanium alloy scaffolds produced by selective laser melting for bone tissue engineering. *Tissue engineering part c: Methods,* 15**,** 115-124.
WOOTEN, M., KARRA, S., ZHANG, M. & GORSKI, W. 2013. On the direct electron transfer, sensing, and enzyme activity in the glucose oxidase/carbon nanotubes system. *Analytical chemistry,* 86**,** 752-757.
XIA, K., YANG, C., CHEN, Y., TIAN, L., SU, Y., WANG, J. & LI, L. 2017. In situ fabrication of Ni (OH) 2 flakes on Ni foam through electrochemical corrosion as high sensitive and stable binder-free electrode for glucose sensing. *Sensors and Actuators B: Chemical,* 240**,** 979-987.
XIAO, Z. & ZHAO, Y. 2013. Heat transfer coefficient of porous copper with homogeneous and hybrid structures in active cooling. *Journal of Materials Research,* 28**,** 2545-2553.
YAN, X., ZHAO, T., AN, L., ZHAO, G. & ZENG, L. 2014. A micro-porous current collector enabling passive direct methanol fuel cells to operate with highly concentrated fuel. *Electrochimica Acta,* 139**,** 7-12.
YAO, M., OKUNO, K., IWAKI, T., AWAZU, T. & SAKAI, T. 2010. Long cycle-life LiFePO 4/Cu-Sn lithium ion battery using foam-type three-dimensional current collector. *Journal of Power Sources,* 195**,** 2077-2081.
YOSHIO, M., BRODD, R. J. & KOZAWA, A. 2009. *Lithium-ion batteries*, Springer.
YU, M., CHEN, J., LIU, J., LI, S., MA, Y., ZHANG, J. & AN, J. 2015. Mesoporous NiCo 2 O 4 nanoneedles grown on 3D graphene-nickel foam for supercapacitor and methanol electro-oxidation. *Electrochimica Acta,* 151**,** 99-108.
YUNUS, C. A. & AFSHIN, J. G. 2011. Heat and mass transfer: fundamentals and applications. *Tata McGraw-Hill, New Delhi, India*.
ZARDIACKAS, L. D., PARSELL, D. E., DILLON, L. D., MITCHELL, D. W., NUNNERY, L. A. & POGGIE, R. 2001. Structure, metallurgy, and mechanical properties of a porous tantalum foam. *Journal of biomedical materials research,* 58**,** 180-187.
ZHANG, L., LI, H., NI, Y., LI, J., LIAO, K. & ZHAO, G. 2009. Porous cuprous oxide microcubes for non-enzymatic amperometric hydrogen peroxide and glucose sensing. *Electrochemistry Communications,* 11**,** 812-815.
ZHANG, L. & ZHAO, Y. 2008. Fabrication of high melting-point porous metals by lost carbonate sintering process via decomposition route. *Proceedings of the Institution of Mechanical Engineers, Part B: Journal of Engineering Manufacture,* 222**,** 267-271.

ZHAO, Y. 2003. Stochastic modelling of removability of NaCl in sintering and dissolution process to produce Al foams. *Journal of Porous Materials,* 10**,** 105-111.
ZHAO, Y., FUNG, T., ZHANG, L. & ZHANG, F. 2005. Lost carbonate sintering process for manufacturing metal foams. *Scripta Materialia,* 52**,** 295-298.
ZHAO, Y. & SUN, D. 2001. A novel sintering-dissolution process for manufacturing Al foams. *Scripta materialia,* 44**,** 105-110.
ZHOU, W., WANG, Q., QIU, Q., TANG, Y., TU, J., HUI, K. & HUI, K. 2015. Heat and mass transfer characterization of porous copper fiber sintered felt as catalyst support for methanol steam reforming. *Fuel,* 145**,** 136-142.
ZHU, P. & ZHAO, Y. 2017a. Effects of electrochemical reaction and surface morphology on electroactive surface area of porous copper manufactured by Lost Carbonate Sintering. *RSC Advances,* 7**,** 26392-26400.
ZHU, P. & ZHAO, Y. 2017b. Mass Transfer Performance of Porous Nickel Manufactured by Lost Carbonate Sintering Process. *Advanced Engineering Materials,* 19**,** 1700392.

APPENDIX

Tables A-1 – 13 show the raw data used in Chapter 4, including the geometric, electroactive and real surface areas for porous Cu samples manufactured using Cu powders with different particle sizes and processed by different treatments.

Table. A-1 Geometric surface areas of the LCS porous Cu

Pore size (μm)	Porosity	A_{VG} (cm^{-1})	A_{MG} (cm^2/g)
250 – 425	0.56	64	16.18
	0.59	72	19.92
	0.64	80	25.21
	0.68	84	29.36
	0.72	92	36.80
	0.77	100	48.31
425 – 710	0.56	44	11.15
	0.60	48	13.52
	0.63	52	15.62
	0.67	56	19.22
	0.72	60	24.23
	0.78	64	32.15
710 – 1000	0.57	32	8.27
	0.62	32	9.43
	0.64	36	11.18
	0.67	38	13.04
	0.72	40	16.15
	0.78	44	22.74
1000 – 1500	0.53	20	4.74
	0.63	22	6.72
	0.65	24	7.61
	0.69	24	8.61
	0.74	28	12.06
	0.76	32	15.17

Table. A-2 Electroactive surface area measured by peak 1 for the LCS porous Cu manufactured by 850 ˚C sintering

Particle size (μm)	Nominal Porosity	A_{VE_p1} (cm^{-1})
<20	0.50	629.64
	0.55	534.44
	0.60	636.71
	0.65	795.10
	0.70	579.06
	0.75	601.33
20 – 45	0.50	783.48
	0.55	741.62
	0.60	807.36
	0.65	787.17
	0.70	790.52
	0.75	834.98
45 – 75	0.50	741.39
	0.55	841.08
	0.60	686.49
	0.65	771.65
	0.70	743.15
	0.75	717.87
75 – 90	0.50	663.71
	0.55	707.05
	0.60	727.10
	0.65	738.72
	0.70	610.27
	0.75	676.93

Table. A-3 Electroactive surface area measured by peak 1 for the LCS porous Cu manufactured by 850 ˚C sintering and chemical etching

Particle size (μm)	Nominal Porosity	A_{VE_p1} (cm^{-1})
<20	0.50	496.10
	0.55	434.54
	0.60	538.45
	0.65	520.13
20 – 45	0.50	621.97
	0.55	631.66
	0.60	605.18
	0.65	624.68
45 – 75	0.50	573.61
	0.55	658.98
	0.60	501.77
	0.65	579.06
75 – 90	0.50	503.64
	0.55	519.45
	0.60	548.41
	0.65	550.01

Table. A-4 Electroactive surface area measured by peak 1 for the LCS porous Cu manufactured by 950 ˚C sintering

Particle size (μm)	Nominal Porosity	A_{VE_p1} (cm^{-1})
<20	0.50	256.91
	0.55	219.15
	0.60	281.76
	0.65	257.27
	0.70	212.35
	0.75	253.47
20 – 45	0.50	279.41
	0.55	222.27
	0.60	246.02
	0.65	269.90
	0.70	312.79
	0.75	345.15
45 – 75	0.50	332.79
	0.55	302.90
	0.60	297.69
	0.65	308.30
	0.70	321.79
	0.75	368.07
75 – 90	0.50	262.05
	0.55	203.75
	0.60	261.14
	0.65	257.99
	0.70	281.77
	0.75	284.49

Table. A-5 Electroactive surface area measured by peak 1 for the LCS porous Cu manufactured by 950 ˚C sintering and chemical etching

Particle size (μm)	Nominal Porosity	A_{VE_p1} (cm^{-1})
<20	0.50	181.91
	0.55	141.57
	0.60	213.04
	0.65	197.37
20 – 45	0.50	202.63
	0.55	177.29
	0.60	191.04
	0.65	214.33
45 – 75	0.50	222.85
	0.55	225.70
	0.60	206.28
	0.65	229.39
75 – 90	0.50	205.39
	0.55	189.19
	0.60	217.16
	0.65	187.87

Table. A-6 Electroactive surface area measured by peak 2 for the LCS porous Cu manufactured by 850 ˚C sintering

Particle size (μm)	Nominal Porosity	A_{VE_p2} (cm^{-1})
<20	0.50	279.24
	0.55	248.72
	0.60	270.50
	0.65	364.66
	0.70	264.66
	0.75	228.07
20 – 45	0.50	317.27
	0.55	276.95
	0.60	295.88
	0.65	304.66
	0.70	323.54
	0.75	370.95
45 – 75	0.50	337.68
	0.55	368.62
	0.60	371.27
	0.65	312.93
	0.70	309.71
	0.75	326.32
75 – 90	0.50	297.69
	0.55	261.84
	0.60	299.67
	0.65	328.97
	0.70	278.08
	0.75	342.57

Table. A-7 Electroactive surface area measured by peak 2 for the LCS porous Cu manufactured by 850 ˚C sintering and chemical etching

Particle size (μm)	Nominal Porosity	A_{VE_p2} (cm^{-1})
<20	0.50	240.56
	0.55	207.52
	0.60	247.96
	0.65	250.05
20 – 45	0.50	276.85
	0.55	245.89
	0.60	237.54
	0.65	320.84
45 – 75	0.50	296.31
	0.55	336.79
	0.60	352.71
	0.65	247.16
75 – 90	0.50	275.10
	0.55	287.64
	0.60	272.35
	0.65	286.99

Table. A-8 Electroactive surface area measured by peak 2 for the LCS porous Cu manufactured by 950 ˚C sintering

Particle size (μm)	Nominal Porosity	A_{VE_p2} (cm^{-1})
<20	0.50	184.98
	0.55	122.89
	0.60	186.12
	0.65	219.05
	0.70	158.40
	0.75	201.41
20 – 45	0.50	180.31
	0.55	144.35
	0.60	166.37
	0.65	185.33
	0.70	188.86
	0.75	178.76
45 – 75	0.50	218.75
	0.55	190.59
	0.60	189.40
	0.65	201.12
	0.70	214.09
	0.75	251.72
75 – 90	0.50	190.76
	0.55	130.42
	0.60	176.39
	0.65	157.74
	0.70	202.80
	0.75	234.76

Table. A-9 Electroactive surface area measured by peak 2 for the LCS porous Cu manufactured by 950 ˚C sintering and chemical etching

Particle size (μm)	Nominal Porosity	A_{VE_p2} (cm^{-1})
<20	0.50	150.40
	0.55	100.57
	0.60	166.37
	0.65	173.59
20 – 45	0.50	171.91
	0.55	132.57
	0.60	162.20
	0.65	193.09
45 – 75	0.50	191.17
	0.55	181.13
	0.60	191.86
	0.65	189.71
75 – 90	0.50	165.28
	0.55	164.70
	0.60	189.46
	0.65	123.73

Table. A-10 Real surface area of the LCS porous Cu manufactured by 850 ˚C sintering

Particle size (μm)	Nominal Porosity	A_{VR} (cm^{-1})
<20	0.50	1741.11
	0.55	1460.96
	0.60	1801.06
	0.65	1901.73
	0.70	1771.13
	0.75	1847.77
20 – 45	0.50	1881.32
	0.55	1720.43
	0.60	1878.02
	0.65	1870.03
	0.70	1895.30
	0.75	2015.12
45 – 75	0.50	1777.77
	0.55	1615.38
	0.60	1884.62
	0.65	1807.69
	0.70	1760.00
	0.75	1732.26
75 – 90	0.50	1670.47
	0.55	1624.39
	0.60	1724.42
	0.65	1689.32
	0.70	1545.48
	0.75	1728.60

Table. A-11 Real surface area of the LCS porous Cu manufactured by 850 ˚C sintering and chemical etching

Particle size (μm)	Nominal Porosity	A_{VR} (cm^{-1})
<20	0.50	1443.87
	0.55	1278.34
	0.60	1456.17
	0.65	1584.77
20 – 45	0.50	1690.83
	0.55	1683.03
	0.60	1678.23
	0.65	1675.24
45 – 75	0.50	1523.46
	0.55	1461.54
	0.60	1615.38
	0.65	1576.92
75 – 90	0.50	1335.24
	0.55	1465.92
	0.60	1379.53
	0.65	1375.02

Table. A-12 Real surface area of the LCS porous Cu manufactured by 950 ˚C sintering

Particle size (μm)	Nominal Porosity	A_{VR} (cm^{-1})
<20	0.50	1089.07
	0.55	676.86
	0.60	964.84
	0.65	1274.09
	0.70	1073.54
	0.75	1138.01
20 – 45	0.50	1156.37
	0.55	928.77
	0.60	1165.85
	0.65	1006.17
	0.70	1143.65
	0.75	1340.83
45 – 75	0.50	1277.13
	0.55	958.52
	0.60	1104.21
	0.65	1250.05
	0.70	1313.90
	0.75	1461.45
75 – 90	0.50	1108.07
	0.55	890.08
	0.60	1005.05
	0.65	1006.17
	0.70	1154.64
	0.75	1252.80

Table. A-13 Real surface area of the LCS porous Cu manufactured by 950 ˚C sintering and chemical etching

Particle size (μm)	Nominal Porosity	A_{VR} (cm^{-1})
<20	0.50	1008.88
	0.55	676.86
	0.60	1165.85
	0.65	1234.27
20 – 45	0.50	1019.97
	0.55	851.38
	0.60	924.64
	0.65	1199.67
45 – 75	0.50	1185.04
	0.55	1210.98
	0.60	1340.83
	0.65	1073.54
75 – 90	0.50	935.75
	0.55	851.38
	0.60	1005.05
	0.65	851.38

Tables A-14 – 21 show the raw data in used Chapter 5, including the geometric, electroactive and real surface areas for porous Ni samples manufactured using Ni powders with different particle sizes.

Table. A-14 Geometric surface area of the LCS porous Ni manufactured using 25 μm particles.

Pore size (μm)	Porosity	A_{VG} (cm^{-1})	A_{MG} (cm^2/g)
250 – 425	0.53	60	14.37
	0.60	73	20.44
	0.62	77	23.02
	0.67	82	28.32
	0.72	92	36.67
	0.77	100	48.13
425 – 710	0.58	46	12.26
	0.62	51	15.01
	0.65	54	17.44
	0.68	57	19.79
	0.72	60	24.32
	0.77	64	30.61
710 – 1000	0.60	32	9.04
	0.60	32	9.04
	0.69	40	14.46
	0.66	38	12.68
	0.74	42	17.96
	0.75	42	19.03
1000 – 1500	0.55	20	5.03
	0.60	22	6.11
	0.64	24	7.39
	0.67	24	8.12
	0.74	30	12.83
	0.73	30	12.49

Table. A-15 Geometric surface area of the LCS porous Ni manufactured using 38 µm particles.

Pore size (µm)	Porosity	A_{VG} (cm^{-1})	A_{MG} (cm^2/g)
250 – 425	0.58	68	18.24
	0.62	74	22.10
	0.66	80	26.61
	0.70	84	31.37
	0.74	94	40.99
	0.79	98	53.41
425 – 710	0.60	46	12.89
	0.61	48	13.93
	0.66	52	17.30
	0.70	56	21.04
	0.75	60	27.49
	0.79	64	34.23
710 – 1000	0.62	30	8.79
	0.63	32	9.75
	0.68	36	12.50
	0.72	38	15.28
	0.76	42	19.60
	0.81	46	27.30
1000 – 1500	0.58	20	5.41
	0.63	22	6.69
	0.69	24	8.63
	0.70	24	8.96
	0.75	28	12.71
	0.80	32	18.09

Table. A-16 Geometric surface area of the LCS porous Ni manufactured using 75 µm particles.

Pore size (µm)	Porosity	A_{VG} (cm^{-1})	A_{MG} (cm^2/g)
250 – 425	0.60	68	19.22
	0.65	76	24.11
	0.70	82	30.35
	0.74	90	38.49
	0.82	96	61.04
425 – 710	0.57	42	11.09
	0.65	50	16.15
	0.69	54	19.42
	0.72	56	22.16
	0.79	60	31.37
710 – 1000	0.66	36	11.77
	0.64	34	10.55
	0.67	36	12.23
	0.73	42	17.49
	0.80	44	24.23
1000 – 1500	0.72	26	10.55
	0.57	20	5.24
	0.66	22	7.17
	0.73	26	10.83
	0.83	30	19.43

Table. A-17 Volumetric specific electroactive surface area of the LCS porous Ni.

Pore size (µm)	Porosity	A_{VE} (cm^{-1})		
		0.005 V/s	0.01 V/s	0.05 V/s
250 – 425	0.58	39.77	53.72	85.28
	0.62	42.87	52.54	84.37
	0.66	44.85	57.75	91.72
	0.70	51.05	64.77	101.15
	0.74	52.32	69.02	104.43
	0.79	61.10	76.74	110.15
	0.80	62.52	78.15	112.58
425 – 710	0.60	41.47	51.84	72.45
	0.61	43.32	53.25	77.78
	0.66	44.85	55.50	80.93
	0.70	48.67	58.65	84.37
	0.75	52.52	63.05	85.94
	0.79	59.10	67.30	92.03
	0.84	59.14	69.05	93.06
710 – 1000	0.62	39.35	45.99	67.30
	0.63	42.50	49.17	70.20
	0.68	41.51	49.72	70.59
	0.72	43.68	50.92	74.15
	0.76	46.93	55.30	75.98
	0.81	49.02	57.72	83.22
	0.82	48.68	61.75	91.26
1000 – 1500	0.58	36.36	40.72	51.71
	0.63	38.25	44.05	62.84
	0.69	39.91	45.92	69.40
	0.70	42.83	51.62	72.32
	0.75	45.59	55.72	79.56
	0.80	44.89	55.20	78.56
	0.84	48.26	58.64	84.84

Table. A-18 Gravimetric specific electroactive surface area of the LCS porous Ni.

Pore size (μm)	Porosity	A_{ME} (cm^2/g)		
		0.005 V/s	0.01 V/s	0.05 V/s
250 – 425	0.58	10.66	14.39	22.85
	0.62	12.79	15.67	25.17
	0.66	14.90	19.19	30.48
	0.70	19.04	24.16	37.73
	0.74	22.79	30.06	45.48
	0.79	33.26	41.77	59.96
	0.80	35.64	44.54	64.17
425 – 710	0.60	11.61	14.51	20.28
	0.61	12.56	15.44	22.56
	0.66	14.90	18.44	26.89
	0.70	18.26	22.01	31.66
	0.75	24.03	28.86	39.33
	0.79	31.58	35.96	49.17
	0.84	40.60	47.40	63.88
710 – 1000	0.62	11.51	13.45	19.69
	0.63	12.94	14.97	21.37
	0.68	14.39	17.24	24.47
	0.72	17.55	20.45	29.79
	0.76	21.88	25.78	35.42
	0.81	29.06	34.22	49.34
	0.82	29.68	37.65	55.65
1000 – 1500	0.58	9.83	11.01	13.98
	0.63	11.61	13.37	19.08
	0.69	14.34	16.50	24.94
	0.70	15.98	19.25	26.98
	0.75	20.67	25.26	36.07
	0.80	25.34	31.16	44.35
	0.84	34.38	41.78	60.44

Table. A-19 Volumetric specific real surface area of the LCS porous Ni manufactured using 25 μm particles.

Pore size (μm)	Porosity	A_{VR} (cm^{-1})	A_{MR} (cm^2/g)
250 – 425	0.53	1581.16	378.25
	0.60	1218.89	340.89
	0.62	1067.20	318.63
	0.67	1049.33	362.04
	0.72	892.05	355.12
	0.77	667.83	321.07
425 – 710	0.58	1008.82	268.65
	0.62	1087.95	319.90
	0.65	1005.80	324.48
	0.68	1027.60	356.29
	0.72	804.35	325.64
	0.77	604.00	288.54
710 – 1000	0.60	985.32	278.14
	0.60	886.86	250.35
	0.69	896.13	323.56
	0.66	910.83	303.61
	0.74	699.59	298.90
	0.75	497.11	224.93
1000 – 1500	0.55	909.03	228.54
	0.60	815.15	226.20
	0.64	804.35	247.49
	0.67	681.57	230.43
	0.74	526.09	224.82
	0.73	531.89	221.27

Table. A-20 Volumetric specific real surface area of the LCS porous Ni manufactured using 38 μm particles.

Pore size (μm)	Porosity	A_{VR} (cm^{-1})	A_{MR} (cm^2/g)
250 – 425	0.58	1392.31	373.04
	0.62	1299.88	387.71
	0.66	1019.97	338.90
	0.70	792.42	295.59
	0.74	645.93	281.32
	0.79	508.92	277.06
425 – 710	0.60	769.25	215.28
	0.61	827.60	239.99
	0.66	917.08	304.71
	0.70	788.41	294.09
	0.75	519.68	237.83
	0.79	433.83	236.18
710 – 1000	0.62	876.46	256.41
	0.63	743.38	226.30
	0.68	738.13	255.93
	0.72	728.66	292.71
	0.76	665.22	310.13
	0.81	477.73	283.19
1000 – 1500	0.58	984.18	266.05
	0.63	731.66	222.73
	0.69	586.75	210.80
	0.70	546.50	203.85
	0.75	429.21	194.58
	0.80	351.05	198.19

Table. A-21 Volumetric specific real surface area of the LCS porous Ni manufactured using 75 μm particles.

Pore size (μm)	Porosity	A_{VR} (cm^{-1})	A_{MR} (cm^2/g)
250 – 425	0.60	947.83	267.56
	0.65	789.33	250.10
	0.70	636.58	235.31
	0.74	593.38	253.52
	0.82	457.44	290.53
425 – 710	0.57	687.32	181.30
	0.65	631.89	200.21
	0.69	528.78	189.98
	0.72	461.08	182.22
	0.79	341.56	178.37
710 – 1000	0.66	618.83	202.09
	0.64	591.10	183.22
	0.67	560.28	190.13
	0.73	417.50	173.68
	0.80	227.40	125.07
1000 – 1500	0.72	451.35	182.95
	0.57	639.22	167.34
	0.66	570.15	185.58
	0.73	455.11	189.33
	0.83	214.89	139.01

Table A-22 shows the raw data used in Chapter 6, including the mass transfer coefficient of porous Ni samples with different pore sizes and porosities at different flow rates.

Table. A-22 Mass transfer coefficient of the LCS porous Ni.

Pore size (μm)	Nominal Porosity	Mass transfer coefficient (cm/s)							
		0.28 mL/s	0.47 mL/s	0.70 mL/s	0.93 mL/s	1.17 mL/s	1.40 mL/s	1.63 mL/s	1.87 mL/s
250 – 425	0.55	1.15E-03	8.87E-04	8.20E-04	6.88E-04	7.07E-04	1.15E-03	8.87E-04	8.20E-04
	0.60	1.72E-03	1.28E-03	1.18E-03	9.84E-04	9.44E-04	1.72E-03	1.28E-03	1.18E-03
	0.65	2.40E-03	1.76E-03	1.61E-03	1.23E-03	1.20E-03	2.40E-03	1.76E-03	1.61E-03
	0.70	3.12E-03	2.17E-03	1.98E-03	1.52E-03	1.40E-03	3.12E-03	2.17E-03	1.98E-03
	0.75	3.79E-03	2.56E-03	2.34E-03	1.79E-03	1.59E-03	3.79E-03	2.56E-03	2.34E-03
425 – 710	0.55	1.61E-03	1.30E-03	1.38E-03	1.38E-03	1.18E-03	1.61E-03	1.30E-03	1.38E-03
	0.60	2.61E-03	2.10E-03	1.89E-03	1.96E-03	1.53E-03	2.61E-03	2.10E-03	1.89E-03
	0.65	3.83E-03	3.17E-03	2.53E-03	2.63E-03	2.21E-03	3.83E-03	3.17E-03	2.53E-03
	0.70	5.04E-03	4.27E-03	3.29E-03	3.38E-03	2.73E-03	5.04E-03	4.27E-03	3.29E-03
	0.75	6.23E-03	5.21E-03	4.11E-03	3.96E-03	3.23E-03	6.23E-03	5.21E-03	4.11E-03
710 – 1000	0.55	1.93E-03	1.34E-03	1.36E-03	1.29E-03	1.93E-03	1.34E-03	1.36E-03	1.29E-03
	0.60	3.06E-03	2.13E-03	2.09E-03	1.95E-03	3.06E-03	2.13E-03	2.09E-03	1.95E-03
	0.65	4.45E-03	3.08E-03	2.95E-03	2.70E-03	4.45E-03	3.08E-03	2.95E-03	2.70E-03
	0.70	5.73E-03	4.01E-03	3.75E-03	3.41E-03	5.73E-03	4.01E-03	3.75E-03	3.41E-03
	0.75	7.41E-03	4.91E-03	4.52E-03	4.08E-03	7.41E-03	4.91E-03	4.52E-03	4.08E-03
1000 –1500	0.55	1.93E-03	1.79E-03	1.46E-03	1.14E-03	1.93E-03	1.79E-03	1.46E-03	1.14E-03
	0.60	3.23E-03	2.96E-03	2.36E-03	1.72E-03	3.23E-03	2.96E-03	2.36E-03	1.72E-03
	0.65	5.00E-03	4.42E-03	3.62E-03	2.43E-03	5.00E-03	4.42E-03	3.62E-03	2.43E-03
	0.70	6.69E-03	5.87E-03	4.77E-03	2.88E-03	6.69E-03	5.87E-03	4.77E-03	2.88E-03
	0.75	8.39E-03	7.31E-03	6.11E-03	3.48E-03	8.39E-03	7.31E-03	6.11E-03	3.48E-03

Tables A23 – 24 show the raw data used in Chapter 7, including the peak and limiting currents in the measurements of ferricyanide concentration using cyclic voltammetry peak current and linear voltammetry limiting current techniques, respectively.

Table A-23 Measurement of the concentration of ferricyanide using the CV technique.

Concentration (mM)	Anodic peak current (mA)			
	0.005 V/s	0.01 V/s	0.05 V/s	0.1 V/s
0.1	0.162	0.272	1.05	1.58
0.2	0.189	0.321	1.15	1.72
0.3	0.215	0.363	1.24	1.89
0.4	0.248	0.42	1.33	2.02
0.5	0.287	0.47	1.49	2.19
0.6	0.331	0.542	1.61	2.3
0.7	0.367	0.615	1.76	2.55
0.8	0.405	0.655	1.93	2.76
0.9	0.448	0.746	2.09	2.96
1	0.49	0.801	2.2	3.16
2	0.806	1.29	3.52	4.92
4	1.38	2.22	5.65	7.91
6	2.1	3.27	8	10.9
8	2.77	4.16	9.8	13.3
10	3.41	5.01	11.6	15.7

Table A-24 Measurement of the concentration of ferricyanide using the LV technique.

Concentration (mM)	Limiting current (mA)		
	16.8 mL/min	42 mL/min	84 mL/min
0.005	0.0406	0.0591	0.0795
0.006	0.0487	0.0708	0.103
0.007	0.0607	0.086	0.124
0.008	0.0694	0.102	0.149
0.009	0.0786	0.12	0.175
0.01	0.0887	0.135	0.211
0.025	0.202	0.338	0.51
0.05	0.38	0.641	0.971
0.075	0.561	0.964	1.46
0.1	0.743	1.31	1.97
0.2	1.51	2.64	4.03
0.3	2.24	3.94	6.12
0.4	3.03	5.42	8.04
0.5	3.67	6.61	10